

**ROCK FALL ENGINEERING: DEVELOPMENT AND CALIBRATION OF AN IMPROVED
MODEL FOR ANALYSIS OF ROCK FALL HAZARDS ON HIGHWAYS AND RAILWAYS**

by

Duncan C. Wyllie

A THESIS SUBMITTED IN PARTIAL FULFILLMENT OF THE REQUIREMENTS FOR THE
DEGREE OF

DOCTOR OF PHILOSOPHY

in

The Faculty of Graduate and Postdoctoral Studies

(Geological Engineering)

THE UNIVERSITY OF BRITISH COLUMBIA

(Vancouver)

June 2014

© Duncan C. Wyllie, 2014

Abstract

My research on rock falls over the last five years is an extension of my 45 year professional career that has included a wide variety of rock fall projects. This experience has provided me with an excellent understanding of rock fall behavior; the objective of my research has been to apply this to developing improvements in rock fall modeling methods and design of rock fall containment structures. My research to meet these objectives has involved the following:

Case studies – details of rock fall behavior at six locations with varied topography and geology are presented, and the results have been used to verify the application of impact mechanics theory to rock falls, and to calibrate modeling programs.

Rock fall trajectories and velocities – the application of Newtonian mechanics to rock fall trajectories and velocities is described, and results compared with actual translational and angular velocities, and trajectory heights.

Impact mechanics – the application of theoretical impact mechanics to rock fall impacts is discussed in terms of [normal impulse – relative velocity] diagrams for rough, rotating bodies, and equations relating impact and restitution velocities and angles.

Coefficient of restitution – it is shown that the normal coefficient of restitution defined by the normal final and impact velocities is related primarily to impact angle rather than slope material properties. Furthermore, for shallow impact angles less than about 20 degrees, the normal coefficient of restitution can be greater than 1.0.

Energy changes – energy is lost during impact and gained during trajectories. Equations for energy changes are developed, as well as diagrams showing values of changing potential, kinetic and angular energies during rock falls.

Rock fall modeling – results of rock fall modeling using the RocScience program *RocFall 4.0* for five case studies are presented; the applicable input parameters are listed.

Design of protection structures – impact mechanics and scale model tests of protection nets show that these structures can be designed to redirect rather than stop rock falls, and to absorb energy uniformly during impact. These properties mean that only a portion of the impact energy is absorbed by the net and that forces induced in the net are minimized.

Preface

This dissertation is original, independent work of the author, Duncan C. Wyllie.

The work includes six case studies. Field data for two of the case studies (Tornado and Mount Stephen) is new data that was collected by the author specifically for this research. The third case study (asphalt) is a rock fall that was carefully documented for a project; permission to use this data for the research has been obtained from the client. The other three studies are published data: Kreuger Quarry rock fall tests in Oregon, Uma-gun Doi-cho rock fall test site in Ehime Prefecture, Japan and laboratory tests at Kanazawa University, Japan. The Oregon case study is public domain data, while permission to use the Japanese data has been obtained from the authors.

Portions of the dissertation will be published in 2014 as follows:

- *Calibration of Rock Fall Parameters*, to be published in the International Journal of rock Mechanics and Mining Sciences; the material for this paper forms part of Chapters 2 and 4 of the thesis.
- *Rock Fall Engineering*, a textbook to be published by Taylor and Francis, in London, U.K.; the book contains Chapters 2 to 7 of the thesis and the appendices, and four additional chapters.

Duncan C. Wyllie, P. Eng.

Dr. Erik Eberhardt, Ph.D., P. Eng.

January 2014

Table of Contents

ABSTRACT	ii
PREFACE.....	iii
TABLE OF CONTENTS	iv
LIST OF TABLES	viii
LIST OF FIGURES	ix
LIST OF SYMBOLS.....	xv
1 INTRODUCTION – OBJECTIVES AND METHODOLOGY	1
1.1 Rock falls – causes and consequences	1
1.2 Background to rock fall research program.....	3
1.3 Objectives of research.....	5
1.3.1 Objective #1 – Document rock fall events	6
1.3.2 Objective #2 – Develop applications of impact mechanics to rock fall..	6
1.3.3 Objective #3 – Calibrate of rock fall modeling parameters.....	6
1.3.4 Objective #4 – Test improved rock fall protection structures	7
1.4 Methodology	7
1.4.1 1 – Documentation of rock fall events	7
1.4.2 2 – Trajectories and translational/rotational velocities	8
1.4.3 3 – Application of impact mechanics to rock falls.....	8
1.4.4 4 – Rock fall modeling	9
1.4.5 5 – Development and testing of attenuator-type rock fall fences.....	9
1.4.6 Conclusions.....	10
2 DOCUMENTATION OF ROCK FALL EVENTS.....	11
2.1 Impacts on rock slopes	12
2.1.1 Mt. Stephen, Canada – 2000 m high rock slope.....	13
2.1.2 Kreuger Quarry, Oregon – rock fall test site	18
2.1.3 Ehime, Japan – rock fall test site	20
2.2 Impacts on talus and colluvium slopes.....	23
2.2.1 Ehime, Japan – rock fall tests on talus	23
2.2.2 Tornado Mountain – rock falls on colluvium	24
2.3 Impact on asphalt.....	30
2.4 Impact with concrete	32
2.5 Summary of case study results.....	32
3 ROCK FALL VELOCITIES AND TRAJECTORIES.....	35
3.1 Trajectory calculations	35
3.1.1 Trajectory equation.....	36

3.1.2	Nomenclature – trajectories and impacts.....	38
3.1.3	Rock fall trajectories.....	38
3.1.4	Trajectory height and length.....	41
3.1.5	Field trajectory heights.....	44
3.2	Rock fall velocities.....	47
3.2.1	Field velocity measurements.....	47
3.2.2	Effect of friction and slope angle on velocity.....	48
3.3	Variation of trajectories with restitution angle.....	51
3.3.1	Calculated trajectories for varying restitution angles (θ_0).....	51
3.3.2	Field values of restitution angles (θ_0).....	52
3.4	Angular velocity.....	56
3.4.1	Field measurements of angular velocity.....	56
3.4.2	Relationship between trajectories and angular velocity.....	59
3.5	Field observations of rock fall trajectories.....	59
3.5.1	Rock falls down gullies.....	60
3.5.2	Run-out distance.....	61
3.5.3	Dispersion in run-out area.....	62
4	IMPACT MECHANICS.....	63
4.1	Principles of rigid body impact.....	63
4.1.1	Rigid body impact.....	63
4.1.2	Kinetics of rigid bodies.....	65
4.2	Forces and impulses generated during collinear impact.....	65
4.3	Energy changes during impact.....	67
4.4	Coefficient of restitution.....	69
4.5	For frictional angular velocity changes during impact, for rough surface.....	73
4.6	Impact behaviour for rough, rotating body.....	76
4.6.1	Impulse calculations.....	77
4.6.2	Final velocities for rock fall impacts.....	79
4.6.3	Example of impact mechanics calculation.....	82
4.6.4	Effect of angular velocity on trajectories.....	83
4.7	Calculated vs. actual restitution velocities.....	85
5	COEFFICIENT OF RESTITUTION.....	87
5.1	Newton’s coefficient of restitution.....	88
5.2	Normal coefficient of restitution.....	89
5.2.1	Theoretical relationship between impact angle and normal coefficient of restitution.....	90
5.2.2	Field data showing relationship between impact angle and normal coefficient of restitution.....	95
5.2.3	Application of $[\theta_i - e_N]$ relationship to rock fall modeling.....	98
5.3	Tangential coefficient of restitution and friction.....	99
5.3.1	Field values of tangential coefficient of restitution.....	100
5.3.2	Application of e_T to rock fall modeling.....	102

6	ENERGY CHANGES DURING IMPACTS AND TRAJECTORIES	104
6.1	Impact mechanics theory and kinetic energy changes	105
6.1.1	Kinetic energy changes for normal impact, non-rotating body	105
6.1.2	Kinetic energy changes for inclined impact, rotating body.....	110
6.2	Rotational energy gains/losses.....	116
6.3	Total energy losses	117
6.4	Energy loss diagrams	118
6.4.1	Energy partition diagram for potential, kinetic and rotational energies 119	
6.4.2	Energy head.....	121
6.5	Loss of mass during impact	122
6.6	Effect of trees on energy losses	127
7	ROCK FALL MODELING	131
7.1	Spreadsheet calculations.....	132
7.2	Terrain model – two dimensional v. three dimensional analysis.....	133
7.3	Modeling methods – lumped mass	134
7.3.1	Rock fall mass and dimensions.....	134
7.3.2	Slope definition parameters.....	135
7.3.3	Rock fall seeder	135
7.3.4	Normal coefficient of restitution.....	136
7.3.5	Tangential coefficient of restitution and friction	137
7.3.6	Surface roughness	138
7.3.7	Rotational velocity.....	139
7.3.8	Probabilistic analysis	140
7.3.9	Data sampling points.....	140
7.4	Modeling methods – discrete element model (DEM).....	141
7.5	Modeling results of case studies	141
7.5.1	Rock fall model of Mt. Stephen events	141
7.5.2	Rock fall model of Kreuger Quarry, Oregon tests	145
7.5.3	Rock fall model of Ehime, Japan test site.....	148
7.5.4	Rock fall model of Tornado Mountain events.....	152
7.5.5	Rock fall model of asphalt impact event	156
7.6	Summary of rock fall simulation results.....	158
8	DESIGN PRINCIPLES OF ROCK FALL PROTECTION STRUCTURES.....	160
8.1	Structure location with respect to impact points	160
8.2	Attenuation of rock fall energy in protection structures	161
8.2.1	Velocity changes during impact with a fence.....	162
8.2.2	Energy changes during impact with a fence	166
8.2.3	Energy efficiency of fences.....	167
8.2.4	Configuration of redirection structures	168
8.2.5	Hinges and guy wires.....	169
8.3	Minimizing forces in rock fall protection fences	171
8.3.1	Time – force behavior of rigid, flexible and stiff structures	171

8.3.2	Energy absorption by rigid, flexible and stiff structures	174
8.4	Design of stiff, attenuator fences.....	178
8.5	Model testing of protection structures.....	180
8.5.1	Model testing procedure.....	180
8.5.2	Model test parameters.....	182
8.5.3	Results of model tests	182
9	CONCLUSIONS AND ON-GOING RESEARCH.....	187
9.1	Conclusions.....	187
9.1.1	Case studies of rock fall events and testing sites.....	187
9.1.2	Impact mechanics theory.....	187
9.1.3	Performance of rock fall protection structures.....	188
9.2	Future research work	190
9.2.1	Additional case studies.....	190
9.2.2	Impact mechanics.....	190
9.2.3	Protection structures.....	190
	REFERENCES	192
	APPENDIX A: DOCUMENTATION OF ROCK FALL IMPACTS AT MOUNT STEPHEN	198
	APPENDIX B: IMPACT MECHANICS – NORMAL COEFFICIENT OF RESTITUTION.....	204
	APPENDIX C: IMPACT MECHANICS – IMPACT OF ROUGH, ROTATING BODIES.....	209
C.1	Equations of relative motion	209
C.2	Equations of planar motion for impact of rough bodies.....	213
C.3	Equations of motion for translating and rotating bodies – final velocities.....	215
	APPENDIX D: ENERGY LOSS EQUATIONS.....	219
	APPENDIX E: CONVERSION FACTORS	223
	INDEX.....	226

List of Tables

Table 2-1: Mt Stephen rock fall site: trajectory S-A-B from 112 m above track	17
Table 2-2: Oregon impact points from source at crest: 15 m high cut at face angle of 76°	18
Table 2-3: Ehime, Japan rock fall test site: trajectory for concrete cube.....	22
Table 2-4: Tornado Mountain rock fall A trajectory from source, fall height 350 m	26
Table 2-5: Impact on asphalt	31
Table 2-6: Summary of rock properties.....	33
Table 2-7: Summary of coefficients of restitution calculated for rock fall case studies	34
Table 3-1: Values of effective friction coefficient μ' for characteristics of slope materials	50
Table 4-1: Volume and radius of gyration of common rock fall body shapes.....	79
Table 7-1: Summary of input parameters used in <i>RocFall 4.0</i> to stimulate case study rock falls	159

List of Figures

Figure 1.1: Consequences of rock falls; a) rock fall that blocked highway; b) rock fall that was struck by car	1
Figure 1.2: Typical slope configuration showing the relationship between slope angle and rock fall behavior	3
Figure 2.1: Mt. Stephen rock fall site. a) view of lower one third approximately of rock face with concrete block barrier at base of slope; b) MSE barrier constructed with concrete blocks, compacted rock fill and Geogrid reinforcing strips, with steel mesh fence along top, to contain rock falls and snow avalanches (courtesy Canadian Pacific Railway)	14
Figure 2.2: Mt. Stephen – cross section of lower part of slope showing ditch and typical trajectories for falls that impact the barrier.....	16
Figure 2.3: Image of rock fall test carried out in Oregon (Pierson <i>et al.</i> , 2001).....	19
Figure 2.4: Kreuger Quarry, Oregon test site - typical rock fall trajectory and impact points for 15 m high, 76 degree rock face with horizontal ditch.....	20
Figure 2.5: Ehime test site in Japan – rock slope with talus deposit at base; concrete cube test block	21
Figure 2.6: Ehime test site, Japan – results of rock fall test showing trajectories, and impact and restitution velocities for concrete cube test block; h' is maximum trajectory height normal to slope, v_i , v_f are impact and final velocities (Ushiro <i>et al.</i> , 2006)	23
Figure 2.7: Images of Tornado Mountain rock fall. a) tree with diameter of about 250 mm (9.8 in) sheared by falling rock at a height of about 1.6 m (5.2 ft); fragment of rock broken off main rock fall visible in lower left corner; b) Boulder A, with volume of about 1.4 cu. m (1.8 cu. yd), at slope distance of about 740 m (2,450 ft) from source	25
Figure 2.8: Tornado Mountain, Boulder A – mapped impact points (total 46) and broken trees (indicated by arrows ↓), with detail of velocity components at impact #A26	29
Figure 2.9: View of 138 m (450 ft) high slope comprising 58 m (190 ft) high rock slope where rock fall originated, colluvium slope at 42 degrees, and 10 m (33 ft) high cut face above the road....	30
Figure 2.10: Final trajectory of a rock falling from a height of 136 m (445 ft) and impacting a horizontal asphalt surface	31
Figure 3.1: Examples of impact points visible in the field. a) Distance successive impact points on slope surface (Christchurch, New Zealand 2011 earthquake); b) impact point on tree showing trajectory height (Tornado Mountain, Canada)	35
Figure 3.2: Definition of trajectory velocity components and directions	37
Figure 3.3: Definition of trajectory parameters. a) Velocity nomenclature for trajectories and impacts; b) parameters used in equation (3.4) to calculate rock fall trajectories	40
Figure 3.4: Trajectory calculations showing rock fall path, impact points, impact velocities and trajectory height and length.....	43
Figure 3.5: Plot of normal trajectory heights from Ehime test site for spherical and cubic concrete blocks, and blocks of rock (see Figure 2.6 for slope section). (Ushiro <i>et al.</i> , 2006)	46

Figure 3.6: Range of velocities for Ehime rock fall test site (see Figure 2.6 for slope section)	48
Figure 3.7: Velocity of rock fall on slope dipping at ψ_s : a) limit equilibrium forces acting on sliding block; b) relationship between free fall height, H and sliding distance, S	49
Figure 3.8: Trajectories related to restitution angle, θ_0 : $\theta_0 = 15$ degrees and $\theta_0 = 45$ degrees	52
Figure 3.9: Ranges of values for restitution angle, θ_0 . a) Tornado Mountain tree impacts (21 points); b) Ehime test site trajectory measurements for spherical, cubic concrete blocks and blocks of rock (Ushiro et al., 2006).....	55
Figure 3.10: Relationship between angular velocity and fall height for rock falls at Ehime test site, Japan for spherical and cubic concrete blocks, and of blocks of rock (Ushiro et al., 2006) ..	58
Figure 3.11: Effect of attitude of block during impact on angular velocity.....	59
Figure 3.12: Mountain slope with three sinuous gullies in which all rock falls are concentrated	61
Figure 4.1: Forces generated at contact point during normal impact	64
Figure 4.2: Variation in force F during impact. a) Relationship between force and deformation at the impact point; b) change in force and impulse with time during impact; p_c is impulse generated up to time of maximum compression ($t = i$ to $t = c$); $(p_f - p_c)$ is impulse generated during restitution phase of impact ($t = c$ to $t = f$)	68
Figure 4.3: Example of plastic impact where a rock fall is embedded in a gabion wall	69
Figure 4.4: Relationship between normal impulse p_N and changes in tangential and normal velocities v_T , v_N , and energy during impact; E_{cN} is the kinetic energy absorbed during the compression phase of impact ($t = c$); $(E_{fN} - E_{cN})$ is the strain energy recovered during the restitution phase ($t = c$ to $t = f$).....	70
Figure 4.5: Changes in rotational (ω) and slip (v_s) velocities during impact, and transition from slip to rolling mode when $v_s = 0$. a) Negative angular velocity: $v_s = (v_T - r \cdot \omega)$; b) positive angular velocity: $v_s = (v_T + r \cdot \omega)$	75
Figure 4.6: Impact of rough, rotating sphere on a slope in plane motion	77
Figure 4.7: Diagram of impact showing equations defining impact and restitution velocity vectors	81
Figure 4.8: Example of rock fall impact showing values calculated final (restitution) velocity and angle	82
Figure 4.9: Influence of impact angular velocity, ω_i on restitution velocity, v_f and angle, ϑ_f . a) $\omega_i = -15 \text{ rad} \cdot \text{s}^{-1}$; b) $\omega_i = -25 \text{ rad} \cdot \text{s}^{-1}$; c) $\omega_i = +15 \text{ rad} \cdot \text{s}^{-1}$	84
Figure 4.10: Plot comparing restitution velocities – actual (Chapter 2) and calculated (equations (4.20) to (4.24)) values	86
Figure 5.1: Impacts between successive trajectories showing typical inelastic behavior and loss of energy during impact where second trajectory (on right) is lower than first trajectory; rock falls will always have lower trajectories than those shown (Micheal Maggs, Wikimedia Commons)	87
Figure 5.2: Normal impulse-velocity plot showing relationships between changes in normal (N) and tangential (T) velocity components and coefficients of restitution – $e_N = (v_{fN}/v_{iN})$ and $e_T = (v_{fT}/v_{iT})$	88

Figure 5.3: Isaac Newton's measurement of normal coefficient of restitution using impact of spheres suspended on pendulums.....	89
Figure 5.4: a) Effect of impact angle θ_i on the normal coefficient of restitution, e_N ; b) Geometry of collinear and eccentric impacts.....	92
Figure 5.5: Relationship between impact angle ϑ_i and normal coefficient of restitution e_N with best fit (power) curve for average values of ϑ_i and e_N each material type	94
Figure 5.6: Measurement of normal coefficient of restitution for concrete using drop test (h_i) to measure rebound height (h_r) (Masuya, <i>et al.</i> , 2001).....	96
Figure 5.7: Relationship between impact angle θ_i and the normal coefficient of restitution e_N for the rock fall sites described in Chapter 2; total of 58 points for five slope materials.....	97
Figure 5.8: Values for tangential coefficient of restitution e_T for 56 impact points at rock fall sites described in Chapter 2	100
Figure 5.9: Test procedure to measure friction coefficient between block of rock and slope material (Masuya, <i>et al.</i> , 2001)	102
Figure 6.1: Rock fall that stopped, just before causing serious damage to a building, when it impacted a horizontal surface that absorbed most of the fall energy.....	105
Figure 6.2: Energy changes (normal) during compression and restitution phases of impact. a) Forces generated at contact point during normal impact; b) energy plotted on [force, F – deformation, δ] graph; c) energy changes plotted on [normal impulse, p_N – relative velocity, v] graph.....	107
Figure 6.3: Reduction in tangential velocity, v_T during impact. a) [p_N – v] diagram showing change in v_T during impact, and corresponding reduction in energy, E_T ; b) changes in velocity components.....	113
Figure 6.4: Translational and angular velocity components at impact point #A26 for Tornado Mountain rock fall event	115
Figure 6.5: Energy loss diagram for cubic, concrete block with constant mass at Ehime test site, Japan – see Figure 2.6 (Ushiro <i>et al.</i> , 2001).....	121
Figure 6.6: Plot of horizontal rock fall distance x against loss of volume ratio, Ω/Ω_0 showing ranges of values of λ for data from Mt. Pellegrino and Camaldoli Hills (Nicolla <i>et al.</i> , 2009).....	124
Figure 6.7: Energy partition plot for diminishing mass at the Ehime rock fall test site – cubic concrete block with initial side length 0.6 m (2 ft).....	126
Figure 6.8: Relationship between maximum energy that can be dissipated by six different tree species and the tree diameter, measured at chest height (Dorren and Berger, 2005)	128
Figure 6.9: Impact of a 5 cu. m (6.5 cu. yd) rock fall with kinetic energy of about 200 to 800 kJ (75 to 300 ft tonf) with a 1.1 m (3.6 ft) diameter cedar tree. Rock was stopped and upper part of tree was broken off about 14 m above base (Vancouver Island, near Ucluelet).....	130
Figure 7.1: Rock falls at Mt. Stephen (see section 2.1). a) Simulation of rock falls showing three typical rock fall paths; b) accumulation of falls that impacted fence on top of barrier	132
Figure 7.2: Plot of normal component of impact velocity and scaled normal coefficient of restitution from equation (7.1)	137

Figure 7.3: Relationship between slope roughness (ϵ) and radius of rock fall (r)	139
Figure 7.4: Simulation of rock falls at Mt. Stephen for three calculated rock trajectories	143
Figure 7.5: Calculated vertical distribution impact points on barrier at Mt. Stephen	144
Figure 7.6: Analysis using <i>RocFall 4.0</i> of rock falls at Mt. Stephen at barrier, analysis point $x = 116.3$ m a) translational velocity distribution; b) total energy (KE + RE) distribution.....	145
Figure 7.7: Calculated trajectories for two 580 kg (1,280 lb) rocks at Krueger Quarry rock fall tests on 15 m (50 ft) high cut at a face angle of 76 degrees; refer to Fig 10.3 for first impact and roll out distances	147
Figure 7.8: Analysis using <i>RocFall 4.0</i> of rock falls at Krueger Quarry for 15 m (50 ft) high cut at a face angle of 76 degrees, analysis point $x = 10$ m (33 ft) a) translational velocity distribution; b) total energy (KE + RE) distribution	148
Figure 7.9: Calculated trajectory using <i>RocFall 4.0</i> for a 520 kg (1150 lb) concrete cube at the test site in Ehime Prefecture in Japan	150
Figure 7.10: Trajectory height envelope comparison between field results and <i>RocFall 4.0</i> simulated results for concrete cube at test site in Ehime Prefecture in Japan.....	151
Figure 7.11: Analysis using <i>RocFall 4.0</i> of rock falls at Ehime test side for 42 m (140 ft) high natural slope comprising bedrock (26 m) (85 ft) and talus (16 m) (50 ft) at analysis point $x = 52.1$ m a) translational velocity distribution; b) total energy (KE + RE) distribution.....	152
Figure 7.12: Calculated trajectories using <i>RocFall 4.0</i> for fall A, a 3750 kg (8300 lb) limestone block at Tornado Mountain.....	154
Figure 7.13: Trajectory height envelope from <i>RocFall 4.0</i> simulated results for a 3750 kg (8300 lb) limestone block at Tornado Mountain.....	154
Figure 7.14: Analysis using <i>RocFall 4.0</i> of rock falls at Tornado Mountain, block A at analysis point $x = 610$ m a) translational velocity distribution; b) total energy (KE + RE) distribution.....	155
Figure 7.15: Calculated trajectories using <i>RocFall 4.0</i> of a single 500 kg (1,100 lb) rock fall from the crest of the slope and impacting the asphalt road; refer to Figure 2.10 for impact details on asphalt	157
Figure 7.16: Analysis using <i>RocFall 4.0</i> of rock fall impacting asphalt at analysis point $x = 140$ m a) translational velocity distribution; b) total energy (KE + RE) distribution.....	158
Figure 8.1: Tornado Mountain rock fall site – for impact #A43 on 8 m (25 ft) wide bench excavated for the railway, 70 per cent of the impact energy is lost during impact.....	161
Figure 8.2: Behavior of flexible and rigid structures. a) Flexible steel cable net that stops rock falls by deflection with no plastic deformation of the steel; b) rigid concrete wall shattered by rock fall impact	162
Figure 8.3: Effect of impact angle with fence on energy absorption. a) Normal impact results in the fence absorbing all impact energy; b) oblique impact results in rock being redirected off the net with partial absorption of impact energy	163
Figure 8.4: Hanging net installed on steep rock face that redirects rock falls into containment area at base of slope, where cleanout of accumulated rock falls is readily achieved	169

Figure 8.5: Low friction hinge at base of post allowed the post to deflect, with no damage to the foundation, during an impact that exceeded the service limit states energy (above Shuswap Lake, British Columbia, Canada).....	170
Figure 8.6: Relationship between time of impact and force generated in rigid, flexible and stiff fences	172
Figure 8.7: Plot of duration of impact against rock fall impulse absorbed by fence; curves are developed by integrating [time-force] equations shown in Figure 8.6 to give the area under [time – force] curves	177
Figure 8.8: [Time – force] -plot for rigid, flexible and stiff structures showing force generated in structure at time taken to absorb impact impulse.....	178
Figure 8.9: Rock fall trajectories impacting attenuator type fence. Trajectory A – low energy impact close to slope impact point; trajectories B and C – high energy impacts distant from prior impact point	180
Figure 8.10: a) Baseball pitching machine and b) wave net.....	181
Figure 8.11: Configuration of rock fall fence used in model tests. Orientations of hinged posts are defined by angles α and β , measured relative to the normal to the slope.....	182
Figure 8.12: Path of deflected projectile after impact with net oriented up-slope ($\beta = +60$ degrees). Approximate velocities at ten frame intervals (0.0083 s) during impact shown	183
Figure 8.13: Relationship between energy efficiency and angle β of upper net, for a non-rotating body.....	184
Figure 8.14: Relationship between the duration of impact and change in velocity during impact	185
Figure 8.15: Relationship between duration of impact and the amount of impulse that is absorbed by the fence; compare with Figure 8.7 for stiff structures	186
Figure A.1: Plan of Lockblock wall/ fence and slope.....	199
Figure A.2: Section #3. a) Cross section view, b) distribution of impact points.....	200
Figure A.3: Section #7. a) Cross section view, b) distribution of impact points.....	201
Figure A.4: Section #12. a) Cross section view, b) distribution of impact points.....	202
Figure A.5: Calculated vertical distribution impact points on barrier at Mt. Stephen.....	203
Figure B.1: Relationship between normal impulse p_N and changes in tangential and normal velocities v_T , v_N , and energy during impact.....	204
Figure C.1: Impact mechanics principles for two dimensional (planar) motion a) forces generated at contact point during normal impact; b) impact of rough, rotating sphere on a slope, v = velocity at center of mass, V = relative velocity at impact point.....	210
Figure C.2: Dimensions of rotating, impacting body defining inertial coefficients for plane motion, rotating about z axis through centre of gravity (+).....	211
Figure C.3: in rotational (ω) and slip (v_s) velocities during impact, and transition from slip to rolling mode when $v_s = 0$; for negative angular velocity: $v_s = (v_T - r \cdot \omega)$	211
Figure C.4: Diagram of impact showing impact and restitution velocity vectors and equations for calculating final velocities.....	218

Figure D.1: Energy changes (normal) during compression and restitution phases of impact. a) Forces generated at contact point during normal impact, with energy changes plotted on [force, F – deformation, δ] graph; b) energy changes plotted on [normal impulse, p_N – velocity, v] graph.....219

List of Symbols

0	Subscript for velocities at the start of trajectory ($t = 0$)
a	Constant used in [time – force] relationship for flexible nets; acceleration
b	Constant used in [time – force] relationship for stiff nets
D	Diameter of falling rock (m)
e_N	Normal coefficient of restitution
e_T	Tangential coefficient of restitution
E_c	Energy absorbed during compression phase of impact (J)
E_e	Energy efficiency for fence design
$(E_f - E_c)$	Energy recovered during restitution phase of impact (J)
E_i, E_f	Impact (i) and restitution (final, f) energies for impact with protection structures (J)
F	Force (N)
f	Subscript for velocities and energies at the completion of impact ($t = f$)
g	Gravitational acceleration ($m \cdot s^{-2}$)
H	Rock fall height (m)
h	Trajectory height – vertical (m)
h'	Trajectory height – normal to slope (m)
I	Moment of inertia ($kg \cdot m^2$)
I'	Tensor defining components of moments of inertia
i	Subscript for velocities at the moment of impact ($t = i$); inclination of asperities (degrees).
k	Radius of gyration (m)
L	Side length of cubic block; length of trajectory between impacts; sliding length of rock falls (m)
m	Mass of rock fall (kg)
$m_{(n)}$	Mass of rock fall at impact point n (kg)
$m_{(0)}$	Mass of rock fall at source (kg)
N	Subscript for the component of velocity normal to the slope
n	Impact number; gradient of line for [time – force] relationship for rigid structures
p	Probability
p_N	Normal impulse ($kg \cdot m \cdot s^{-1}$)
p_T	Tangential impulse ($kg \cdot m \cdot s^{-1}$)
R	Frictional resistance at impact point
r	Radius of rock fall body (m)
s	Dimension defining slope roughness (m)
T	Subscript for the component of velocity tangential to the slope
t	Time (s)
v	Relative velocity at contact point ($m \cdot s^{-1}$)
v_N	Normal component of relative velocity at contact point ($m \cdot s^{-1}$)
v_T	Tangential component of relative velocity at contact point ($m \cdot s^{-1}$)
V_i	Velocity of centre of mass at impact time $t = i$ ($m \cdot s^{-1}$)
V_f	Velocity of centre of mass, final or restitution at time $t = f$ ($m \cdot s^{-1}$)
V_{iN}	Normal component of impact velocity of centre of mass ($m \cdot s^{-1}$)
V_{iT}	Tangential component of impact velocity of centre of mass ($m \cdot s^{-1}$)
V_{fN}	Normal component of final velocity of centre of mass ($m \cdot s^{-1}$)

V_{JT}	Tangential component of final velocity of centre of mass ($m \cdot s^{-1}$)
x	Horizontal coordinate (m); exponent in time – force power relationship
z	Vertical coordinate (m)
α	Angle of velocity vector relative to positive x-axis (degrees)
$\beta_1, \beta_2, \beta_3$	Inertial coefficients related to rotation of block during impact
ε	Angle defining slope roughness
η	Slope resistance factor used in velocity calculations
θ_i	Impact angle relative to slope surface (degrees)
θ_f	Final or restitution angle relative to slope surface (degrees)
κ	Slope gradient, trajectory calculations
μ	Friction coefficient at impact point
μ'	Effective friction coefficient of slope surface
$\sigma_{u(r)}$	Uniaxial compressive strength of rock (MPa)
ϕ	Friction angle (degrees)
ψ	Dip angle – slope (s), face (f), plane (p), (degrees)
Ω	Volume of rock fall (m^3)
Ω_0	Volume of rock fall at source (m^3)
ω	Angular velocity ($rad \cdot s^{-1}$)

1 Introduction – objectives and methodology

1.1 Rock falls – causes and consequences

In mountainous terrain, infrastructure such as highways, railways and power generation facilities, as well as houses and apartment buildings, may be subject to rock fall hazards that can result in economic losses due to service interruptions, equipment and structural damage, and loss of life. Figure 1.1 shows two examples of the consequences of rock falls: a) a fall with a volume of about 80 cu. m from a height of 350 m that shattered an unreinforced concrete wall and caused severe traffic delays; b) a fall with dimensions of about 150 mm that bounced on the asphalt and then was struck by a car with the rock passing through the windshield.



Figure 1.1: Consequences of rock falls; a) rock fall that blocked highway; b) rock fall that was struck by car

It is well established that rock fall hazards are particularly severe in areas with heavy precipitation, frequent freeze-thaw cycles (Hung and Hazzard, 1999; Peckover, 1975; TRB, 1996). These climatic conditions exist, for example, in the Alps, on the west coast of North America and in Japan. In contrast, in Hong Kong, where temperatures are more mild but intense rainfall events occur, rock fall hazards can also be severe because of the high population density (Chau *et al.*, 2003).

Another cause of rock falls are ground motions caused by seismic events (Harp and Jibson, 1995; Harp *et al.*, 2003). Although rock falls due to earthquakes only occur in seismic-prone zones and these events are much less frequent than rock falls induced by weathering, the consequence of earthquake induced events can be widespread and severe as shown by the extensive damage caused by the 2008 Christchurch earthquake in New Zealand (Dellow, *et al.*, 2011).

As a consequence of these damaging effects of rock falls, and my experience in this field over the past 40 years, I decided to undertake the research discussed in this thesis. The work was carried out between 2009 and 2013 with the objectives of understanding rock fall behavior in detail, and developing methods to improve the design and construction of protection structures.

As part of the background material for my research, Figure 1.2 shows a typical rock fall site comprising possible four components of a fall:

- a) Source area and high velocities on a steep rock face;
- b) Shallow trajectories on a colluvium slope that is steeper than the angle of repose;
- c) A talus slope where most of the falls accumulate;
- d) A run-out area where a few of the larger, higher energy blocks fall beyond the toe of the talus.

The research covers all four of these rock fall components.

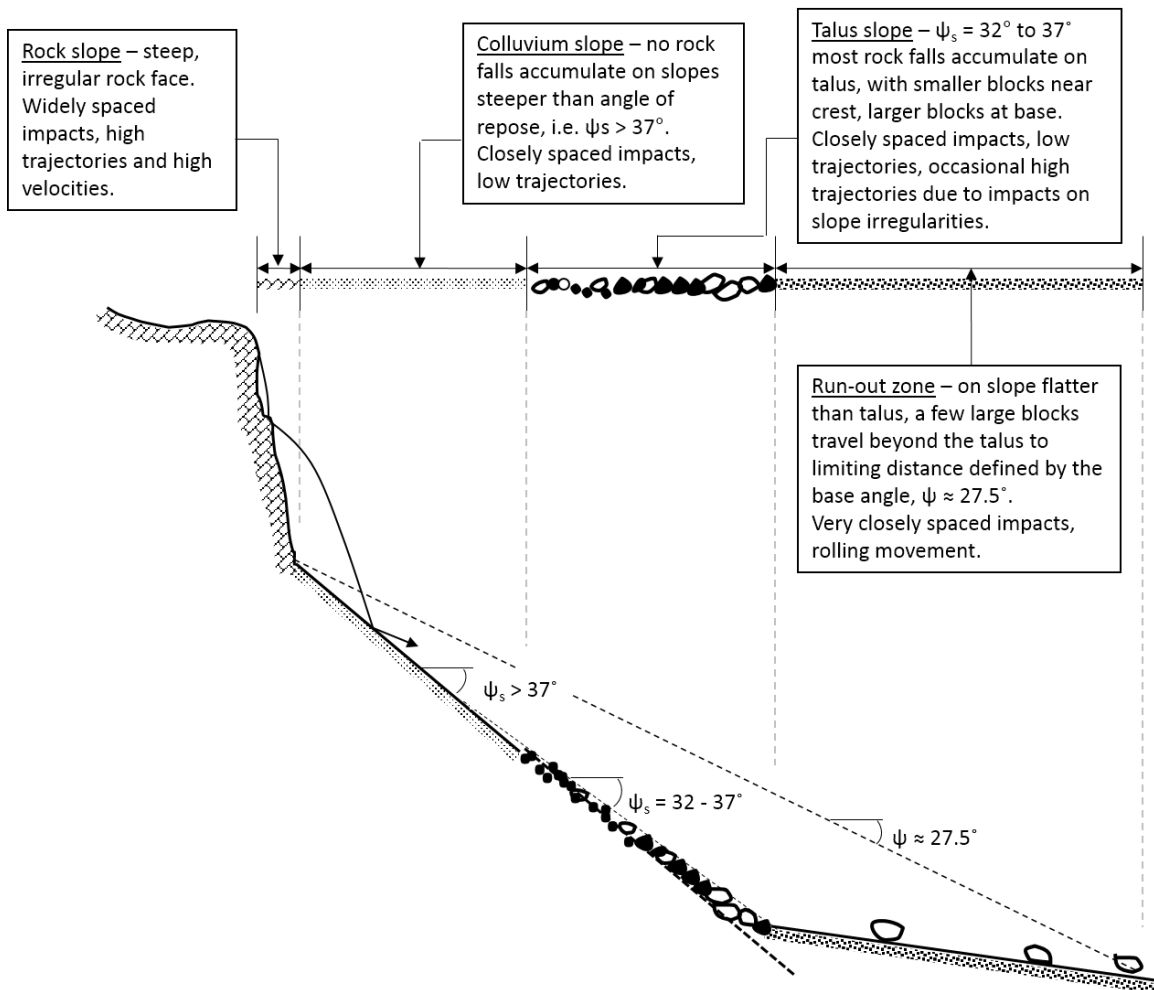


Figure 1.2: Typical slope configuration showing the relationship between slope angle and rock fall behavior

1.2 Background to rock fall research program

I had my first experience with rock falls in 1968 when working as an underground miner in Broken Hill, Australia where I was hit by a fall from the “back” (roof) of a development “drive” (tunnel). Fortunately, my injuries had no lasting effect, and I learnt the significant benefits of “barring down” (removing loose rock).

My next rock fall experience was in Canada in March 1974, nearly 40 years ago, when a rock fall caused the derailment of a freight train, with fatal consequences. I was involved in the design and construction of the remediation work for this incident and this was the start of my professional career in the field of rock slope engineering for civil engineering projects.

Since 1974 I have been involved in many hundreds of other rock fall projects, mainly in western Canada, but also in the United States from Alaska to New Jersey, and in Peru, New Zealand,

Hong Kong, Greece and Turkey. These projects have involved the investigation, design, construction and maintenance of remedial measures that have provided me with extensive experience on the actual behavior of rock falls.

In the 1970's and 1980's the only rock fall protection methods available were a simple, but reliable ditch design chart developed from field tests (Ritchie, 1963), and double twist draped wire mesh and gabions (rock filled wire baskets) produced by the Maccaferri company in Italy. Another development in the 1970's was a rock fall modeling program that was used to examine rock fall behavior at Hells Gate in the Fraser Canyon, British Columbia; this was probably one of the first modeling programs (Piteau, 1980).

In the late 1980's and early 1990's two significant developments occurred that resulted in a rapid expansion in the availability in north America of reliable rock fall protection measures.

The first development was the up-grading of Interstate Highway I-70 west of Denver, Colorado through Glenwood Canyon. One of the project requirements was the retention of the aesthetics of the canyon by avoiding the excavation of high cuts and wide ditches to contain rock falls. Because of the significant rock fall hazards from the natural mountain slopes in the canyon, a comprehensive research program was initiated to develop alternate protection measures to ditches. The research resulted in the development of mechanically stabilized earth (MSE) rock fall barriers, attenuator-type structures and Flexpost fences (Barrett and Pfeiffer, 1989; Barrett and White, 1991; Hearn, 1991). Another development in Colorado at this time was the rock fall modeling program CRSP (Colorado Rockfall Simulation Program) that was calibrated against some of the rock fall tests used to evaluate the rock fall protection structures (Pfeiffer and Bowen, 1989). CRSP has undergone several up-grades and continues to be widely used today. I have visited Glenwood Canyon and worked with members of CODOT who were responsible for the research.

The second significant development of the 1980's was the introduction in North America by Geobruigg of Switzerland of rock fall fences fabricated with woven wire mesh. One of their early products was tested in California that demonstrated the viability of using these types of structures to provide protection against rock falls (Smith and Duffy, 1990). The woven cable nets have now been replaced by more effective Ringnets, and several other companies (Trumer, Maccaferri) supply comparable products. I have been involved with several dozen projects using

a variety of rock fall fences, and am working with Geobrugg to develop improved protection products.

I have also been involved for many years with the activities of the Transportation Research Board (TRB) in Washington, DC that has an active committee on rock fall research. It was through the TRB that I became acquainted with rock fall mitigation in Japan, and the work of Dr. Yoshida and Dr. Masuya of Kanazawa University, and Mr. Toshimitsu Nomura of Protec Engineering in Niigata. I have visited Japan several times to study their approach to rock fall mitigation. Of particular interest is their work on reinforced concrete rock fall sheds that incorporate flexible, energy absorbing features (Yoshida et al., 2007). I have also had access to the results of some of their rock fall testing as described in Chapter 2.

In summary, developments over the last 25 years in the fields of both computer modeling and mitigation products have provided engineers with the ability to design and build protection structures that have significantly improved public safety from rock fall hazards. I am very familiar with all these developments, which, together with my experience on numerous rock fall projects over the last 40 years, comprises the background to my research.

1.3 Objectives of research

As a result of my experience in rock fall mitigation as described in the previous section, I have made two observations regarding the design and performance of protection structures where I thought that it would be possible to make improvements. These two observations were:

- i. **Fence dimensions** – the dimensions of fences are determined by calculating likely rock fall trajectory heights to make sure that few, if any, rocks pass over the fence. I found that fences designed with commercially available software such as RocFall 4.0 (RocScience, 2012) and CRSP (2011), were much higher than required to contain more rock falls. That is, impacts on the fence were occurring in the lower one third to one quarter with virtually no impacts in the upper two thirds. These observations were made in about 12 fences where the sources of the rock falls were at height of up to 250 m, and many hundreds of impacts had occurred. This clearly demonstrated that the simulation programs were calculating trajectories that were significantly higher than reality, and that fences were higher, and more expensive, than required.
- ii. **Impact energy absorption of protection structures** – in the 1960's and 1970's, a number of rigid concrete walls were constructed for rock fall protection. While these walls were

effective in containing small falls because of their steep up-slope faces, they were sometime shattered by larger falls. The wire rope fences introduced in the 1990's were much more effective in containing falls than concrete walls because of their flexibility. However, I observed that most of the impact energy absorption occurred near the point of maximum deformation when the flexibility of the fence components had diminished and the forces in the structure suddenly increased. I considered that stiff structures would absorb impact energy more uniformly during the entire impact period, resulting in the development of lower forces in the fence. The construction of stiff fences would require modifications to the configuration and design of fences.

As a result of these observations, four research objectives were developed as discussed below.

1.3.1 Objective #1 – Document rock fall events

Because it is not possible to precisely model rock falls using impact mechanics theory, my objective has been to carefully document actual rock fall events and use these data to test impact mechanics theory and calibrate rock fall simulation programs. The events that have been documented for this research include three sites in British Columbia where I have collected unique data on impact locations and trajectory paths, and two cases, one in Oregon (Pierson et al., 2000) and Japan (Ushiro et al., 1999) where details of rock fall tests have been documented in the literature.

1.3.2 Objective #2 – Develop applications of impact mechanics to rock fall

Rock falls comprise a series of trajectories each followed by an impact. While trajectories can be readily calculated from Newtonian mechanics, impact is a more complex process involving a translating and rotating, rough body making an oblique, non-compliant contact with an irregular slope. My objective was to make a detailed study of impact mechanics theory as developed by Goldsmith (Goldsmith, 1960) and Stronge (Stronge, 2000) and adapt this theory to rock fall impacts. Impact mechanics provides detailed information of changes in translational and rotational velocities, and energies, that occur during the impact process that can be compared with the field data.

1.3.3 Objective #3 – Calibrate rock fall modeling parameters

The data obtained from the documented rock fall events together with the theoretical velocity changes during impact can be used to calibrate rock fall modeling programs. My objective has

been to run the commercially available program RocFall 4.0 (RocScience 2012) to determine the values of the input parameters that are needed to closely simulate the documented rock fall events. The parameters have been compared to the values predicted by impact mechanics theory. The program RocFall 4.0 was selected because it is widely used and details of the modeling algorithms are provided.

1.3.4 Objective #4 – Test improved rock fall protection structures

Impact mechanics theory can be applied to the study of how fences and nets contain rock falls. That is, rock falls are either stopped or redirected by the structure depending on the impact geometry. Where the rock is stopped, all the impact energy is absorbed by the fence. However, where rocks are redirected, and not stopped, by the fence, only a portion of the impact energy is absorbed with the remainder of the energy being retained in the moving body. My objective was to carry out both impact mechanics analysis and model tests to investigate the relationship between the impact geometry and the energy absorption of the fence, and determine if this could be used to design more energy efficient fences.

1.4 Methodology

Section 1.3 above describes the four objectives of my research. The following is a discussion of the methods used to meet these objectives.

1.4.1 1 – Documentation of rock fall events

My files contain information of 14 rock fall sites, most of which are projects on which I had worked, together with events that have been reported in the literature. My plan has been to select sites where the data on impacts and trajectories was both reliable and detailed so that calculated impact parameters would also be reliable. Also, it was necessary to select sites with a wide range of both topographic and geologic properties that would encompass most of the rock fall conditions that occur in nature. I selected five sites, three of which are my own data and two from the literature, to be my reference rock fall events, as follows:

- i. Tornado Mountain in the east Kootenays of British Columbia;
- ii. Mt. Stephen near the village of Field in south eastern British Columbia;
- iii. A highway location where an impact on asphalt was documented in detail;
- iv. Kreuger Quarry in Oregon where 11,500 rock fall tests were documented in detail;

- v. Test site in Ehime Prefecture on Shikoku Island in Japan where 100 tests were conducted on blocks of rock, and concrete spheres and cubes.

For each site, the [x –z] co-ordinates of each impact, and the trajectory impact angle (θ_0) were known or measured. A spreadsheet was then written that calculated at each impact the velocity components (normal, tangential and vertical, horizontal), as well as the normal and tangential coefficients of restitution (e_N , e_T). The spreadsheet also calculated the energy loss at each impact point and the energy gained during each trajectory.

It is intended that these case studies can be used by others to calibrate rock fall modeling programs.

This work is described in Chapter 2. In addition, Appendix A provides details of the locations of 466 impacts on the barrier at Mt. Stephen.

1.4.2 2 – Trajectories and translational/rotational velocities

The trajectory phase of rock falls involves the application of Newtonian mechanics to determine the path of the fall through the air and the change in the translational velocity during the trajectory. This procedure was used to calculate trajectories for the five reference case studies, and compare actual and theoretical translational velocities.

With respect to rotational velocity, detailed information on these velocities was available from the Shikoku test site in Japan. These test results are a useful set of data showing the range of rotational velocities that occur for rock falls, and the relationship between the size of the body and its rotational velocity.

This subject is addressed in Chapter 3.

1.4.3 3 – Application of impact mechanics to rock falls

The impact mechanics model used in my research is a co-linear (planar) impact of a rough (frictional), translating and rotating body of any shape defined by its radius (r) and radius of gyration (k) impacting a stationary, planar but irregular surface (slope). This is a non-compliant impact where no interpenetration of the bodies occurs. Appendices B, C and D show the derivation of equations for the changes in velocity and energy during impact for a spherical body.

I have found that a very valuable means of illustrating the impact process is to use [normal impulse, p_N – relative velocity, v] plots. These plots clearly illustrate the changes in translational and rotational velocity, and energy that occur during impact, and how the frictional and compression components of impact can be separated. Impact mechanics also shows the effect of the impact angle for a rough, rotating body on the restitution velocity, and how the normal coefficient of restitution e_N , can be greater than 1 for shallow angle impacts.

Chapters 4, 5 and 6 discuss respectively the principles of impact mechanics, the coefficients of restitution e_N and e_T , and energy changes during impact.

1.4.4 4 – Rock fall modeling

I used the simulation program RocFall 4.0 to model the five reference rock fall events. For each rock fall, the values of the input parameters required to closely match the actual rock fall events were determined. I found that minor changes in the values of the impact parameters have a significant effect on rock fall behavior. For each of the reference cases, the required values of the input parameters – seeder velocities, normal and tangential coefficients of restitution and surface roughness - are listed.

I intend that these parameter values will provide a guideline to others using this program on appropriate values to use to simulate actual rock falls.

The analysis results are discussed in Chapter 7.

1.4.5 5 – Development and testing of attenuator-type rock fall fences

I have used the principles of impact mechanics to examine how rock falls interact with rock fall fences, and the benefit of having fences redirect rather than stop falls. This is, if a rock fall is redirected, and not stopped, by the fence then only a portion of the impact energy is absorbed by the net and the rest is retained in the rock fall. Furthermore, if the fence is “stiff” rather than highly flexible, energy is absorbed uniformly over the duration of the impact resulting in reduced forces being induced in the fence.

Stiff structures that redirect rock falls are termed “attenuators”.

The theoretical performance of fences with different stiffnesses when impacted by rock falls is demonstrated by the use of [force – time] diagrams. In order to test this theoretical performance, I carried out a series of 1/20 scale model tests of a wire mesh fence to investigate the effect of impact angle on the performance of attenuator-type protection structures. That is,

these structures redirected rather than stopped the impacting body such that the velocity was attenuated during the time of contact. The tests involved using a baseball pitching machine to project spherical bodies at the wire mesh models. The motion of the body during contact with the fence and canopy was captured by a high speed camera running at 1205 frames per second to record the changes in translational and rotational velocity that occurred during contact.

The translational and angular velocities on the high speed videos were analyzed with ProAnalyst motion analysis software.

The study of attenuator structures is discussed on Chapter 8.

1.4.6 Conclusions

In Chapter 9 I discuss the conclusions that can be drawn from my research, and what further work may be carried out to develop the theoretical and applied results.

In summary, the research presented in this thesis is a combination of my 40 years of practical experience with projects involving rock falls, and the last five years of detailed study of five case studies, impact mechanics theory and model testing of attenuator-type rock fall protection structures. My overall objective has been to show that the theory can be applied to rock falls such that rock fall analysis programs can more closely simulate actual field conditions, and that the principle of attenuation can be used to design more efficient protection structures.

2 Documentation of rock fall events

This chapter documents five rock fall events that encompass many commonly occurring rock fall conditions. These data are from both natural events where it has been possible to precisely map impact points and trajectories, and from carefully documented, full-scale rock fall tests. These case studies are for a variety of slope geometries and fall heights, and for slope materials comprising rock, colluvium, talus and asphalt. For these sites, the velocity components in directions normal and parallel to the slope have been calculated from the impact co-ordinates, and the results have been used to calculate normal and tangential coefficients of restitution, and the energy losses.

The documented events provide reliable data that can be used to calibrate impact and trajectory models. Each of the case studies has been modeled using the program *RocFall 4.0* (RocScience, 2012) as described in Chapter 7, where values for the input parameters that are required to fit the calculated trajectories to the field conditions are listed.

Rock falls comprise a series of impacts, each followed by a trajectory and methods of modeling both impacts and trajectories are required to simulate these events. The basic attributes of trajectories and impacts are as follows:

Trajectory – rock fall trajectories follow well defined parabolic paths according to Newtonian mechanics, where three points on the parabola completely define the fall path (Chapter 3). In calculating trajectories at sites where information on precise impact points and trajectory paths is not available, it is necessary to select the two end points for each trajectory and to make an assumption for the angle at which the rock leaves the slope surface. These data have been obtained from measurements at the fully documented rock fall sites, and from only using trajectories that are found to be both realistic, and mathematically feasible.

Impact – the theory of impact mechanics (Chapter 4) can model rock falls, but it is necessary to make simplifying assumptions compared to the actual conditions that occur. Natural conditions includes irregularly shaped, translating and rotating blocks of rock impacting a slope that may be comprised of a different material and also be rough and irregular.

In examining velocity changes during impact, it is useful to calculate the changes in normal and tangential velocity components that occur as the result of deformation and friction at the contact surface. The changes in the velocity components can be quantified in terms of the

normal (e_N) and tangential (e_T) coefficients of restitution as defined in the following two equations:

$$\text{Normal coefficient of restitution, } e_N = -\frac{\text{final normal velocity, } v_{fN}}{\text{impact normal velocity, } v_{iN}} \quad (2.1)$$

$$\text{Tangential coefficient of restitution, } e_T = \frac{\text{final tangential velocity, } v_{fT}}{\text{impact tangential velocity, } v_{iT}} \quad (2.2)$$

For each documented rock fall site described in this chapter, insets on the impact drawings show arrows, the lengths and orientations of which are proportional to the velocity vectors. The notation on the vectors include the subscript “ i ” referring to values at the moment of impact (time, $t = i$), and the subscript “ f ” refers to values at the end of the impact (time, $t = f$); the final velocity is also referred to as the “restitution” velocity. Also, the subscript “ N ” refers to the component of the vector normal to the slope and the subscript “ T ” refers to the component of the vector tangential to the slope at each impact point. The included angle between the vector and the slope is shown by the symbol θ , with the same subscript designations for impact and final angles.

It is also noted that normal impact velocities ($-v_{iN}$) are negative because the positive normal axis is in the direction out of the slope, and consequentially normal restitution velocities (v_{fN}) are positive. The positive tangential axis is down slope so all tangential velocities are positive.

This chapter documents actual final velocities and angles measured in the field, while Chapter 3 derives the trajectory equations, and Chapter 4 shows the derivation, based on impact mechanics theory, of equations defining the final velocities and angles. Section 4.7 compares the actual and calculated sets of data for the five documented case studies. Each case study gives the shape, dimensions, mass and radius of gyration of typical blocks of rock. It has been assumed that the rock fall shapes are either cuboid for falls from low heights, or ellipsoidal where cubic blocks have had the sharp edges and corners broken off by successive impacts on the slope.

2.1 Impacts on rock slopes

Data have been analyzed for falls at locations in Canada, the United States and Japan, for slopes ranging in height from 2000 m to 15 m (6550 to 50 ft). The following is a discussion on falls at three locations where the falls impacted rock slopes.

2.1.1 Mt. Stephen, Canada – 2000 m high rock slope

Mt. Stephen in the Canadian Rocky Mountains near the village of Field is a source of both rock falls and snow avalanches that originate on a rock face with a height of nearly 2000 m (6550 ft) at an overall slope angle of about 50 degrees. As shown in Figure 2.1, it has been necessary to construct a barrier to protect a railway operating at the base of the slope. The geology is a strong, tabular, horizontally bedded limestone containing thin but widely spaced shale beds; the shale weathers more rapidly than the limestone resulting in the formation of overhangs and falls of the stronger rock.



Figure 2.1: Mt. Stephen rock fall site. a) view of lower third, approximately, of rock face with concrete block barrier at base of slope; b) MSE barrier constructed with concrete blocks, compacted rock fill and Geogrid reinforcing strips, with steel mesh fence along top, to contain rock falls and snow avalanches (courtesy Canadian Pacific Railway)

The barrier comprises a mechanically stabilized earth (MSE) wall built with pre-cast concrete blocks (dimensions 1.5 m long, 0.75 m in section; 5 by 2.5 ft) forming each face, with Geogrid reinforcement and compacted gravel fill between the walls, and a steel cable fence along the top of the wall. The total height of the structure is 11.6 m (38 ft). Figure 2.2 shows a typical section of the lower 120 m (400 ft) of the slope that was generated from an aerial Lidar survey of the site. Figure 2.2 also shows a range of feasible trajectories of rock falls that impacted the lower part of the rock slope and were then contained by the barrier.

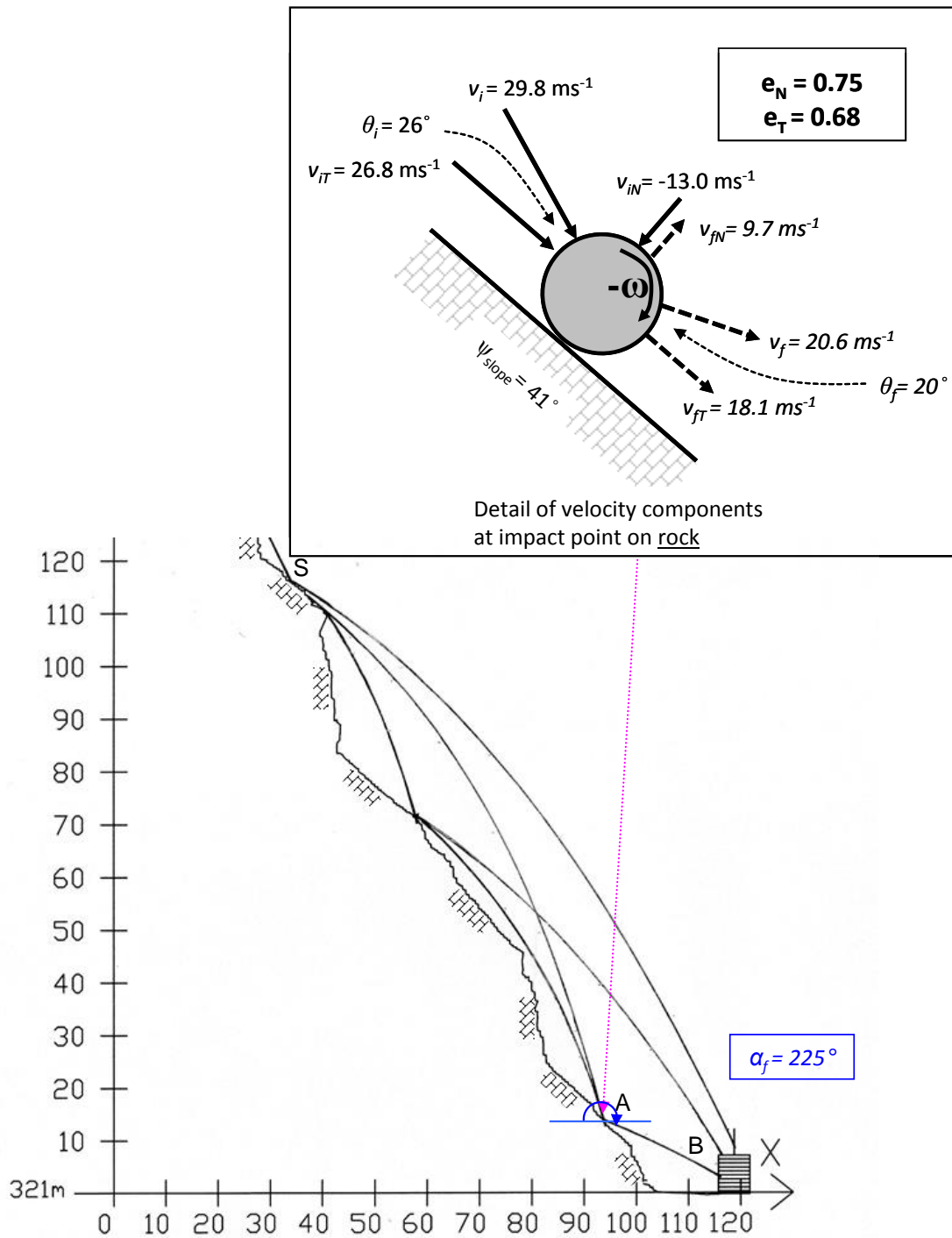


Figure 2.2: Mt. Stephen – cross section of lower part of slope showing ditch and typical trajectories for falls that impact the barrier

Table 2-1: Mt Stephen rock fall site: trajectory S-A-B from 112 m above track

Impact point from source (n)	Impact Coordinates		Trajectory angle, restitution from horizontal, x axis (α_f)	Slope angle (above impact point) ψ_s	Coefficients of restitution		Kinetic energy lost during impact (J)
	x co-ordinate (m)	z co-ordinate, elevation (m)			Normal coefficient of restitution, e_N	Tangential coefficient of restitution, e_T	
Trajectory S-A-B							
1: Source area	40.00	112.00		-			
2: Rock face	60.00	71.50	200.0	41.0	0.75	0.68	-10,270
3: Barrier impact	117.00	8.00	-	-	-	-	-

It was possible to identify rock fall impact points on both the steel mesh fence and the concrete blocks, and to define the co-ordinates of each point relative to one end of the wall. In total, 466 impacts were documented. Analyses of typical trajectories that were mathematically and physically feasible allowed the impact velocity (v_i) and restitution velocity (v_r) to be calculated at each impact point from which the velocity components, and tangential (e_T) and normal (e_N) coefficients of restitution were determined. The inset on Figure 2.2 shows the velocity components at impact point A for trajectory S – A – B. Table 2-1 shows detail of trajectory S – A – B.

The inset shows that velocities at the point of impact for this height of fall can be as great as $30 \text{ m} \cdot \text{s}^{-1}$ ($100 \text{ ft} \cdot \text{s}^{-1}$). Furthermore, calculation of velocities at the point of impact with the barrier after trajectories that originate at heights of 70 to 100 m (230 to 330 ft) above the barrier can be as high as $48 \text{ m} \cdot \text{s}^{-1}$ ($160 \text{ ft} \cdot \text{s}^{-1}$). Velocities of this magnitude are consistent with the height of the fall and the steepness of the slope.

The impact energies can be calculated from the mass and velocities of the falls. The rocks tended to break up on impact with the rock slope, and the maximum block dimensions of ellipsoid shaped blocks at the barrier location are about 300 to 500 mm (12 to 20 in), with masses in the range of 50 to 150 kg (110 to 330 lb). Based on a typical velocity at the point of impact with the barrier of about $45 \text{ m} \cdot \text{s}^{-1}$ ($150 \text{ ft} \cdot \text{s}^{-1}$), the impact energies ($KE = \frac{1}{2} m \cdot v^2$) are approximately 60 to 180 kJ (22 to 66 ft tonf). It was found that the unreinforced concrete blocks

forming the face of the MSE wall were readily able to withstand these impacts, with damage being limited to chips a few millimeters deep.

Analyses of these rock falls using the program *RocFall 4.0* are given in Section 7.5.1.

Typical rock fall properties: ellipsoidal block with axes lengths 0.4 m (1.3 ft), 0.4 m (1.3 ft) and 0.2 m (0.7 ft), mass of 44 kg (97 lb) (unit weight of 26 kN · m⁻³ (165 lbf · ft⁻³)) and radius of gyration of 0.13 m (0.43 ft) (see Table 4.1 for ellipsoid properties).

2.1.2 Kreuger Quarry, Oregon – rock fall test site

An extensive rock fall test program was carried out at the Kreuger Quarry in Oregon to determine the required ditch configurations to contain rock falls on highways (Pierson *et al.*, 2001). The geometries of the excavated rock cuts included cut heights ranging between 8 m (25 ft) and 24 m (80 ft), face angles ranging between vertical and 45 degrees and ditches inclined at 4H:1V and 6H:1V (towards the slope), and horizontal; in total 11,250 separate rock fall tests were conducted (see Figure 2.3). For each rock fall, the data collected included the first impact position in the ditch, and the roll-out distance. The rock at the test site was a strong, blocky basalt that was excavated with controlled blasting on the design final line to produce a face with few irregularities.

Table 2-2: Oregon impact points from source at crest: 15 m high cut at face angle of 76°

Impact point from source (n)	Impact Coordinates		Trajectory angle, restitution from horizontal, x axis (α_f)	Slope angle (above impact point) ψ_s	Coefficients of restitution		Kinetic energy lost during impact (J)
	x co-ordinate (m)	z co-ordinate, elevation (m)			Normal coefficient of restitution, e_{N^*}	Tangential coefficient of restitution, e_{T^*}	
Crest (1)	0.00	15.00		0			
76° face (2)	1.50	7.00	225.0	76.0	-2.51	0.59	-14,248
Ditch impact (3)	6.25	0.10	140.0	0.0	0.24	0.55	-56,122
2nd impact (4)	9.00	0.00			-	-	-

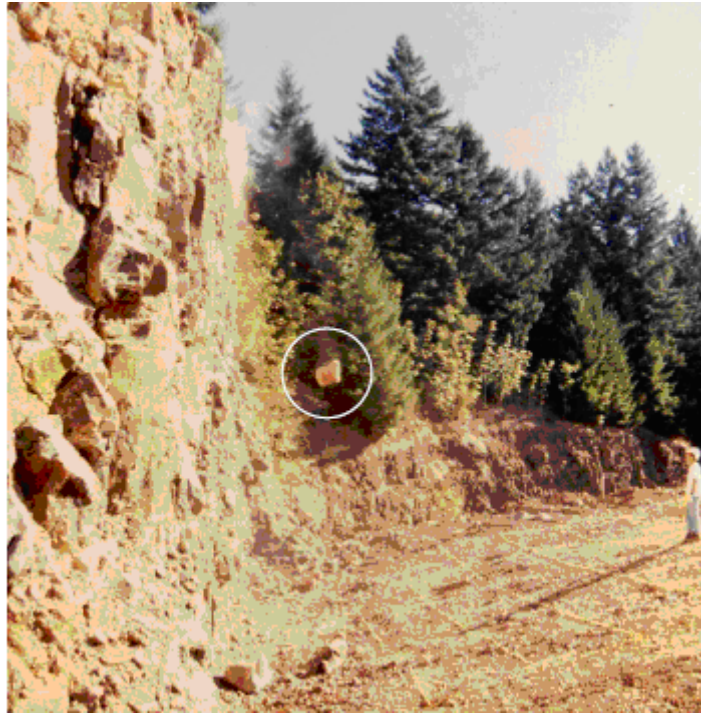


Figure 2.3: Image of rock fall test carried out in Oregon (Pierson *et al.*, 2001)

Figure 2.4 and Table 2-2 show that test results for a 15 m (50 ft) high cut at a face angle of 76 degrees ($\frac{1}{4}H:1V$) with a horizontal ditch. The diagram shows the measured location of the first impact point in the ditch for the 95th percentile of the test rocks, and the assumed trajectories for a rock fall from the crest of the cut initially impacting the face and then the ditch. The second impact point in the ditch is an estimated location based on common rock fall behavior. The inset on Figure 2.4 shows the calculated velocity components, using the spreadsheet described in Section 7.1, at the impact point on the cut face, and the values for e_T and e_N for the first two impact points. These calculated values show the difference in behavior of rock falls that impact at a shallow angle (on the rock face) and at a steep angle (in the ditch). That is, for shallow angle impacts, the normal coefficient is greater than 1, while for steep angle impacts the normal coefficient is less than 1. These field tests and impact mechanics theory show that e_N is related to the impact angle θ_i , and that e_N is generally greater than 1 when θ_i is less than about 20 degrees – see Figures 5.5 and 5.7. In contrast, the tangential coefficient is less than 1 for both impacts and the similar values of e_T for the two impacts shown in Figure 2.3 indicate that e_T is a function of the slope material rather than the impact conditions. Coefficients of restitution are discussed in Chapter 5.

Analyses of these rock falls using the program *RocFall 4.0* are given in Section 7.5.2.

Typical rock fall properties: cubic block with side lengths 0.6 m (2 ft), mass of 580 kg (1280 lb) (unit weight of $26 \text{ kN} \cdot \text{m}^{-3}$ ($165 \text{ lbf} \cdot \text{ft}^{-3}$)) and radius of gyration of 0.245 m (0.80 ft).

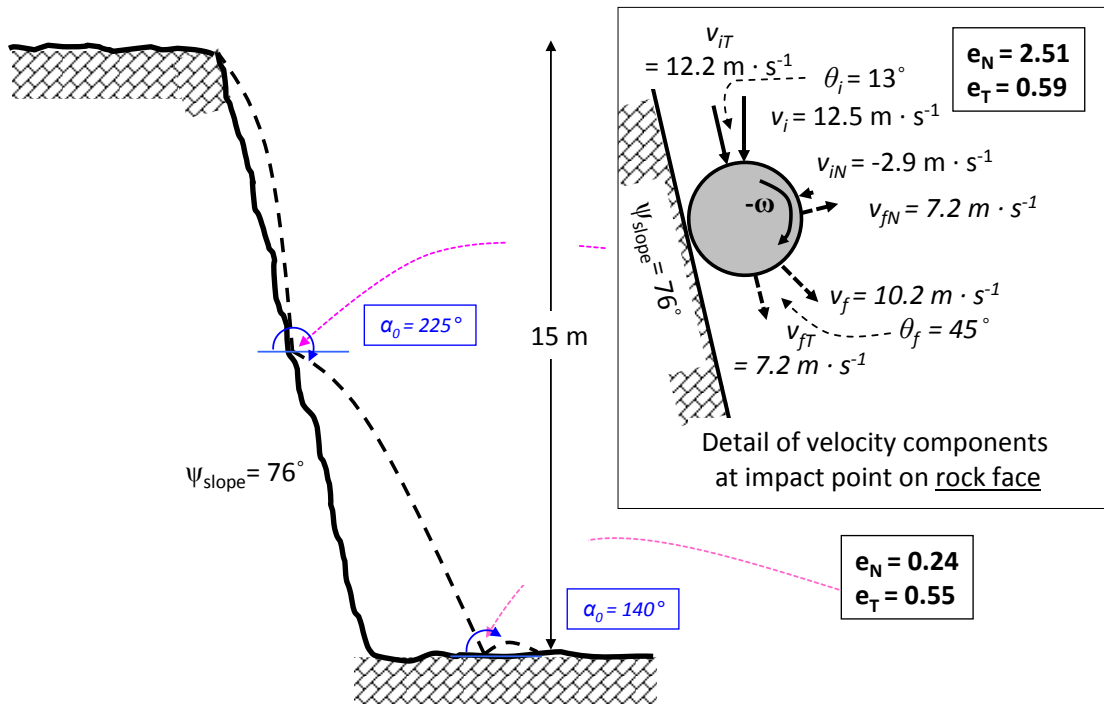


Figure 2.4: Kreuger Quarry, Oregon test site - typical rock fall trajectory and impact points for 15 m high, 76 degree rock face with horizontal ditch

2.1.3 Ehime, Japan – rock fall test site

In 2003 a rock fall study was carried out on a 42 m (140 ft) high rock and talus slope at the Umagun Doi-cho test site in Ehime Prefecture on Shikoku Island (Ushiro *et al.*, 2006). The slope comprised a 26 m (85 ft) high rock slope in horizontally bedded sandstone and mudstone with a face angle of 44 degrees, above a 16 m (50 ft) high talus slope at angle of 35 degrees (Figure 2.5).



Figure 2.5: Ehime test site in Japan – rock slope with talus deposit at base; concrete cube test block

Table 2-3: Ehime, Japan rock fall test site: trajectory for concrete cube

Impact point from source (n)	Impact Coordinates		Trajectory angle, restitution from horizontal, x axis (α_r)	Slope angle (above impact point) ψ_s	Coefficients of restitution		Kinetic energy lost during impact (J)
	x co-ordinate (m)	z co-ordinate, elevation (m)			Normal coefficient of restitution, e_N	Tangential coefficient of restitution, e_T	
0 – source	0.00	45.00					
1 – rock	1.00	44.00	181.0	45.0	0.64	1.01	-1,851
2 – rock	3.00	42.50	205.0	36.9	0.89	0.95	-1,263
3 – rock	6.00	39.70	198.0	43.0	1.71	0.49	-17,403
4 – rock	12.00	31.75	209.7	53.0	0.34	0.94	-8,303
5 – rock	15.00	29.67	189.7	34.7	4.58	0.58	-30,832
6 – talus	28.00	18.23	209.1	41.3	0.22	0.73	-45,806
7 – talus	31.00	16.19	185.6	34.2	5.47	0.71	-17,642
8 – talus	49.00	2.57	184.5	37.1	0.00	0.00	-25,873
9 – stop	53.00	2.00					-148,973

The test involved both natural boulders, and spherical and cubic concrete blocks containing embedded three dimensional accelerometers and a data acquisition system recording data at a frequency of 1/2000 seconds. The instrumentation together with high speed cameras, gave the precise location, and translational and rotational velocities over the full extent of the fall path. Figure 2.6 shows the impact points and trajectories of a typical test of a concrete cube, together with the impact and final velocities, v_i and v_f and the maximum trajectory height h' measured normal to the slope (see also Figure 3.5).

Also shown on Figure 2.6 are the calculated velocity components and the values for e_N and e_T at impact point #3 on rock, and the e_N and e_T values for impact points # 6 and #7 on talus. Table 2-3 shows detail of rock fall trajectory for a concrete cube. For the rock impact, the value for e_N is greater than 1, and has a similar value to that for the Oregon test for the shallow impact angle point on the steep rock face. At both the Oregon and Ehime test sites, e_N values greater than 1 occurred for shallow angle impacts where the impact angles (θ_i) were small (13 and 12 degrees respectively).

Analyses of these rock falls using the program *RocFall 4.0* are given in Section 7.5.3.

Typical rock fall properties: cubic concrete block with side lengths of 0.6 m (2 ft), mass of 520 kg (1,150 lb) (unit weight of $24 \text{ kN} \cdot \text{m}^{-3}$ ($150 \text{ lbf} \cdot \text{ft}^{-3}$)) and radius of gyration of 0.245 m (0.80 ft).

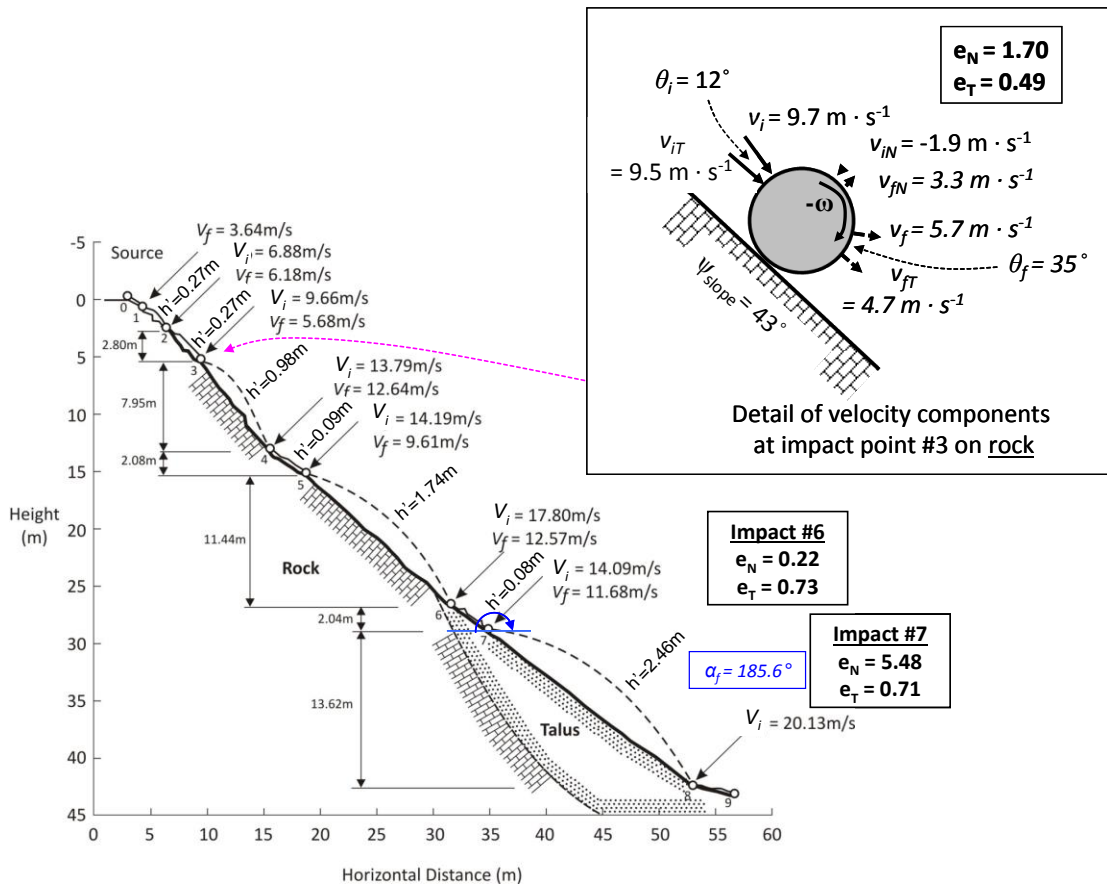


Figure 2.6: Ehime test site, Japan – results of rock fall test showing trajectories, and impact and restitution velocities for concrete cube test block; h' is maximum trajectory height normal to slope, v_i , v_f are impact and final velocities (Ushiro *et al.*, 2006)

2.2 Impacts on talus and colluvium slopes

Information of impacts on talus and colluvium have been obtained from the Ehime test site in Japan (Figure 2.6), and from two rock falls on Tornado Mountain in south-east British Columbia, Canada (Figure 2.8).

2.2.1 Ehime, Japan – rock fall tests on talus

The calculated e_N and e_T values for impact #6 at Ehime on talus are shown on Figure 2.6. It is of interest that the e_T values of #6 and #7 impacts are nearly identical, while the e_N values are very different; the trajectory after impact #6 barely leaves the slope surface, while the trajectory after impact #7 is the longest and highest of the rock fall. The difference in the trajectories is probably due to a combination of slope roughness and the attitude of the block as it impacted the surface. The e_N value of 5.48 at impact point #7 is a reliable, measured value that is a significantly higher than other calculated values at this site.

2.2.2 Tornado Mountain – rock falls on colluvium

The Tornado Mountain site comprises a 50 m (165 ft) high rock face in very strong, blocky limestone, above a colluvium slope at an angle varying from 35 degrees on the upper slope in talus to 22 degrees on the lower slope (Figures 2.7 and 2.8). The colluvium is a mixture of gravel and soil forming a uniform slope with no significant irregularities, and no previous rock falls. The slope is sparsely vegetated with pine trees having diameters ranging from about 300 to 500 mm (12 to 20 in).



Figure 2.7: Images of Tornado Mountain rock fall. a) tree with diameter of about 250 mm (9.8 in) sheared by a falling rock at a height of about 1.6 m (5.2 ft); fragment of rock broken off main rock fall visible in lower left corner; b) Boulder A, with volume of about 1.4 cu. m (1.8 cu. yd), at slope distance of about 740 m (2,450 ft) from source

Table 2-4: Tornado Mountain rock fall A trajectory from source, fall height 350 m

Impact point from source	Impact Coordinates		Trajectory angle, restitution from horizontal, x axis (α_f)	Slope angle (above impact point) ψ_s	Coefficients of restitution		Kinetic energy lost during impact (J)
	x co-ordinate (m)	z co-ordinate, elevation (m)			Normal coefficient of restitution, e_N	Tangential coefficient of restitution, e_T	
A - source	0.00	350.00					
B - rock	8.00	316.00	213.0	76.7	0.24	0.97	-597,368
C - rock	28.00	295.00	205.0	46.4	0.98	0.74	-636,093
D - talus	48.00	280.00	200.0	36.9	1.12	0.84	-383,565
E	72.00	265.00	185.0	32.0	1.19	0.74	-649,674
1	98.00	255.45	167.6	20.2	1.35	0.35	-968,096
2	117.70	244.60	176.2	28.8	0.78	0.53	-428,292
3	132.60	236.15	177.0	29.6	0.88	0.53	-346,394
4	144.60	229.50	176.4	29.0	1.11	0.60	-227,818
5	158.80	221.05	168.0	30.8	1.23	0.52	-291,750
6	176.60	210.90	177.1	29.7	0.82	0.60	-349,399
7	192.20	202.45	175.8	28.4	0.82	0.48	-396,086
8	202.40	197.10	175.1	27.7	1.29	0.72	-119,311
9	218.70	188.05	176.4	29.0	0.63	0.41	-458,078
10	225.70	184.40	174.9	27.5	1.50	0.79	-42,725
11	240.20	176.05	177.3	29.9	0.90	0.60	-294,735
12	253.30	169.30	174.7	27.3	1.26	0.68	-188,389
13	272.00	159.25	175.7	28.3	0.68	0.44	-498,765
14	281.20	154.60	174.2	26.8	1.10	0.62	-163,044
15	291.60	149.15	175.1	27.7	1.00	0.54	-218,672
16	301.70	143.10	178.3	30.9	0.99	0.62	-195,226
17	312.60	136.75	177.6	30.2	1.46	0.79	-80,514
18	335.00	123.10	178.8	31.4	0.85	0.48	-585,150
19	351.60	112.65	179.6	32.2	1.02	0.65	-312,023
20	370.40	102.20	194.5	29.1	0.59	0.85	-218,275
21	383.50	95.25	175.3	27.9	1.44	0.44	-542,278
22	395.60	89.00	189.0	27.3	0.72	0.60	-259,761
23	416.40	77.90	171.0	33.4	1.36	0.57	-200,941
24	427.20	72.65	173.3	25.9	0.94	0.65	-179,329
25	437.70	67.90	171.7	24.3	0.89	0.53	-224,677
26	445.60	64.25	142.6	24.8	1.29	0.27	-179,883
27	452.10	61.20	172.5	25.1	0.89	1.03	-6,012
28	463.00	56.55	158.0	23.1	1.03	0.42	-248,912

2 Documentation of rock fall events

Impact point from source	Impact Coordinates		Trajectory angle, restitution from horizontal, x axis (α_f)	Slope angle (above impact point) ψ_s	Coefficients of restitution		Kinetic energy lost during impact (J)
	x co-ordinate (m)	z co-ordinate, elevation (m)			Normal coefficient of restitution, e_N	Tangential coefficient of restitution, e_T	
29	470.90	53.40	169.1	21.7	0.78	0.65	-117,853
30	477.40	50.75	166.0	22.2	1.24	0.75	-56,926
31	486.70	47.20	168.0	20.9	1.10	0.67	-114,798
32	497.80	42.15	171.9	24.5	1.00	0.69	-165,182
33	519.30	33.30	174.0	23.4	1.17	0.71	-190,159
34	531.90	28.75	167.3	19.9	0.89	0.48	-296,884
35	539.60	25.80	168.4	21.0	0.95	0.65	-116,052
36	546.70	23.05	145.0	21.2	1.21	0.32	-148,602
37	552.30	20.60	171.0	23.6	0.85	0.92	-29,584
38	560.20	17.25	170.4	23.0	0.90	0.55	-158,313
39	566.30	14.50	171.7	24.3	0.98	0.60	-106,242
40	572.20	11.65	173.2	25.8	0.98	0.76	-71,215
41	578.80	9.10	168.5	21.1	1.24	0.68	-87,017
42	587.20	5.55	171.8	22.9	1.30	1.22	135,811
43	605.80	0.00	164.0	16.6	0.57	0.73	-296,779
44	614.50	0.00	147.4	0.0	0.40	0.12	-
45 (STOPPED)	634.00	-4.00	-	-	-	-	-

In 2004, two separate rock falls originating on the rock face travelled a total distance of 740 m (2,450 ft) down the slope – distances of 340 m (1,115 ft) vertically and 610 m (2,000 ft) horizontally. Because no similar rock falls had occurred in the past and each rock followed a separate path, it was possible to locate each impact point on the slope and define its coordinates with a GPS (global positioning system) unit and a laser rangefinder. In total, 45 impact points were identified for Boulder A and 69 impact points for Boulder B. The final masses for the boulders were about 3,750 kg (8,300 lb) (maximum dimension 1.6 m or 5 ft) for Boulder A, and 5,600 kg (12,400 lb) (maximum dimension 2.5 m or 8 ft) for Boulder B. Both rocks impacted a horizontal bench in the lower part of the slope that had been excavated in the colluvium beside a railway and the loss of energy on this bench was sufficient to stop the rocks within 30 m (100 ft).

In addition to the impact points on the colluvium, it was also possible to locate a total of 21 trees that had been impacted and broken off by the boulders, and measure the height of the impact and the distance of the tree from the two adjacent impact points (see Figure 2.7a)). It is considered that the trees did not impede the trajectories because of their small diameter and low strength. Using information on the co-ordinates of successive impact points on the slope and the impact with the trees it was possible for these 21 cases to calculate precise trajectories and velocities, including angles θ_f at the completion of impact and start of the new trajectory. The average value of θ_f for the tree impacts was 33 degrees, with a range of 6 to 63 degrees (see Figure 3.9a)); this range of θ_f was entirely due to the variation in the orientation of the blocks of rock at the impact points because the slope surface was uniform. The average value of θ_f was used to calculate likely velocities components for all other impacts.

Details of the distributions of measured θ_f values at the Tornado Mountain and Ehime sites are shown in Figure 3.9.

For Boulder A, at impact #26 where the precise trajectory could be determined from a broken tree and the impact angle θ_i was 22 degrees, the calculated value of e_N is 1.29, a value that is consistent with other sites where shallow angle impacts occurred. For all 114 impacts on both fall paths where the paths of the rock falls comprised shallow, “skipping” trajectories, the average value of e_N was 1.02. The calculated value for e_T at impact #A26 was 0.27 as shown on Figure 2.8, with the average value of e_T for Boulders A and B being 0.65.

Figure 2.7a) shows images of a 250 mm (9.8 in) diameter tree that was sheared by the rock fall at a height of about 1.6 m (5 ft) above the ground. Also shown in the image is a block that broke away from the main block at this impact point. This rock fragment is one of about 20 similar blocks that were observed on the slope over the lower half of the rock fall path; relationships between loss of mass and the run out distance are discussed in Section 6.5.

The trajectories were also analyzed to determine the maximum height of the fall path, measured normal to the ground surface. It was found that the average height was 1.3 m (4 ft).

Analyses of these rock falls using the program *RocFall 4.0* are given in Section 7.5.4.

Typical rock fall properties: ellipsoidal block (Boulder A) with axes lengths 1.6 m (5.2 ft), 1.3 m (4.3 ft) and 1.3 m (4.3 ft), mass of 3750 kg (8300 lb) (unit weight of $26 \text{ kN} \cdot \text{m}^{-3}$ ($165 \text{ lbf} \cdot \text{ft}^{-3}$)) and radius of gyration of 0.46 m (1.5 ft).

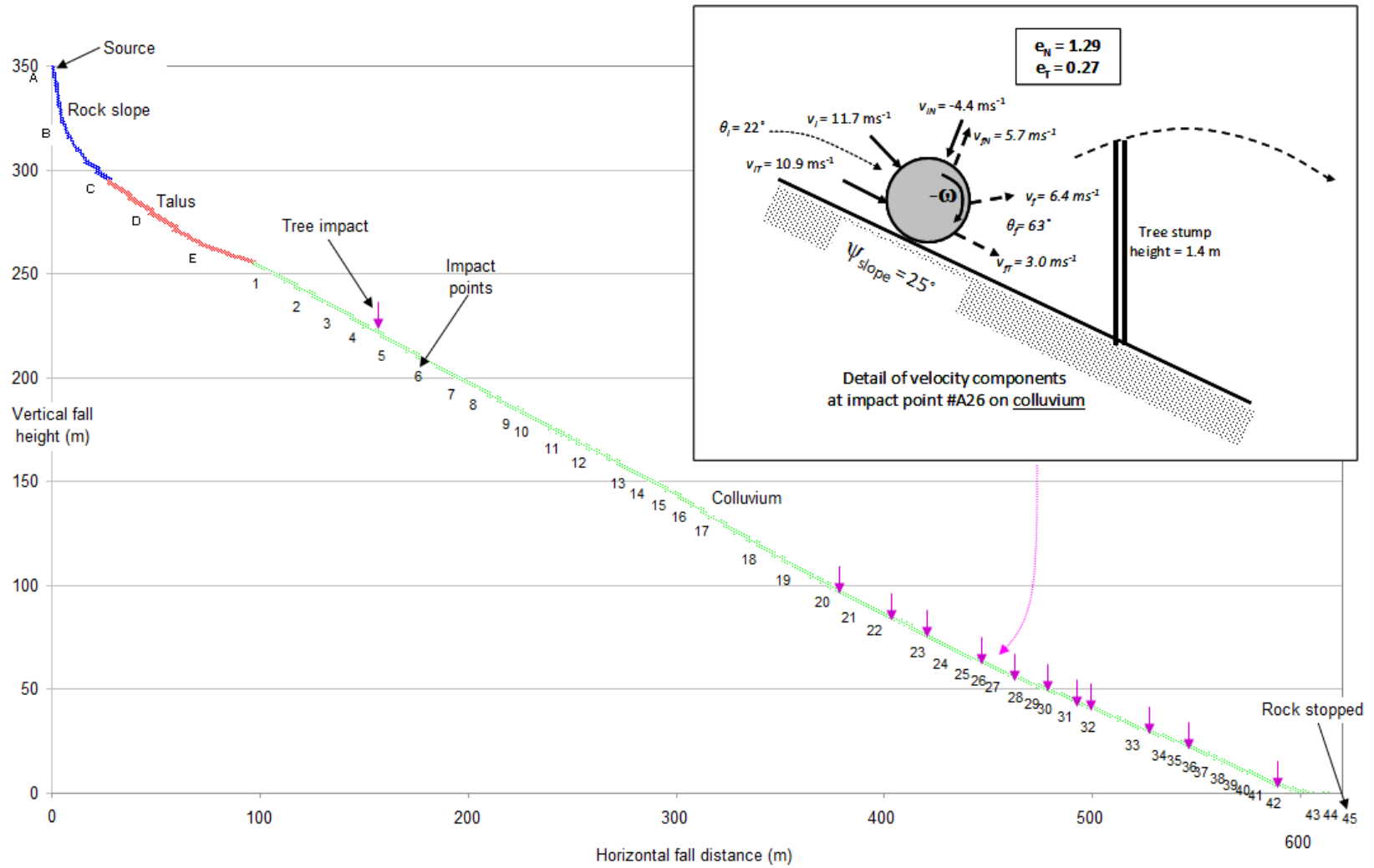


Figure 2.8: Tornado Mountain, Boulder A – mapped impact points (total 46) and broken trees (indicated by arrows ↓), with detail of velocity components at impact #A26

2.3 Impact on asphalt

Figure 2.9 shows a 138 m (450 ft) high slope where a single rock fall occurred, that originated at the crest and finally impacted the asphalt road surface. The 138 m (450 ft) high slope comprises a 58 m (190 ft) high rock slope in very strong, volcanic rock at an angle of 60 degrees, a 70 m (230 ft) high colluvium slope at an angle of 42 degrees, and a 10 m (33 ft) high rock cut above the road.



Figure 2.9: View of 138 m (450 ft) high slope comprising 58 m (190 ft) high rock slope where rock fall originated, colluvium slope at 42 degrees, and 10 m (33 ft) high cut face above the road

Table 2-5: Impact on asphalt

Impact point from source (n)	Impact Coordinates		Trajectory angle, restitution from horizontal, x axis (α_f)	Slope angle (above impact point) ψ_s	Coefficients of restitution		Kinetic energy lost during impact (J)
	x co-ordinate (m)	z co-ordinate, elevation (m)			Normal coefficient of restitution, e_N	Tangential coefficient of restitution, e_T	
Source	0.00	637.00					
1 – rock	113.00	511.00	212.0	41.0	0.17	27.60	-570,123
2 – asphalt	124.00	501.00	118.0	0.0	0.38	0.24	-106,024
3 – 2 nd impact	127.10	502.63					

Figure 2.10 shows the final trajectories of the fall from the top of the 10 m (33 ft) high rock cut to just after the impact on the road. These trajectories were precisely defined by a survey of the site and the inset on Figure 2.10 shows the calculated velocity components at the asphalt impact point. Although this is a single record of an impact with asphalt, the author has investigated several similar events where comparable trajectories were generated for impacts on asphalt.

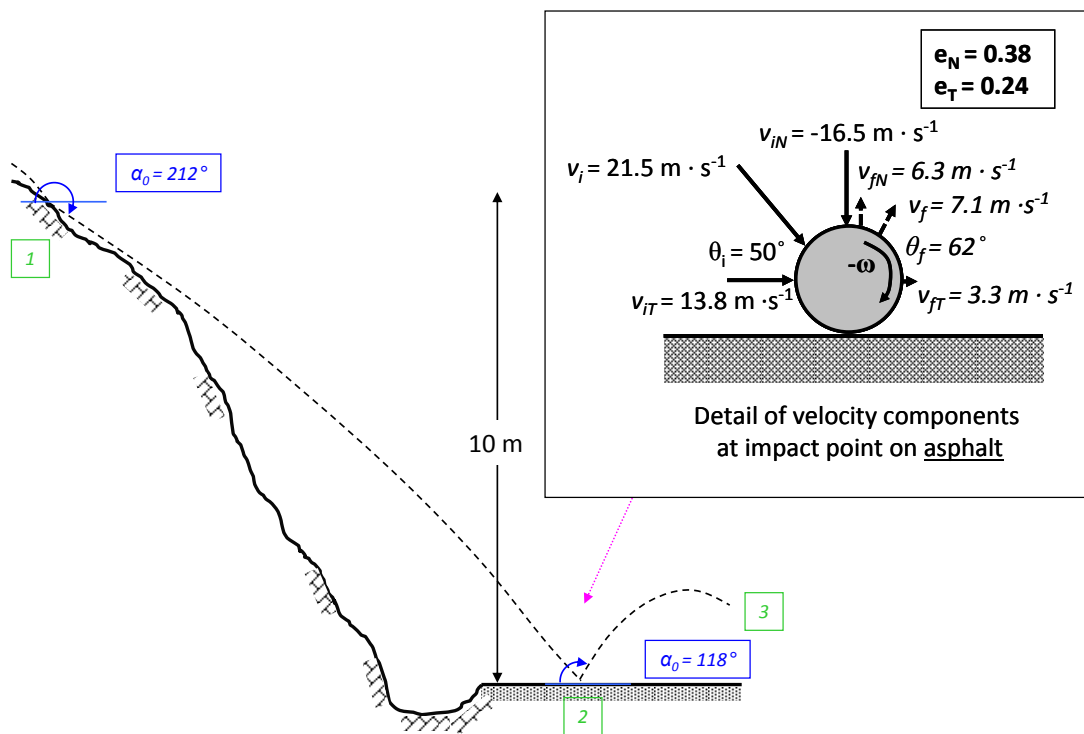


Figure 2.10: Final trajectory of a rock falling from a height of 136 m (445 ft) and impacting a horizontal asphalt surface

The trajectory shown in Figure 2.10 is a relatively steep angle impact (i.e., $\theta_i = 50$ degrees) compared to the shallow angle impacts at Tornado Mountain and the Oregon test site, and for

this condition the value of e_N is 0.38. As discussed in Chapter 5, the value of e_N for steep impacts is low compared to shallow impacts. The value for e_T for this relatively smooth impact surface is 0.24.

Analyses of these rock falls using the program *RocFall 4.0* are given in Section 7.5.5.

Typical rock fall properties: cuboid block with axes lengths 0.84 m (2.8 ft), 0.58 m (1.9 ft) and 0.4 m (1.3 ft), mass of 500 kg or 1100 lb (unit weight of $26 \text{ kN} \cdot \text{m}^{-3}$ or $165 \text{ lbf} \cdot \text{ft}^{-3}$), and radius of gyration of 0.295 m (1 ft).

2.4 Impact with concrete

Tests were conducted to find the normal restitution coefficient of concrete. The tests involved dropping a boulder from a known height (h_i) on to a horizontal concrete slab and measuring the rebound height (h_f). It was found that the normal coefficient of restitution e_N for the concrete under these impact conditions was 0.18 ($e_N = (v_f/v_i) = \sqrt{h_f/h_i}$) – see also Section 5.2.2, Figure 5.6 (Masuya et al., 2001).

2.5 Summary of case study results

This section summarizes the conditions at each of the documented case studies (Table 2-6) and the calculated normal and tangential coefficients of restitution (Table 2-7).

Table 2-6: Summary of rock properties

Site	Mt. Stephen, Canada	Kreuger Quarry, Oregon	Ehime, Japan	Tornado Mt., Canada	Highway (asphalt)
Geology	Strong, massive, horizontally bedded limestone containing thin but widely spaced shale beds	Hard durable basalt	Horizontally bedded sandstone and mudstone, with talus	Rock face in very strong, massive limestone, talus and colluvium on slope	Approx 60 m of rock slope, 70 m of colluvium (sand & gravel) and 8 m of rock cut
Slope angle (deg)	60	76	43	30	47
Dimension	ellipsoidal block with axes lengths 0.4 m (1.3 ft), 0.4 m (1.3 ft) and 0.2 m (0.7 ft)	cubic block with side lengths 0.6 m (2 ft)	cubic concrete block with side lengths of 0.6 m (2 ft)	ellipsoidal block (Boulder A) with axes lengths 1.6 m (5.2 ft), 1.3 m (4.3 ft) and 1.3 m (4.3 ft)	cuboid block with axes lengths 0.84 m (2.8 ft), 0.58 m (1.9 ft) and 0.4 m (1.3 ft)
Radius (m)	0.2	0.3	0.3	0.8	0.36
Radius of gyration	0.13 m or 0.43 ft	0.245 m (0.80 ft)	0.245 m (0.80 ft)	0.46 m (1.5 ft)	0.295 m (1 ft)
Mass	44 kg (97 lb)	580 kg (1280 lb)	520 kg (1,150 lb)	3750 kg (8300 lb)	500 kg or 1100 lb

Table 2.7 summarizes the calculated normal and tangential coefficients of restitution for the five case studies, as well as the results of a rock dropped vertically on to a concrete surface. The tabulated results show that e_N has a range of values that are greater than 1 for shallow angle impacts and as low as 0.24 for steep angle impacts, and 0.18 for the vertical drop test on concrete; Chapter 5 discusses the relationship between the angle of impact θ_i and e_N .

The results for e_T have a narrower range from 0.25 and 0.27 for relatively smooth asphalt and colluvium surfaces, to 0.49 and 0.73 for rock and talus surfaces. The e_T results show a trend between low values for smooth, soft surfaces to higher values for rough, hard surfaces that is consistent with frictional properties of rock surfaces.

Chapter 4 (impact mechanics) and Chapter 5 (coefficients of restitution) discuss the theoretical relationship between the values of e_N and e_T , and impact conditions. In addition, Section 4.7

compares the final velocities and angles for the five case studies discussed in this chapter, with the calculated final velocities and angles based on impact mechanics theory.

Table 2-7: Summary of coefficients of restitution calculated for rock fall case studies

Site no.	Rock fall site	Slope material	Normal coefficient of restitution, e_N	Tangential coefficient of restitution, e_T
1	Mt. Stephen, Canada	rock	0.75	0.68
2	Oregon ditch study (rock face impact)	rock	2.51	0.59
2	Oregon ditch study (ditch impact)	rock	0.24	0.55
3	Ehime, Japan (rock slope, #3)	rock	1.70	0.49
3	Ehime, Japan (talus slope, #6)	talus	0.22	0.73
3	Ehime, Japan (talus slope, #7)	talus	5.48	0.71
4	Tornado Mountain, Canada	colluvium	1.29	0.27
5	Highway	asphalt	0.38	0.24
6	Drop test, Japan (see Figure 5.6)	concrete	0.18	-

3 Rock fall velocities and trajectories

Analysis of rock falls involves study of both trajectories and impacts. This chapter discusses trajectories and how they depend on the translational and angular velocities of the falling bodies. Also discussed are physical characteristics of rock fall sites such as run-out distance, dispersion of falls in the run-out area and the influence of gullies on rock fall behavior.

Trajectories are defined by the distance between impact points and the height of the rock fall path above the ground surface. In a few instances it is possible to measure these two parameters in the field, as was the case with the two rock falls at Tornado Mountain discussed in Section 2.2.2 where impacts with trees and the ground could be used to precisely define trajectories. Figure 3.1 shows examples of well-defined impact points.



Figure 3.1: Examples of impact points visible in the field. a) Distance successive impact points on slope surface (Christchurch, New Zealand 2011 earthquake); b) impact point on tree showing trajectory height (Tornado Mountain, Canada)

3.1 Trajectory calculations

The trajectories that rock falls follow are exactly defined by Newtonian mechanics, assuming that no air resistance occurs. This section defines the basic equations that govern trajectories,

and how these are applied to the analysis of rock falls to determine the location of impact points, and the height and length of trajectories.

3.1.1 Trajectory equation

The trajectory portion of rock falls between impacts, that is, the flight path and changes in the translational velocity, is governed by Newtonian mechanics and gravitational acceleration. The calculations are based on acceleration in the vertical direction being equal to gravity ($a_z = -g$), with no acceleration in the horizontal direction ($a_x = 0$). Figure 3.2 shows a body moving with an initial velocity V_0 in direction α_0 relative to a horizontal [x] and vertical [z] co-ordinate system. Determination of the vertical and horizontal co-ordinates of the falling rock, and its velocity V_t at any time t during the trajectory, involves integration between the start of the trajectory at time $t = 0$ and time t , of the following expressions for acceleration and velocity.

$$\begin{array}{ll} \text{Vertical acceleration, } a_z = -g; & \text{horizontal acceleration, } a_x = 0 \\ \text{Vertical velocity, } V_{tz} = \int_0^t a_z dt; & \text{horizontal velocity, } V_{tx} = \int_0^t a_x dt \\ = -g \cdot t + c & = c' \end{array}$$

At the start of the trajectory when $t = 0$, the velocity components are:

$$\begin{array}{ll} V_{tz} = v_{0z} = c & \text{and} & V_{tx} = V_{0x} = c' \\ V_{tz} = -g \cdot t + V_{0z} & & V_{tx} = V_{0x} \end{array}$$

$$\begin{array}{ll} \text{Vertical location, } z = \int_0^t (-g \cdot t + V_{0z}) dt; & \text{horizontal location, } x = \int_0^t (V_{0x}) dt \\ z = -\frac{1}{2} g \cdot t^2 + V_{0z} \cdot t + c'' & x = V_{0x} \cdot t + c''' \quad (3.1) \end{array}$$

When $t = 0$, $z = 0$, $x = 0$ and $c'' = c''' = 0$

$$\text{Therefore: } z = -\frac{1}{2} g \cdot t^2 + V_{0z} \cdot t ; \quad x = v_{0x} \cdot t \quad \text{or} \quad t = \frac{x}{V_{0x}} \quad (3.2)$$

where V_{0z} and V_{0x} are respectively, the velocity components in the vertical and horizontal directions at the start of the trajectory.

Equations (3.2) defines a parabolic curve, that gives the [x, z] co-ordinates of rock fall trajectories, and other projectiles, as a function of time of flight, t .

The angle α_0 , measured counter-clockwise from the positive x axis, defines the direction of the velocity vector V_0 at time $t = 0$ (Figure 3.2) from which the following expressions can be obtained:

$$\tan \alpha_0 = \frac{V_{0z}}{V_{0x}} \quad \text{and} \quad V_{0x} = V_0 \cdot \cos \alpha_0 \quad (3.3)$$

Equations (3.2) and (3.3) can be combined to define the location of the body in terms of $[x, z]$ co-ordinates, the initial velocity v_0 and angle α_0 as shown in equation (3.4):

$$z = -\frac{g}{2} \left(\frac{x}{V_0 \cdot \cos \alpha_0} \right)^2 + x \cdot \tan \alpha_0 \quad (3.4)$$

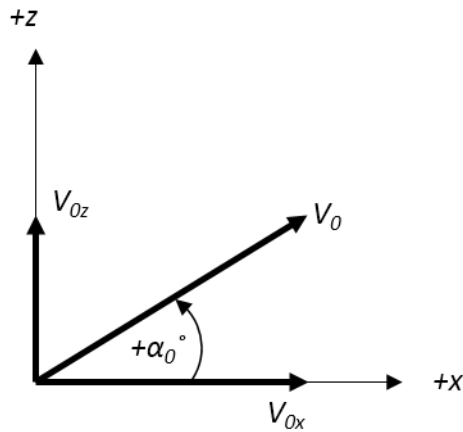


Figure 3.2: Definition of trajectory velocity components and directions

Equation (3.4) can be rearranged to show the relationship between the initial velocity V_0 , of the body, its angle relative to the x-axis α_0 , and the distance travelled by the body from the initial point to the point defined by the co-ordinates $[x, z]$ ¹:

$$V_0 = \frac{x}{\cos \alpha_0 \left[\frac{2(x \cdot \tan(\alpha_0) - z)}{g} \right]^{0.5}} \quad (3.5)$$

¹ Equation (3.5) can also be used for applications other than rock falls. For example, for water discharging from a pipe, the vertical and horizontal distances of the jet from the discharge point can be measured as well as the angle of the pipe. These values can be entered in equation (3.5) to find the discharge velocity, from which the flow rate can be calculated knowing the discharge area.

Worked example 3A – trajectory co-ordinates: if the initial velocity, $V_0 = 20 \text{ m} \cdot \text{s}^{-1}$ at an angle $\alpha_0 = 35$ degrees, the vertical and horizontal components of the initial velocity are:

$$V_{0z} = 20 \sin 35 = 11.5 \text{ m} \cdot \text{s}^{-1}; \quad V_{0x} = 20 \cos 35 = 16.4 \text{ m} \cdot \text{s}^{-1}$$

and the co-ordinates at time $t = 2$ seconds are given by equation (3.2):

$$z = -(0.5) \cdot (9.81) \cdot (2)^2 + (11.5) \cdot (2) = 3.38 \text{ m}$$

If $t = 4$ seconds, $z = -32.5 \text{ m}$, showing that, at this time when $x = 65.6 \text{ m}$, the body has descended below the x-axis and now has a negative z value.

3.1.2 Nomenclature – trajectories and impacts

The nomenclature used to define the velocities and angles of trajectories and impacts is shown in Figure 3.3. For trajectories, the start of the trajectory is designated by the subscript “0” (time, $t = 0$) and the end of the trajectory where the next impact starts is designated by the subscript “i” (time, $t = i$).

With respect to the impact, the moment of impact at the end of the trajectory is designated by the subscript “i” (e.g. V_i, θ_i), and the end of the impact and the start of the next trajectory by the subscript “f” (e.g. V_f, θ_f). That is, $V_f = V_i$ and $\theta_f = \theta_i$, and the velocity at the end of the impact equals the velocity at the start of the next trajectory. The final velocity and angle are also termed the “restitution” parameters. Chapter 4, Impact Mechanics discusses methods of calculating velocity components during impact.

3.1.3 Rock fall trajectories

The trajectory equations discussed in Section 3.1.1 can be applied directly to the analysis of rock falls to determine parameters such as impact and restitution velocities, and trajectory lengths and heights.

Figure 3.3 shows a typical rock fall configuration at the completion of an impact where a body is just leaving the ground (impact point (n)) at a final (restitution) velocity V_f , equal to the velocity at the start of the trajectory, V_0 . The orientation of this velocity vector can be defined by either of two angles, α_0 or θ_0 . The angle α_0 is relative to the positive x-axis, measured either counter-clockwise (positive) or clockwise (negative) and can have values between 0 and 360 degrees. Angle α_0 is used for the application of equations (3.1) to (3.5); in applying these equations,

values of α_0 of +330 degrees or -30 degrees, for example, give identical results. That is, $\alpha_0 = -30$ degrees is equivalent to $\alpha_0 = +330$ degrees because $\sin(-30) = \sin(330) = (-0.5)$.

The angle θ_0 , at the start of the trajectory, is used to define the orientation of the velocity vector relative to the ground surface, and is a parameter that is more readily used in the analysis of field data. If the slope angle is ψ_s , then the relationship between these three angles is given by:

$$\theta_0 = (\psi_s + \alpha_0) \quad (3.6)$$

Equation (3.6) is applied for positive and negative values of α_0 .

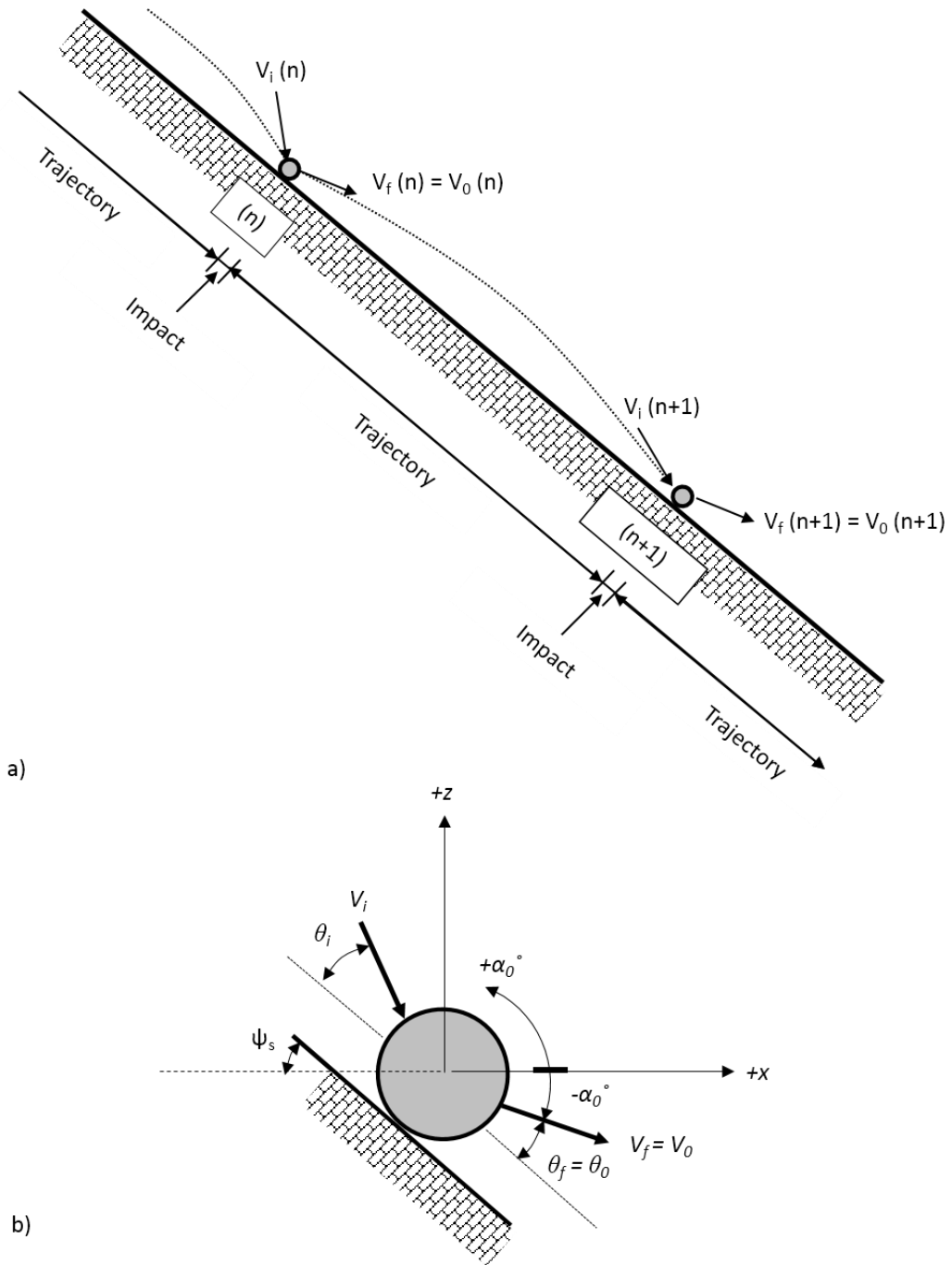


Figure 3.3: Definition of trajectory parameters. a) Velocity nomenclature for trajectories and impacts; b) parameters used in equation (3.4) to calculate rock fall trajectories

An essential premise of Newtonian mechanics applied to rock falls is that while the vertical component of the translational velocity changes during the trajectory as a result of gravitation acceleration, both the horizontal velocity and the angular velocity are constant during the trajectory because no forces act on the body to change these velocity components.

The full trajectory of the rock fall, defined by the $[x, z]$ co-ordinates, can be obtained from equation (3.4) for specified values of V_0 , θ_0 and ψ_s . Figure 3.4 shows successive locations of a rock fall following a parabolic trajectory between impact points (n) and $(n+1)$.

3.1.4 Trajectory height and length

The trajectory equations discussed in Section 3.1.1 above that define the rock fall path through the air, can also be used to find the next impact point, the slope distance between impact points, and height of the rock fall above the slope surface. These data are useful in designing the location and height of fences and barriers on the slope.

Figure 3.4 shows the calculated trajectory between impact points (n) and $(n+1)$ for the velocity vector and slope angle parameters at point (n) , where the velocity at the start of the trajectory V_0 is equal to the velocity at the completion of impact at point (n) , or $V_{f(n)}$. The co-ordinates of impact point $(n+1)$ can be found from the point of intersection between the equations for the trajectory and slope. If the average slope between the impact points has gradient κ , then the equation of the slope is:

$$z = \kappa \cdot x \quad (3.7)$$

and the point of intersection is found by equating equations (3.4) and (3.7) as follows:

$$\kappa \cdot x = -\frac{g}{2} \left(\frac{x}{V_0 \cdot \cos \alpha} \right)^2 + x \cdot \tan \alpha$$

and

$$x_{impact} = \frac{-2(\kappa - \tan \alpha)}{g \left(\frac{1}{V_0 \cdot \cos \alpha} \right)^2} \quad (3.8)$$

Once the x co-ordinate of the impact point is known, it can be substituted in either equation (3.4) or (3.7) to find the z co-ordinate.

The trajectory equation can also be used to find the vertical height h of the body above the slope at any point, as well as the maximum height h_{max} , and the x co-ordinate of this height. The height of the body above the slope is equal to the difference in z co-ordinates given by equations (3.2) and (3.7).

$$h = (z_{traj} - z_{slope})$$

3 Rock fall velocities and trajectories

$$= (a \cdot x^2 + b \cdot x) - (\kappa \cdot x)$$

$$= (a \cdot x^2) + x(b - \kappa) \quad (3.9a)$$

$$\text{where } a = -\frac{g}{2} \left(\frac{1}{V_0 \cdot \cos \alpha} \right)^2 \quad \text{and} \quad b = \tan \alpha \quad (3.9b)$$

Equations (3.9a) and (3.9b) define the height of the body above the slope for any value of the horizontal co-ordinate [x].

The maximum height of the body above the slope can be found by differentiation of equation (3.9a), and equating the result to zero. The differential of equation (3.9a) is

$$\frac{dh}{dx} = 2 \cdot a \cdot x + (b - \kappa) \quad (3.10)$$

and the value of the x co-ordinate where the height is a maximum is:

$$x = \frac{-(b - \kappa)}{2a} \quad (3.11)$$

This value of x can then be substituted in equation (3.9a) to calculate the maximum trajectory height, h_{max} (Figure 3.4).

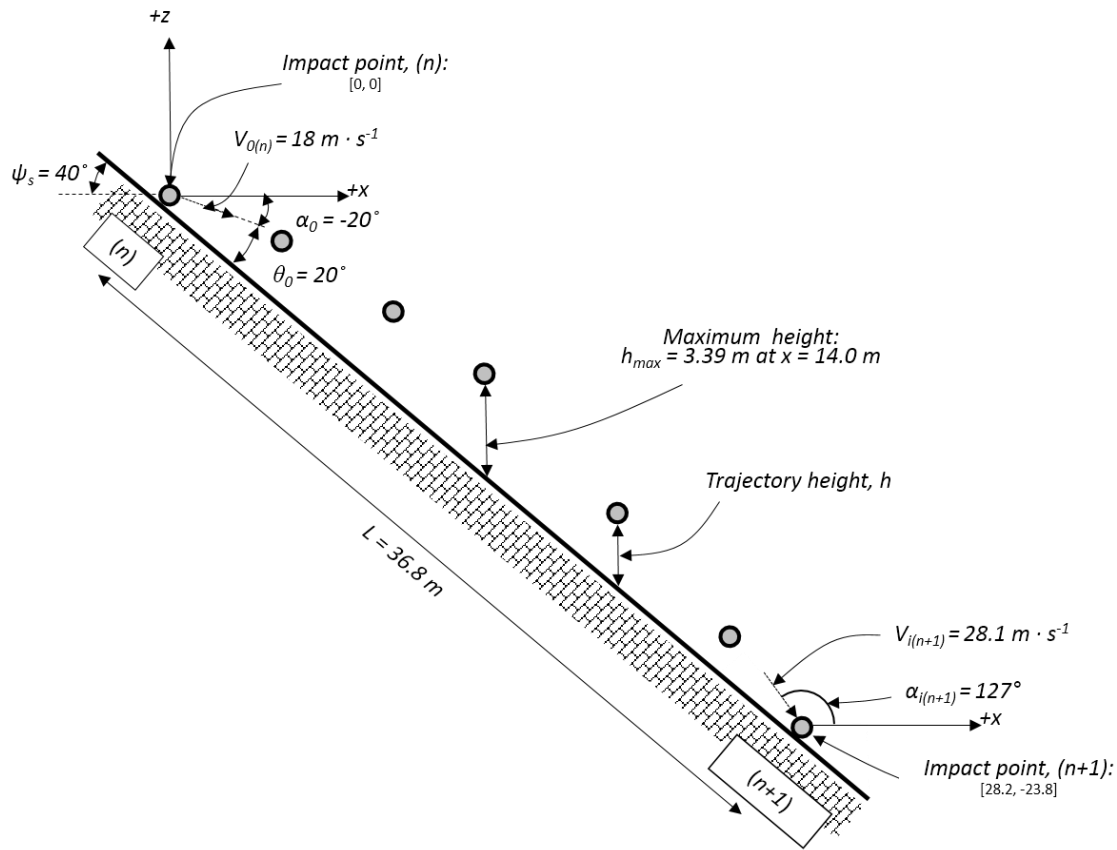


Figure 3.4: Trajectory calculations showing rock fall path, impact points, impact velocities and trajectory height and length

Worked example 3B – trajectory calculations: a rock fall comprises a series of impacts with a slope at a uniform angle $\psi_s = 40$ degrees (gradient, $\kappa = -0.84$). At impact point (n) with co-ordinates $[0, 0]$, the velocity at the start of the trajectory is $V_{0(n)} = 18 \text{ m} \cdot \text{s}^{-1}$ (Figure 3.4), and the angle of the velocity vector at this point is $\theta_{0(n)} = 20$ degrees. The angle α_0 defining the orientation of the velocity vector can be found from equation (3.6) to be $\alpha_0 = -20$ degrees.

Based on these parameters, the co-ordinates of any point on the parabolic trajectory can be found from equation (3.4):

$$z = -0.017x^2 - 0.36x$$

The equation of the slope is $(z = -0.84 x)$, so the co-ordinates of the next impact point $(n+1)$ can be found from equating these two expressions for z . The co-ordinates of impact point $(n+1)$ are: $[x_{(n+1)} = 28.2 \text{ m}, z_{(n+1)} = -23.8 \text{ m}]$.

The slope length L between these two impact points is obtained from the difference Δ , of their vertical (z) and horizontal (x) co-ordinates:

$$L = (\Delta x^2 + \Delta z^2)^{0.5}$$

$$= 36.8 \text{ m}$$

From equation (3.11), the maximum vertical height of the trajectory above the slope is 3.39 m, which occurs at x co-ordinate 14.0 m.

It is also possible to calculate the impact velocity at impact point (n+1), $V_{i(n+1)}$ as follows. The horizontal and vertical components of the velocity at impact point (n) at the start of the trajectory are respectively:

$$V_{0x(n)} = V_{0(n)} \cos \alpha = 16.9 \text{ m} \cdot \text{s}^{-1} \quad \text{and} \quad V_{0z(n)} = V_{0(n)} \sin \alpha = 6.2 \text{ m} \cdot \text{s}^{-1}$$

During the trajectory to impact point (n+1), the vertical velocity component will increase due to gravitational acceleration and the vertical velocity at point (n+1) is:

$$V_{iz(n+1)} = \sqrt{(V_{0z(n)})^2 + 2g(\Delta z)}$$

$$= 22.4 \text{ m} \cdot \text{s}^{-1}$$

The horizontal velocity component will not change during the trajectory so that the two components of the impact velocity at impact point (n+1) are $V_{ix(n+1)} = 16.9 \text{ m} \cdot \text{s}^{-1}$ and $V_{iz(n+1)} = 22.4 \text{ m} \cdot \text{s}^{-1}$. The resultant impact vector at point (n+1) has a velocity of $V_{i(n+1)} = 28.1 \text{ m} \cdot \text{s}^{-1}$. The angle $\theta_{i(n+1)}$ of the vector is given by:

$$\theta_{i(n+1)} = \text{atan}\left(\frac{22.4}{16.9}\right) = 53 \text{ degrees}$$

at an angle of $\alpha_{i(n+1)} = 180 - 53 = 127 \text{ degrees}$.

3.1.5 Field trajectory heights

Section 3.1.4 above and Figure 3.4 show the calculated theoretical trajectory height measured vertically from the slope surface for a parabolic rock fall trajectory. Information on actual trajectory heights is available from the Ehime test site in Japan where the test blocks comprised concrete spheres with a diameter of 0.54 m (1.8 ft), concrete cubes with a side length of 0.6 m (2 ft) and blocks of rock with masses ranging from 120 kg to 2060 kg (260 lb to 4550 lb). The test program consisted of 10 spheres, 10 cubes and 20 blocks of rock, with half of the tests carried out on a treed slope and the second half after the trees had been removed (see Section 6.6

regarding the energy dissipation of trees growing in the rock fall path). The concrete bodies contained embedded three dimensional accelerometers that provided detailed information on the positions and velocities of the blocks through the fall. The slope at the test site was 42 m (140 ft) high, made up of a 26 m (85 ft) high sandstone and mudstone rock slope with a face angle of 44 degrees, and a 16 m (50 ft) high talus cone at an angle of 35 degrees (see Section 2.1 and Figure 2.6).

A component of the data collected was the height of the trajectories above the slope surface, in a direction at right angles to the slope. These data are shown on Figure 3.5 where the height is plotted against the fall height from the source. The results show that the heights vary from zero, i.e., a rolling block, to a maximum height of about 2 m (6.5 ft), with no significant difference in the trajectory heights between the three block shapes. Further analysis of the data shows that, for a total of 235 trajectories, 233 (or 99 per cent) had heights of less than 2 m (6.5 ft), and that 56 per cent had heights less than 0.5 m (1.6 ft). For the 11 trajectories (4.7 per cent) where the heights exceeded 1.5 m (5 ft), the preceding impact involved a projecting rock or tree that deflected the fall away from the slope.

It is noted that, while equations (3.9a) and (3.9b) define the vertical height of the trajectory above the slope surface, the data shown in Figure 3.5 is for the height (h') normal to the slope. The normal trajectory height is defined as follows:

$$h' = \frac{(V_0 \cdot \sin \theta_0)^2}{2 \cdot g \cdot \cos \psi_s} \quad (3.12)$$

For the rock fall parameters used in Worked example 3B, the maximum normal trajectory height is:

$$h' = \frac{(18 \sin[20])^2}{2 \cdot g \cdot \cos(40)} = 2.52 \text{ m}$$

This maximum height in the normal direction compares with the maximum vertical height of 3.38 m.

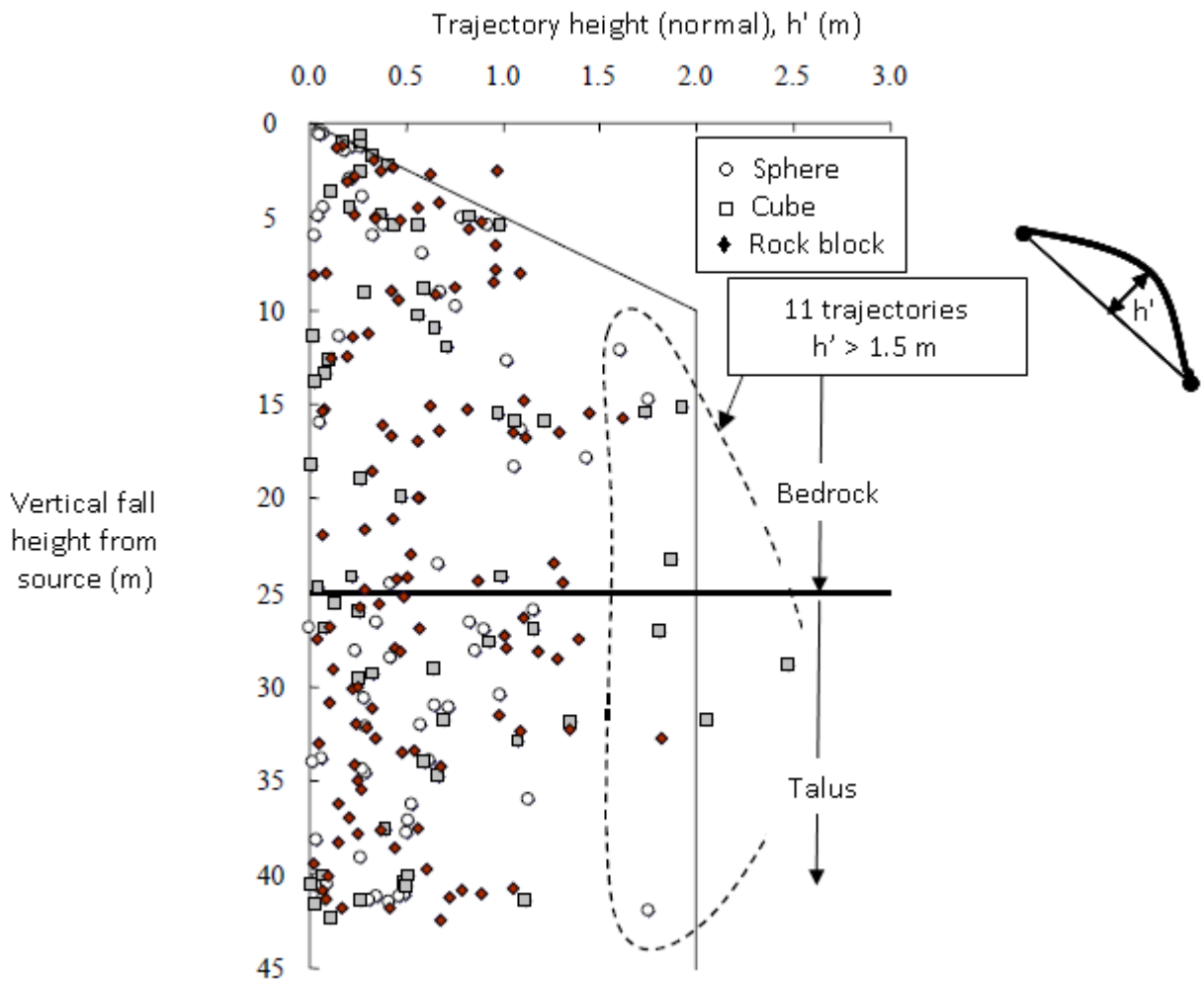


Figure 3.5: Plot of normal trajectory heights from Ehime test site for spherical and cubic concrete blocks, and blocks of rock (see Figure 2.6 for slope section). (Ushiro et al., 2006)

In the design of nets and barriers, it is often acceptable to provide protection for about 90 to 95 per cent of the falls. Under these conditions, the height of a net at Ehime, for example, would need to be 1.5 m (5 ft) high to contain 95 per cent of the falls (Figure 3.5).

The trajectory heights shown in Figure 3.5 are in agreement with the author's experience of other rock fall locations where observations of impacts on trees have shown that trajectory heights are usually in the range of 1 to 2 m (3.3 to 6.6 ft). For example, at Tornado Mountain as discussed in Section 2.2.2 where the total horizontal fall distance was about 610 m (2000 ft) on a slope with an angle of about 22 to 30 degrees, the average trajectory height was 1.5 m (5 ft). An exception to these low trajectory heights is another location where the fall height was 210 m (700 ft) on a slope at a uniform angle of 43 degrees. The frequent falls had produced a polished

rock surface on the well-defined rock fall path, and in the lower part of the slope, trajectory heights of up to 4 m (13 ft) were observed.

3.2 Rock fall velocities

Section 3.1 above discussed trajectory paths with respect to their height and length, and the equations that define these characteristics. This section discusses rock fall velocities, and the conditions that influence velocity.

When a rock fall involves a series of impacts and trajectories, the velocity will increase if the energy lost due to plastic deformation of the slope during impact is less than the energy gained due to gravitational acceleration during the subsequent trajectory. Eventually, as the slope angle flattens and/or the energy absorbing properties of the slope increase from bare rock to soil, for example, the energy losses on impact will exceed the energy gains during the trajectory, and the velocity will decrease.

3.2.1 Field velocity measurements

Typical velocities for the Ehime test site in Japan, as a function of the fall height, are shown in Figure 3.6, in which the impact (V_i) and restitution (V_r) velocity components are shown separately (see Figure 2.6 for slope section). The plot shows that impact velocities are greater than restitution velocities, representing the loss of energy at the impacts; the variation in the velocities is the result of the details of differing geometric conditions at the impact points.

Features of the plot in Figure 3.6, which are typical of rock falls, are that the velocities increase in the early part of the fall over a height of about 15 m (50 ft) in this case, and then reach an approximate terminal velocity of about 15 to 18 m · s⁻¹ (50 to 60 ft · s⁻¹). The plot also shows that velocities in the rock and talus portions of the slope, with the velocities on the talus being somewhat less than those on the rock. The velocities decrease at fall heights greater than 40 m (130 ft) where the rocks roll past the base of the talus slope on to flatter ground and stop moving.

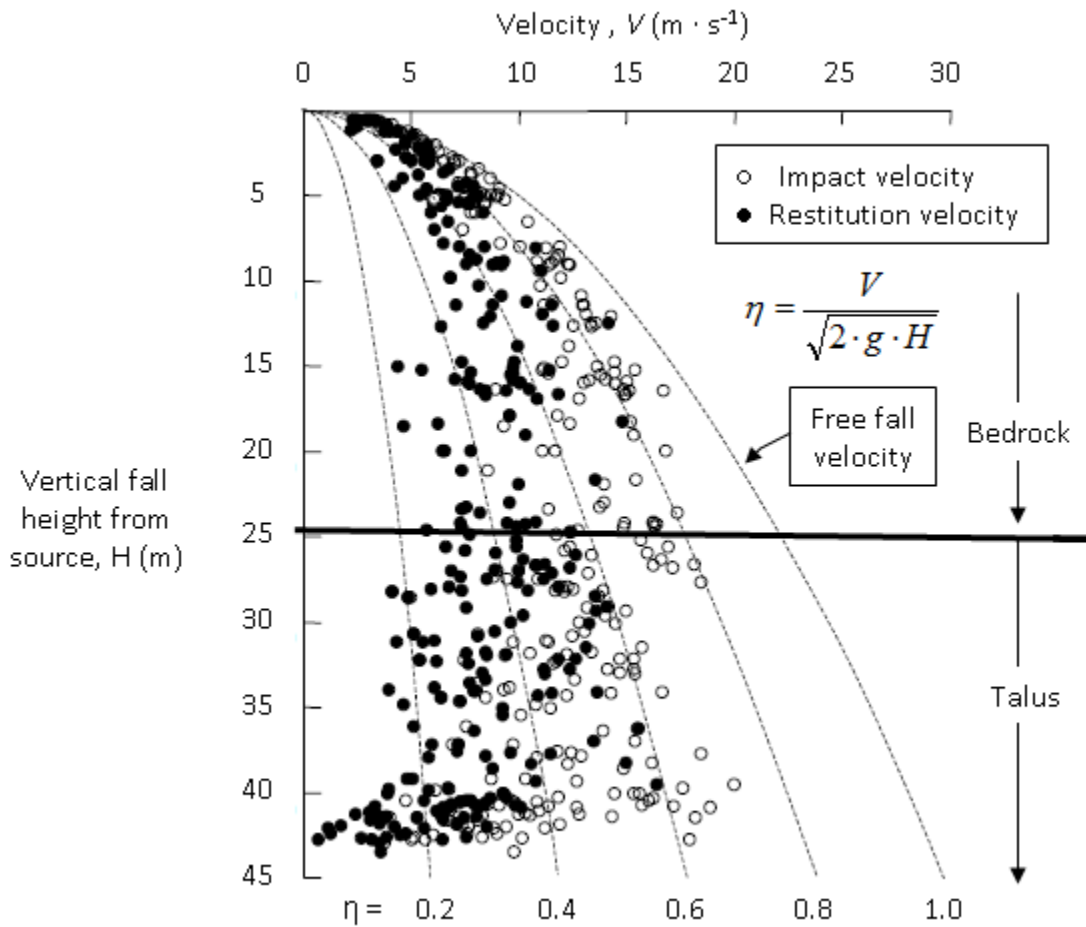


Figure 3.6: Range of velocities for Ehime rock fall test site (see Figure 2.6 for slope section)

3.2.2 Effect of friction and slope angle on velocity

The main site characteristics that influence rock fall velocities, in addition to the fall height, are the slope angle and the material(s) on the slope surface, with lower velocities for shallow slopes and softer, more energy absorbing material compared to higher velocities for steep, hard rock slopes. The relationship between velocity and height, incorporating the slope angle and the characteristics of the slope material, is discussed below.

Referring to Figure 3.7a), a block of rock with mass m , is sliding on a slope dipping at ψ_s degrees with the surficial material having an effective friction coefficient μ' . The motion of this block can be studied using limit equilibrium methods that compare the relative magnitudes of the driving and resisting forces (Wyllie and Mah, 2002). If the driving force is greater than the resisting force, then the out-of-balance force ($m \cdot a$), causes acceleration a , of the block according to the following relationship:

$$\begin{aligned}
 m \cdot a &= (\text{driving force} - \text{resisting force}) \\
 &= (m \cdot g \cdot \sin \psi_s - \mu' \cdot m \cdot g \cdot \cos \psi_s) \\
 a &= g \cdot \sin \psi_s \left(1 - \frac{\mu'}{\tan \psi_s} \right)
 \end{aligned}$$

Referring to Figure 3.7b), the velocity V , of the block sliding down the sloping plane over a distance S is:

$$V^2 = 2 \cdot a \cdot S = \frac{2 \cdot a \cdot H}{\sin \psi_s}$$

and the rock fall velocity expressed in terms of the vertical fall height H is:

$$V = \left[2 \cdot g \cdot H \left(1 - \frac{\mu'}{\tan \psi_s} \right) \right]^{0.5} \quad (3.13)$$

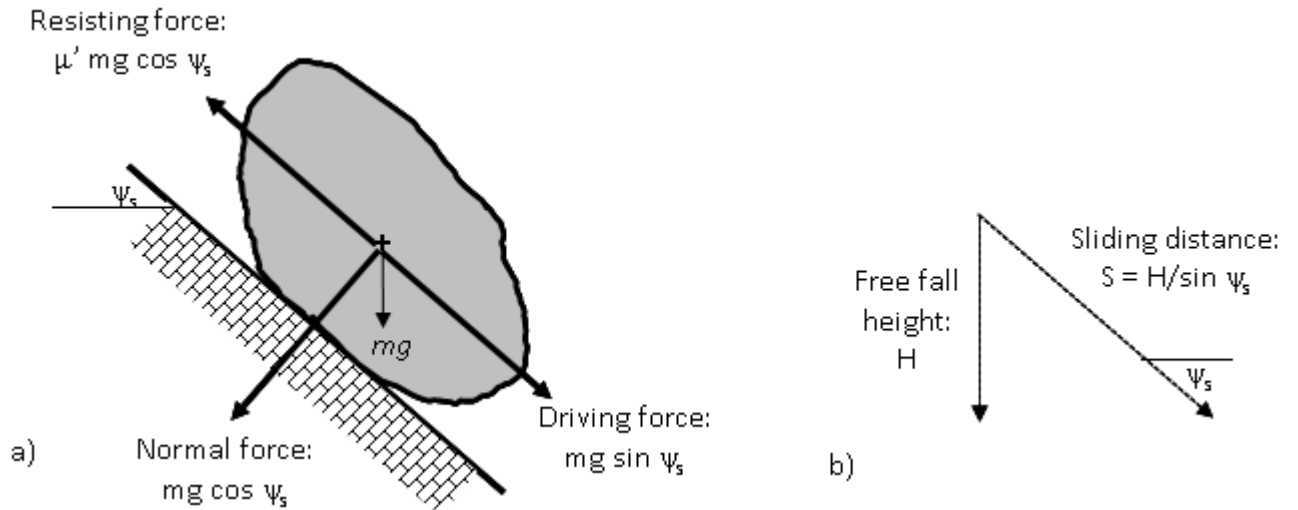


Figure 3.7: Velocity of rock fall on slope dipping at ψ_s : a) limit equilibrium forces acting on sliding block; b) relationship between free fall height, H and sliding distance, S

Equation (3.13) can also be expressed in the following manner:

$$\eta = \frac{V}{(2 \cdot g \cdot H)^{0.5}} \quad (3.14)$$

where η is a parameter representing the slope characteristics:

$$\eta = \left(1 - \frac{\mu'}{\tan \psi_s}\right)^{0.5} \quad (3.15)$$

or

$$\mu' = (\tan \psi_s)(1 - \eta^2) \quad (3.16)$$

The parameter μ' is an effective friction coefficient that incorporates both the material forming the slope surface and the roughness of this surface. As the result of extensive field testing of rock falls in Japan, values for the effective friction coefficient μ' have been determined as shown in Table 3.1 (Japan Road Association, 2000).

Table 3-1: Values of effective friction coefficient μ' for characteristics of slope materials

Slope category	Characteristics of slope surface materials	Design μ' values*	Range of μ' from field tests
A	Smooth, strong rock surfaces and uniform slope profile; no tree cover.	0.05	0.0 to 0.1
B	Smooth to rough, weak rock surfaces with medium to high roughness slope profile; no tree cover.	0.15	0.11 to 0.2
C	Smooth to rough, weak rock, soil, sand or talus with low to medium roughness slope profile; no tree cover.	0.25	0.21 to 0.3
D	Talus with angular boulders exposed at surface, medium to high roughness slope profile; no tree cover or few trees.	0.35	~0.31

* These values for μ' tend to give upper bound velocity values.

Referring to Figure 3.6, the series of dashed curves show the relationship between values of η and the measured rock fall velocities. When $\eta = 1$ and $V = \sqrt{2 \cdot g \cdot H}$, the curve shows the free fall velocity. For values of η less than 1, the velocity decreases as shown by the set of curves for η values of 0.8 to 0.2.

Worked example 3C – fall velocities: the Ehime test site has two slope components: a 26 m high rock slope at an average angle of 44 degrees, and a 16 m high talus slope at an angle of 35 degrees (see Sections 2.1 and 2.2, and Figure 2.6). From Table 3.1, the approximate friction coefficients are 0.15 for the rock and 0.35 for the talus.

Figure 3.6 shows the measured velocities at the site, together with curves representing values for the parameter η . On Figure 3.5, the maximum velocities correspond to values of η of $\eta_{rock} = 0.9$ and $\eta_{talus} = 0.7$, equation (3.16) gives values for the friction coefficients as follows:

$$\mu'_{rock} = \tan 44 (1 - 0.9^2) = 0.18 \text{ and for talus, } \mu'_{talus} = \tan 35 (1 - 0.7^2) = 0.36$$

Comparison of these calculated values for μ' with the values shown on Table 3.1, shows that equation (3.13) gives values for the maximum velocities if the friction angles given in Table 3.1 are applied.

In another example, at Tornado Mountain (see Section 2.2 and Figure 2.8) where the slope has low roughness comprising gravel and soil, the impact velocities are in the range of 10 to 15 m · s⁻¹ on the lower part of the slope where the slope angle is 22 degrees and the fall height H , is about 250 m. The value for η is given by (equation (3.14):

$$\eta = \frac{12.5}{(2 \cdot g \cdot 250)^{0.5}} = 0.39 \quad \text{and} \quad \mu'_{colluvium} = \tan 22 (1 - 0.39^2) = 0.34$$

This value for $\mu'_{colluvium}$ is consistent with values for the friction coefficient given in Table 3.1 for talus.

These back analyses for the relationship between velocity, slope angle and friction show that the friction coefficients given on Table 3.1 can be used to estimate velocity values, although these velocities may be at the high end of the actual velocity values.

The relationships in equations (3.12) to (3.14) and the effective friction coefficients shown in Table 3.1 are used in Japan to estimate fall velocities and impact energies in the design of protection structures. The application of these relationships to the Ehime and Tornado rock fall sites illustrates that this is a useful method to estimate rock fall velocities when no field data are available.

3.3 Variation of trajectories with restitution angle

This section discusses the variation of the angle at the start of the trajectory θ_0 , following an impact, and its influence on the length and height of trajectories. This can be an important factor in the design of protection structures that should be positioned at low trajectory and low velocity locations on the slope.

3.3.1 Calculated trajectories for varying restitution angles (θ_0)

Figure 3.8 shows two possible trajectories between a pair of impact points, (n) and ($n+1$) on the slope dipping at angle $\psi_s = 30$ degrees, together with the initial velocities and angles at point (n). At the start of the trajectory, the body leaves the slope with a restitution velocity V_0 , and at

angle θ_0 relative to the slope surface. The $[x, z]$ co-ordinates of the body at any point during the trajectory can be calculated using equation (3.4). Figure 3.8 shows the successive positions of the body for two possible trajectories defined by the initial angles $\theta_0 = 15$ degrees and $\theta_0 = 45$ degrees. In applying equation (3.4) to calculate the $[x, z]$ co-ordinates of the trajectories, the α_0 angles for the upper and lower trajectories are respectively $\alpha_0 = +15$ degrees and $\alpha_0 = -15$ degrees, where α_0 is defined by equation (3.6) - ($\alpha_0 = \theta_0 - \psi_s$).

Also, equation (3.5) can be used to calculate the velocity required for the body to reach the impact point (point $(n+1)$) with co-ordinates: $[x_i = 14]$ and $[z_i = -8]$. For the low angle trajectory ($\theta_0 = 15$ degrees), the required velocity is $15.5 \text{ m} \cdot \text{s}^{-1}$ ($50.9 \text{ ft} \cdot \text{s}^{-1}$), while for the higher angle trajectory ($\theta_0 = 45$ degrees), the required velocity is only $9.3 \text{ m} \cdot \text{s}^{-1}$ ($30.5 \text{ ft} \cdot \text{s}^{-1}$). That is, as the height of the trajectory increases, the velocity required for the body to reach a defined point decreases.

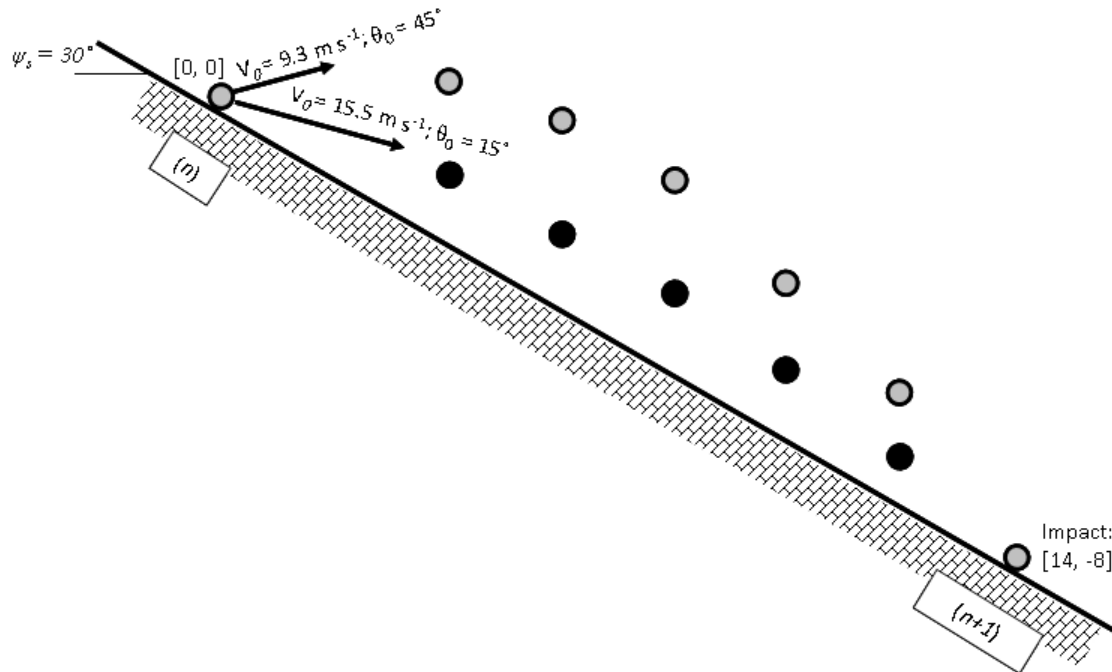


Figure 3.8: Trajectories related to restitution angle, θ_0 : $\theta_0 = 15$ degrees and $\theta_0 = 45$ degrees

3.3.2 Field values of restitution angles (θ_0)

Studies of the rock falls at Tornado Mountain and Ehime in Japan discussed in Chapter 2, have been carried out to investigate the variation in restitution angles θ_0 that occurs in the field (Figure 3.9a) and b)).

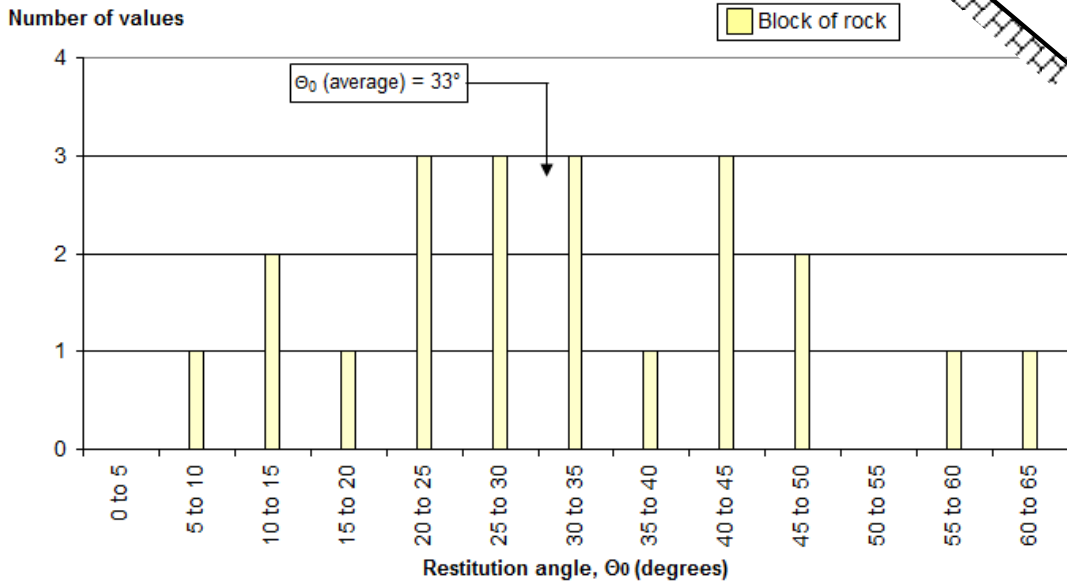
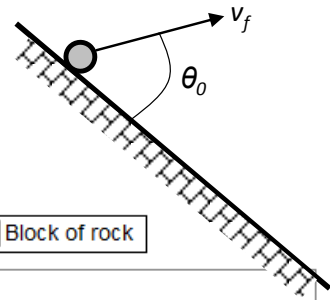
For the two Tornado Mountain rock falls (see Section 2.2.2), the co-ordinates for a total of 114 impact points were measured in the field from which it was possible to determine the slope length and inclination of each trajectory. However, it was only possible to determine the trajectory path from equation (3.4) if information was also available on the magnitude of the angle α_0 defining the inclination of the initial velocity relative to the x-axis (Figure 3.2). This information was provided at 21 locations along the trajectories where rock falls impacted trees and it was possible to measure the height of the impact, and the distance of the tree from the preceding impact point. These measurements provided three points on the parabolic path of the rock fall from which the trajectory parameters, including the value of the angle α_0 , could be precisely calculated.

From the 21 calculated values of α_0 angles and the measured slope angle ψ_s between the two impact points on the slope, values of the initial angle θ_0 were calculated using equation (3.6). It was found that the values of θ_0 ranged from 6 to 63 degrees, a difference of 57 degrees, with an average value of 33 degrees (Figure 3.9a)). That is, the impact process caused the restitution angle to vary from a shallow angle in which the block barely left the slope surface, to larger angles where the block follows a relatively high trajectory. Analysis of trajectories shows that the height of the trajectory does not significantly influence the distance between impact points because the restitution velocity decreases as the trajectory height increases, i.e., high angle trajectories have velocities that are less than shallow angle trajectories.

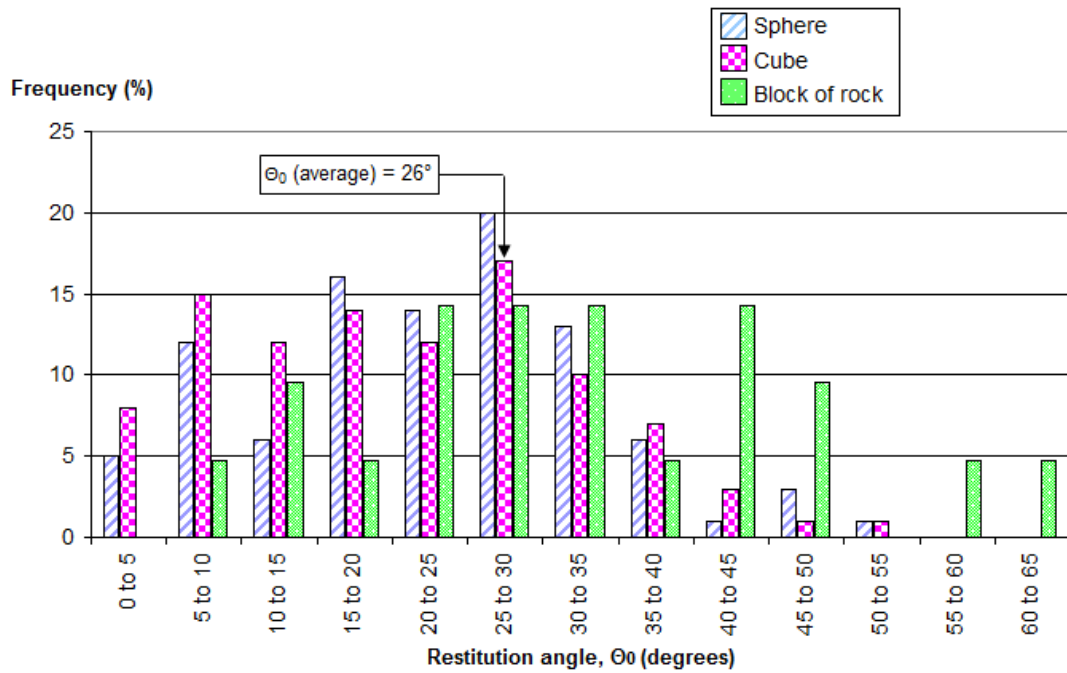
A particular feature of the Tornado Mountain site is the uniform slope, at an angle of between 22 to 30 degrees, composed of gravel and soil with essentially no surface roughness or irregularities. Therefore, variation in the restitution angle would be entirely the result of the attitude of the rotating, irregular block as it impacted the slope.

Values of restitution angles were also measured at the Ehime test site (see Sections 2.1 and 2.2) using data from the embedded accelerometers and high speed cameras (Figure 3.9b). The slope materials comprised weak rock in the upper 25 m (80 ft) and talus in the lower part of the slope. The values of θ_0 ranged from about 5 to 55 degrees, with an average of 26 degrees, discounting two outlying values between 65 and 70 degrees (Figure 3.9b). The histogram also shows the θ_0 values for spherical and cubic concrete blocks, and blocks of rock. It may be expected that the spherical blocks would show less variation than the more irregular cubes and blocks of rock, but Figure 3.9b) shows that the distribution of θ_0 values is similar for all three block shapes.

The two plots in Figure 3.9a) and b) are similar with respect to both range and form of the distributions, despite the significantly different site characteristics. This range of θ_0 values accounts for the variation of trajectories that are usually observed in the field, even where conditions are similar for each impact. An additional factor influencing variations in the values of the angle θ_0 is the angular velocity of the block as discussed in Section 3.4 below.



a)



b)

Figure 3.9: Ranges of values for restitution angle, θ_0 . a) Tornado Mountain tree impacts (21 points); b) Ehime test site trajectory measurements for spherical, cubic concrete blocks and blocks of rock (Ushiro et al., 2006)

3.4 Angular velocity

Measurement of angular velocity of rock falls in the field requires the use of high speed cameras, or embedded accelerometers in concrete blocks as used at the Ehime test site in Japan.

3.4.1 Field measurements of angular velocity

For the rock falls at the 42 m (140 ft) high Ehime test site in Japan, the rotational velocity was accurately measured throughout the fall. The tests were conducted on spherical concrete blocks (diameter 0.54 m (1.8 ft)) and cubic concrete blocks (side length 0.6 m (2 ft)), as well as 20 irregularly shaped blocks of rock with masses ranging from 120 to 2060 kg (260 lb to 4550 lb) (see Section 2.2).

Figure 3.10 is a plot relating the measured angular velocity ω , to the fall height, H for the Ehime test site. The data shows that the range of angular velocities was 6 to 33 $\text{rad} \cdot \text{s}^{-1}$. For the first 10 m (30 ft) approximately of the fall height, ω increases with each impact, and thereafter the blocks rotate at a terminal velocity that ranges between about 12 and 30 $\text{rad} \cdot \text{s}^{-1}$. That is, at each successive impact, the angular velocity may increase or decrease depending on the attitude of the blocks as they impact the slope.

Further analysis of the data on Figure 3.10 shows the relationship between the dimensions and shapes of the blocks and the angular velocity. The range of angular velocities shown in Figure 3.10 is similar for all three block shapes, with the spherical and cubic concrete blocks reaching slightly higher angular velocities of about 32 $\text{rad} \cdot \text{s}^{-1}$ than that for the irregular blocks of rock at 27 $\text{rad} \cdot \text{s}^{-1}$.

The angular velocity measurements have also been analyzed to show the relationships between the translational and angular velocities at the start of the trajectory v_0 and ω_0 , respectively of the blocks and their dimensions r . The theoretical relationship between these three parameters is as follows:

$$\omega_0 = \frac{V_0}{r}$$

or

$$r = \frac{V_0}{\omega_0} \tag{3.17}$$

For the three types of blocks used at the Ehime test site, the following values were obtained for values of the radius r , as defined by equation (3.17).

- Spheres with radius, $r = 0.27$ m,

$$\frac{V_0}{\omega_0} = 0.2 \text{ to } 0.54 \text{ m}$$

- Cubes with side length 0.6 m and semi-diagonal length, $r = 0.42$ m,

$$\frac{V_0}{\omega_0} = 0.25 \text{ to } 0.7 \text{ m}$$

- Blocks of rock with an average radius, $r = 0.65$ m,

$$\frac{V_0}{\omega_0} = 0.3 \text{ to } 1.0 \text{ m}$$

For all three types of block, the theoretical relationship defined by equation (3.17) is reasonably consistent with the field values. That is, the actual radius of the rotating body lies within the range of field values for the ratio (V_0/ω_0) . Also, the tests showed that the range of field values for the ratio (V_0/ω_0) is wider for irregularly shaped blocks of rock than for the more uniform concrete spheres and cubes.

These results indicate that the relationship given by equation (3.17) can be used to estimate values for the angular velocity of blocks with known dimensions and velocities.

3 Rock fall velocities and trajectories

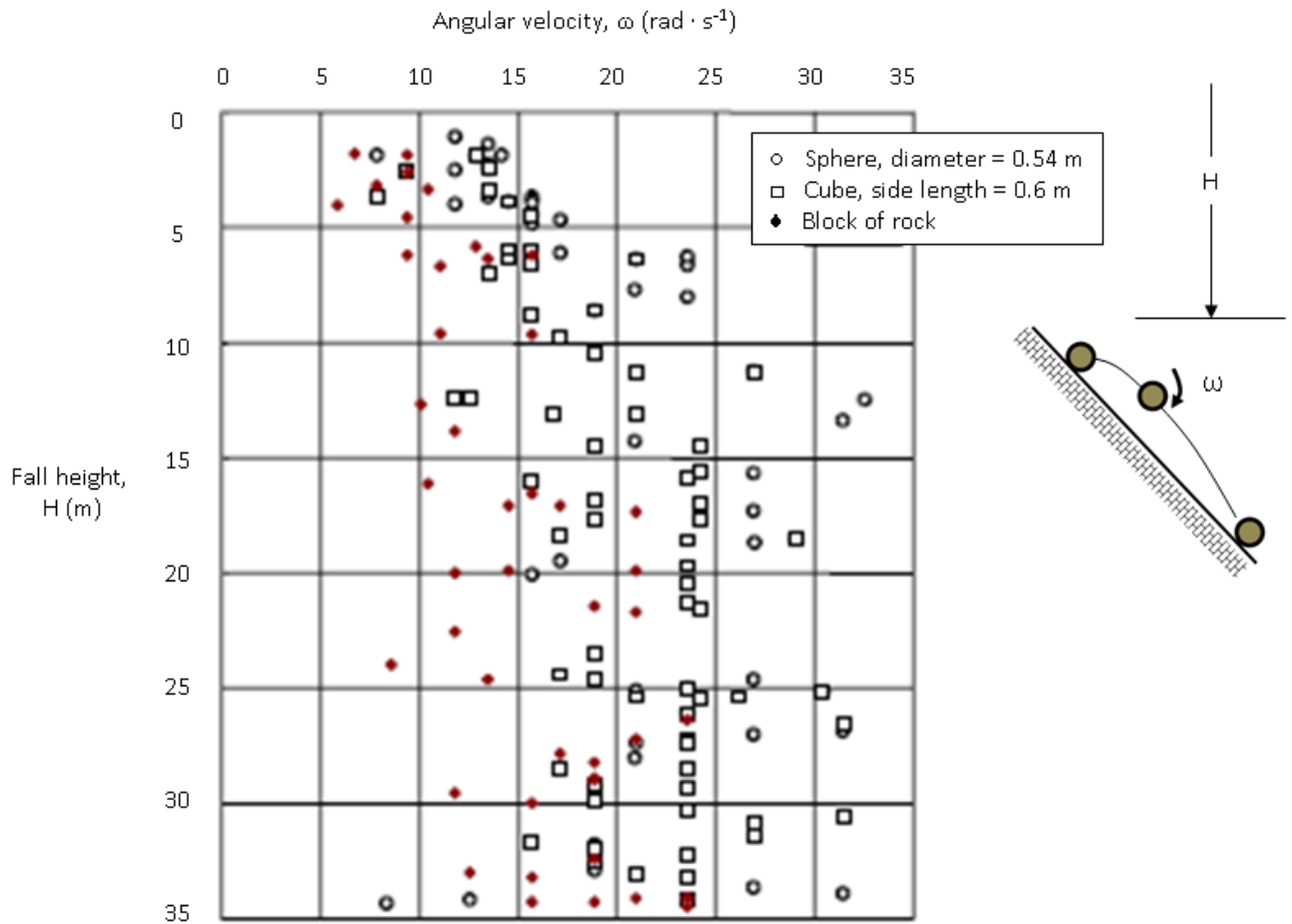


Figure 3.10: Relationship between angular velocity and fall height for rock falls at Ehime test site, Japan for spherical and cubic concrete blocks, and of blocks of rock (Ushiro et al., 2006)

Figure 3.10 shows that for actual rock falls, considerable scatter occurs in the value of ω , and it is likely that ω will sometimes increase and sometimes decrease during impact. This variation in the angular velocity depends on the attitude of the irregular block as it impacts the rough slope surface. Figure 3.11 shows two successive impacts (n , $n+1$) of an irregular block, with frictional resistance R , generated at the impact points. At point n , the normal and tangential velocity components generate moments about the impact points that tend to increase the angular velocity, while at point $(n+1)$, the moments produced by the two velocity components are in opposite directions and tend to decrease ω .

Further discussion on rotational velocity is provided in Section 4.5 related to changes in rotational velocity during impact produced by friction acting at the contact during impact.

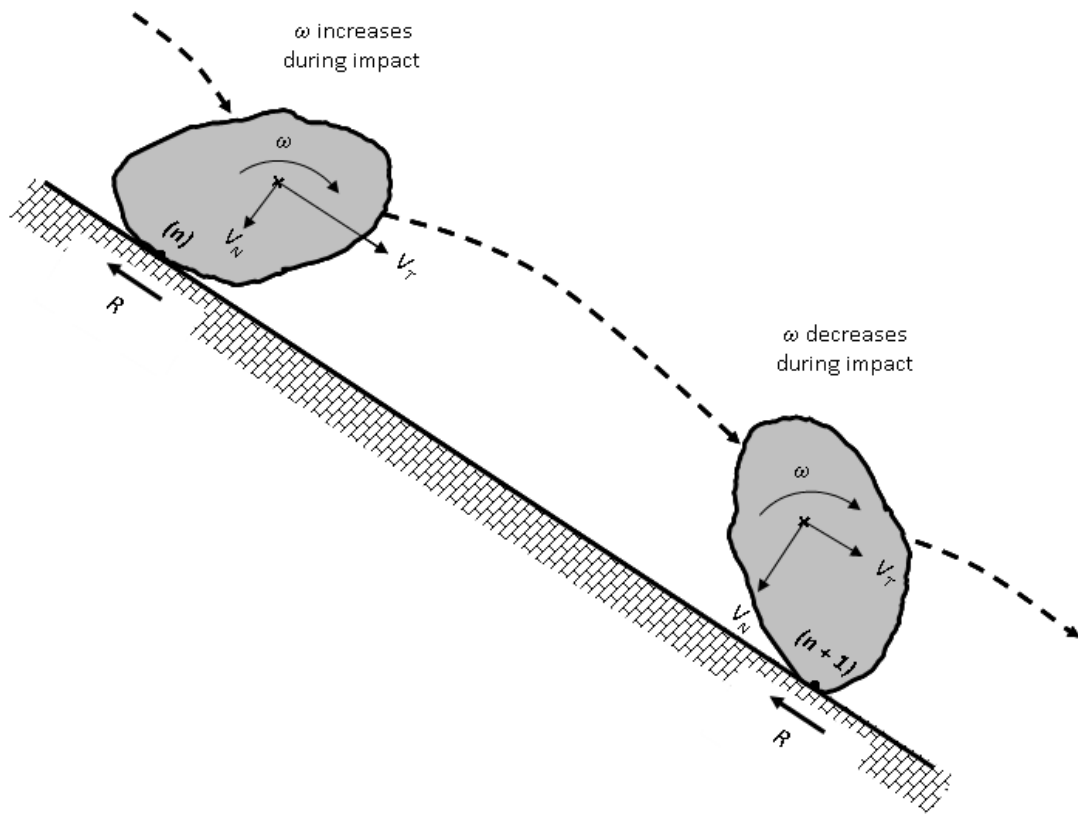


Figure 3.11: Effect of attitude of block during impact on angular velocity

3.4.2 Relationship between trajectories and angular velocity

For a perfectly elastic impact of a smooth, non-rotating block, the impact and restitution velocities and angles will be identical. However, for actual rock falls where the block is rotating with frictional resistance being developed at the impact point and plastic compression of the slope materials occurring, the restitution parameters will change during impact.

Impact mechanics theory discussed in Chapter 4 shows that the effect of clockwise rotation as shown on Figure 3.11, for a frictional impact is to flatten the trajectory, i.e. reduce the value of θ_0 . Also, the higher the clockwise angular velocity, the smaller the value of θ_0 with a flatter trajectory. Furthermore, as the trajectory becomes flatter (closer to the slope surface), the velocity increases as shown in Figure 3.8 where two trajectory paths are compared.

Impact mechanics also shows that the effect of counter clockwise rotation is to produce higher, slower trajectories.

3.5 Field observations of rock fall trajectories

This section briefly describes some of the characteristics of rock fall trajectories in the field.

3.5.1 Rock falls down gullies

Rock falls on steep slopes are similar to water flow in that falls will tend to concentrate in gullies. That is, minor gullies in the upper part of the slope act as a “water shed” in which falls over a wide area on the upper slope combine into a single gully at the base of the slope. For example, at one active rock fall site, falls were originating from a maximum height of about 250 m (820 ft) over a slope length of about 120 m (400 ft), but they were almost all contained by a 12 m (40 ft) long fence in a gully at the base of the slope. This shows that careful examination of the rock fall geometry can result in substantial savings in construction of protection measures.

Another effect of rock falls concentrating in gullies, is that the fall path is not a straight line down the maximum gradient line. Figure 3.12 shows a slope about 500 m (1,640 ft) high on which rock falls are entirely concentrated into three, sinuously-shaped gullies in which the rock fall paths are significantly longer and flatter than the slope cross-section. This shows that rock falls can be much more accurately modeled in three dimensions than in two dimensions. That is, cross sections of the slope shown in Figure 3.12 would be irregular where the section crossed the gullies, and modeling of this slope would probably show significant trajectory heights where falls impacted the sides of the gullies. In contrast, a section down a gully would be an essentially uniform slope in which trajectory heights would probably not exceed 2 m (6.6 ft).

Figure 3.12 also shows how all rock falls over a length of several hundred meters along crest can be contained by just three fences located in the base of the gullies, each about 20 m (65 ft) long.



Figure 3.12: Mountain slope with three sinuous gullies in which all rock falls are concentrated

3.5.2 Run-out distance

The maximum distance that a rock fall will travel from the source zone can be an important parameter in the location and/or protection of facilities in the run-out area. Figure 1.1 shows a typical rock fall site made up of four areas – the rock face where the fall originates, a colluvium slope, a talus slope where most of the rock falls accumulate, and a run-out zone, or rock fall “shadow area”, between the base of the talus cone and the maximum travel distance. The maximum travel distance is defined by a line drawn at a dip angle of 27.5 degrees from the base of the rock face to the intersection with the ground surface (Hungr and Evans, 1988).

Depending on the level of risk acceptance for the facilities, the run-out area could be designated an exclusion zone in which no continuously occupied structure such as a house, could be located. Alternatively, it may be acceptable to locate such facilities as a lightly used

road or a golf course within the run-out zone, perhaps with some protection such as a ditch along the up-slope edge.

Section 8.5.5 discusses the application of decision analysis to rationally evaluate the cost benefit of alternate rock fall protection measures based on the probability of rock falls occurring, the consequence of such falls, and the cost of constructing protection measures.

3.5.3 Dispersion in run-out area

Where a talus cone has developed at the base of a rock fall area, over time falls will disperse uniformly over the talus to build up the cone equally over its full area. This is a progressive process whereby the accumulation of rock falls on one area of the cone will then divert subsequent rock falls to a lower area that is built up in turn.

At the Ehime test site discussed in Chapter 2, it was found that the falls dispersed over an area subtended by an angle of 60 degrees, with about 93 per cent of the falls within a 30 degree angle. At other test sites in Japan, the angle defining the width of the dispersal area varied from 45 to 70 degrees (Ushiro and Hideki, 2001). At Tornado Mountain, the horizontal distance between the two rock falls was 87m (285 ft) after falling 740 m (2450 ft), or a dispersion angle of 7 degrees.

This information can be used to determine the length of rock fall fence that may be required to contain falls.

4 Impact mechanics

The theory of impact mechanics is used in a wide variety of fields (Goldsmith, 1960; Stronge, 2000) and builds on earlier work carried out by Sir Isaac Newton (Newton, 1687) and others such as Poisson and Hertz in the 19th century. The theories generally apply to the impact between two bodies, made of different materials, that are both translating and rotating, have unequal masses and are moving in three dimensional space. For rock falls, the impact conditions are somewhat simplified because one of the bodies (the slope) is stationary and has infinite mass. However, the roughness of the slope and irregularity of the rock falls introduces complexities in the modeling that can be accounted for by probabilistic analyses. Furthermore, the theory needs to account for the condition that the two bodies are not be of the same material.

This chapter summarizes the application of impact mechanics theory to rock falls, and how the theory can be applied to the actual rock fall events documented in Chapter 2. Chapters 5 and 6 cover respectively coefficients of restitution and energy losses, and show how the field results can be used to calibrate impact mechanics theory and modeling programs.

The theory for impact mechanics described in this thesis is based primarily on the work of W. J. Stronge (2000).

4.1 Principles of rigid body impact

The theory of impact mechanics can be applied to rock falls in order to understand the impact process, and to develop algorithms for modeling rock falls. This work involves the application of rigid body impact and kinetics to rock fall behavior as described below.

4.1.1 Rigid body impact

The particular physical conditions that are applicable to rock falls are low velocity (i.e., less than about $40 \text{ m} \cdot \text{s}^{-1}$ ($130 \text{ ft} \cdot \text{s}^{-1}$)), and impact of initially nonconforming hard, rigid bodies that result in minor deformations but high stresses generated over the small area of the impact, and to a very shallow depth. During impact, the shapes of the two surfaces are briefly conformable. These contact conditions, in which no inter-penetration or adhesion of the two bodies occurs, are referred to as *low compliance* impacts.

The highly stressed contact area of the rock fall and the slope can be considered as a short, stiff spring, or an infinitesimally small, deformable particle (Figure 4.1). The spring or particle is compressed during the compression phase of impact, and then releases energy to force the rock fall away from the slope after the time of maximum compression and during the restitution phase of impact.

The duration of the impact is very short, possibly a few tenths of a second, which has a number of implications for modeling rock falls. First, changes to the position of the rock fall are negligible during impact, and second, gravitational forces can be ignored because they are very low compared to the high induced forces at the impact point.

Based on these assumed conditions of impact, the change in velocity of the rock fall during impact can be resolved as a function of the normal component of impulse, where the normal impulse is equal to the integral of the normal contact force over the time of the impact. Since the impact involves only compression, and not extension of the spring or particle, the normal component of impulse is a monotonously increasing function of time after impact. Thus, variations in velocity during impact are resolved by choosing as an independent variable the normal component of impulse, p_N , rather than time. This principle gives velocity changes during impact that are a continuous, smooth function of impulse (Stronge, 2000).

Throughout this thesis, impacts are modeled in terms of the relationship between changes in normal and tangential relative (between the periphery of the body and the slope) velocity components, v_N and v_T , and the normal component of impulse, p_N .

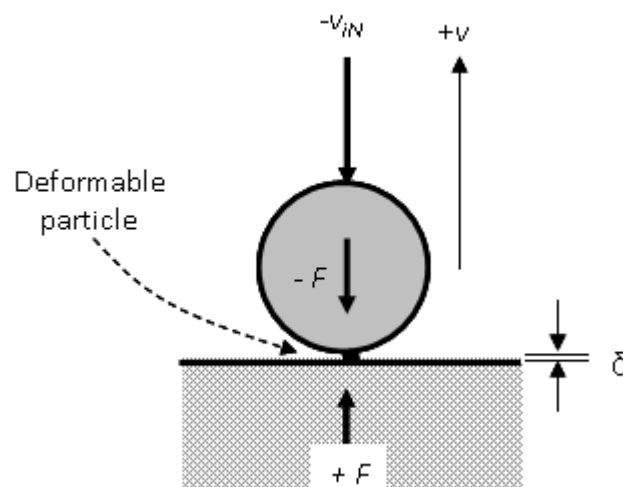


Figure 4.1: Forces generated at contact point during normal impact

4.1.2 Kinetics of rigid bodies

Kinetics is a means of examining the change in velocity of the body when forces act on the body during impact.

A rock fall is a rigid body as defined in Section 4.1.1 above, and can be considered as a point mass, of infinitesimal size. If the body has mass m and is moving with velocity V (at the center of gravity), then the momentum of the body is $(m \cdot V)$. If a resultant force F acts on the body, this causes a change in momentum according to Newton's second law of motion.

Second Law: the momentum $(m \cdot v)$, of a body has a rate of change with respect to time that is proportional to, and in the direction of, any resultant force $F(t)$ acting on the body.

Assuming that the mass of the body is constant during impact, then the change in velocity is a continuous function of the impulse, p . The forces F , $-F$ acting on the rock fall and the slope that prevent interpenetration of the two bodies are related by Newton's third law of motion:

Third law: two interacting bodies have forces of action and reaction that are equal in magnitude, opposite in direction and collinear, i.e., $F = -F$.

The application of the second and third laws to rock falls is shown in the following sections.

4.2 Forces and impulses generated during collinear impact

Calculation of the forces and impacts during rock fall impacts applies Newton's second and third laws discussed in Section 4.1.2 above.

The impact process for a non-rotating, rigid body moving with relative velocity v_N and impacting a stationary surface at right angles can be simulated with an infinitesimal, deformable particle at the contact point between the two bodies (Figure 4.1). The particle acts as a short, stiff spring that, during impact, generates equal and opposite reaction forces F , $-F$ at the point of impact that are parallel to the velocity direction.

The reaction forces change the momentum of the body, and for a constant mass during impact, the velocity is changed. The change in momentum generated by the impact produces a finite impulse p that continuously changes the velocity during the impact time. During impact of a body with mass m , a change in normal velocity occurs from v_{iN} at impact (time $t = i$) to v_N at time

t . The normal component of impulse p_N , generated by the normal component of the contact force $F(t)$ is given by the relationship:

$$dp_N = m(v_N - v_{iN}) = F dt \quad (4.1a)$$

$$\text{where } F = m \frac{dv}{dt}$$

$$\therefore dp_N = m \frac{dv}{dt} dt$$

$$\therefore dv_N = \frac{dp_N}{m} \quad (4.1b)$$

$$\text{and } m(v_N - v_{iN}) = \int_i^t F dt = p_N \quad (4.1c)$$

The relative normal velocity v_N at any time t during the impact can be obtained by integration, for the limit that at the moment of impact $t(i)$, the normal velocity is given by:

$$v_N = \int_{t(i)}^t \frac{1}{m} dp_N \quad (4.2)$$

$$v_N = v_{iN} + \frac{p_N}{m} \quad \text{where } v_{iN} < 0 \quad (4.3)$$

The impacting normal velocity is negative because, as shown in Figure 4.1, the positive normal axis is in the direction away from the point of impact.

Equation (4.3) shows that the normal component of the relative velocity is a linear function of the normal impulse. This relationship between v and p is the basis for determining changes in impulse during impact, and finding the terminal impulse p_f , at the termination of impact ($t = f$) when the body separates from the slope.

Equation (4.3) can also be used to find the impulse values at maximum compression (p_{cN}). At the point of maximum compression, the normal velocity is momentarily equal to zero and the corresponding normal impulse has a value p_{cN} given by equation (4.3)

$$0 = v_{iN} + \frac{p_{cN}}{m}$$

and

$$p_{cN} = -m \cdot v_{iN} \quad (4.4)$$

At the end of the impact ($t = f$), the final normal velocity is v_{fN} and the final normal impulse (p_{fN}) can also be found from equation (4.3),

$$p_{fN} = (m \cdot v_f - m \cdot v_i) \quad (4.5)$$

4.3 Energy changes during impact

The impact process results in compression δ of the deformable particle during the compression phase (Figure 4.1), followed by expansion during the restitution phase. The changes in the normal contact force F during impact are illustrated in Figure 4.2a) where the force (F_c) and deformation (δ_c) are at a maximum at the end of the compression phase, followed by partial recovery (δ_f), for inelastic impact, at the completion of the recovery phase. The recovery of kinetic energy is the process that drives the bodies apart in the final phase of the impact after maximum compression.

Figure 4.2b) shows the changes in the normal contact force as a function of time. The area under the $[t - F]$ curve up to time t_c is the impulse p_c generated during the compression phase and represents the kinetic energy of relative motion converted into internal energy of deformation. The area between times t_c and t_f is the change in impulse ($p_f - p_c$) and represents the energy recovered during the restitution phase. The changes in velocity during impact can be quantified in terms of the normal coefficient of restitution, e_N that is the ratio of the final normal velocity v_{fN} to the impact normal velocity, v_{iN} .

On Figure 4.2b), for an elastic impact the two areas are identical - $e_N = 1$, while for a perfectly plastic impact no energy is recovered - $e_N = 0$.

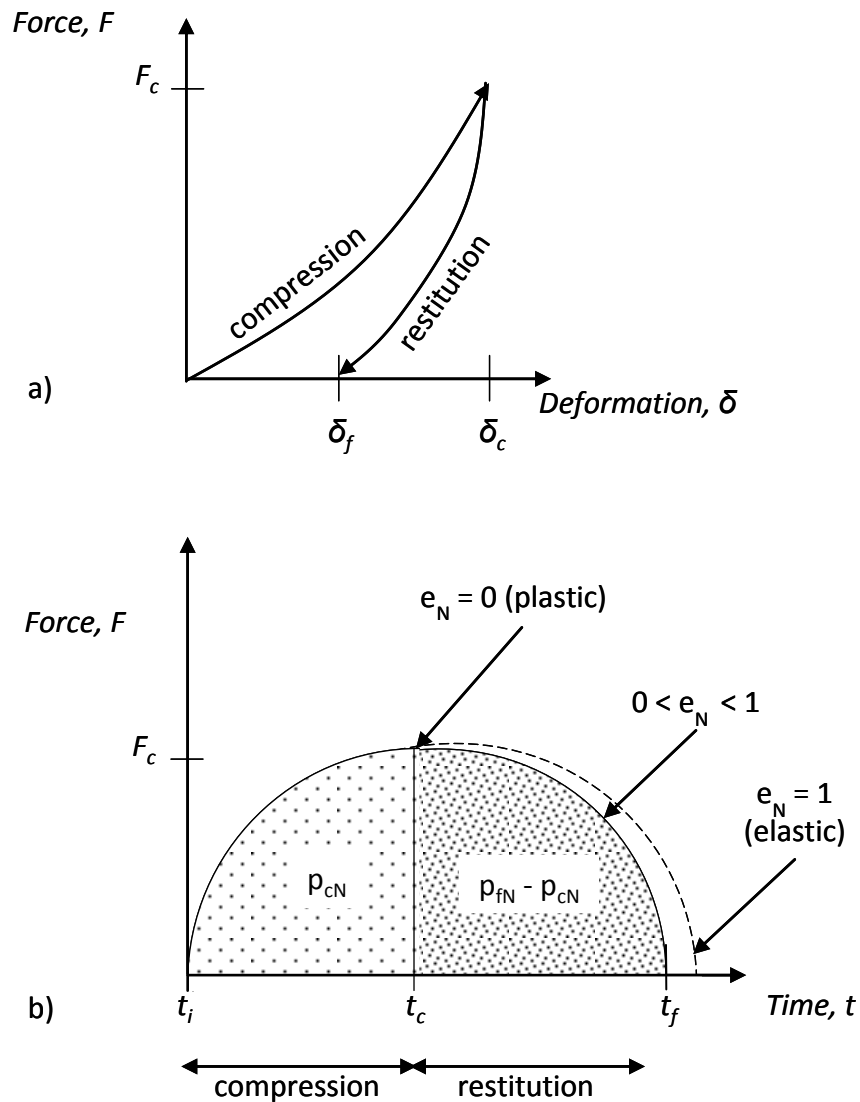


Figure 4.2: Variation in force F during impact. a) Relationship between force and deformation at the impact point; b) change in force and impulse with time during impact; p_c is impulse generated up to time of maximum compression ($t = i$ to $t = c$); ($p_f - p_c$) is impulse generated during restitution phase of impact ($t = c$ to $t = f$)

A fully plastic impact in which no recovery of energy occurs is shown in Figure 4.3 where a rock fall is embedded in a wall constructed with gabions ($e_N = 0$). In this case, almost all the impact energy has been absorbed by the plastic deformation of the gabions, with only a little energy being absorbed by the elastic deformation of the rock fall. The design of MSE (mechanically stabilized earth) rock fall barriers is discussed in Section 10.2.



Figure 4.3: Example of plastic impact where a rock fall is embedded in a gabion wall

4.4 Coefficient of restitution

The principle of separating the compression and restitution phases of impact can be demonstrated on a normal impulse $[(p_N) - \text{relative velocity } (v)]$ plot as shown in Figure 4.4. On this plot, the normal velocity changes during impact, starting with a negative value $(-v_{iN})$ at the point of impact, increasing to zero at the point of maximum compression p_c , and finally reaching a positive value (v_{fN}) at the point of separation. Also, the tangential velocity v_T decreases continuously during impact from v_{iT} at the point of impact, to v_{fT} at the point of separation, as the result of frictional resistance on the contact surface. The role of friction on impact behavior is discussed in Section 4.5.

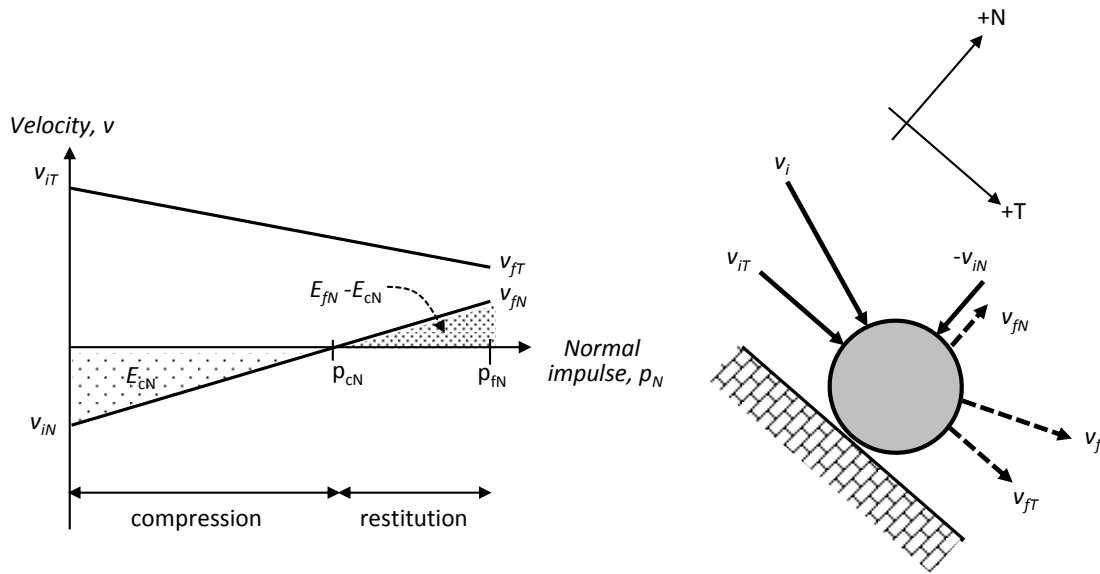


Figure 4.4: Relationship between normal impulse p_N and changes in tangential and normal velocities v_T , v_N , and energy during impact; E_{cN} is the kinetic energy absorbed during the compression phase of impact ($t = c$); ($E_{fN} - E_{cN}$) is the strain energy recovered during the restitution phase ($t = c$ to $t = f$)

The $[p_N - v]$ plot on Figure 4.4 shows the changes in both the normal (v_N) and tangential (v_T) velocities, and the magnitude of the internal energy of deformation generated during impact. These changes in velocity and energy can be quantified in terms of the coefficient of restitution², e that has normal and tangential components as follows:

$$e_N = -\frac{v_{fN}}{v_{iN}} \quad (4.6)$$

and

$$e_T = \frac{v_{fT}}{v_{iT}} \quad (4.7)$$

The parameter e_N , which is related to compression/hysteresis at the contact point, is used to determine the normal velocity and energy changes that occur during impact as discussed in this chapter. The parameter e_T , which quantifies the changes in tangential velocity during impact, is

² In this treatment of impact mechanics as it applies specifically to rock falls, the term coefficient of restitution is used to quantify the changes in both velocity and energy, and it encompasses the terms kinetic, kinematic and energetic coefficients of restitution that apply in certain impact conditions (Stronge, 2000).

a function of the friction acting on the contact surface and the effect of friction on the angular velocity of the body.

Examples of actual changes in normal and tangential velocities during impact and the corresponding values of e_N and e_T are discussed in the documentation of rock fall events discussed in Chapter 2, and are listed in Table 2.1.

With respect to the energy of deformation, the triangular area E_{cN} in Figure 4.4 represents the kinetic energy of normal motion that is absorbed in compressing the deformable region, while triangular area $(E_{fN} - E_{cN})$ represents the elastic strain energy recovered during restitution. The expression for the energy change during compression is:

$$E_{cN} = \int_0^{p_{cN}} v_N dp = \int_0^{p_{cN}} \left(v_{iN} + \frac{p_N}{m} \right) dp$$

$$= \left(v_{iN} \cdot p_{cN} + \frac{p_{cN}^2}{2m} \right)$$

since $p_{cN} = -m \cdot v_{iN}$ (equation (4.4))

$$E_{cN} = -\frac{1}{2} m \cdot v_{iN}^2 \quad (4.8)$$

and the energy change during restitution is:

$$(E_{fN} - E_{cN}) = \int_{p_{cN}}^{p_{fN}} \left(v_{iN} + \frac{p_N}{m} \right) dp = \left[v_{iN} \cdot p_N + \frac{p_N^2}{2 \cdot m} \right]_{p_{cN}}^{p_{fN}}$$

$$= \frac{1}{2} m \cdot v_{iN}^2 \left(\frac{p_{fN}}{p_{cN}} - 1 \right)^2 \quad (4.9)$$

where $v_{iN} < 0$.

Derivation of equations (4.8) and (4.9) is shown in Appendix B. Equations (4.8) and (4.9) are also derived in Chapter 6 that discusses energy losses during impact.

The expressions in equations (4.8) and (4.9) for the partially irreversible changes in kinetic energy of normal motion that occur during impact can be used to define the normal coefficient of restitution, e_N as follows:

$$e_N^2 = -\frac{E_N(p_{fN}) - E_N(p_{cN})}{E_N(p_{cN})} \quad (4.10)$$

This definition of the coefficient of restitution where the impulse is an independent variable, separates the energy loss due to compression and hysteresis of the contact forces from that due to friction and slip between the colliding bodies. As shown in Figure 4.2, the value for e_N can range from $e_N = 1$ for a perfectly elastic material where no loss of energy occurs during impact, to $e_N = 0$ for a perfectly plastic material where no separation occurs during impact and no recovery of the initial kinetic energy occurs.

Also, the relationships shown in equations (4.8), (4.9) and (4.10) can be combined, for normal impact, to find the following expression for the normal coefficient of restitution in terms of the normal impulses at maximum compression (p_{cN}) and at the completion of the impact (p_{fN}):

$$e_N^2 = \left(\frac{p_{fN}}{p_{cN}} - 1 \right)^2 \quad (4.11)$$

Substitution of the expressions for p_{cN} and p_{fN} in equations (4.4) and (4.5) into equation (4.11), yields the following expression relating impulse to the coefficient of restitution:

$$p_{fN} = -m \cdot v_{iN} (1 + e_N) = p_{cN} (1 + e_N) \quad (4.12)$$

and for the normal coefficient of restitution,

$$e_N = -\frac{v_{fN}}{v_{iN}} \quad (4.6)$$

$$e_N = \frac{(p_{fN} - p_{cN})}{p_{cN}} \quad (4.13)$$

As shown in Figure 4.4 and expressed in equations (4.6) and (4.13), the normal coefficient of restitution is the ratio of final normal velocity to the impact normal velocity, and is also the square root of the negative ratio of the energy recovered during the restitution phase of the impact to the energy lost during the compression phase (equation (4.10)).

For rough bodies where slip occurs at the contact point, but the direction of slip is constant, the two expressions for the coefficient of restitution in equations (4.6) and (4.13) are equivalent.

4.5 For frictional angular velocity changes during impact, for rough surface

For oblique impact of a rock fall with a slope, the impulse acting at the contact point gives an impulsive moment about the centre of mass of the rock fall (Figure 4.5). This impulsive moment changes the angular and translational velocities during the period of contact.

Changes in the rotational and translational velocities during impact can be attributed to friction at the rock-slope contact. According to Coulomb's definition of friction, the coefficient of friction μ , is the ratio of the tangential to normal forces acting at the contact point. Furthermore, the ratio of the tangential to normal forces is a constant such that the friction coefficient is also a constant that is independent of the slip velocity and the normal force.

It is noted that in rock mechanics, it is usually assumed that the coefficient of friction decreases with increasing normal stress due to breakdown of the asperities on the rough rock surfaces during shear movement. However, for rock fall impacts that are of short duration and have limited shearing distance, the friction coefficient is considered to be independent of the normal force.

When a translating and rotating body impacts a stationary slope, slip will initially occur between the two bodies and frictional forces will be generated at the contact point. In accordance with the usual concept of friction relating normal and tangential impulses, slip of the body on the slope is assumed to occur at the value of limiting friction, requiring that

$$p_T = |\mu \cdot p_N| \quad (4.14a)$$

while slip stops and the body rolls during impact when

$$(p_T \leq \mu \cdot p_N) \quad (4.14b)$$

This transition from slip to rolling is illustrated on Figure 4.5. The behavior of a rotating body during impact can be demonstrated on the [normal impulse (p_N) – relative velocity (v)] plot on Figure 4.5. For a spherical body with radius r and rotating at angular velocity $-\omega$, the velocity at the periphery of the body ($-r \cdot \omega$) is parallel, but opposite in direction, to the translational tangential velocity v_T . If the magnitudes of $|r \cdot \omega|$ and v_T are unequal, then slip will occur between the moving body and the stationary ground, with the slip velocity v_s , being given by:

$$v_s = v_T + r \cdot \omega \quad (4.15)$$

The direction of rotation is negative if the peripheral velocity ($r \cdot \omega$) is in the opposite direction to the positive tangential axis. For rock falls, the angular velocity is usually negative because the tangential translational velocity acting down slope and the friction force ($\mu \cdot p_N$) acting upslope interact to spin the rock clockwise as shown in Figure 4.5.

The slip velocity depends on the both the magnitude and direction of the angular velocity relative to the tangential velocity as defined by equation (4.15) and shown on Figure 4.5. If the angular velocity is negative, then the slip velocity is less than the initial tangential velocity (Figure 4.5a)), while if the angular velocity is positive, the slip velocity is greater than the initial tangential velocity (Figure 4.5b)).

Depending on the details of the impact process, the values of ($r \cdot \omega$) and v_T may equalize during impact, in which case slip will cease at impulse p_{sN} and from this point the body will roll with no change in angular velocity. In other conditions related to the attitude of the irregular body impacting the slope, slip may continue throughout the impact.

The [$p_N - v$] plot in Figure 4.5 also shows that the tangential velocity decreases during the slip phase of the impact from v_{iT} to v_{fT} . This reduction in tangential velocity can be attributed to the friction force acting at the contact between the impacting body and the slope, and to the irregularities of the slope at the impact point. Equations developed in Section 4.6 show the slope of the tangential velocity line.

The [$p_N - v$] plots in Figure 4.5 show the angular velocity increasing during the slip phase ($\omega_s > \omega_i$). However, for irregularly shaped, rotating blocks impacting the slope at a variety of attitudes, the velocity components may combine under some conditions to reduce the velocity during impact, rather than increasing with each impact (see also Figure 3.11). At the Ehime test site described in Sections 2.1.3 and 2.2.1, the rotational velocities of about 100 test blocks on the 42 m (140 ft) high slope varied between 6 and 33 $\text{rad} \cdot \text{s}^{-1}$. The measured values of ω at Ehime are plotted against the fall height on Figure 3.10 and show that while ω does generally increase during the fall, low values for ω occur in the lower part of the fall showing that some impact conditions can result in the rotational velocity decreasing during impact.

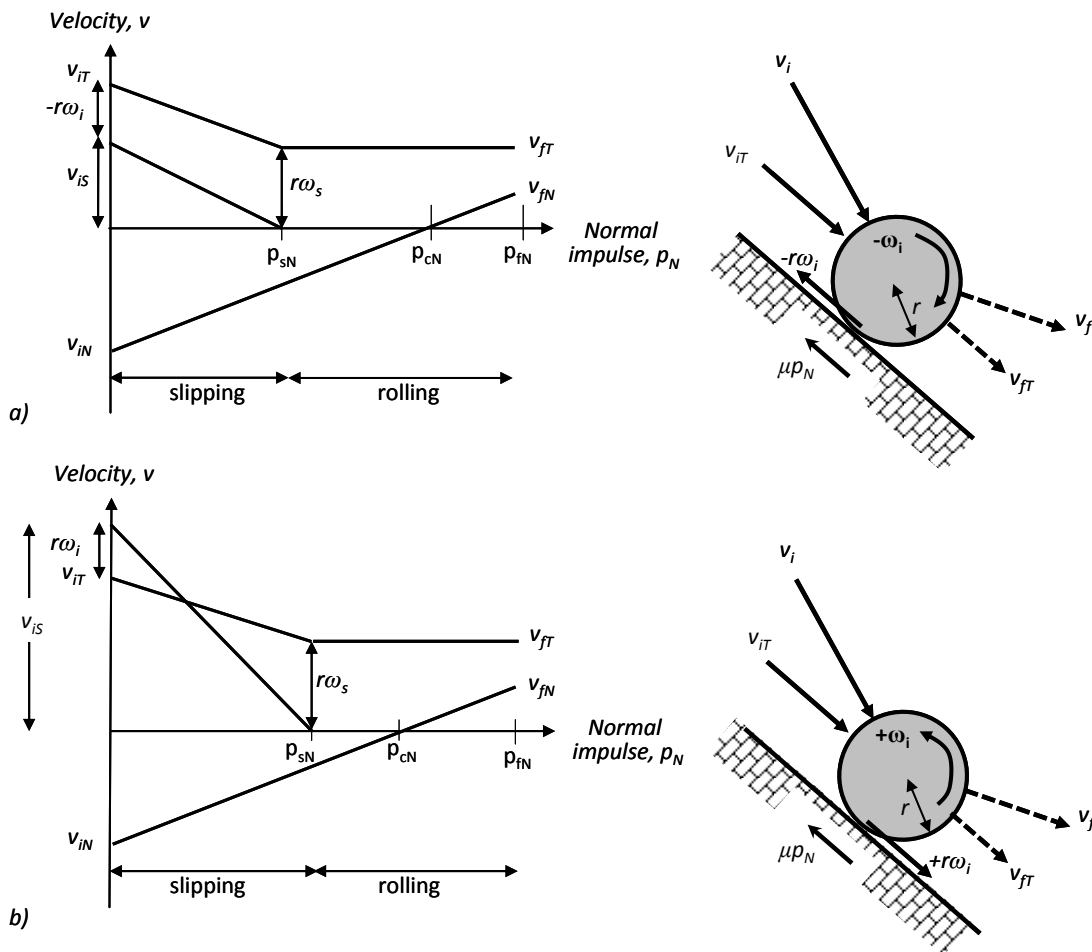


Figure 4.5: Changes in rotational (ω) and slip (v_s) velocities during impact, and transition from slip to rolling mode when $v_s = 0$. a) Negative angular velocity: $v_s = (v_T - r \cdot \omega)$; b) positive angular velocity: $v_s = (v_T + r \cdot \omega)$

Another characteristic of a rotating body is that the angular velocity changes only during impact as the result of the frictional force that acts during contact between the body and the slope. However, during the trajectory phase of the fall when contact between the body and the slope ceases, no forces act to change the angular velocity that remains constant during the trajectory. This also means that the rotational energy remains constant during the trajectory.

The effect of friction during contact can be understood by considering that for a completely frictionless, smooth contact, no change in tangential or angular velocity occurs during impact because no shear resistance is generated at the contact surface. That is, the v_T and v_s lines are horizontal on the $[p_N - v]$ plot for frictionless contact. However, v_N will still change during impact because of energy losses produced by compression of the body and slope at the contact point.

4.6 Impact behaviour for rough, rotating body

When a rock fall impacts a slope, the parameters defining the impact conditions are the translational and rotational velocities at the moment of impact ($t = i$), and the impact angle relative to the slope (θ_i). In addition, the characteristics of the slope are defined by the normal coefficient of restitution, and the friction coefficient. In order to model rock fall behavior, it is necessary to calculate the final translational and rotational velocities ($t = f$), and the angle at which the body leaves the slope. These three final parameters can then be used to calculate the subsequent trajectory of the body. This section describes how impact mechanics can be used to derive the equations defining changes in velocity components and angles during impact. The impact mechanics model discussed in this section is based on the work of Stronge (2000) and Goldsmith (1960) on collision between solid bodies, with modifications to suit the particular conditions of rock falls.

The theory of impact mechanics can be used to model impact between two irregularly shaped, rough, rotating bodies moving in three dimensional space; for rock falls, the model can be simplified by making one of the bodies (the slope) stationary and of infinite mass. For the purpose of developing equations to model impact in this thesis, further simplifications will be made that friction is developed at the impact point, and the body is moving in two-dimensional space (plane motion) (Figure 4.6). The size and shape of the body are defined by the radius (r) and the radius of gyration (k).

The equations of motion are referenced to coordinate axes set up at the impact point in directions normal N and tangential T to the slope surface. The positive normal axis is away from the slope and the positive tangential axis is down-slope such that the impact normal velocity is negative and the tangential velocity is positive. In addition, the angular velocity is negative when it is in the $-T$ direction at the contact point. Subscript “ i ” refers to conditions at impact (time, $t = i$), and subscript “ f ” refers to restitution conditions at the end of impact (time, $t = f$). The radius of the spherical body is r .

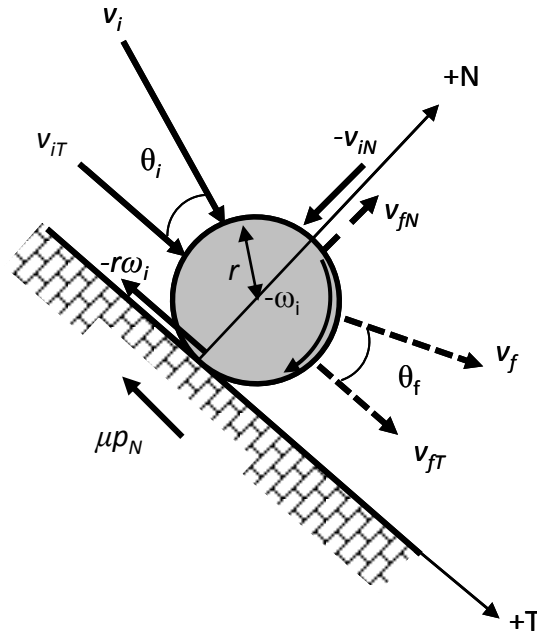


Figure 4.6: Impact of rough, rotating sphere on a slope in plane motion

4.6.1 Impulse calculations

The impact of the rock fall with the slope in plane motion produces normal and tangential impulses p_N and p_T respectively at the contact point that alter the normal and tangential velocity components of the rock during impact. The velocity changes are governed by the magnitude of the normal coefficient of restitution e_N and the limiting value of the coefficient of friction μ . Values of the coefficient of restitution have been determined by documenting actual rock fall events as described in Chapter 2, and for the coefficient of friction from both laboratory tests and rock fall events.

Figure 4.6 shows a body with mass m , radius r and radius of gyration k impacting the slope at a shallow angle. Following the nomenclature defining impact velocities shown in previous sections of this chapter, at any time during the impact, the linear impulse-momentum equation (4.1c) provides the following relationship for the normal impulse p_N related to the change in the normal component of the velocity:

$$m(v_N - v_{iN}) = p_N \tag{4.1c}$$

And the equivalent tangential impulse equation p_T :

$$m(v_T - v_{iT}) = -p_T \tag{4.16}$$

where v_{iT} and v_{iN} are respectively the initial tangential and normal translational velocity components at impact (time, $t = i$).

With respect to the rotation of the block with angular velocity ω at time t , initial angular velocity ω_i and moment of inertia I , the angular impulse-momentum equation is:

$$I(d\omega) = I(\omega - \omega_i) = \int_0^t F \cdot r \, dt \quad (4.17)$$

and

$$m \cdot k^2 (\omega - \omega_i) = p_T \cdot r \quad (4.18)$$

where $I = m \cdot k^2$, and k is the radius of gyration of the body.

The volumes and radii of gyration of bodies that may simulate rock falls are listed in Table 4-1.

Table 4-1: Volume and radius of gyration of common rock fall body shapes

Body shape	Volume, Ω	Axial radius of gyration, k
Cube: side length L	L^3	$\frac{L}{\sqrt{6}}$ – axis normal to face, or along diagonal
Sphere: radius r	$\frac{4}{3}\pi \cdot r^3$	$\left(\frac{2}{5}\right)^{0.5} r$
Cylinder: length L , radius r	$\pi \cdot r^2 \cdot L$	$\left(\frac{3r^2 + L^2}{12}\right)^{0.5}$ – axis through mid-height ("tumbling" motion)
Ellipsoid: axes $2a, 2b, 2c$	$\frac{4}{3}\pi \cdot a \cdot b \cdot c$	$\left[\frac{(a^2 + b^2)}{5}\right]^{0.5}$ – rotation about axis c

4.6.2 Final velocities for rock fall impacts

For a rotating rock fall impacting a slope at an oblique angle, the rock will have both translational v , and angular ω , velocities, with the translational velocity expressed as normal and tangential components relative to the slope surface (Figure 4.6). At the contact point, equal and opposite forces, F , $-F$ are developed that oppose interpenetration of the rock into the slope and give differentials of impulse dp in the normal and tangential directions that are related by:

$$dp_N = F dt \quad (4.1a)$$

Newton's second law (see Section 4.1.2), gives equations of motion for translation of the centre of the rock fall mass in the normal N , and tangential T , planes:

$$dv_N = \frac{dp_N}{m}$$

and

$$dv_T = \frac{dp_T}{m}$$

and for planar rotation of the rock fall:

$$d\omega = \frac{r}{m \cdot k^2} dp_N \quad (4.19)$$

The impact mechanics principles discussed in this chapter of relating velocity and impulse changes during impact can be used to derive equations for the final tangential and normal velocity components. Appendix C shows the method of deriving these equations, in the case of frictional impact where transition from sliding to rolling occurs during impact, from which the expressions for the final velocity components for a spherical body are as follows:

$$v_{fT} = v_{iT} - \frac{(v_{iT} + r \cdot \omega_i)}{\left(1 + r^2/k^2\right)} \quad (4.20)$$

$$v_{fN} = -v_{iN} \cdot e_N \quad (4.21)$$

and the final rotational velocity is:

$$\omega_f = \omega_i - \frac{r}{k^2} \frac{(v_{iT} + r \cdot \omega_i)}{\left(1 + r^2/k^2\right)} \quad (4.22)$$

Equations (4.20) and (4.21) for the final tangential and normal velocity components respectively can then be solved to find the final restitution velocity v_f and angle θ_f as follows:

$$v_f = \sqrt{v_{fT}^2 + v_{fN}^2} \quad (4.23)$$

$$\theta_f = \text{atan}\left(\frac{v_{fN}}{v_{fT}}\right) \quad (4.24)$$

Figure 4.7 shows the final velocities and angles diagrammatically, in terms of the three impact parameters: v_i , θ_i and ω_i , and the size and shape of the body (r , k).

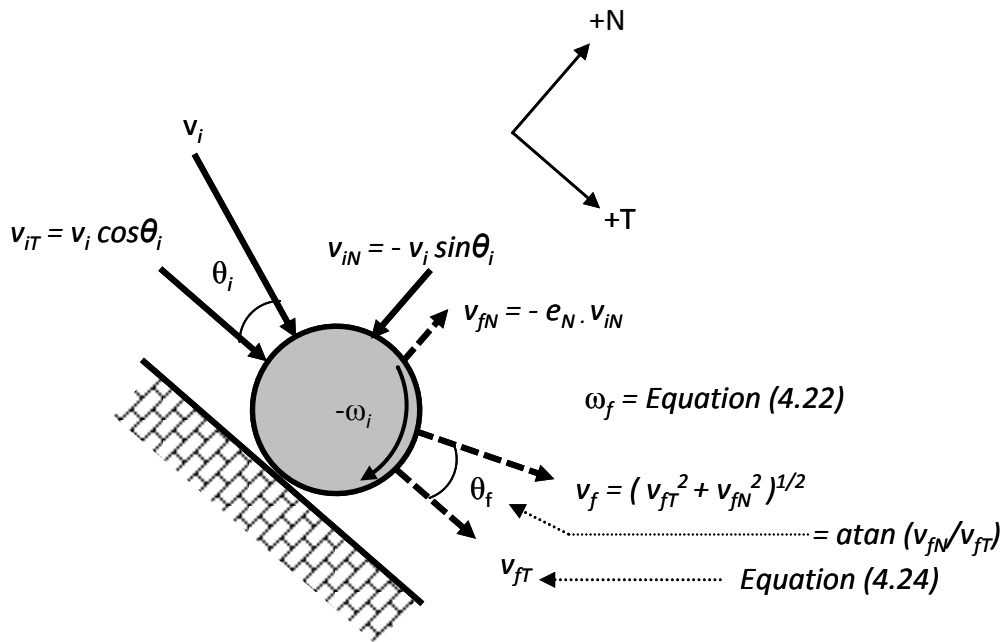


Figure 4.7: Diagram of impact showing equations defining impact and restitution velocity vectors

It is of interest that in equations (4.20) to (4.24) defining the final velocities and restitution angle, the only physical property of the slope/rock fall that is incorporated is the normal coefficient of restitution. The friction coefficient, which relates tangential and normal impulses during slip (Equation (4.14a)), is used to calculate the reduction in tangential velocity during impact as shown in Appendix C, Section C.2. Also, Chapter 6 shows the calculation of energy losses for rotating bodies incorporating the coefficient of friction.

When slip halts and the block rolls, no additional change in tangential velocity occurs because sliding friction does not operate in this phase of the impact process. Furthermore, while the size (radius, r) and shape (radius of gyration, k) of the body influences the final velocity and angle calculations, these values are independent of the mass because the forces generated at the impact point are much larger than gravity so body forces can be neglected (see Section 4.1). The equations presented in this chapter demonstrate the basic behavior of a rough, rotating sphere impacting a stationary slope surface, for a two-dimensional (planar) condition. If necessary, the equations can be modified to analyze other block shapes such as ellipsoids or slabs. While the equations are a simplification of actual rock fall behavior, they provide a useful framework for understanding the various factors that influence rock fall behavior, and can be used to examine actual rock falls and assist in the design of protection measures. Section 4.7 compares actual velocities documented in Chapter 2 with velocities calculated from the theoretical equations.

4.6.3 Example of impact mechanics calculation

Correct application of the equations in this chapter requires careful attention to the signs (negative and positive) of the velocities and angles according to the system of axes as shown in Figure 4.6. The following worked example illustrates a sample calculation.

Worked example 4A – impact final velocities: for a 1.5 m diameter spherical rock fall, the impact translational and rotational velocities (v_i and ω_i), and impact angle θ_i relative to the slope, are shown in Figure 4.8. The tangential and normal components of the impact velocity are calculated as follows:

$$v_{iT} = v_i \cdot \cos \theta_i = 19.9 \text{ m} \cdot \text{s}^{-1}; \quad v_{iN} = v_i \cdot \sin \theta_i = -9.3 \text{ m} \cdot \text{s}^{-1}$$

The radius of gyration k of the sphere is $r \sqrt{2/5} = 0.47 \text{ m}$.

The coefficient of restitution e_N is determined from the relationship between θ_i and e_N as discussed in Chapter 5 (Section 5.2, equation (5.4)) where it is demonstrated that:

$$\begin{aligned} e_N &= 19.5 \cdot \theta_i^{-1.03} \\ &= 0.71 \end{aligned}$$

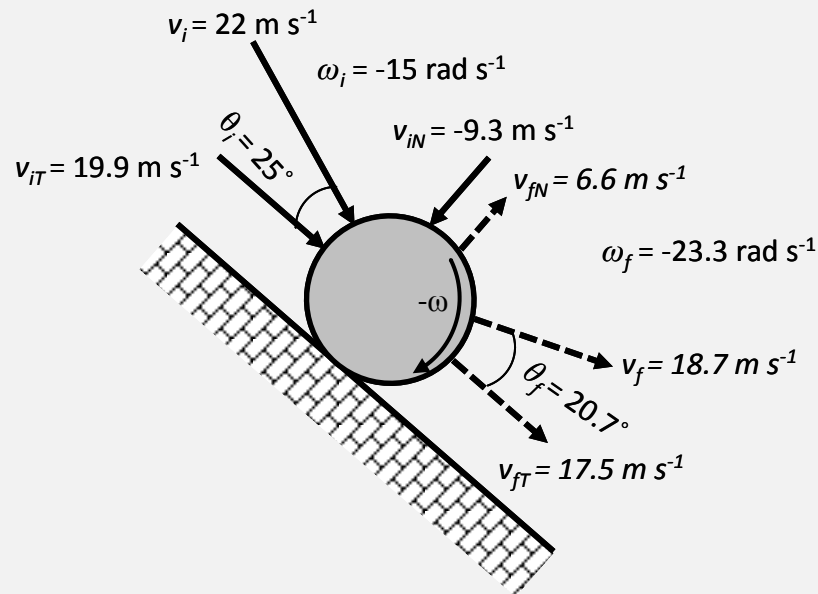


Figure 4.8: Example of rock fall impact showing values calculated final (restitution) velocity and angle

Application of equations (4.20) to (4.24) gives the values for the final translational and angular velocity components, and the restitution as shown on Figure 4.8. These results show that during

impact the normal velocity component changes from $-9.3 \text{ m} \cdot \text{s}^{-1}$ towards the slope to $+6.6 \text{ m} \cdot \text{s}^{-1}$ away from the slope, while the tangential velocity component reduces from 19.9 to $17.5 \text{ m} \cdot \text{s}^{-1}$, and the angular velocity increases, in the negative direction, from -15 to $-23.3 \text{ rad} \cdot \text{s}^{-1}$. The overall effect of the impact is to reduce the velocity of the rock by $3.3 \text{ m} \cdot \text{s}^{-1}$, or 15 per cent. The final angle, $\theta_f = 20.7$ degrees.

The effect of rotation on the impact process is illustrated by letting $\omega_i = 0$, for which the new values for the calculated final velocities are: $v_{fT} = 14.2 \text{ m} \cdot \text{s}^{-1}$, $\omega_f = -19 \text{ rad} \cdot \text{s}^{-1}$ and $\theta_f = 24.8$ degrees. That is, the effect of a rotational velocity of $-15 \text{ rad} \cdot \text{s}^{-1}$, compared to the body not rotating at impact, is to increase v_{fT} from 14.2 to $17.5 \text{ m} \cdot \text{s}^{-1}$, and produce a flatter trajectory as θ_f changes from 24.8 to 20.7 degrees.

4.6.4 Effect of angular velocity on trajectories

Worked example 4A and Figure 4.8 show the influence of the angular velocity on the restitution velocity and angle. That is, an increasing negative angular velocity produces a flatter, greater velocity trajectory. The impact mechanics equations can also be used to find the effect of positive rotational velocity on trajectories as follows.

Equation (4.20) shows the relationship between the impact rotational velocity ω_i and the restitution tangential velocity v_{fT} . Also, equation (4.21) relates the restitution normal velocity v_{fN} to the normal coefficient of restitution e_N , and equations (4.23) and (4.24) can then be used to find the restitution velocity v_f and angle θ_f .

The influence of the impact angular velocity ω_i on the restitution velocity and angle is shown in Figure 4.9. In these three models, the impact velocity is $v_i = 22 \text{ m} \cdot \text{s}^{-1}$ at angle $\theta_i = 25$ degrees. Impacts have been studied for three angular velocities: Model a) - $\omega_i = -15 \text{ rad} \cdot \text{s}^{-1}$; Model b) - $\omega_i = -25 \text{ rad} \cdot \text{s}^{-1}$; Model c) - $\omega_i = +15 \text{ rad} \cdot \text{s}^{-1}$. As shown on Figure 4.5, the angular velocity is negative if its direction at the contact point is in the opposite direction to the positive tangential axis, i.e., clockwise in this model.

The calculation of the final velocities and angles for the three conditions on Figure 4.9 confirms that the effect of an increasing negative angular velocity is to increase the final velocity and produce a flatter trajectory. That is, for conditions a) and b), the final velocity increases from $18.7 \text{ m} \cdot \text{s}^{-1}$ to $20.7 \text{ m} \cdot \text{s}^{-1}$, while the final angle decreases from 20.6 degrees to 18.6 degrees.

In model 4.9c), the body is rotating in a counter-clockwise (positive) direction, and the restitution velocity now decreases to $12.9 \text{ m} \cdot \text{s}^{-1}$ at a larger angle of $\theta_f = 27.1$ degrees.

In rock falls, rotation is almost always in the negative direction because the frictional resistance at the contact between the slope surface and the moving body sets up a moment acting clockwise. The calculations show that the negative angular velocity flattens the trajectory which is consistent with the low trajectory heights shown on Figure 3.5. Furthermore, the distributions of θ_f values plotted in Figures 3.9 a) and b) show that the majority of θ_f values are less than about 30 degrees, with few high angle trajectories; that is, θ_f values greater than 60 degrees are rare. An exception to this condition is for very shallow angle impacts ($\theta_i < 15^\circ$) where high angle final trajectories can occur (see Section 5.2).

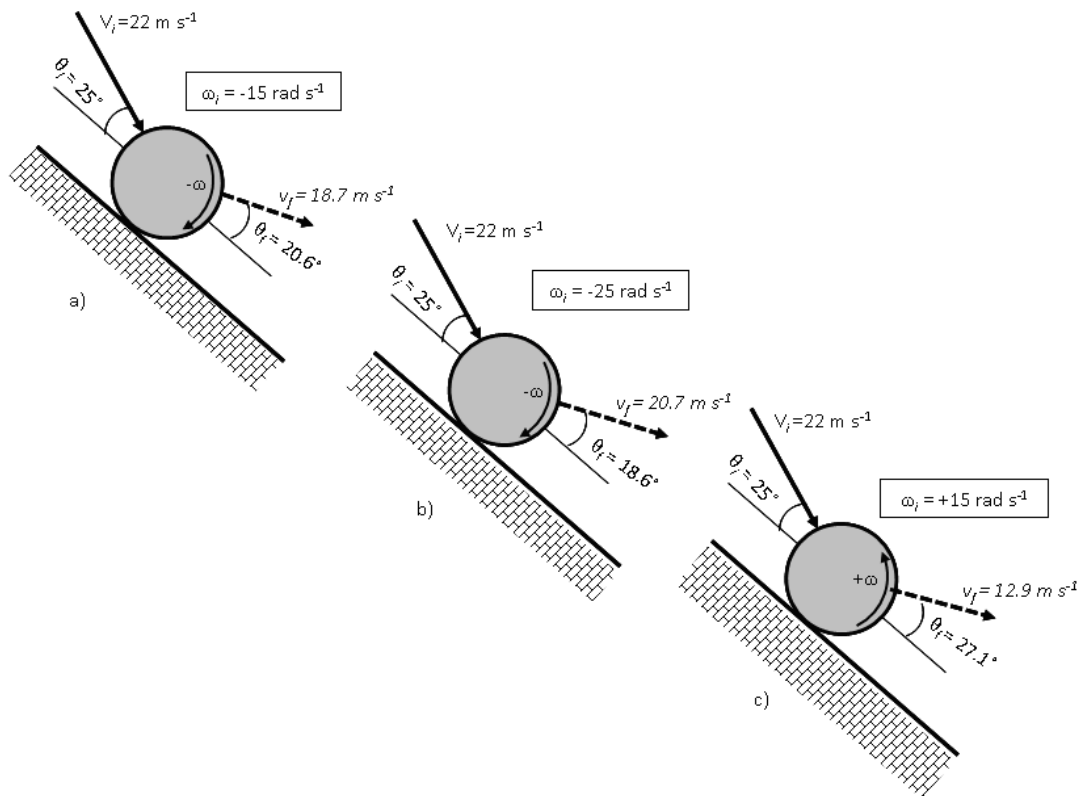


Figure 4.9: Influence of impact angular velocity, ω_i on restitution velocity, v_f and angle, θ_f . a) $\omega_i = -15 \text{ rad} \cdot \text{s}^{-1}$; b) $\omega_i = -25 \text{ rad} \cdot \text{s}^{-1}$; c) $\omega_i = +15 \text{ rad} \cdot \text{s}^{-1}$

Calculation of ω_f using equation (4.22) shows that for a sphere, ω_f will increase with every impact. In fact, field studies show that the angular velocity may increase or decrease on impact, depending on the attitude of the non-spherical block relative to the slope at the point of impact. Measured values of ω_f shown on Figure 3.10 illustrate the variation in ω_f values, and that ω_f may increase or decrease during impact after the initial 5 to 10 m of fall height (see Section 3.4.1).

The trajectories of rock falls are important in the selection of appropriate heights for protection structures such as fences and barriers. Both field data and impact mechanics theory show that low trajectories are more common than high trajectories and this may be taken into account in fence design.

4.7 Calculated vs. actual restitution velocities

Chapter 2 describes five rock fall events where the impact and restitution velocities and angles were carefully documented; vectors of these velocities for a typical impact at each sites are shown on the insets in Figures 2.2 to 2.10. Information is also available on the shape, dimensions, radius and radius of gyration of a typical block at each site.

These actual restitution velocities can be compared with velocities calculated using equations (4.20) to (4.24) in Section 4.6.2 based on impact mechanics theory. In applying these equations, values are required for the initial angular velocity ω_i , and the normal coefficient of restitution e_N , at the impact points. Values for these two parameters were obtained from the following relationships:

$$\omega_i = \frac{v_i}{r} \quad (3.17)$$

where v_i is the impact velocity and r is the radius of the body.

and

$$e_N = 19.5 \cdot \theta_i^{-1.03} \quad (5.4)$$

where θ_i is the impact angle.

Figure 4.10 is a plot comparing the two sets of restitution velocities. The plot shows that the calculated velocities are in all cases greater than the actual velocities by values ranging from 20 to 50 per cent. Sensitivity analyses of these calculations shows that the calculated and actual values are closer when the angular velocity is reduced and the normal coefficient of restitution is increased. However, reasonable changes to these parameters are not sufficient to make the calculated velocities equal to the actual values.

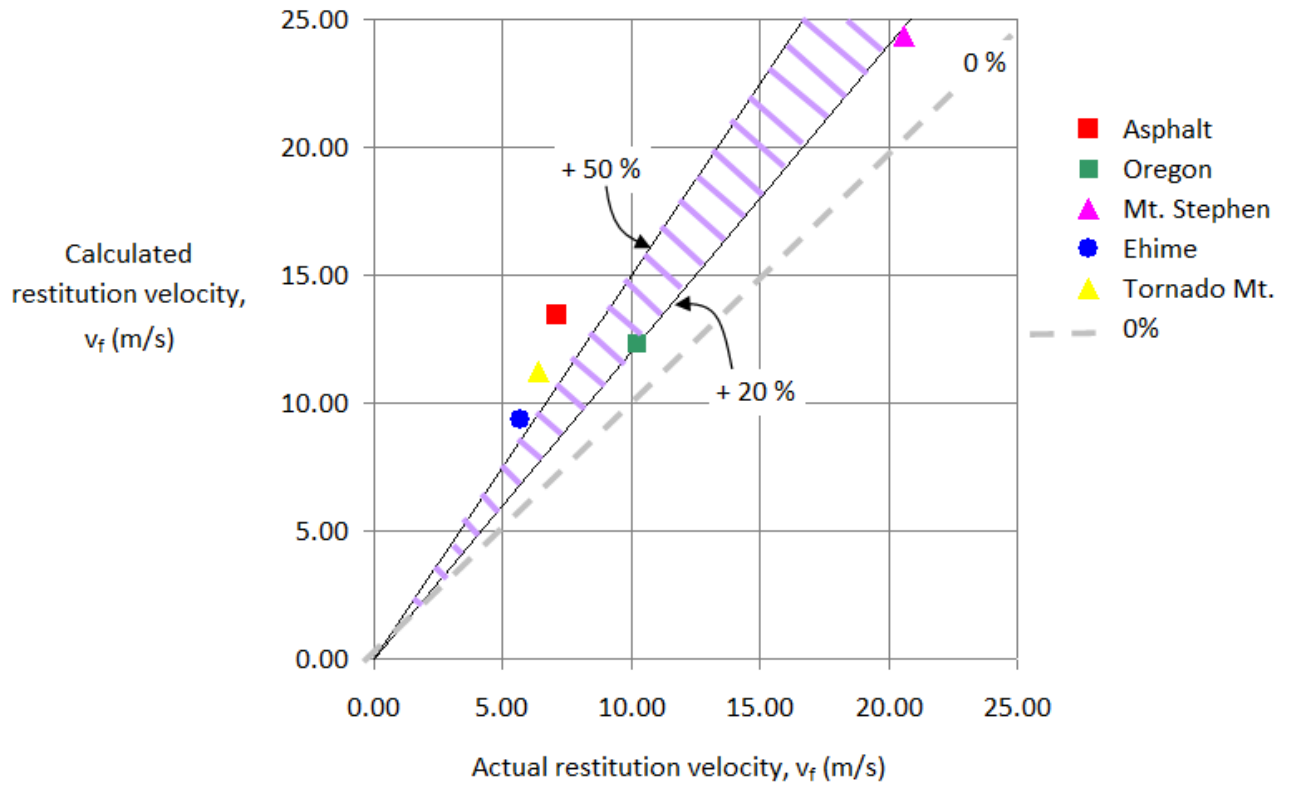


Figure 4.10: Plot comparing restitution velocities – actual (Chapter 2) and calculated (equations (4.20) to (4.24)) values

5 Coefficient of restitution

The results of the field studies in Chapter 2 and the discussion of impact mechanics in Chapter 4 illustrate how rock fall behavior can be defined by values for the normal and tangential coefficients of restitution (e_N and e_T) that are applicable to the particular site conditions. The coefficients of restitution quantify velocity changes during impact and help in understanding how conditions at the impact points influence rock fall behavior. Figure 5.1 shows three impacts and two trajectories and clearly illustrates the reduced velocity and height of the second trajectory due to the loss of energy at the first impact, i.e., $e_N < 1$. Figure 5.1 shows typical behavior of a rubber ball – rock falls will always have lower trajectories than these because of the relatively low e_N of rock.

Changes in the velocity components during impact and the corresponding coefficients of restitution are also illustrated in Figure 5.2 on the [normal impulse, p_N – relative velocity, v] diagram. The normal coefficient of restitution defines the change in normal velocity during impact and is related to the impact angle as discussed in this chapter, and the inelastic compression of the slope materials. The tangential coefficient of restitution defines the reduction in tangential velocity during impact and is related to the friction force generated between the slope and the body. This chapter discusses how these coefficients are correlated with impact conditions and are not purely material properties.



Figure 5.1: Impacts between successive trajectories showing typical inelastic behavior and loss of energy during impact where second trajectory (on right) is lower than first trajectory; rock falls will always have lower trajectories than those shown (Micheal Maggs, Wikimedia Commons)

This chapter summarizes the results of the e_N and e_T values obtained from the five field studies described in Chapter 2, encompassing four different slope materials and 57 impacts. A sixth location is a laboratory test where blocks of rock were dropped on to a concrete floor and the rebound heights were measured to give values for e_N .

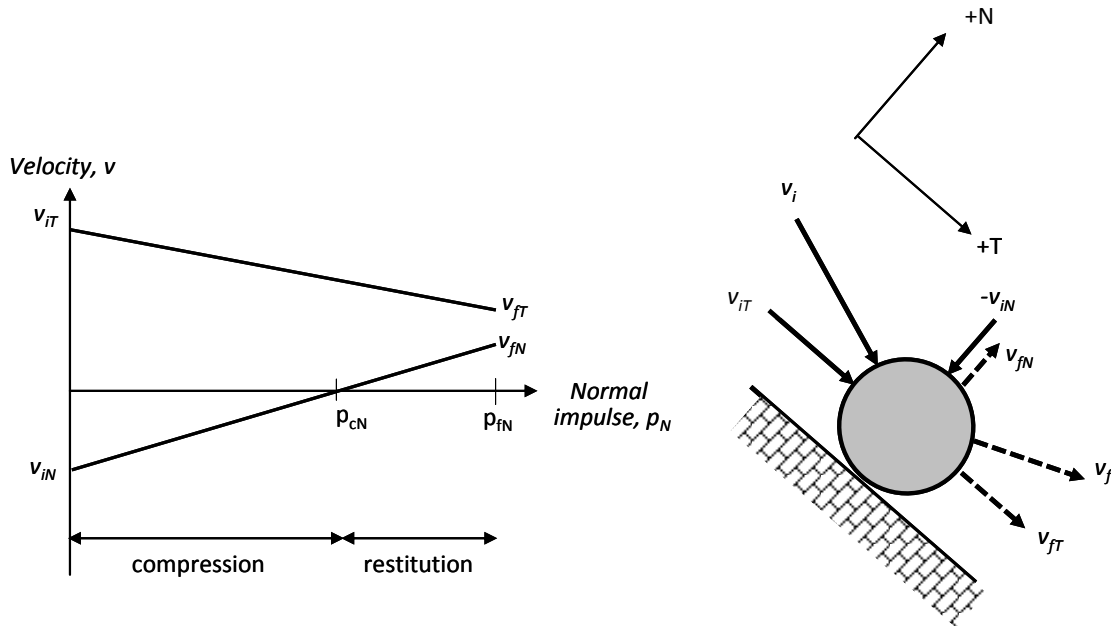


Figure 5.2: Normal impulse-velocity plot showing relationships between changes in normal (N) and tangential (T) velocity components and coefficients of restitution – $e_N = (v_{fN}/v_{iN})$ and $e_T = (v_{fT}/v_{iT})$

5.1 Newton’s coefficient of restitution

The concept of the coefficient of restitution, which in this case was the normal coefficient, was first developed by Isaac Newton (1686) who suspended spheres of the same material on pendulums and measured how high they rebounded after impact (Figure 5.3); the measurements incorporated corrections for velocity losses due to air friction. Values for the coefficient of restitution found by Newton included 0.56 for steel and 0.94 for glass. One of the purposes of the experiments was to prove the Third law of motion – every action has an equal and opposite reaction.

It was assumed at the time of Newton’s experiments that the coefficients of restitution were material properties. However, it is now understood for impact between rough, rotating bodies of different materials, such as rock falls, reductions in velocity depend not only on the material forming the body, but also on the impact conditions such as mass and shape of the impacting body, and the impact angle and velocity.

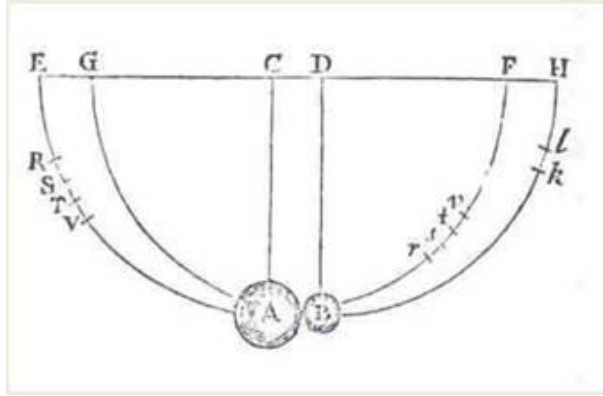


Figure 5.3: Isaac Newton's measurement of normal coefficient of restitution using impact of spheres suspended on pendulums

5.2 Normal coefficient of restitution

Equation (4.6) and the $[p_N - v]$ diagram shown on Figure 5.2 define the normal coefficient of restitution as the ratio of the final to impact normal velocities:

$$e_N = -\frac{v_{fN}}{v_{iN}} = \sqrt{\frac{h_f}{h_i}} \quad (4.6)$$

where v_{fN} ($t = f$) and v_{iN} ($t = i$) are the final (restitution) and impact velocities respectively, and e_N is negative because v_{iN} , acting in the negative direction of the normal axis, has a negative value.

Equation (4.6) indicates that the value of the normal coefficient can be determined by dropping blocks of rock from height (h_i) on to different surfaces and measuring the height of the rebound (h_f) in a similar manner to the procedure used by Newton. However, this is not applicable to rock falls where the irregular, rotating blocks are impacting rough slope surfaces at oblique angles. In fact, for rock falls, it is difficult to measure the value of e_N in the laboratory because of the complexity of the impact process. Field measurement of coefficients of restitution involves carefully documenting impacts and trajectories, by locating impact points or using a high speed camera, and then calculating the normal and tangential components of the impact and restitution velocities.³

³ Because rock fall impacts differ significantly from Newtonian-type impacts (Figure 5.3), the ratio of final to impact normal velocities for rock falls (e_N) may be termed the “apparent” coefficient of restitution. In this thesis, e_N always refers to rock fall impacts where e_N is not a material property, and can have a value greater than 1.

A further complication with the velocity measurements is that considerable scatter occurs in the values as the result of the wide variation in the impact conditions of the rotating, irregular blocks impacting the rough slope surface. This variation can best be handled using probabilistic methods in which the design values of velocity, coefficient of restitution and rock fall mass are expressed as probability distributions rather than discrete values. This result in turn means that the design of protection structures can be based on probabilistic methods in which the structure is designed to withstand, for example, impact of 90 per cent or 95 per cent of likely rock fall energies rather than the largest event that may ever occur. Where these large events rarely occur, the cost of providing protection against all rock falls would have to be balanced against the likely consequence of the fall.

5.2.1 Theoretical relationship between impact angle and normal coefficient of restitution

The [normal impulse, p_N – relative velocity, v] diagram in Figure 5.4a) illustrates the influence of impact conditions on the normal coefficient of restitution e_N , keeping in mind the discussion in Section 5.1 that e_N is not a material property, but depends on the impact characteristics. The two dashed lines on Figure 5.4a) represent changes in the normal velocity during impact for two identical, non-spherical eccentric impacts with respect to mass and impact translational velocity. The approximate relationship between the normal impulse p_N and the normal velocity v_N is assumed to be linear with gradient equal to $(1/m)$.

$$v_N = v_{iN} + \frac{p_N}{m} \quad (4.3)$$

On Figure 5.4a), the only difference between the two lines is the impact angles θ_i, θ_i' . The lines show the change in normal velocity during impact from a negative value acting towards the slope at the point of impact ($t = i$), to zero at the point of maximum compression ($t = c$), to a positive velocity acting away from the slope at the end of the impact ($t = f$).

The upper dashed line on Figure 5.4a) represents a shallow angle impact close to the slope surface, while the lower dashed line represents a steeper angle impact ($\theta_i' < \theta_i$). For the shallow impact, the normal velocity component is small relative to the normal component for the steep

impact ($v'_{iN} < v_{iN}$). However, the slope of the $[p_N - v]$ line is the same for both impacts because the mass is unchanged.

Examination of the final and initial normal velocities for the two impact conditions on Figure 5.4a) shows that $e'_{iN} > e_{iN}$, and that $e'_{iN} > 1.0$ for the shallow angle impact. A normal coefficient of restitution that is greater than 1 does not mean that energy is created during the impact process; $e'_{iN} > 1$ because the geometry of the impact results in the final normal velocity component being greater than the impact vertical velocity component.

With respect to energy changes during impact, the final velocity will always be less than the impact velocity ($v'_f < v'_i$ and $v_f < v_i$) resulting in a net loss of energy during impact (Giacomini, A. *et al.*, 2010; Buzzi, O. *et al.*, 2012; Asteriou, H. *et al.*, 2012; Spadari, M. *et al.*, 2012). Energy changes during impact are discussed in more detail in Chapter 6.

Figure 5.4a) also shows that the value of the normal impulse at maximum compression is also influenced by the impact angle ($p_c > p'_c$). That is, a shallow impact results in a “softer” impact than a steeper impact. For steep angle impacts, the body will cause more compression of the slope material, compared to shallow angle impacts, resulting in less rebound and a smaller value of v_{fN} .

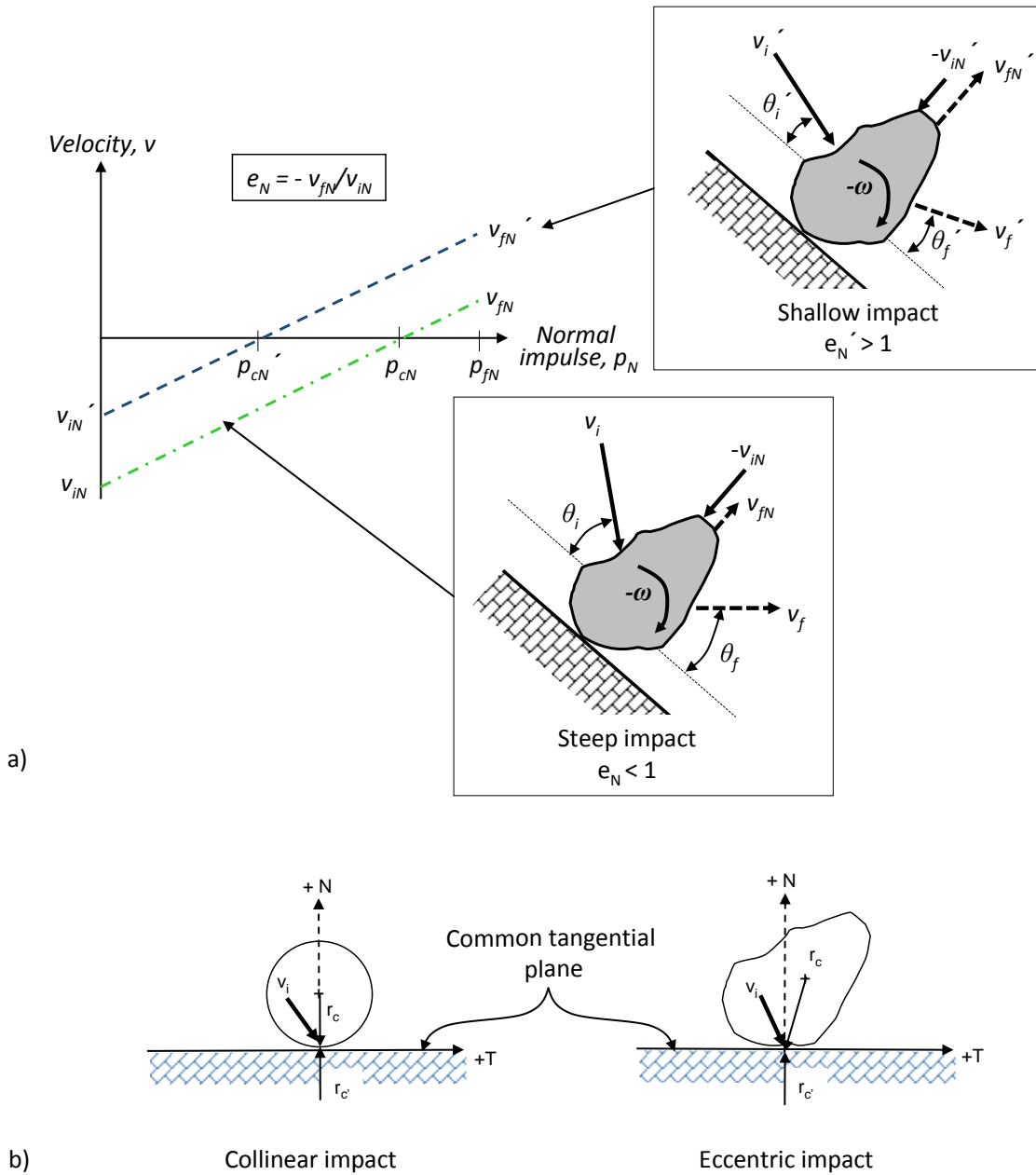


Figure 5.4: a) Effect of impact angle θ_i on the normal coefficient of restitution, e_N ; b) Geometry of collinear and eccentric impacts

The relationship between the impact angle θ_i and e_N shown graphically on Figure 5.4a) can also be expressed mathematically using the theory of impact mechanics. In developing this relationship it is necessary to distinguish between collinear and eccentric impacts, the geometrical features of which are shown in Figure 5.4b) where a common tangential plane is established at the contact point that is coincident with the slope surface. The geometry of impact relates to the orientation of the lines r_c and r_c' joining the centre of mass of the impacting body with the contact point, as discussed below.

Collinear impact – collinear impact occurs where the line between the centre of mass of the impacting body lies on the normal to the common tangent plane; this will occur for a spherical body. For these conditions, the equations of motion for normal and tangential directions can be decoupled such that spin and friction do not contribute to the normal component of the final velocity. That is, the normal coefficient of restitution is equal to the ratio of the final to impact normal velocity components and will be less than 1.0.

Appendix C shows, for collinear impacts, the derivation of equations for the final translational and angular velocities and the restitution angle relative to the slope for conditions where slip stops during impact. These equations can be rearranged to find a mathematical relationship between the final and impact angles, θ_f and θ_i as follows.

The restitution (final, $t = f$) angle θ_f is related to the final normal and tangential velocities as shown in equation (4.24):

$$\tan \theta_f = \left(\frac{v_{fN}}{v_{fT}} \right) \quad (4.24)$$

For a rough, rotating sphere, the final tangential (v_{fT}) and normal velocities (v_{fN}) are given by equations (4.20) and (4.21) that can be combined with equation (4.24) as follows:

$$\tan \theta_f = - \frac{v_{iN} \cdot e_N}{v_{iT} - \left(\frac{v_{iT} + r \cdot \omega_i}{v_{iN} \left(1 + r^2/k^2 \right)} \right)} \quad (5.1)$$

Since the impact angle θ_i is related to the impact velocity components as follows

$$\tan \theta_i = \left(\frac{v_{iN}}{v_{iT}} \right)$$

equations (5.1) and (4.24) can be rearranged to show the relationship between θ_f and θ_i :

$$\tan \theta_f = \frac{\tan \theta_i \cdot e_N}{\left[1 - \frac{1}{1 + r^2/k^2} \left(1 + \frac{r \cdot \omega_i}{v_i \cdot \cos \theta_i} \right) \right]} \quad (5.2)$$

For an impacting sphere where $k^2 = r^2 \cdot (2/5)$ and $(1+r^2/k^2)^{-1} = 0.29$, equation (5.2) simplifies to:

$$\tan \theta_f = \left[\frac{\tan \theta_i \cdot e_N}{0.71 - \left(1 + \frac{0.29 \cdot r \cdot \omega_i}{v_i \cdot \cos \theta_i} \right)} \right] \quad (5.3)$$

Equations (5.1) to (5.3) are applicable to collinear impact conditions.

Eccentric impact – for actual rock falls where the body is non-spherical and rough, and impact occurs at an oblique angle, eccentric impact conditions apply as defined in Figure 5.4b). For these conditions, the line r_c from the centre of mass of the impacting body does not lie on the normal to the common tangent plane, and the equations of motion each involve both normal and tangential forces, such that the effects of friction and normal forces are not separable.

For both collinear and eccentric impact, Goldsmith (1960) provides a graphical solution for finding the final impulses, velocities and angles. These plots show how the normal and tangential impulses vary throughout the duration of impact, and are related to the impact angle and the friction at the contact point. Also, the normal impulse decreases as the impact angle becomes shallower, which is consistent with the impact model shown in Figure 5.4a).

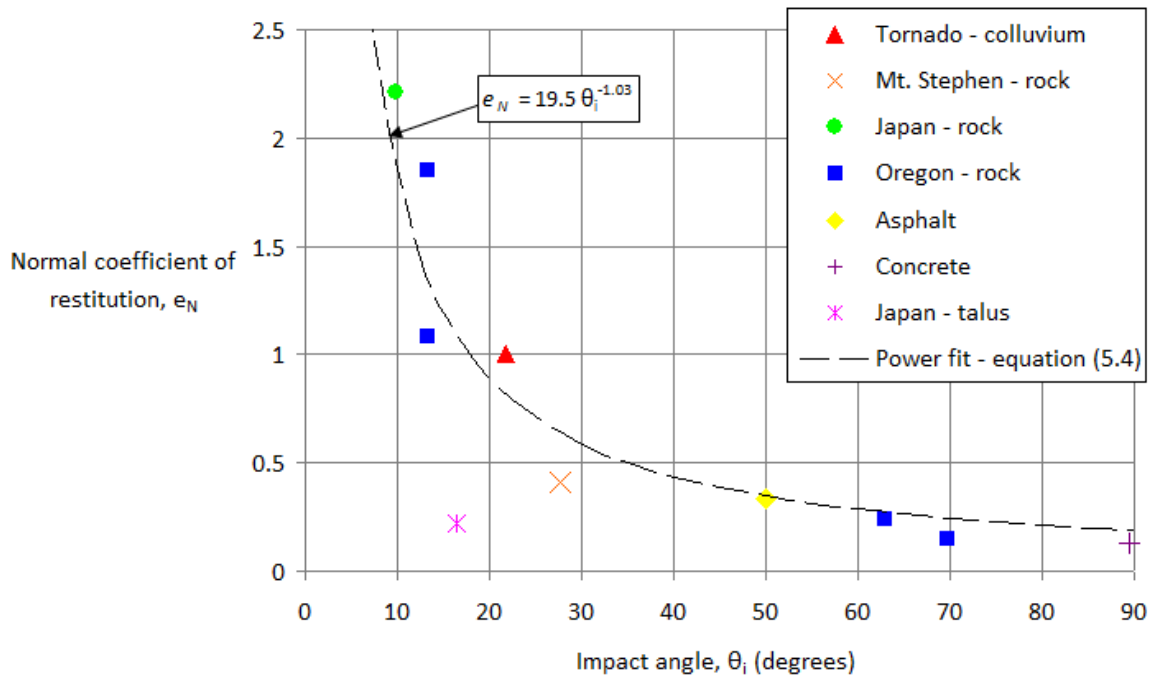


Figure 5.5: Relationship between impact angle θ_i and normal coefficient of restitution e_N with best fit (power) curve for average values of θ_i and e_N each material type

5.2.2 Field data showing relationship between impact angle and normal coefficient of restitution

In order to examine the influence of the impact angle θ_i on the normal coefficient of restitution e_N , actual values of θ_i and e_N have been obtained from the field data described in Chapter 2 where impacts and trajectories were carefully documented (Figure 5.5). For each material type and test site, as well as a drop test on concrete (Figure 5.6), the average $[\theta_i - e_N]$ value has been plotted on Figure 5.5. The best fit line for the average field data points is defined by the following relationship:

$$e_N = 19.5 \cdot \theta_i^{-1.03} \quad (5.4)$$

Figure 5.5 show that for steep impacts ($\theta_i > \sim 60$ degrees), e_N is less than about 0.3 and little rebound occurs. Also, for shallow skidding impact of rotating blocks ($\theta_i < \sim 20$ degrees), values of e_N are greater than 1 such that the final normal velocity is greater than the impact normal velocity ($v_{fN} > v_{iN}$). The relationship between θ_i and e_N shown on Figure 5.5 supports the $[p_N - v]$ plot in Figure 5.4 illustrating the influence of the impact angle on the normal coefficient of restitution.

On Figure 5.5, the reference data point for the field values of e_N is for $\theta_i = 90$ degrees, i.e., a non-rotating block dropped on to a horizontal surface. This is the basic definition of the normal coefficient of restitution as shown in Newton's measurements (Figure 5.3). Figure 5.6 shows a test to measure e_N for concrete in which a block of rock was dropped on a horizontal concrete surface; measurements of the average rebound height showed that $e_N = 0.18$ (Masuya *et al.*, 2001). While similar tests on other slope materials were not carried out, it is reasonable to expect that e_N values for sound rock may be close to 0.18, while impacts on soil and talus would be less than 0.18. In fact, simple observations of dropping rocks on to various ground surfaces shows that rebound heights are always less than about 5 percent of fall height ($e_N \nlessgtr 0.2$). This observation is in contrast with e_N values quoted in the literature of about 0.46 for bare rock (RocScience, 2003).

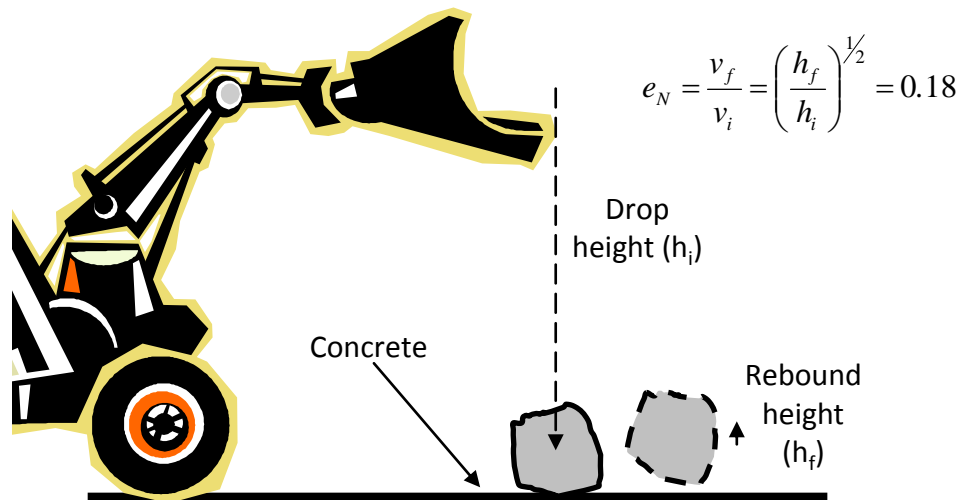


Figure 5.6: Measurement of normal coefficient of restitution for concrete using drop test (h_i) to measure rebound height (h_f) (Masuya, *et al.*, 2001)

It is noted that it would be unusual that a non-rotating rock fall would impact a slope at right angles, and that almost all conditions would tend to have impact angles significantly less than 90 degrees. Therefore, the Newtonian definition for e_N is generally inapplicable to rock falls.

Figures 2.2 to 2.10 show details of the velocities and angles for selected impact points at the various field sites that have been studied to research rock fall characteristics and calculate values for e_N . These sites were selected in order to incorporate a wide variety of both geometric and geologic conditions. That is, the impact angles (θ) varied from about 50 degrees at the asphalt site and 70 degrees for the impact in the ditch at the Oregon test site, to about 13 degrees for the $\frac{1}{4}$ H:1V face at the Oregon site and 22 degrees on Tornado Mountain. The slope materials studied included rock (Mt. Stephen, Oregon, Ehime), talus (Ehime), colluvium (Tornado Mountain), asphalt and concrete. The total number of impacts included in this summary is 58.

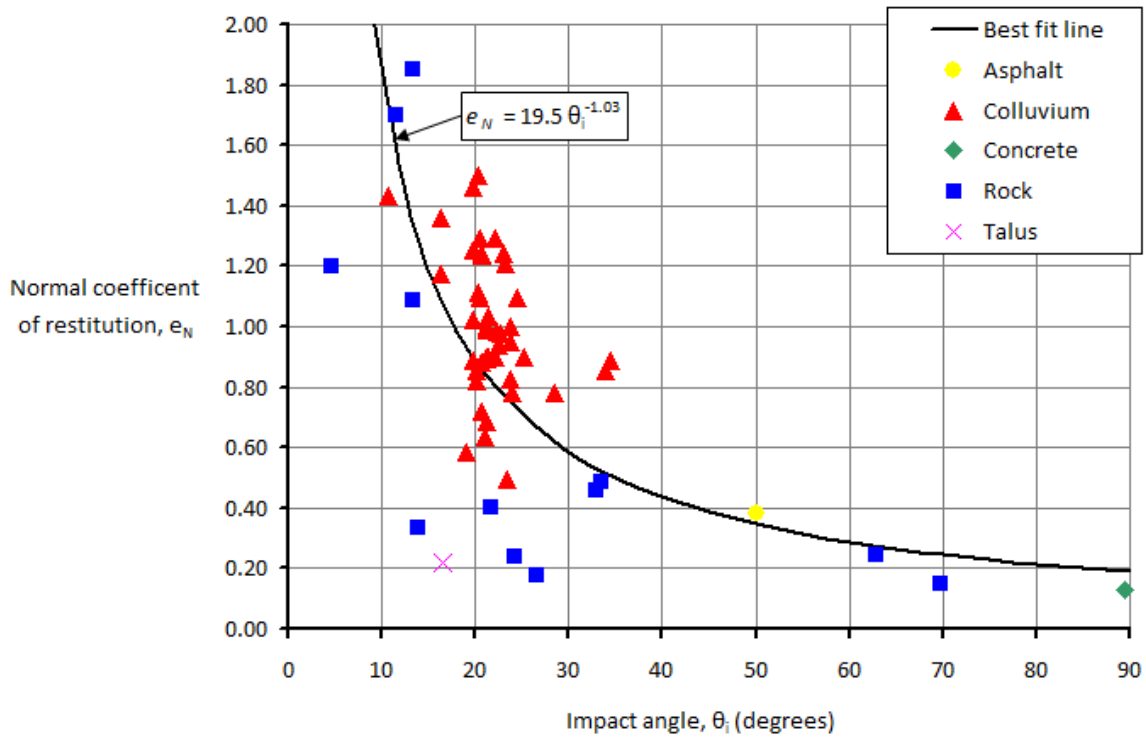


Figure 5.7: Relationship between impact angle θ_i and the normal coefficient of restitution e_N for the rock fall sites described in Chapter 2; total of 58 points for five slope materials

For each impact at the case study sites, the $[\theta_i - e_N]$ co-ordinates are plotted on Figure 5.7, with the symbols indicating the slope material. The point on the extreme right side of the plot ($\theta_i = 90$ degrees) is the drop test on concrete. The colluvium points are from the Tornado Mountain site where most θ_i values are in the range of 15 to 25 degrees (see Figure 2.8). The scatter in the Tornado Mountain points can be attributed primarily to the irregularity in the shape of the falling rock and the variation in the impact angle, because the colluvium was at a uniform slope with no significant roughness. For impacts on talus, two points are available from the Ehime site – impacts #6 and #7 (see Figure 2.6). These two impacts had significantly different behavior with the rock barely leaving the slope after #6, while the trajectory after impact #7 is the longest and highest of the rock fall. As shown in the inserts on Figure 2.6, the values of e_N range from 0.22 for impact #6 to 5.48 for impact #7; impact #6 is plotted on Figure 5.5. For impacts on rock, the range of θ_i values is 11 to 70 degrees and while values of e_N are scattered, they do exhibit a trend with high e_N values at shallow impact angles, to low e_N values at steeper impact angles.

The best fit curve fitted to the field data on Figure 5.7 shows that θ_i and e_N are related by a power curve defined by equation (5.4) for which the correlation coefficient R^2 is -0.48. This reasonably high correlation is driven by the points with values of θ_i less than 15 degrees and

more than 35 degrees where the scatter is limited compared to points with θ_i in the range of 35 to 70 degrees.

The data plotted on Figure 5.7 shows how the value of e_N decreases as the impact angle θ_i increases from very shallow impacts (low values of θ_i) to a value of 0.18 for normal impacts ($\theta_i = 90$ degrees). For shallow impacts, i.e., θ_i less than about 15 degrees, the value of e_N may be greater than 1. As discussed in Section 5.2.1 above and demonstrated in Figure 5.4, values of e_N greater than 1 does not mean that energy is being created during impact, but only that the impact geometry causes the final normal velocity to be greater than the impact normal velocity. Because the tangential velocity (and energy) always decreases during impact, a net energy loss occurs during impact (see Section 6.1.2).

The symbols on Figure 5.7 show $[e_N - \theta_i]$ values for the five different slope materials listed in the legend. It is noted that values for each slope material are not grouped together, but tend to follow the best fit line according to the value of the impact angle. This would indicate that e_N is correlated more closely with the impact geometry, particularly at shallow impact angles that tend to occur in rock falls, than with the slope material properties. The values for colluvium occur over a narrow range of θ_i values because they were obtained from the Tornado Mountain site where the slope geometry is uniform, whereas the θ_i values for impacts on rock have a wider range because they were obtained from three sites, each with different geometries.

In Figure 5.7, considerable scatter occurs in the plotted values. This scatter is due to the interaction during impact between the irregularly shaped, rotating rock fall and the rough slope surface. The degree of scatter caused by these interactions can be observed on Figure 5.7 for the colluvium impacts. These 43 points are for one ellipsoid-shaped block with a major axis of 1.6 m (5.2 ft.) and a minor axis of 1.3 m (4.3 ft.), impacting a planar colluvium slope with a slope angle of between 20 and 33 degrees and no significant roughness. Because of the uniformity of the slope, the scatter in the e_N values is almost entirely the result of the attitude and angular velocity of the block as it impacted the slope.

5.2.3 Application of $[\theta_i - e_N]$ relationship to rock fall modeling

One of the input parameters for rock fall modeling programs is the normal coefficient of restitution e_N , for each slope material along the fall path. The program *RocFall 4.0* (RocScience, 2012), for example, lists suggested values for e_N that have been obtained by users of the

program from their experience of actual rock falls; typical values for e_N listed in RocFall are as follows:

Bare rock – 0.46; asphalt – 0.4; soil – 0.34; talus – 0.32

These values listed for e_N are clearly greater than values that would be obtained by dropping blocks of rock on to these surfaces and measuring the rebound height. Figure 5.6, for example, shows a block of rock dropped on to concrete where the measured value of e_N was 0.18. Since the quoted values for e_N have been obtained by back analysis of rock fall events, it is expected that the back analysis values may be consistent with the $[\theta_i - e_N]$ relationship shown in Figures 5.5 and 5.7. That is, e_N values of 0.4 to 0.5 correspond to impact angles of between 30 and 40 degrees that are consistent with the values measured in the case studies described in Chapter 2.

The relationship between the impact angle θ_i and the normal coefficient of restitution e_N developed from both field studies and impact mechanics theory shown in Figures 5.4, 5.5 and 5.7 demonstrates that e_N depends more on the impact geometry than on the properties of the slope material. This conclusion is supported by the values for e_N from *RocFall 4.0* listed above that are similar for the four materials, and all greater than the measured value for concrete.

It is possible that the $[\theta_i - e_N]$ relationship given by equation (5.4) can be used in rock fall modeling where the geometry of the trajectory just prior to impact, in relation to the slope, defines the impact angle θ_i . This value for θ_i can then be input in equation (5.4) to determine the value of e_N used to calculate, for that impact, final velocities and angles using equations (4.20) to (4.24). An example of this procedure is shown in the Worked example 4A (Section 4.6.3) where the value of θ_i was 25 degrees and the corresponding value of e_N from equation (5.4) was 0.71. This value of e_N was then used in equation (4.21) to calculate the final normal velocity v_{fN} .

5.3 Tangential coefficient of restitution and friction

The reduction in tangential velocity during impact, as shown on the $[p_N - v]$ plot in Figure 5.2, can be quantified in terms of the tangential coefficient of restitution, e_T that is defined as follows:

$$e_T = \frac{v_{fT}}{v_{iT}} \quad (4.7)$$

when v_{fT} is the final tangential velocity, and v_{iT} is the impact tangential velocity.

5.3.1 Field values of tangential coefficient of restitution

The values of e_T measured at the five rock fall locations described in Chapter 2 have been plotted on Figure 5.8 showing a total of 56 impact points for rock (12 points), talus (one point), colluvium (43 points) and asphalt (one point). The legend also shows the average e_T values for impacts on rock and colluvium.

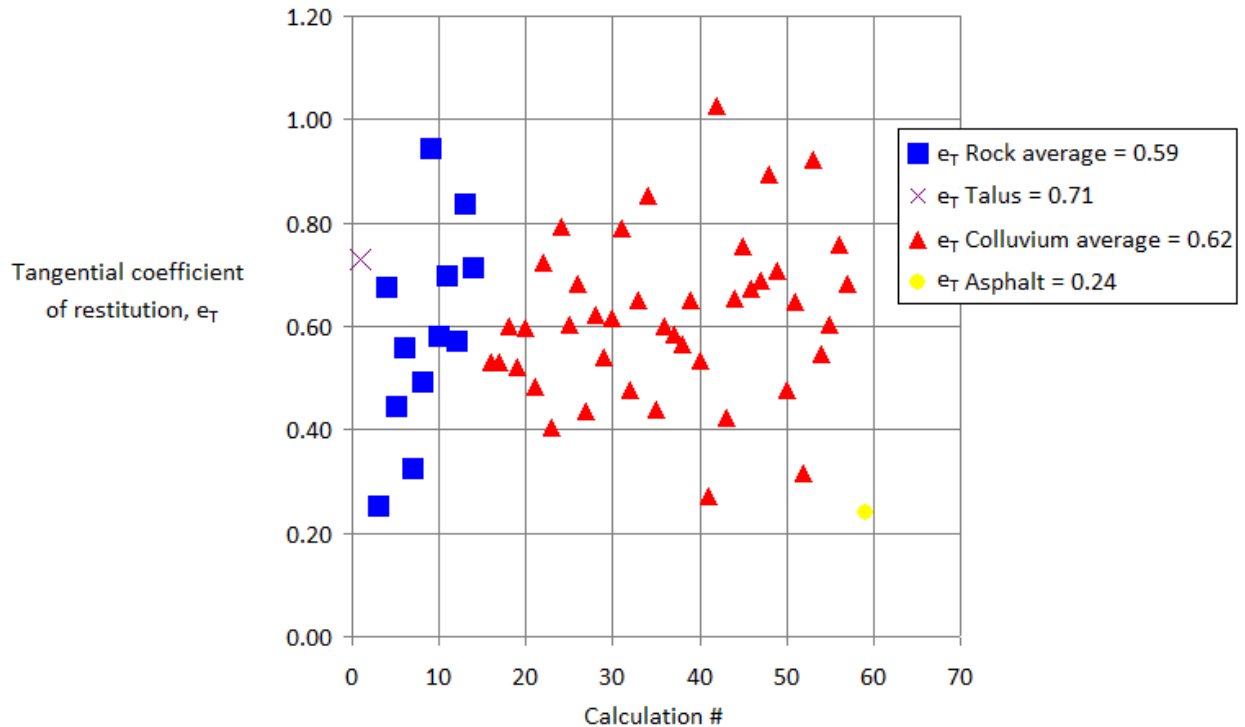


Figure 5.8: Values for tangential coefficient of restitution e_T for 56 impact points at rock fall sites described in Chapter 2

Figure 5.8 shows considerable scatter in the e_T values, as would be expected for the site conditions where the slope surfaces are rough and the rock falls are irregular blocks. In fact, no significant difference is evident in the values of e_T for rock, talus and colluvium. The lowest value for e_T of 0.24 is that for asphalt that is a relatively smooth surface compared to the rock and talus slopes.

The impact process for a rock fall involves the development of shear and normal forces between the rock fall and the slope, and the shear displacement of the rock along this surface. This is typical shearing behavior in which frictional resistance is developed between the two surfaces according to Coulomb's law of friction. Therefore, the tangential coefficient of restitution is analogous to the coefficient of friction μ , and the plot in Figure 5.8 provides an indication of the coefficient of friction values that are developed during impact of rock falls.

The values of e_T plotted on Figure 5.8 appear to be independent of the impact velocity and angle, which is consistent with Coulomb's law in which the friction coefficient is independent of velocity and normal force. The usual practice in rock mechanics is to combine the effects of the frictional properties of the rock material with the roughness, or asperities, of the surface to determine the effective friction angle of a rock surface. If the friction angle of the rock is φ_r and the asperities are simulated as saw teeth-shaped ridges inclined at angle i , then the effective friction angle of the surface is (Wyllie and Mah, 2002; Patton, 1966):

$$\varphi = (\varphi_r + i) \quad (5.5)$$

and

$$\mu = \tan \varphi$$

Equation (5.5) demonstrates that slopes in strong rock with rough surfaces and high values of i , can have friction coefficients, μ , that are greater than 1. In rock mechanics, it is usual to assume that the asperities are sheared off as the normal stress increases relative to the rock strength so that the value of i decreases with increasing normal stress. It is possible that similar behavior may occur with rock falls in which fragments of the rock fall break off on impact to form a smoother, more uniform shape with the progression of the fall; the loss of mass during falls is discussed in more detail in Section 6.5. Although the asperities may break down at the impact points, this will not change the basic friction coefficient of the rock that is independent of the normal stress and shearing velocity.

In Figure 5.8, the values of e_T for each field site are plotted as a separate set of points with the "calculation #" referring to successive impacts. The plot shows that the e_T values do not decline during the course of the fall indicating that loss of mass of the body and the formation of a smoother shape does not result in a significant reduction in the value of e_T .

Furthermore, analysis of correlations for e_T shows no relationship between e_T and the impact angle θ_i . However, a negative correlation exists between e_T and e_N – at high values of e_N , values of e_T are low, and as e_N decreases, e_T increases. That is, at shallow impact angles, when the normal restitution velocities can be high, a significant loss of tangential velocity occurs due to friction on the impact surface.

As a comparison with the field values of e_T , direct measurements have been made of the friction coefficient for blocks of rock sliding on various geological materials (Masuya *et al.*, 2001). These tests involved pulling a natural block of rock with a mass of 433 kg (950 lb.) on surfaces

comprising concrete, a gravel road and soil (Figure 5.9). The friction coefficient was calculated from the shear force that was recorded by a load cell on the pulling cable, and the shear displacement that was measured with a laser displacement meter. It was found that the average friction coefficients μ for these materials were:

$$\mu_{concrete} = 0.59; \mu_{gravel} = 0.68; \mu_{soil} = 0.90.$$

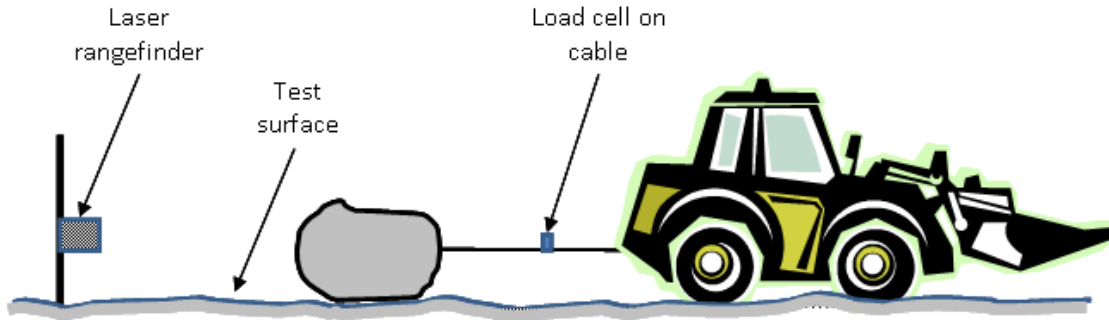


Figure 5.9: Test procedure to measure friction coefficient between block of rock and slope material (Masuya, *et al.*, 2001)

These measured values of the friction coefficient are comparable to the field values of e_T plotted on Figure 5.8, considering the wide scatter in the results. Also, the lowest values for the tangential coefficients of restitution, e_T , are for the smoothest surfaces - asphalt and concrete.

Another application of the effective coefficient of friction to rock fall behavior is in the calculation of fall velocities. Section 3.2.2 describes how fall velocities are related to the fall height, slope angle and the effective friction coefficient of the slope surface. Equation (3.13) relates the fall velocity to these three parameters, and Table 3-1 lists values for effective friction coefficients for a number of slope materials determined from equation (3.13) for field measurements of actual rock fall velocities.

5.3.2 Application of e_T to rock fall modeling

Reference to equations (4.20) to (4.24) that define the final velocities and angles for conditions where slip stops during impact, shows that the friction coefficient at the impact point does not directly influence the calculated values of these parameters. The final velocity and angle depends on the normal coefficient of restitution and the size (radius, r) and shape of the body (radius of gyration, k).

As discussed in Chapter 6 on energy losses during impact, the friction coefficient is a component of the equations defining the loss of energy for a rotating body where energy is lost due to friction during the slip phase of the impact process.

6 Energy changes during impacts and trajectories

A rock fall event comprises a series of impacts, each followed by a trajectory. When the velocity and energy that are lost during impact are less than the velocity and energy that are gained during the subsequent trajectory, the rock fall will continue down the slope. However, as the slope angle decreases such that the impacts occur at a steeper angle with the slope surface and the trajectories become shorter, then the energy lost at the point of impact will be greater than the energy gained during the trajectory and the rock fall will come to a stop. For example, the relationship between slope geometry and energy loss is illustrated in Figure 6.1 where a high velocity rock fall on a steep rock face was stopped in a short distance when it impacted a level bench and no significant damage occurred to the building.

A similar situation is shown in Figure 2.8 for the Tornado Mountain case study where the rock fall continued for a slope distance of about 700 m (2,300 ft) where the slope angle was uniform at 30 to 22 degrees, with little reduction in velocity. However, once the rock impacted the level ditch beside the railway, about 70 per cent of the energy was lost and it stopped within a distance of about 30 m or 100 ft (see Figure 9.1).

For any rock fall, each impact and trajectory will be different as the result of variations in the slope properties, slope angle, material type and roughness, and the attitude of the rock at the impact point. These differences in site conditions result in corresponding differences in the translational and rotational velocities at each impact point. Regardless of these velocity variations, the energy changes that occur during a fall comprise a reduction in kinetic energy during impact as a result of compression and friction, followed by an increase in kinetic energy during the trajectory as a result of gravitational acceleration. The rotational energy will also change during impact, but will remain constant during the trajectory.

This chapter discusses changes in the translational and rotational energies that occur during rock falls, and how they can be quantified. This information can be used in the design of rock fall containment structures, such as barriers and fences, with respect to both their location and allowable impact energy capacity. A technique is demonstrated (Section 6.4) in which the potential, kinetic and rotational energies can be partitioned and then plotted for every stage of the rock fall. Such a plot will indicate the lowest energy location along the rock fall path, and the optimum location for the barrier or fence.



Figure 6.1: Rock fall that stopped, just before causing serious damage to a building, when it impacted a horizontal surface that absorbed most of the fall energy

6.1 Impact mechanics theory and kinetic energy changes

This section shows the development of equations defining the changes in kinetic energy that occur during impact. Two cases are considered: first, a non-rotating body impacting the slope in the normal direction, and second, a rotating body impacting the slope at an oblique angle such that energy changes occur in both the normal and tangential directions.

6.1.1 Kinetic energy changes for normal impact, non-rotating body

The theory of impact mechanics addresses the normal force generated in an infinitesimal, deformable particle at the contact point (Figure 6.2a)). As discussed in Chapter 4 (Section 4.1) it was demonstrated that the impact comprises two phases – a compression phase up to the point of maximum compression (impulse = p_{cN}), followed by a restitution phase from the point of maximum compression to the point of separation (impulse = p_{fN}) (Figure 6.2b)). In terms of the kinetic energy changes during impact, energy is absorbed by both the rock and the slope material during compression, and then a portion of this energy is recovered during restitution. The recovered elastic strain energy is converted into kinetic energy, and it is this energy that drives the rock away from the slope. For perfectly elastic materials no energy is lost during

impact, while for perfectly plastic materials all the impact energy is absorbed in compression and the rock fall remains in contact with the slope because no energy is recovered to produce separation (see Figure 4.3).

The process of energy loss and recovery during impact can also be expressed in terms of [deformation, δ – normal force, F] plots, and [normal impulse, p_N – relative velocity, v] plots as shown in Figure 6.2. In Figure 6.2b), the deformation at maximum compression is δ_c , while the deformation at the completion of the impact is δ_f , where $\delta_c > \delta_f$ because, for a partially elastic impact, only part of the deformation is recovered during the restitution phase. The energy associated with each phase of the impact is equal to the area under curve on the [$\delta - F$] plot, with the energy lost during normal compression being E_{cN} , and the energy recovered during normal restitution being $(E_{fN} - E_{cN})$ (Figure 6.2b)). On the [$p_N - v$] plot, these energies are equal to the triangular areas for the impulse at maximum compression p_{cN} and the final impulse p_{fN} (Figure 6.2c).

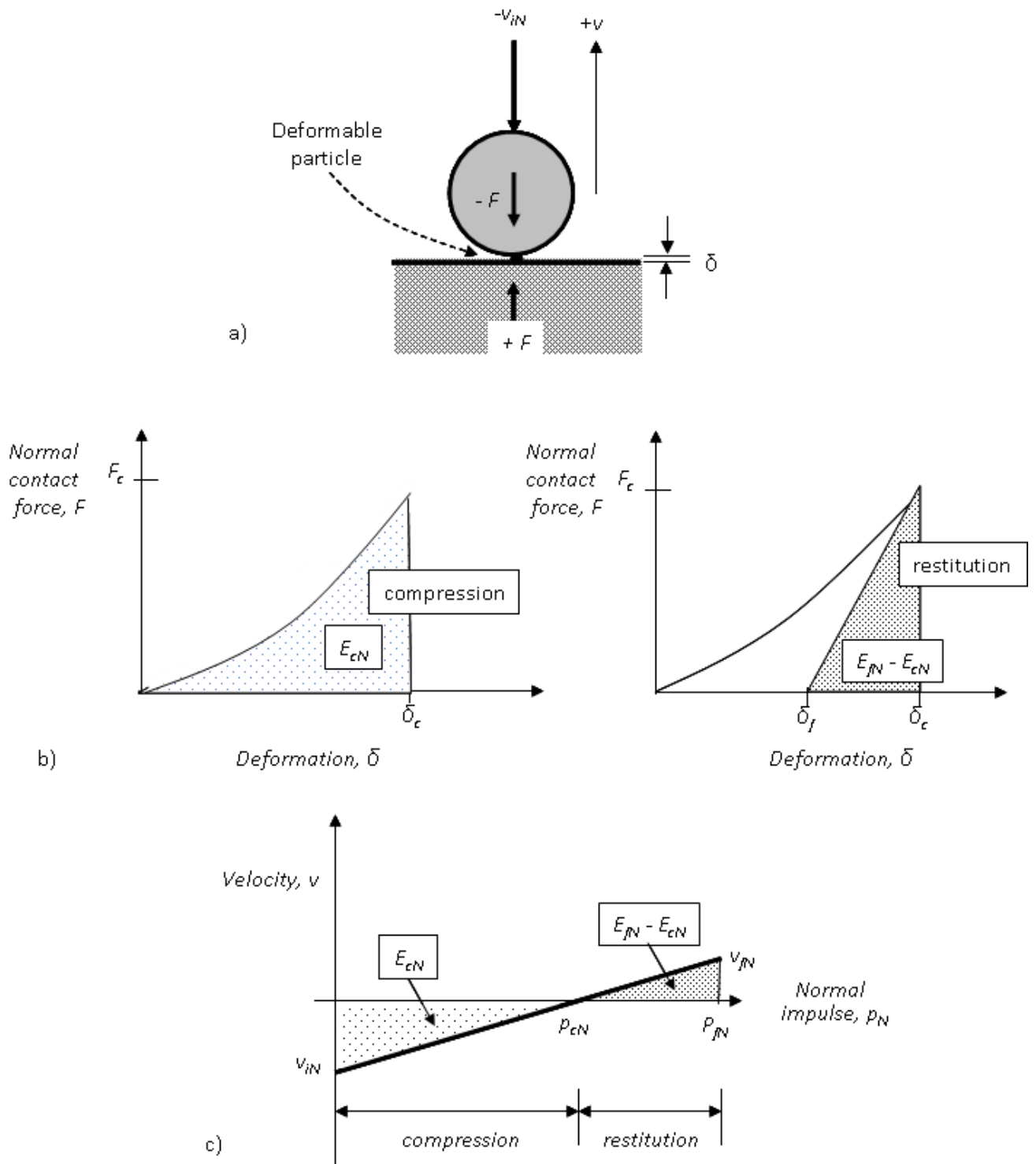


Figure 6.2: Energy changes (normal) during compression and restitution phases of impact. a) Forces generated at contact point during normal impact; b) energy plotted on [force, F – deformation, δ] graph; c) energy changes plotted on [normal impulse, p_N – relative velocity, v] graph

Equations for energy changes during impact can be developed from the $[p_N - v]$ plot illustrated in Figure 6.2c), with the impact process simulated by the infinitesimal deformable particle at the impact point. During impact, the energy E_N generated in the particle by the normal component of the force F_N can be calculated from the relationship between the force and the differential normal impulse: $dp_N = F_N dt = m dv$ (see equation (4.1a)), so that the energy generated from the moment of impact ($p_N = 0$) up to time t and impulse p_N is:

$$E_N = \int_0^t F_N \cdot v dt = \int_0^{p_N} v dp_N \quad (6.1)$$

For the compression phase of the impact up to the impulse p_{cN} , the relationships between impulse and velocity are as follows:

$$v_N = v_{iN} + \frac{p_N}{m} \quad (\text{see equation (4.3)})$$

and the impulse at maximum compression is:

$$p_{cN} = -m \cdot v_{iN} \quad (\text{see equation (4.4)})$$

where v_{iN} is negative because it acts towards the slope in the direction of the $(-N)$ axis (Figure 6.2a)).

Therefore, the energy lost during the compression phase of the impact is given by the area on the $[p_N - v]$ plot between impact ($p_N = 0$) and maximum compression ($p_N = p_{cN}$):

$$\begin{aligned} E_N(p_{cN}) &= \int_0^{p_{cN}} v_N dp_N \\ &= \int_0^{p_{cN}} \left(v_{iN} + \frac{p_N}{m} \right) dp_N \\ &= \left(v_{iN} \cdot p_{cN} + \frac{p_{cN}^2}{2m} \right) \\ &= -\frac{1}{2} m \cdot v_{iN}^2 \end{aligned} \quad (6.2)$$

where v_{iN} is the normal impact velocity and m is the mass of the body.

Equation (6.2) shows that all the impact kinetic energy is lost ($E_N(p_{cN})$ is negative) up to the point of maximum compression, δ_c when the normal velocity is reduced to zero ($v_N = 0$).

A similar approach can be used to find the energy recovered during the restitution phase of the impact, $(E_N(p_f) - E_N(p_c))$ between the impulse at maximum compression (p_{cN}) and the impulse at the end of the impact (p_{fN}). The energy recovered, which is termed the elastic strain energy, is the area on the $[p_N - v]$ plot between these two impulses:

$$\begin{aligned}
 E_N(p_{fN}) - E_N(p_{cN}) &= \int_{p_{cN}}^{p_{fN}} \left(v_{iN} + \frac{p_N}{m} \right) dp_N \\
 &= \left[v_{iN} \cdot p_{fN} + \frac{p_{fN}^2}{2m} \right] - \left[v_{iN} \cdot p_{cN} + \frac{p_{cN}^2}{2m} \right] \\
 &= \frac{m \cdot v_{iN}^2}{2} \left(1 - \frac{p_{fN}}{p_{cN}} \right)^2
 \end{aligned} \tag{6.3}$$

Derivation of this equation is shown in Appendix B, equation (B.9). Alternatively, the elastic strain energy can be calculated from the area of the restitution triangle between impulse values p_{cN} and p_{fN} on Figure 6.1c). Derivation of equation (6.3) from the area of this triangle is also shown in Appendix D (equation D.3).

Equations (6.2) and (6.3) together define the net energy loss during normal impacts as;

$$\begin{aligned}
 E_N(\text{net}) &= [\text{energy lost in compression}] + [\text{energy gained in restitution}] \\
 &= [E_N(p_{cN})] + [E_N(p_{fN}) - E_N(p_{cN})] \\
 &= -\frac{m \cdot v_{iN}^2}{2} + \frac{m \cdot v_{iN}^2}{2} \left(1 - \frac{p_{fN}}{p_{cN}} \right)^2 \\
 &= -\frac{m \cdot v_{iN}^2}{2} \left[1 - \left(1 - \frac{p_{fN}}{p_{cN}} \right)^2 \right]
 \end{aligned} \tag{6.4}$$

Equation (4.12) defines the relationship between normal impulses p_{fN} , p_{cN} and the normal coefficient of restitution e_N , as:

$$p_{fN} = -m \cdot v_{iN} (1 + e_N) = p_{cN} (1 + e_N) \tag{4.12}$$

and

$$\frac{p_{fN}}{p_{cN}} = (1 + e_N)$$

and

$$e_N^2 = \left(1 - \frac{P_{fN}}{P_{cN}} \right)^2$$

Substitution of equation of (4.12) into equation (6.4) gives the following expression for the net energy loss during normal impact:

$$E_N(\text{net}) = -\frac{1}{2} m \cdot v_{iN}^2 (1 - e_N^2) \quad (6.5)$$

In the development of equation (6.5) for normal impact, the value of the normal coefficient of restitution, e_N is always less than 1 because it is defined by the energy losses for a non-rotating body. In contrast, Figures 5.5 and 5.7 show the conditions that result in $e_N > 1$, that is, when a rotating body impacts the slope at a shallow angle, $\theta_i < 15$ degrees approximately. Therefore, for shallow impact of a rotating, rough body, e_N may be greater than 1, but energy will be lost for the overall impact because energy is also lost in the tangential component of impact.

Worked example 6A – energy loss for normal impact: as an illustration of the application of equation (6.5), consider the test to determine the value of e_N for concrete shown in Figure 5.6. If the block of rock is dropped vertically on to the concrete from a height of 5 m, then $v_{iN} = \sqrt{2gh} = 9.9 \text{ m} \cdot \text{s}^{-1}$. The tests described in Figure 5.6 show that $e_N = 0.18$ for these conditions, so that $(1 - e_N^2) = 0.97$. If the block mass is 1000 kg, then the impact kinetic energy is $\frac{1}{2} m \cdot v_{iN}^2 = 49 \text{ kJ}$, and the net energy loss, $E_N(\text{net}) = -49 \times 0.97 = -47.5 \text{ kJ}$, or 97 per cent of the impact energy.

In energy calculations it is necessary to use the mass and not the weight of the body. That is, the unit weight of rock is generally equal to $26 \text{ kN} \cdot \text{m}^{-3}$, or 1 cu. m. of rock weighs 26000 N. Since weight is a force, the mass is related to the weight by the gravitational acceleration, $g = 9.81 \text{ m} \cdot \text{s}^{-2}$, and the mass of 1 cu. m. of rock is $26000/9.81 = 2650 \text{ kg}$.

6.1.2 Kinetic energy changes for inclined impact, rotating body

The usual impact condition for a rock fall is an oblique impact of the body with the slope, with the body rotating in the negative direction, i.e., the peripheral velocity ($-r \cdot \omega_i$) is in the direction opposite to the positive tangential axis. Calculation of the energies lost during compression, and gained during restitution, uses the same principles as shown in Figure 6.2, and described in Section 6.1.1 for normal impact of a non-rotating body. However, for oblique impact of a rotating body, energy losses occur to the normal and tangential components of kinetic energy, as well as the rotational energy.

The kinetic energy changes are separated into the normal and tangential components, with the normal component comprising loss of energy up to the point of maximum compression, δ_c followed by partial recovery during restitution at the final compression δ_f ($\delta_f < \delta_c$). In the tangential direction, energy is lost throughout the impact process as the result of friction acting at the contact point defined by the friction coefficient μ . These energy changes can then be combined to find the net kinetic energy loss during impact.

The energy calculations assume that the direction of slip is constant throughout the impact, which occurs if the initial slip velocity (v_{is}) is large so that slip does not halt during contact, or the initial slip velocity is zero. For rock falls, this assumption is valid because of the high friction at the impact points combined with the generally high tangential velocity component that generates spin in the negative direction as demonstrated in Figure 6.3.

Normal component of energy loss – the equation defining the normal velocity v_N at any time during oblique impact of a rotating body is given in Appendix C which shows that v_N is related to inertial coefficients β , the friction coefficient μ and the mass of the body m :

$$v_N = v_{iN} + \frac{(\beta_3 + \mu \cdot \beta_2)p_N}{m} \quad (C.15b)$$

where inertial coefficients β_2 and β_3 are as defined in Appendix C.1, equations (C.11); inertial coefficients are defined by the size (radius, r) and shape (radius of gyration, k) of the rotating body.

At the point of maximum compression when the body is momentarily stopped, $v_N = 0$ at impulse p_c (Figure 6.2c)). Therefore,

$$p_{cN} = \frac{-m \cdot v_{iN}}{(\beta_3 + \mu \cdot \beta_2)} \quad (6.6)$$

The partial energy lost during the period of compression from the time of impact ($p_N = 0$) up to impulse at maximum compression ($p_N = p_{cN}$) is determined by integration of the area on the [p_N – v] plot:

$$\begin{aligned} E_N(p_{cN}) &= \int_0^{p_{cN}} v_N dp_N \\ &= \int_0^{p_{cN}} \left(v_{iN} + \frac{(\beta_3 + \mu \cdot \beta_2)p_N}{m} \right) dp_N \end{aligned}$$

$$\begin{aligned}
 &= \left[v_{iN} \cdot p_{cN} + \frac{(\beta_3 + \mu \cdot \beta_2) p_{cN}^2}{2m} \right] - [0] \\
 &= \frac{-m \cdot v_{iN}^2}{(\beta_3 + \mu \cdot \beta_2)} + \left(\frac{(\beta_3 + \mu \cdot \beta_2)}{2m} \right) \left(\frac{-m \cdot v_{iN}}{(\beta_3 + \mu \cdot \beta_2)} \right)^2 \\
 &= \frac{-m \cdot v_{iN}^2}{(\beta_3 + \mu \cdot \beta_2)} \tag{6.7}
 \end{aligned}$$

The same approach can be taken to find the partial energy recovered during restitution, determined by integration of the area on the $[p_N - v]$ plot between impulses p_{cN} and p_{fN} :

$$\begin{aligned}
 E_N(p_f) - E_N(p_c) &= \int_{p_{cN}}^{p_{fN}} v_N dp_N \\
 &= \int_{p_{cN}}^{p_{fN}} \left(v_{iN} + \frac{(\beta_3 + \mu \cdot \beta_2) p_N}{m} \right) dp_N \\
 &= \left[v_{iN} \cdot p_{fN} + \frac{(\beta_3 + \mu \cdot \beta_2) p_{fN}^2}{2m} \right] - \left[v_{iN} \cdot p_{cN} + \frac{(\beta_3 + \mu \cdot \beta_2) p_{cN}^2}{2m} \right] \\
 &= v_{iN} (p_{fN} - p_{cN}) + \left[\frac{(\beta_3 + \mu \cdot \beta_2)}{2m} \right] (p_{fN}^2 - p_{cN}^2)
 \end{aligned}$$

From equations (B.15b) and (4.4),

$$v_{iN} = -\frac{(\beta_3 + \mu \cdot \beta_2)}{m} p_{cN}$$

Therefore:

$$E_N(p_{fN}) - E_N(p_{cN}) = \frac{(\beta_3 + \mu \cdot \beta_2)}{2m} (p_{fN} - p_{cN})^2 \tag{6.8}$$

The net normal kinetic energy loss during impact is found by adding equations (6.7) and (6.8) where:

$$E_N(\text{net}) = [\text{energy lost in compression}] + [\text{energy gained in restitution}]$$

Tangential component of energy loss – because shearing occurs during the rock/slope contact for an oblique impact, a frictional force is generated at this point. The tangential component of

the reaction force is in the opposite direction to the slip direction, and the tangential velocity reduces from the impact value v_{iT} to a final velocity of v_{fT} as shown on Figure 6.3a). The uniform velocity reduction during impact assumes that the body slips throughout the impact (see Section 4.5). This reduction in velocity results in a loss of energy during the impact defined by the triangular area on Figure 6.3a) follows:

$$E_T(p_f) = \int_0^{p_f} v_T dp$$

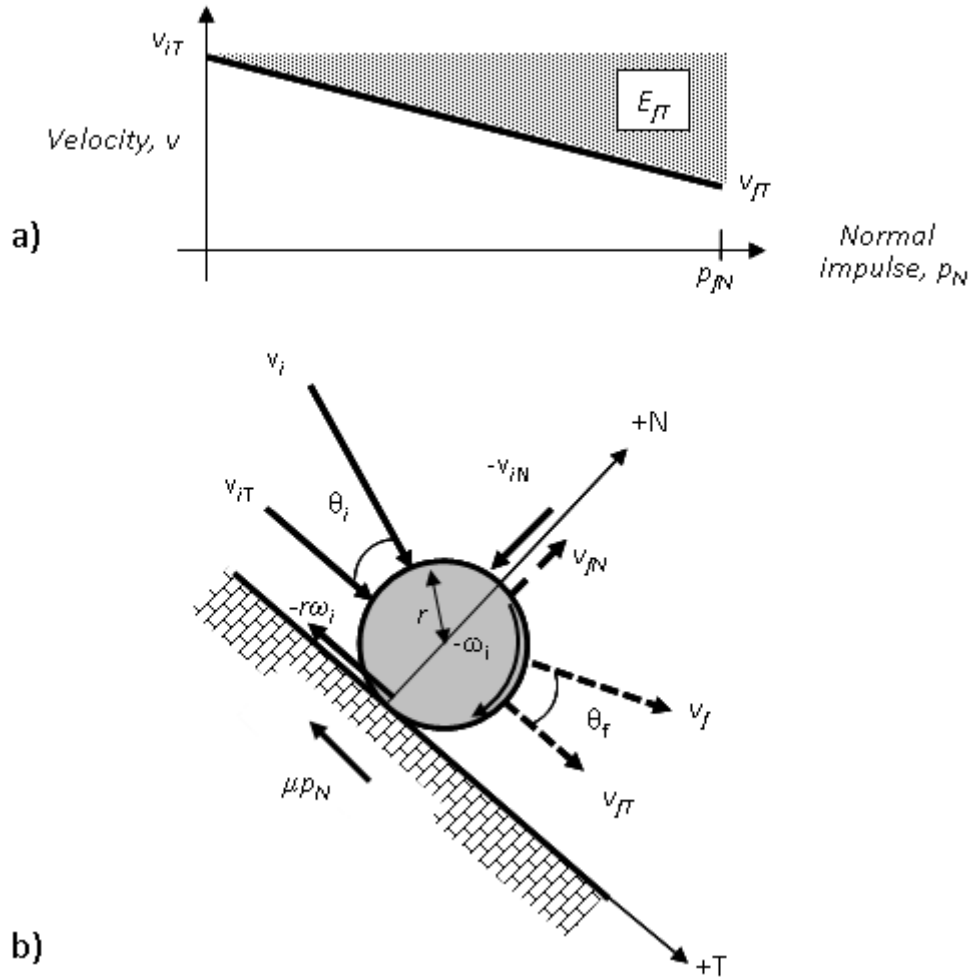


Figure 6.3: Reduction in tangential velocity, v_T during impact. a) $[p_N - v]$ diagram showing change in v_T during impact, and corresponding reduction in energy, E_T ; b) changes in velocity components

According to Coulomb's definition of friction, the coefficient of friction μ is the ratio of the tangential to normal impulses or forces acting at the contact point, and the relationship between the impulse components is as follows:

$$dp_T = -\mu dp_N \tag{4.14a}$$

The negative sign denotes that the friction force acts in the opposite direction to the positive tangential impulse.

The equation defining the tangential velocity v_T at any time during oblique impact of a rotating body is given in Appendix C which shows that v_T is related to inertial coefficients β_1 and β_2 , the friction coefficient μ and the mass of the body m as follows:

$$v_T = v_{iT} - \frac{(\beta_2 + \mu \cdot \beta_1) p_N}{m} \quad (\text{C.15a})$$

where inertial coefficients β_1 and β_2 are as defined in Section B.1, equations (B.11); inertial coefficients are defined by the size (r) and shape (k) of the rotating body.

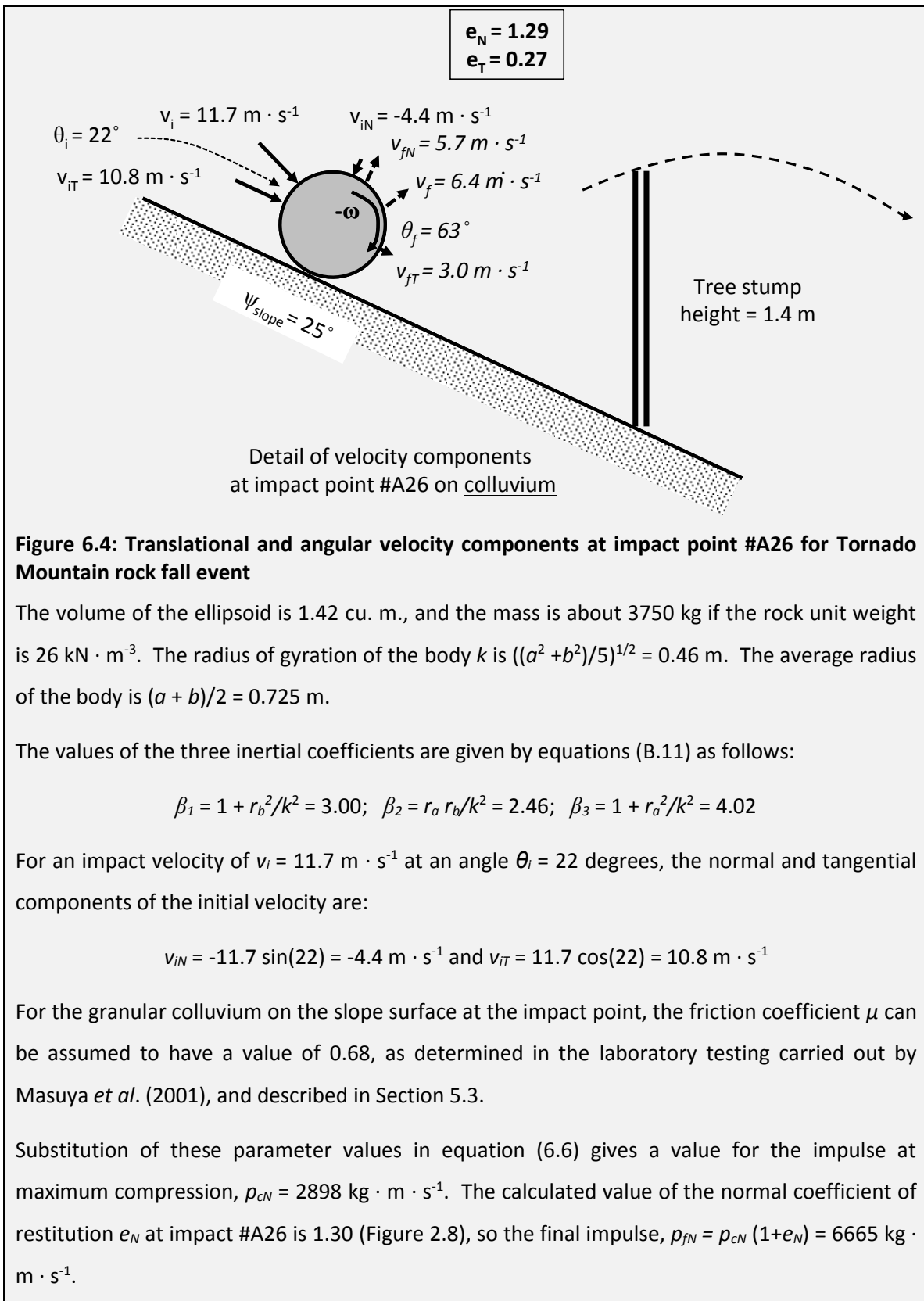
The energy lost by the tangential component of impulse is:

$$\begin{aligned} E_T(p_{fN}) &= -\mu \int_0^{p_{fN}} v_T dp_N \\ &= -\mu \int_0^{p_{fN}} \left(v_{iT} - \frac{(\beta_2 + \mu \cdot \beta_1) p_N}{m} \right) dp_N \\ &= -\mu \left[v_{iT} \cdot p_{fN} - \frac{(\beta_2 + \mu \cdot \beta_1) p_{fN}^2}{2m} \right] \\ &= -\frac{\mu \cdot p_{fN}}{2} \left(2v_{iT} - \frac{(\beta_2 + \mu \cdot \beta_1) p_{fN}}{m} \right) \end{aligned} \quad (6.9)$$

The net kinetic energy loss during impact, comprising normal and tangential energy components, can be found by adding equations (6.7), (6.8) and (6.9).

Worked example 6B – energy loss for oblique impact: as an illustration of the application of energy loss equations (6.7) to (6.9), consider the case study of the rock falls on Tornado Mountain as described in Section 2.2.1 with the impact and restitution velocity components shown in Figure 2.8 for impact #A26. The boulder was assumed to be an ellipsoid with semi-major axes as follows:

$$a = 0.8 \text{ m}; b = 0.65 \text{ m and } c = 0.65 \text{ m, where the body is rotating about axis } c.$$



Using these values for impulses p_{fN} and p_{cN} , the changes in energy at impact #A26 are calculated as follows:

$$E_N(p_c) = -12.9 \text{ kJ}; \quad E_N(p_f) - E_N(p_c) = 10.7 \text{ kJ}; \quad E_T(p_f) = -31.3 \text{ kJ}$$

and the net energy loss during impact due to changes in translational velocities, is equal to the sum of these energy changes, $\Delta E = -33.5 \text{ kJ}$.

6.2 Rotational energy gains/losses

The rotational energy E_r of a falling body depends on its mass and shape as defined by its moment of inertia I , and the angular velocity ω , as follows:

$$E_r = \frac{1}{2} I \cdot \omega^2 \quad (6.10)$$

As an example of measured angular velocities of rock falls, Section 3.4.1 (Figure 3.10) describing the Ehime test site in Japan shows that ω first increases with the fall distance and then tends to a terminal velocity in the range of about 15 to 35 $\text{rad} \cdot \text{s}^{-1}$. Furthermore, the angular velocity may increase or decrease during impact depending on the geometry of the impact, so the rotational energy may also increase or decrease during impact.

Based on equation (6.10), where the angular velocity changes from ω_i at the point of impact to ω_f at the termination of impact, the change in rotational energy during impact is:

$$E_r = -\frac{1}{2} I (\omega_i^2 - \omega_f^2) \quad (6.11)$$

Worked example 6C – change in rotational energy: as an illustration of the application of equations (6.10) and (6.11), consider rock fall impact #A26 at Tornado Mountain discussed in the previous section. This body was assumed to be an ellipsoid with semi-axes of $a = 0.8 \text{ m}$, $b = 0.65 \text{ m}$ and $c = 0.65 \text{ m}$, and mass, m of approximately 3750 kg. The moment of inertia of an ellipsoid rotating about axis c is (see Table 4.1):

$$I = \frac{m}{5} (a^2 + b^2) = 797 \text{ kg} \cdot \text{m}^2 \quad (6.12)$$

No measurements of the angular velocity are available for this fall. However, an approximate value for the angular velocity can be obtained from equation (3.17) where a relationship

between the angular velocity ω , the final translational velocity v_f and the radius r of the body has been developed from the measurements of the angular velocity of test rocks. That is,

$$\omega_f \approx \frac{v_f}{r} \quad (3.17)$$

If the radius $r = 0.725$ m, and the final translational velocity, $v_{f(A26)} = 6.4 \text{ m} \cdot \text{s}^{-1}$ (Figure 2.8), then the final angular velocity, $\omega_{f(A26)} = -8.8 \text{ rad} \cdot \text{s}^{-1}$.

The impact angular velocity at #A26, $\omega_{i(A26)}$ is equal to the final angular velocity at impact point #A25, equal to $\omega_{i(A25)}$, because the angular velocity does not change during the trajectory from #A25 to #A26. Trajectory calculations for the rock fall show that the final velocity at #A25 was $v_{f(A25)} = 8.07 \text{ m} \cdot \text{s}^{-1}$, and from equation (3.17), $\omega_{i(A26)} = -11.1 \text{ rad} \cdot \text{s}^{-1}$. Based on these translational velocity parameters, the angular velocity decreased from -11.1 to $-8.8 \text{ rad} \cdot \text{s}^{-1}$ during impact #A26. From equation (6.11), the change in rotational energy during the impact is

$$\begin{aligned} \Delta E_r &= -\frac{1}{2} 797 ((-11.1)^2 - (-8.8)^2) \\ &= -18.3 \text{ kJ} \end{aligned}$$

6.3 Total energy losses

The total energy loss during impact is the sum of the translational and rotational energy losses. Referring to the calculated energy losses for Tornado Mountain impact #A26 that are calculated in Worked examples 6B and 6C above, the total energy loss is equal to:

$$\Delta E = \Delta KE + \Delta RE = (-33.5) + (-18.3) = -51.8 \text{ kJ}$$

These calculations show that the rotational energy loss is about 35 per cent of the total energy loss; the field data (Chapter 2) shows that this ratio between the kinetic and rotational energies is typical for rock falls.

The theoretical energy losses calculated using impact mechanics as described in Sections 6.1 and 6.2 and demonstrated in Worked examples 6A, 6B and 6C, can be compared with the change in kinetic energy, ΔKE calculated from the initial and final velocities for impact #A26 as shown in Figure 6.4 where $v_i = 11.7 \text{ m} \cdot \text{s}^{-1}$ and $v_f = 6.4 \text{ m} \cdot \text{s}^{-1}$.

$$\Delta KE = -\frac{1}{2} m (v_i^2 - v_f^2) = -\frac{1}{2} 3750 (11.7^2 - 6.4^2) = -180 \text{ kJ}.$$

These values for the theoretical and field net energy losses show that the theoretical value calculated from impact mechanics theory is less than the actual energy losses. That is, for the translational velocities, the theoretical energy loss is only 19 per cent ($-33.5/-180 = 0.19$) of the actual energy loss, or for the combined kinetic and rotational energies, the theoretical energy loss is about 29 per cent ($-51.8/-180 = 0.29$) of the field value. It is expected that this difference is because the impact mechanics theory does not fully account for the plasticity that occurs in actual rock fall impact, or the loss of mass due to fragmentation of the block (see Section 6.5).

For impacts in the other case studies described in Chapter 2, the theoretical energy losses are also less than the actual energy losses, with the differences being similar to those for Tornado Mountain impact #A26. Furthermore, the differences between the theoretical and actual energy losses shows no apparent relationship to the type of slope material, although further studies of the available data may provide information on a factor to be included in the energy loss equations to account for the plastic deformation at the impact points.

6.4 Energy loss diagrams

One of the design requirements of rock fall protection structures is locating the structure where the rock fall energy is at a relatively low value along the rock fall path. The general behavior of rock falls with respect to energy changes during the series of impacts and trajectories is as follows:

- Potential energy (*PE*) will decrease continuously during the fall in proportion to the loss of elevation;
- Translational kinetic energy (*KE*) will decrease during impact in proportion to the reduced velocity, as a result of compression of the slope material in the normal direction, and frictional losses in the tangential direction;
- Rotational energy (*RE*) may decrease or increase during impact depending on the attitude of the body at the point of impact (see Figure 3.11);
- Translational energy will increase during the trajectory phases of the fall as the result of gravity acting on the body to increase the vertical velocity component;
- Rotational energy will remain constant during trajectories because no rotational forces act on the body when it is moving through the air.

It is assumed that no energy losses due to air friction occur during trajectories because they would be very small compared to impact energy losses. Also, gravity effects during impacts can be ignored because reaction forces are large compared to the body force and act for a very short time, and no significant change in the position of the body occurs during impact.

These energy changes during a rock fall can be illustrated on energy loss diagrams, of which two types are discussed in the following sections.

6.4.1 Energy partition diagram for potential, kinetic and rotational energies

At the moment that a rock fall detaches from the slope, it will possess potential energy equal to

$$PE = m \cdot g \cdot h \quad (6.13)$$

where m is the mass of the body, g is the gravitational acceleration and h is the total fall height. As the body falls during the first trajectory, the potential energy is converted into kinetic energy that increases as the body accelerates. At the first impact point, the velocity decreases as the slope deforms and the body slips, causing the kinetic energy to decrease. Also at the impact point, the body starts to rotate and gain rotational energy as the result of friction forces acting on the periphery of the body. Once the body leaves the slope, the translational velocity and kinetic energy increase due to gravitational acceleration, while the angular velocity remains constant. This sequence of events is repeated with each impact.

Figure 6.5 illustrates an energy partition diagram for a cubic concrete block at the Ehime test site in which the PE , KE , RE are all represented at each every impact point and during each trajectory. The vertical axis shows the overall vertical height of the fall from the source, with the elevation of each impact point defined. The horizontal axis shows the partition of the energy throughout the fall, with the maximum value equal to the potential energy at the source; the potential energy decreases continually during the fall. At each impact point, the decrease in velocity, and corresponding kinetic energy loss, is represented by the decrease in the width of the KE area. The rotational energy area remains constant during trajectories, but for this test the rotational energy increases with each impact as shown by the increase in width of the area representing RE during impact. The relative widths of the KE and RE bands indicate the low ratio between RE and KE .

The area between the potential energy area and the combined kinetic-rotational area represents the cumulative energy loss at the impact points that becomes wider with each impact. All the energy has been dissipated when the rock stops moving.

The value of the energy partition diagram is that it enables low energy locations on the slope to be identified that are the optimum locations for rock fall fences or barriers. That is, energy will be high on the steep, upper part of the face but will diminish as the slope angle is reduced. Also, the trajectories will be close to the ground on the lower slope, which will limit the height of protection structures.

Another factor to consider in the location of fences or barriers is to find areas immediately after an impact point where the kinetic energy has been lost during impact and before gravity has caused the velocity to increase during the next trajectory. Impact points will often occur on benches where rock falls accumulate.

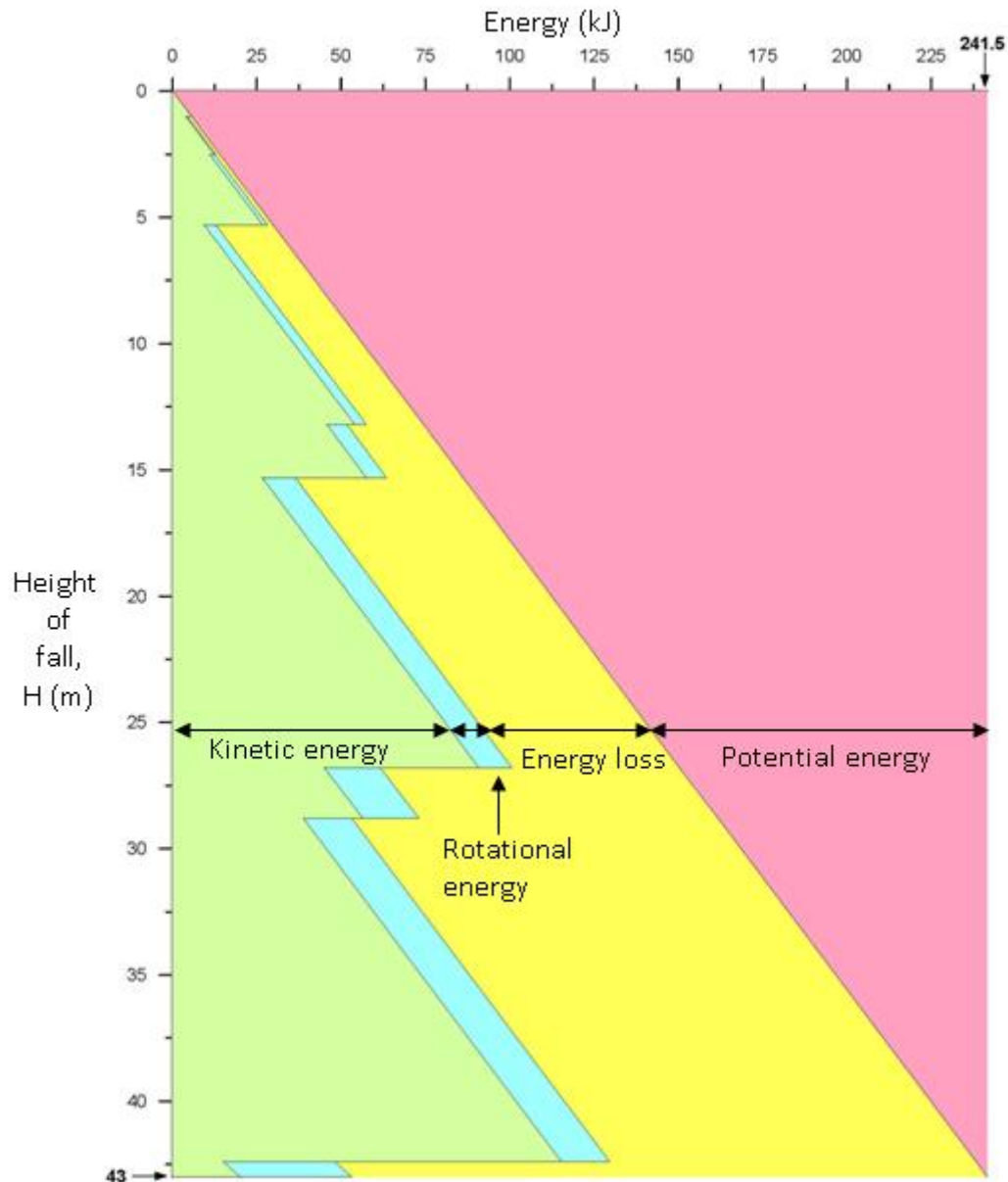


Figure 6.5: Energy loss diagram for cubic, concrete block with constant mass at Ehime test site, Japan – see Figure 2.6 (Ushiro et al., 2001)

6.4.2 Energy head

An alternative method of showing the progressive energy loss for a series of impacts is to plot the “energy head”, given by:

$$E = z + \frac{v^2}{2g} \quad (6.14)$$

where z is the body elevation and v is the length of the velocity vector (Hung and Evans, 1988).

A plot of energy head comprises a horizontal line during each trajectory where the energy head

is constant, and a drop in the energy head representing the loss of energy at each impact point. Plots of this type have been used to show the transition from trajectory to rolling phase of rock falls where the slope of the energy line equals the coefficient of rolling friction for the slope material.

6.5 Loss of mass during impact

The energy change calculations discussed previously in this chapter all assume that the mass of the rock fall remains constant throughout the fall. In reality, falls will break up to some extent at the impact points so that the final mass will be less than the mass at the source. Possible reasons for breakup of the body are that the initial block contains planes of weakness along which fracture can readily occur during impact with the slope. Also, the initial body may have an irregular form that will progressively break down into a more uniform spherical or ellipsoidal shape that will spin and bounce more readily than an elongated shape.

Quantitative information on the loss of mass during the course of a rock fall can be obtained from studies carried out in Italy (Nicolla *et al.*, 2009), and from the Tornado Mountain rock fall site described in Section 2.2.1. The Italian studies involved two natural rock fall sites where previous events could be observed, as well as a test site where the falls were carefully documented. These data have been used to develop a relationship between the body size and the distance travelled from the source.

A summary of the two Italian rock fall sites and the Tornado Mountain case study described in Chapter 2 is as follows:

- **Camaldoli Hill, Naples** – the slope geometry at the rock fall locations comprised a 200 m (660 ft) high upper rock slope at an overall angle of about 56 degrees, above a 60 m (200 ft) high talus slope at an angle of 37 degrees. The maximum horizontal fall distance was about 200 m (660 ft). The rock forming the cliff is a tuff (Neapolitan yellow tuff) of varying composition that had a uniaxial compressive strength up to about 10 MPa and deformation modulus of about 10 GPa. The rock contains sets of sub-vertical joints that are parallel and normal to the slope, and a sub-horizontal joint set that dips at 5 to 38 degrees and forms the base of columnar blocks. The joint spacing has a maximum value of about 3 to 5 m (10 to 15 ft) which defines the maximum block size.

Block sizes were assessed by mapping the dimensions of blocks in-place on the cliff face, and of fallen blocks on the slope. A total of 298 blocks were mapped on the face with volumes ranging from 1 cu. m (1.3 cu. yd) to 50 cu. m (65 cu. yd), with about 34 per cent of the blocks having volumes less than 2.5 cu. m. (3.3 cu. yd). A total of 120 fallen blocks were mapped, of which 96 per cent had volumes less than 5 cu. m (6.6 cu. yd) indicating the fragmentation of blocks during falls.

In addition to the natural falls, a test was conducted on a slope with similar geometry where images of the falls were analyzed to determine the approximate size of blocks before and after impact. The initial volumes of the test blocks ranged from 1 to 12 cu. m (1.3 to 16 cu. yd).

- **Monte Pellegrino, Palermo** – the slope geometry comprised a 100 m (330 ft) high slope at a face angle of about 42 degrees gradually flattening to a slope angle of 23 degrees; the maximum vertical fall height was 290 m (950 ft) and the horizontal distance was about 300 m (980 ft). The rock forming the cliffs is a strong, blocky limestone with a compressive strength of about 100 MPa and a modulus of about 100 GPa.

Similarly to the Camaldoli Hill site, block sizes were measured *in situ* and on the run-out area. Most of the *in situ* blocks had volumes up to 2.5 cu. m (3.3 cu. yd), with the largest volume being about 27 cu. m (35 cu. yd), while 87 per cent of the fallen blocks had volumes of less than 5 cu. m (6.6 cu. yd).

- **Tornado Mountain, Canada** – at this site where the two separate rock fall paths were clearly distinguishable on the slope, it was possible to measure the final dimensions of the rock fall, as well as fragments that had broken from the block at specific impact locations (see Figure 2.7). It was not possible to access the source area on a steep rock face to measure the dimensions of the original rock falls. However, from observations of the size of the clearly visible source area, and of the very strong, massive limestone forming the slope it is estimated that the original rock falls had volumes in the range of 30 to 50 cu. m (40 to 65 cu. yd).

The Italian field data were used to develop the following relationship between the volume of the source rock fall Ω_0 , and the volume Ω at any horizontal distance x from the source:

$$\frac{\Omega}{\Omega_0} = \frac{1}{(1 + x \cdot \lambda)} \quad (6.15)$$

where λ (m^{-1}) is a reduction coefficient defining the loss of mass with distance fallen.

Figure 6.6 shows the values of the coefficient λ defining the envelopes of loss of mass data for the Mt. Pellegrino and Camaldoli Hill rock fall sites. For the Mt. Pellegrino data, the values of λ are in the range of 0.0035 and 0.01 m^{-1} , while for the Camaldoli Hills, the values of λ values are in the range of 0.008 to 0.02 m^{-1} . These results demonstrate that as much as 80 per cent of the original rock mass is lost during the course of the rock fall, with most of this loss probably occurring in the first few impacts where the rock is falling fast down the steep face, and the irregular shape is broken down at the impact points. Also, the initial impacts may be on the rock face where more fragmentation may occur compared to the talus or soil lower on the slope.

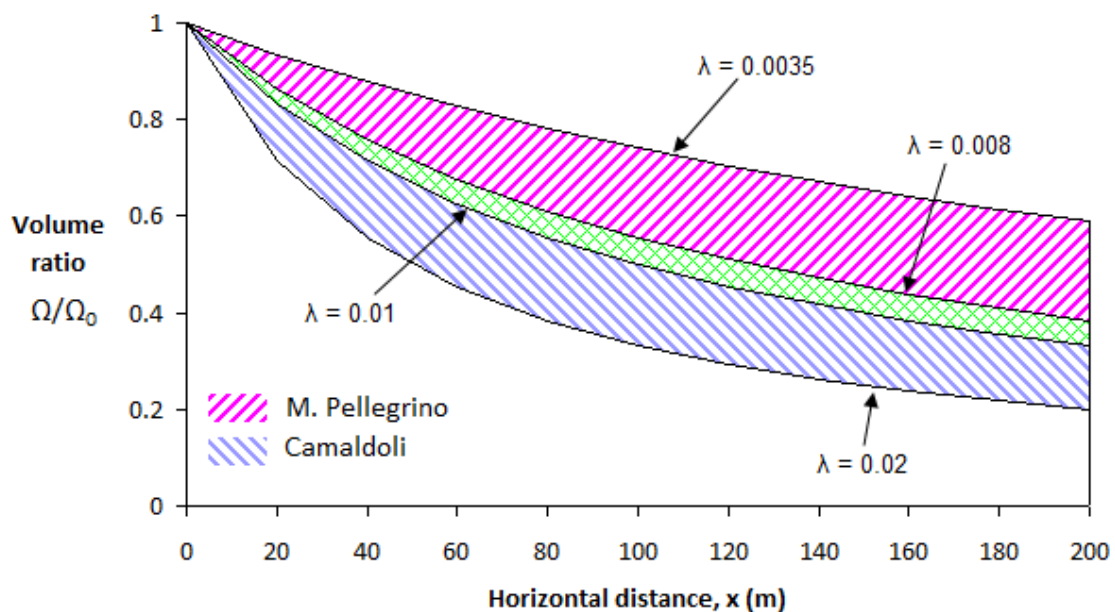


Figure 6.6: Plot of horizontal rock fall distance x against loss of volume ratio, Ω/Ω_0 showing ranges of values of λ for data from Mt. Pellegrino and Camaldoli Hills (Nicolla *et al.*, 2009)

It is of interest that the limestone at Mt. Pellegrino is an order of magnitude stronger than the tuff in the Camaldoli Hills and that the reduction in mass is less at Mt. Pellegrino than at the Camaldoli Hills. These results indicate that the values of λ may have a relationship with the rock strength.

For the Tornado Mountain rock fall site (see Section 2.2), the dimensions of selected rock fragments broken off the main rock fall in the lower part of the slope were recorded, together with the corresponding impact number. For rock fall A, where the final volume was about 1.42 cu. m (1.86 cu. yd) (mass = 3750 kg) (8,300 lb), it was estimated that fragments with a total volume of about 8 cu. m (10.5 cu yd) broke off the body after impact #A10, of which a total of

ten blocks with a total volume of about 2 cu. m (2.6 cu. yd) broke off between impacts #26 and #31. It was not possible to distinguish rock fragments from above impact #A10, but it is expected that much of the loss of volume occurred early in the fall where the rock fell 40 m (130 ft) on to a bare rock bench. Using this data, the following approximate relationship was developed between the volume $\Omega_{(n)}$ at impact number n , the initial volume $\Omega_{(0)}$:

$$\frac{\Omega_{(n)}}{\Omega_{(0)}} = n^{-0.8} \quad (6.16)$$

Equation (6.16) shows that if $\Omega_{(46)} = 1.42$ cu. m (2 cu. yd) after 46 impacts, then the original volume $\Omega_{(0)}$ was about 30 cu. m (40 cu. yd); a rock fall with this volume is feasible for this strong, massive limestone. That is, about 95 per cent of the original rock volume was lost during this fall over a total horizontal distance of about 610 m (2,000 ft).

In order to compare the results of equations (6.15) for the Italian data and (6.16) for the Tornado Mountain events, the positions of the impacts at Tornado were converted into horizontal distances from the source x , with the fall stopping at a distance of $x = 610$ m (2,000 ft), and the ratio $\Omega/\Omega_0 = 1.42/30 = 0.047$. Substitution of these values into equation (6.15) gives a value for the reduction coefficient λ , of 0.03, and a curve on slightly below those show on Figure 6.6. It is considered that this value for λ is consistent with the Italian data considering the relatively limited information available at Tornado Mountain.

The loss of volume (and mass) during the course of rock falls obviously has an effect on the potential, kinetic and rotational energy losses. While the energy partition diagram in Figure 6.5 shows the loss of energy for each impact at the Ehime test site for a constant mass, Figure 6.7 shows the loss of energy for the mass decreasing at each impact point according to the relationship given in equation (6.15).

The test block was a cubic-shaped concrete body with side dimensions of 0.6 m (2 ft), and an initial volume, $\Omega_0 = 0.22$ m³ (0.30 yd³) (mass = 520 kg) (1150 lb), and the total horizontal (x) distance travelled was 57 m or 190 ft (Figure 2.6). Assuming a reduction factor of $\lambda = 0.02$, the decrease in volume is calculated using equation (6.15), for a final volume of 0.1 m³ (0.1 yd³).

Figure 6.7 shows details of the changes in potential, kinetic and rotational energy for the fall at the Ehime test site in Japan described in Section 2.2 for a mass that reduces with each impact according to equation (6.15), from an initial volume of 0.22 m³ (0.3 yd³) to a final volume of 0.1

m³ (0.13 yd³). In preparing the plot shown in Figure 6.7, the calculated progressively reduced mass at each impact during the fall was used to calculate the corresponding reduced values of the potential and kinetic energies, as well as the reduced moment of inertia of the body to calculate the changes in rotational energy (see equation (6.10)). For a cubic body with side length L , the moment of inertia, I is given by (see Table 4-1):

$$I = m \frac{L^2}{6}$$

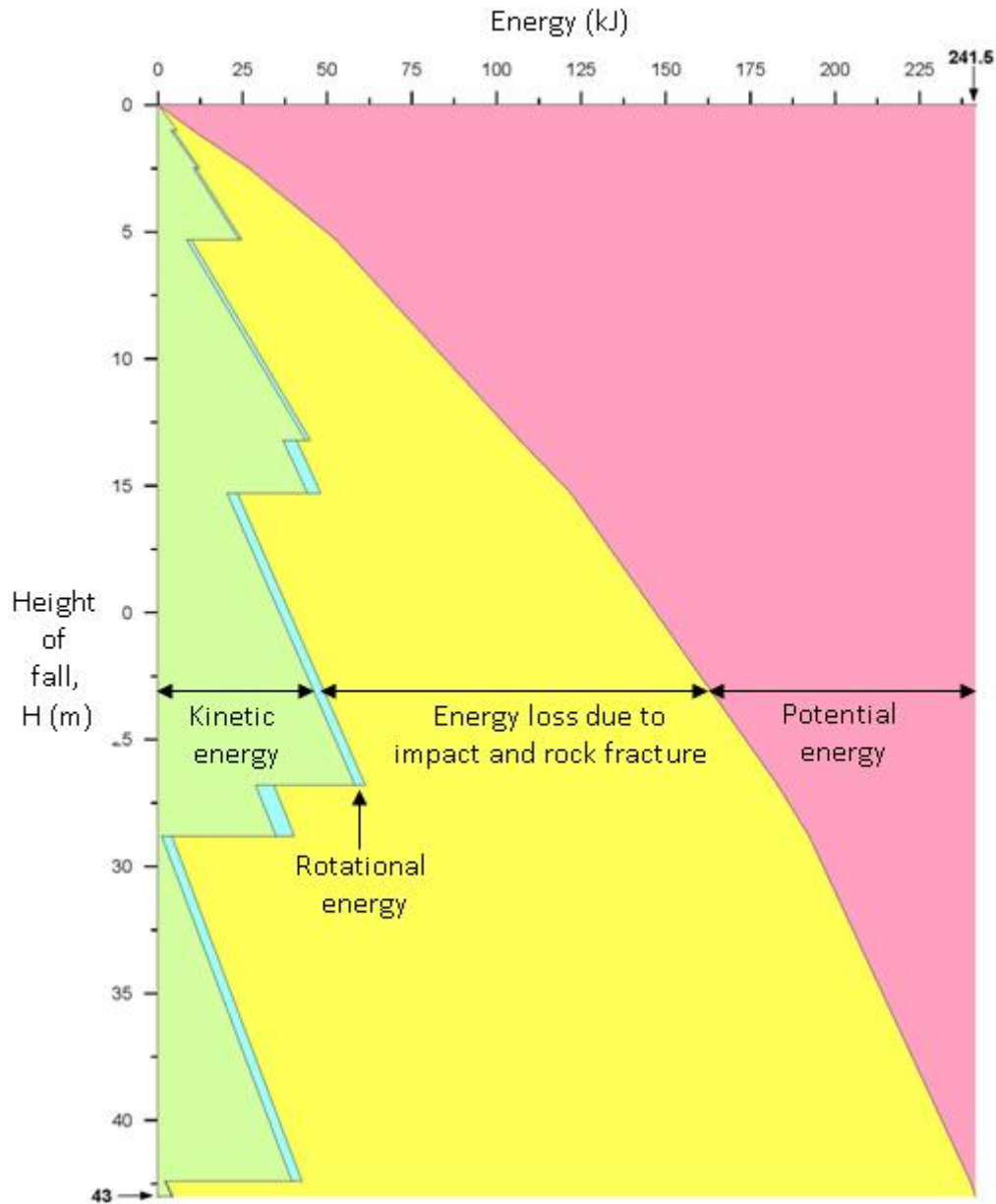


Figure 6.7: Energy partition plot for diminishing mass at the Ehime rock fall test site – cubic concrete block with initial side length 0.6 m (2 ft)

Comparison of the two sets of energy partition lines shown in Figures 6.5 and 6.7 clearly demonstrate the effect of the rock mass diminishing during the fall, assuming that the translational velocities at the impact points are the same for each case. The increased width of the energy loss area on Figure 6.5 compared to Figure 6.7 represents the energy required to fracture the falling rock.

An application of the concept of rock mass loss during falls, is in the design of rock fall fences. For a fence located at some distance from the source, the impact energy will be less than for a fence located close to the source.

6.6 Effect of trees on energy losses

Rock falls often occur on forested slopes because falls occur in wet, cold climates that are conducive to tree growth, and falls are triggered by water and ice pressures. Also, growth of tree roots in cracks can be a triggering mechanism as discussed in Section 1.4.

Studies have been carried out in both Japan (Masuya, *et al.*, 2009; Ushiro *et al.*, 2006) and Europe (Dorren and Berger, 2012; Dorren, Berger and Putters, 2006; Dorren and Berger, 2005) to quantify the effect of trees on rock fall behavior. The Japanese tests by Ushiro were part of the Ehime study (see Section 2.1) where fall velocities and run-out distances were measured for tests conducted before and after the trees were removed. At Ehime, the talus was sparsely forested with pine and oak having trunk diameters in the range of 100 to 500 mm (4 to 20 in). Measurements of impact velocities showed no significant difference in the velocities between tests conducted with the trees on the slope and after they were removed. Similar results were obtained at Tornado Mountain where the impacted trees were about 200 mm (8 in) in diameter. Where trees were impacted by rock falls, they were sheared off with apparently no reduction in the velocity of the fall; Figure 2.7 shows a typical tree on Tornado Mountain that was impacted and sheared off by a rock fall.

Masuya *et al.* (2009) have developed a rock fall simulation model that incorporates the tree height, trunk diameter and a probability density function expressed as the number of trees per square meter of slope surface. Collisions between a rock and a tree are modeled in the same manner as collisions with the slope, but with a restitution coefficient of 0.1 and a friction coefficient of 0.03. The model showed that the effect of trees is to approximately halve the velocity of the falls, and to cause a wider dispersion of the falls on the slope compared to a bare slope. Section 3.5.3 discusses dispersion areas of rock falls on talus slopes.

In the European study by Dorren and Berger (2005), tests were conducted on two similar parts of a talus cone with a slope angle of 38 degrees and a slope length of 302 m (990 ft). One part of the talus was denuded of trees, while the other part was forested with trees having an average diameter of 310 mm (12 in) and density of 290 trees per hectare. This slope configuration allowed two near identical rock fall tests to be conducted – one slope with trees and one without trees. For each test, 100 rocks were rolled with their impacts and trajectories recorded at 25 frames per second by five high speed cameras mounted in nearby trees; the rocks had an average diameter of 0.91 m (3 ft) and volume of 0.49 cu. m (0.6 cu. yd). The effect of the trees on the rock fall behavior was to reduce the average velocity from $13.4 \text{ m} \cdot \text{s}^{-1}$ (44 ft · s⁻¹) to $11.2 \text{ m} \cdot \text{s}^{-1}$ (37 ft · s⁻¹), and the maximum velocity from $14.8 \text{ m} \cdot \text{s}^{-1}$ (49 ft · s⁻¹) to $11.6 \text{ m} \cdot \text{s}^{-1}$ (38 ft · s⁻¹). From these results, as well as other tests on the resistance of trees to impact, it was possible to find a relationship between the diameter of tree trunks (measured at chest height, approximately where impacts occur), and the energy dissipated per tree for six tree species as shown in Figure 6.8. The tests also showed the relative wider dispersion of the rock falls by the tree impacts compared to bare slopes, similarly to that modeled by Masuya (2009).

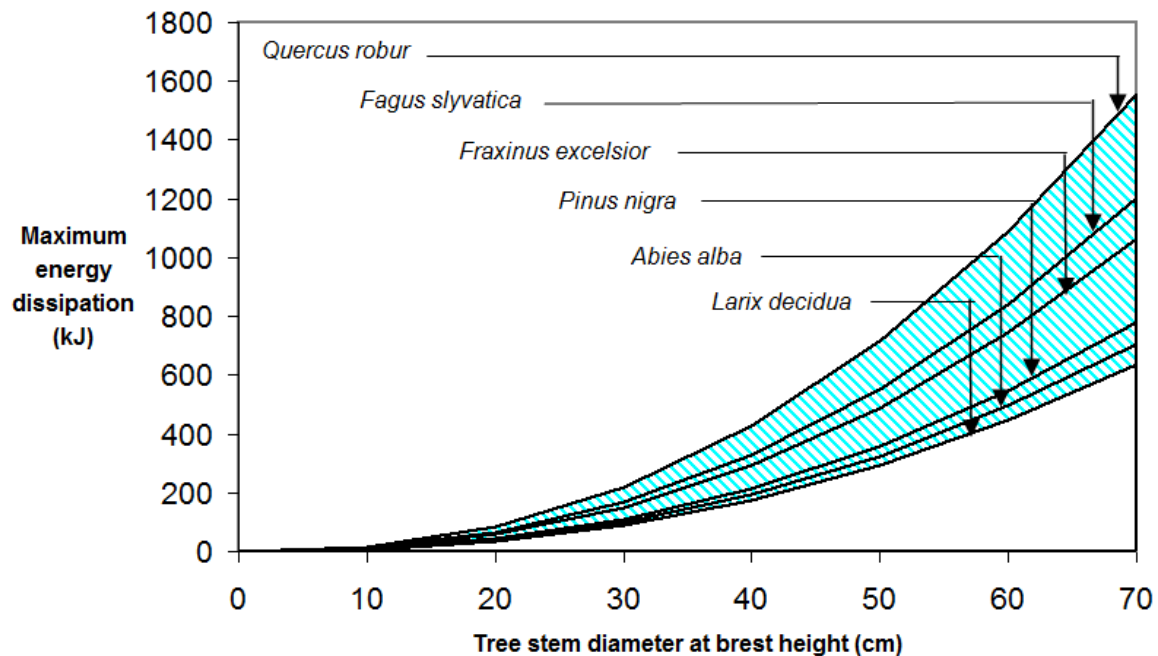


Figure 6.8: Relationship between maximum energy that can be dissipated by six different tree species and the tree diameter, measured at chest height (Dorren and Berger, 2005)

The energy dissipation data shown on Figure 6.8 can be used to evaluate the results obtained from the Ehime test site and the Tornado Mountain rock fall events. In both these cases, the tree diameters were in the range of 100 to 200 mm (4 to 8 in) where the energy dissipation

would be negligible. This low energy dissipation is consistent with the observation that the tree impacts at Ehime and Tornado Mountain had no significant effect on rock fall velocities and run-out distance.

Another characteristic of tree impact observed by Dorren and Berger is for rocks that are entirely or partially stopped by a tree. In some of these cases, the “whipping” action of the tree during impact can break off the upper part of the tree well above the impact point. Figure 6.9 shows a cedar tree with a diameter of 1.1 m (3.6 ft) that stopped a rock with a volume of about 5.5 cu. m (190 cu. ft.) moving at an estimated velocity of 5 to 10 m s⁻¹ (15 to 30 ft · s⁻¹); the approximate impact kinetic energy was 200 to 800 kJ (80 to 300 ft tonf). The tree was tilted and broke off at a height of about 14 m (46 ft) above the ground. Comparison of these impact parameters with Figure 6.8 confirms the capacity of this 1.1 m diameter tree to absorb this impact energy.



Figure 6.9: Impact of a 5 cu. m (6.5 cu. yd) rock fall with kinetic energy of about 200 to 800 kJ (75 to 300 ft tonf) with a 1.1 m (3.6 ft) diameter cedar tree. Rock was stopped and upper part of tree was broken off about 14 m above base (Vancouver Island, near Ucluelet)

7 Rock fall modeling

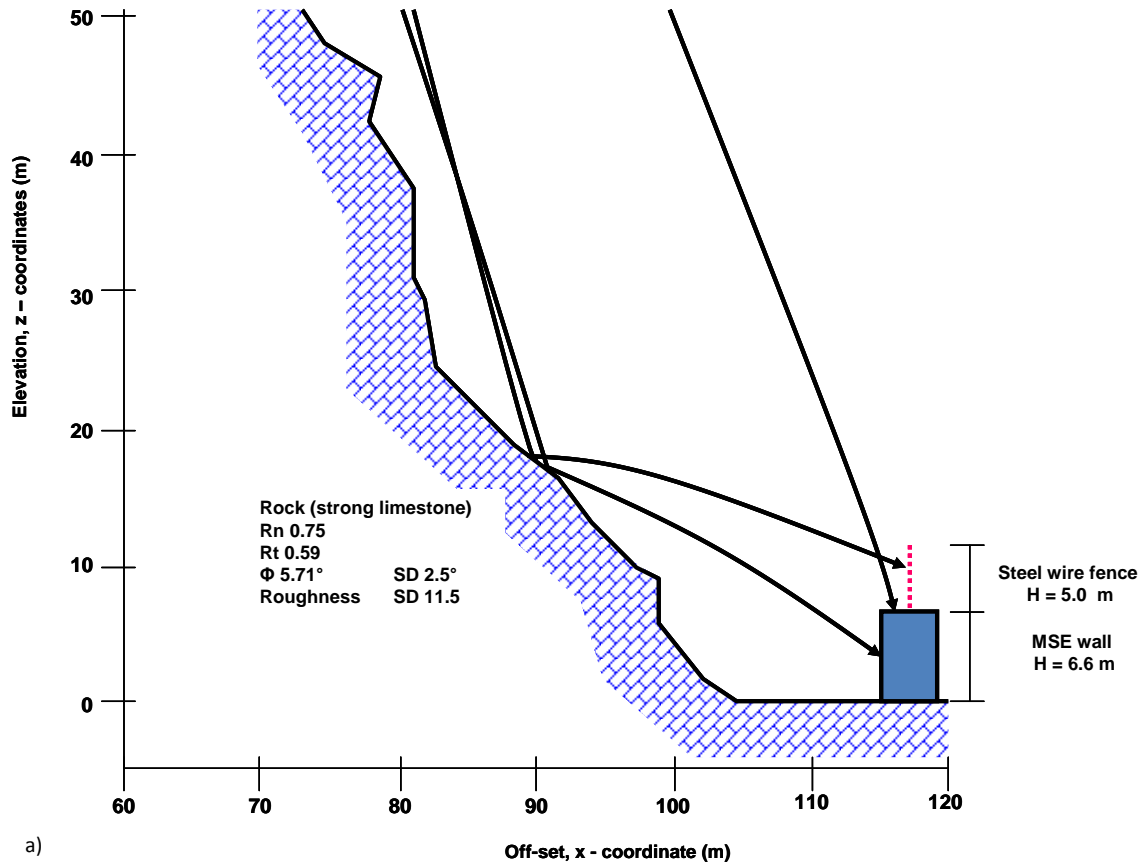
Design of rock fall protection structures requires information on the mass and impact velocity of the fall to determine the impact energy, and the fall trajectories to determine the height and location of the structure on the slope. These design parameters are usually obtained from computer simulation programs. Numerous modeling programs have been developed since the late 1980's that include programs, and a variety of university research tools. The complexity of these programs varies from simple two-dimensional, lumped mass models, to three-dimensional models in which the shape and size of the body can be defined and its orientation is tracked during the fall.

This chapter discusses first, the general principles of rock fall modeling, the required input parameters and the outputs that are generated. Second, analysis results are presented that model the rock falls for the five case studies described in Chapter 2; the modeling was carried out using the RocScience program *Rocfall 4.0*. The purpose of carrying out these back analyses was to determine the values of the input parameters that are required to closely model the actual events. It is intended that these analyses will provide benchmarks for rock fall modeling, because comparisons of the results of rock fall analysis programs with commonly used parameters show that calculated trajectories are often higher than those that occur in the field.

The consequence of unrealistically high, calculated trajectories is that many fences and barriers are higher, and more expensive, than required. For example, the author has observed fences that were designed using commercial software, where all the impacts were in the lower one third of the structure.

Another purpose of providing the case study information in Chapter 2 is to provide actual rock fall data that can be used by developers of modeling software to calibrate their programs.

The modeling methods discussed in this chapter are based on the programs ***RocFall 4.0*** (RocScience, 2012) and ***CRSP*** – Colorado Rockfall Simulation Program (Pfeiffer and Higgins (1995); Jones, *et al.*, (2000)). These two programs are commercially available and the calculations methods are documented in detail. Also, the two programs can produce identical results with the use of appropriate input parameters. Figure 7.1 shows the results of a typical rock fall simulation for the Mt. Stephen site using *RocFall 4.0* (Section 2.1.1).



a)



b)

Figure 7.1: Rock falls at Mt. Stephen (see section 2.1). a) Simulation of rock falls showing three typical rock fall paths; b) accumulation of falls that impacted fence on top of barrier

7.1 Spreadsheet calculations

A detailed analysis of rock fall trajectories and impacts for a lumped mass can be carried out on a spreadsheet using the basic principles of trajectories and impact mechanics described in the previous chapters. The calculation method is summarized in this section.

Chapter 2 provides documentation on rock fall events at five locations for a variety of slope geometries and geologic conditions. The information available for these events are the slope geometry and the co-ordinates of successive impact points. This information can be used to calculate the trajectory path, and the restitution and impact velocities of the body using equation (3.4) that relates the $[x, z]$ co-ordinates along the path to the velocity (V_0), gravity acceleration g , and the restitution angle of the body relative to the x-axis, α . Measured values for the rebound angle θ_0 relative to the slope [$\theta_0 = (\alpha + \psi_s)$ where ψ_s is the slope angle] are available from the test site at Ehime in Japan (Section 2.1.3) and at Tornado Mountain in Canada (Section 2.2.1); values for θ_f are plotted in Figures 3.9a) and b). These two plots show both the range, and the most frequent values, of θ_0 that occur on natural slopes.

Values for the angle θ_0 at the Ehime test site were measured from the trajectory paths using accelerometers embedded in the test blocks, while at Tornado Mountain, it was possible to map impact points and locate the positions of 21 trees that had been impacted by rock falls, and measure the height of the impacts. If three points on the trajectory path are known (i.e., successive impact points with the slope, and an intermediate tree impact), then it is possible to exactly calculate the rock fall path and determine the values for α and θ_0 .

Once successive trajectories have been calculated, it is possible to determine the impact and restitution velocities at each impact point, and their normal and tangential, and horizontal and vertical, velocity components. This information in turn allows the normal and tangential restitution coefficients to be calculated from the changes in velocity components that occur during impact. These same changes in velocity during impact allow the energy losses to be calculated at the impact points, as well as the energy gained during the trajectory due to gravitational acceleration. The result of these energy calculations is an energy partition diagram such as that shown in Figure 6.5.

A spreadsheet calculating these velocities, restitution coefficients and energy changes can extend to 60 columns. This is an interesting amount of information that can be generated from the co-ordinates of successive impact points.

7.2 Terrain model – two dimensional v. three dimensional analysis

Early rock fall modeling programs were two dimensional (Piteau, 1980; Pfeiffer and Bowen, 1989), but with the development of methods of scanning rock slopes, such as Lidar, to produce

digital terrain models (DTM)) it has become possible to import DTM's into rock fall modeling programs and run three dimensional analyses.

Modeling of a slope in two dimensions will only provide reliable results if the cross section is reasonably uniform along the slope. However, as discussed in Section 3.5.1, it is found that rock falls often accumulate in gullies in a similar manner to which water flows down slopes. Figure 3.12 shows a slope in which all the rock falls over a slope length of several hundred meters along the crest are concentrated in three narrow gullies. Modeling of rock falls on this slope using a two dimensional program would give erroneous results because the model would not simulate the sinuous shape of the gullies and the generally uniform slope profile along the path of the gullies. A two dimensional analysis of the slope in Figure 3.12 would show a series of ridges and hollows that would not be realistic model of the rock fall path.

7.3 Modeling methods – lumped mass

The primary components of rock fall modeling programs are first, algorithms to calculate the rock fall impacts and trajectories and second, routines to process the graphics of the slope and the rock fall paths. Of these components, the calculation of the impacts and trajectories can be readily accomplished if a lumped mass model is used, as is the case with the programs *RocFall 4.0* and *CRSP*; the calculations can be handled on a spreadsheet as described in Section 7.1. However, the calculations are more complex if the shape and size of the body are defined such that the program tracks the orientation of the body during both the trajectory and impact phases of the fall. Still more complexity is introduced if the rock breaks up during impact.

This section reviews the methods used to calculate trajectories and impacts for a lumped mass model such as used in the programs *RocFall 4.0* and *CRSP*. Section 7.4 discusses models that use bodies with defined dimensions and shapes.

The component of the modeling programs that processes the graphics is beyond the scope of this thesis.

7.3.1 Rock fall mass and dimensions

The lumped mass model , which is used in the programs *RocFall 4.0* and *CRSP*, assumes that the body is infinitely small, which allows the use of Newtonian mechanics as described in the earlier chapters, to calculate impact and trajectory behavior, ignoring the effect of air friction. The mass of the body is used to determine energies from the calculated velocities, and it is assumed

that the mass is constant during the fall; loss of mass during the course of a fall is discussed in Section 6.5.

Calculation of the effects of slope roughness (see Section 7.3.6) and rotational velocity (see Section 7.3.7) requires a value for the dimensions of the body. In *CRSP*, the default body shape is a sphere, because it yields the maximum volume for a given radius, and the program calculates the radius of the body from the mass and rock density. It is also possible to define cylindrical and discoid shaped bodies in order to calculate corresponding moments of inertia.

7.3.2 Slope definition parameters

Development of a rock fall model requires definition of the slope parameters that comprise the slope geometry, and the material properties. The slope geometry is defined, for a two-dimensional model, by a series of [x - z] co-ordinates that join straight line segments. Each segment is assigned a slope material, the properties of which are the normal and tangential coefficients of restitution, the surface roughness and the friction angle. These parameters are discussed in the following sections.

Some models use a “spline” function to create a smooth curved surface between the defined points, but this approach does not allow a series of horizontal benches and steep cut slopes to be modeled.

7.3.3 Rock fall seeder

The rock fall models incorporate a “seeder” that defines the rock fall conditions at the origin of the falls in the model. In *RocFall 4.0*, the seeder parameters are the horizontal and vertical translational velocity components, the rotational velocity and the mass of the fall. These parameters allow falls to be modeled either where the source of the falls is the same point as the seeder ($v_x = v_z \approx 0$), or where the source of the falls is outside the model area and the falls have finite velocities at the origin of the model ($v_x, v_z > 0$). The relative values of v_x and v_z are selected to obtain the required trajectory angle.

With respect to angular velocity, either a negative or positive value can be input. However, it appears that the direction of rotation makes little difference to the calculated trajectories. Typical *RocFall 4.0* analyses show that the effect of rotational velocity is to flatten trajectories, which is consistent with impact mechanics theory for negative direction of rotation (see Section 4.6.4 and Figure 4.9).

7.3.4 Normal coefficient of restitution

The coefficient of restitution, e relates the velocity of the falling body at the end of impact with the velocity at the moment of impact (see Chapter 4). It is also usual to examine the velocity changes in the normal (N) and tangential (T) components of velocity during impact and the corresponding normal e_N , and tangential e_T , coefficients of restitution. This section discusses the normal coefficient, while Section 7.3.5 discusses the tangential coefficient and its relationship to the frictional properties of the slope surface.

The normal coefficient of restitution is defined as follows:

$$e_N = -\frac{v_{fN}}{v_{iN}} \quad (4.6)$$

where v_{fN} is the normal component of the velocity at the completion of the impact ($t = f$), and v_{iN} is the normal component of velocity at the moment of impact ($t = i$).

It is recognized in the *CRSP* and *RocFall 4.0* models that e_N is not a material property, but is dependent on impact conditions and to a lesser degree on the type of slope material. That is, for a high velocity impact the body will tend to penetrate further into the ground in an inelastic impact, compared to a lower velocity impact that will tend to be a more elastic and have a greater rebound height. This behavior is modeled by the following empirical equation that scales the normal component of the restitution velocity v_{fN} , according to the following equation:

$$v_{fN} = \left(\frac{v_{iN} \cdot e_N}{1 + (v_{iN}/K)^2} \right) \quad (7.1)$$

where v_{iN} is the normal component of the impact velocity, and K is a constant. The term $[(1+(v_{iN}/K)^2)^{-1}]$ is a scaling factor that is equal to 0.5 for the default value of $K = 9.14 \text{ m} \cdot \text{s}^{-1}$ (30 ft · s⁻¹). Figure 7.2 is a plot of the scaling factor given by equation (7.1) for values of K ranging from 9 to 40 m · s⁻¹ (30 to 130 ft · s⁻¹). The curves show that v_{fN} equals v_{iN} (i.e., $e_N = 1$) for low velocity impacts when the scaling factor approaches 1 for elastic impact.

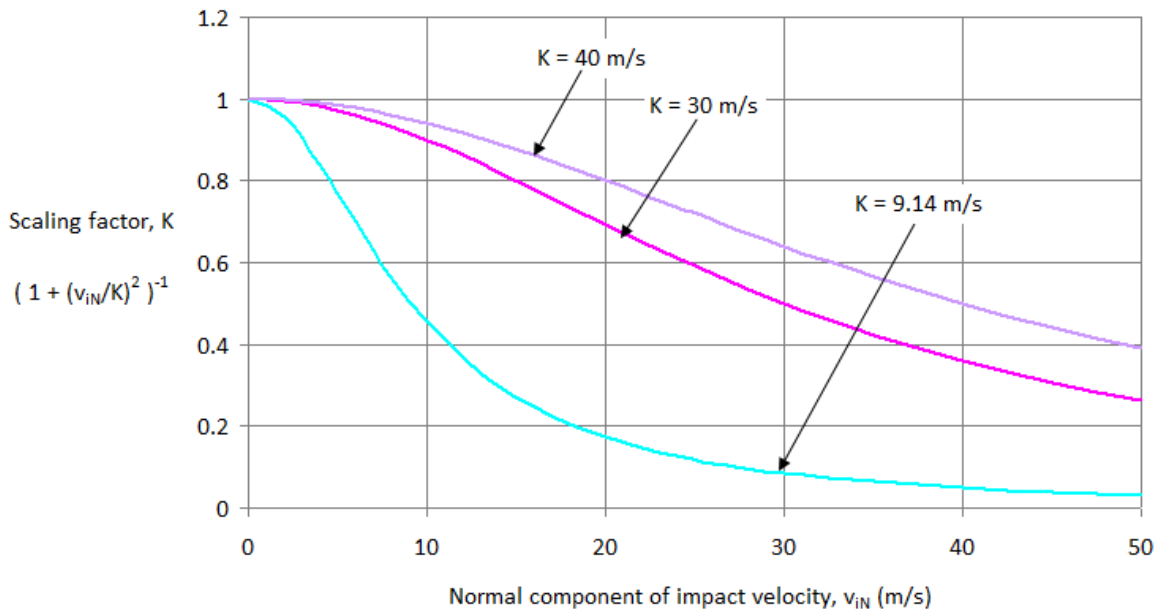


Figure 7.2: Plot of normal component of impact velocity and scaled normal coefficient of restitution from equation (7.1)

The form of the relationship given by equation (7.1) and plotted in Figure 7.2 is similar to that discussed in Section 5.2.1 and in Figure 5.5 that relates the normal coefficient of restitution e_N to the impact angle θ_i . That is, high normal velocities occur when the impact is close to normal, or $\theta_i > \sim 60$ degrees. Under these conditions, e_N has a low value close to the basic coefficient of restitution determined by a drop test (see Figure 5.6). However, for shallow impacts where $\theta_i < \sim 30$ degrees and the normal velocity component is small, the value of e_N becomes larger. Equation (7.1) shows that the maximum value of e_N scaled is 1.0, while the field data and impact mechanics show that e_N can have values greater than 1 for shallow impact angles. The relationship between θ_i and e_N is given by the equation:

$$e_N = 19.5 \cdot \theta_i^{-1.03} \quad (5.4)$$

7.3.5 Tangential coefficient of restitution and friction

The tangential coefficient of restitution e_T , is defined by the ratio of the final and initial tangential velocities during impact as follows:

$$e_T = \frac{v_{fT}}{v_{iT}} \quad (4.7)$$

Tangential velocity changes depend on the extent of slip and rolling that occurs during impact, and the effects of friction at the rock-slope contact.

In *CRSP*, the tangential coefficient of restitution is scaled by a friction factor $f(F)$, and a scaling factor SF that incorporate the impact translational and rotational velocities, and the normal coefficient of restitution (Pfieffer and Bowen, 1989). In *RocFall 4.0*, analysis values for e_T incorporate data from back analysis of rock falls.

Since e_T is related to an effective friction coefficient μ' , guidance on appropriate values for e_T can be obtained from measurements of fall velocity related to the fall height and the slope angle (Japan Road Association, 2000); Table 3.1 lists values for μ' for characteristics of different slope materials. For example, $\mu' \approx 0.05$ for “smooth, strong rock surfaces with no tree cover”, and $\mu' \approx 0.35$ for “talus with angular boulders exposed at the surface, no tree cover”. In addition, values for e_T have been calculated by back analysis for the five case studies discussed in Chapter 2 and are listed in Table 2-1; these values have been used in the *RocFall 4.0* modeling of these five sites as presented in Section 7.5.

In *RocFall 4.0*, the friction angle ϕ input parameter is related to calculate the distance that the body slides down the slope when the trajectory phase of the fall is complete. The value of ϕ used in the analysis is a function of the body shape since a spherical body will have less frictional resistance to sliding than a tabular body. The distance L that a body will slide along a surface dipping at ψ_s degrees and with a friction angle ϕ is:

$$L = \frac{(v_{iT}^2 - v_{fT}^2)}{2 \cdot g(\sin \psi_s - \cos \psi_s \cdot \tan \phi)} \quad (7.3)$$

where v_{iT} is the tangential velocity at the start of sliding and v_{fT} is the velocity when the body has slid distance L (Stevens, 1998).

7.3.6 Surface roughness

The surface roughness of the slope materials has a significant effect on rock fall behavior, i. e., trajectory heights generally increase with increased roughness.

Surface roughness can be quantified by relating the perpendicular variation s , of the slope from the average slope inclination, within a slope distance equal to the radius r , of the body (Pfieffer and Bowen, 1989) as shown in Figure 7.3. The angle ε is defined by the dimensions r and s as follows:

$$\varepsilon = \tan^{-1} \left(\frac{s}{r} \right) \quad (7.4)$$

Figure 7.3 shows that the value of the angle ε diminishes with increasing radius of the body. That is, for approximately the same slope roughness, the roughness angle will diminish as the body size increases, ($r_1 > r_2$) and ($\varepsilon_2 > \varepsilon_1$).

In *CRSP*, the slope roughness is input as the dimension s from which the angle ε is calculated using the defined radius of the spherical body. In *RocFall 4.0*, the roughness is defined as a standard deviation in the dip angle of the slope segment.

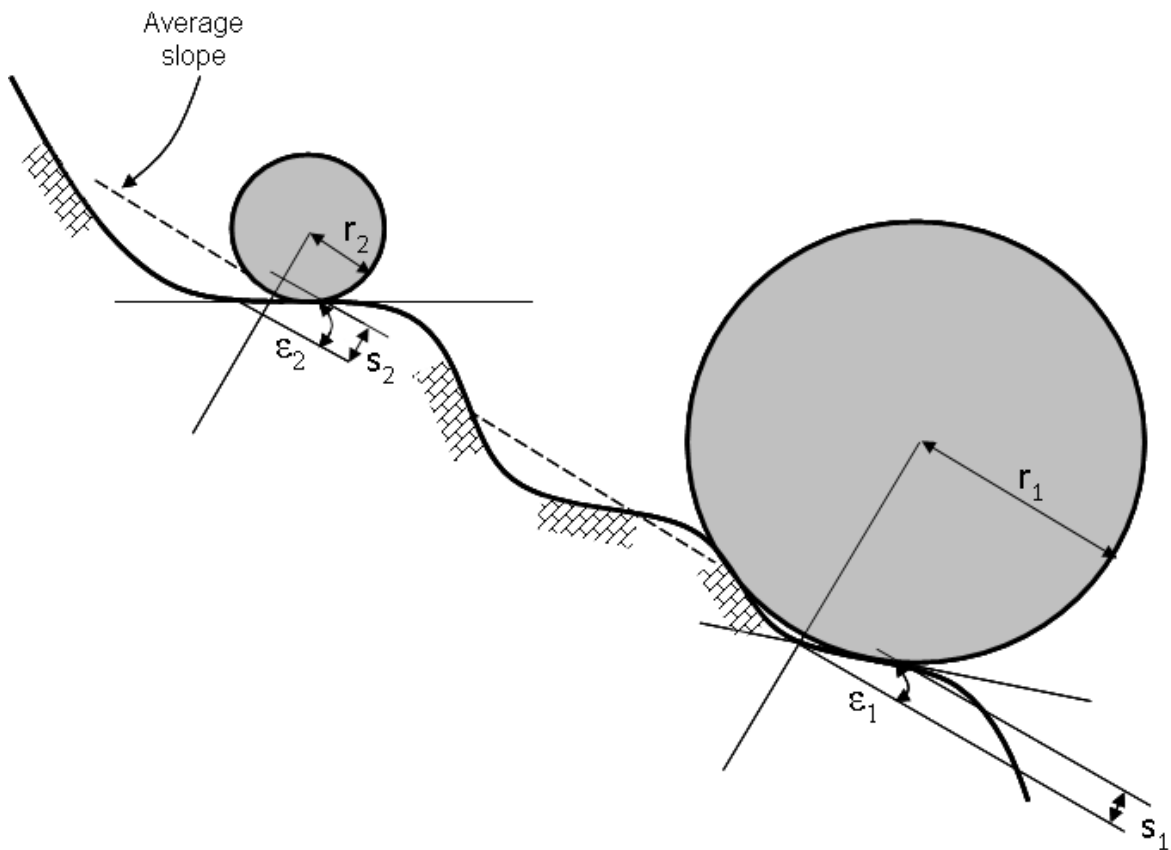


Figure 7.3: Relationship between slope roughness (ε) and radius of rock fall (r)

7.3.7 Rotational velocity

Rock falls rotate as the result of the moment generated by the tangential velocity and the frictional resistance at the contact of periphery of the body and the slope surface. Rotation of the body has two main effects on rock fall behavior. First, rotation causes the trajectories to be flatter than for a non-rotating body (see Section 4.6.4), and second, the rotating body has rotational energy that contributes to the total impact energy (see Section 6.2).

Body rotation is incorporated in the *CRSP* and *RocFall 4.0* models by calculating the rotational velocity ω for a body with radius r with tangential translational velocity v_T from the following relationship:

$$\omega = \frac{v_T}{r} \quad (7.5)$$

The rotational energy (RE) of the body can be calculated using the moment of inertia, I , for the selected body shape and the calculated rotational velocity ($RE = \frac{1}{2} I \cdot \omega^2$).

7.3.8 Probabilistic analysis

Modeling of rock falls must take into account the natural variability of site conditions that includes irregularly shaped blocks of rock, and variability of the coefficients of restitution and slope roughness. Actual site conditions are modeled by probabilistic analyses in which the average input parameters include standard deviations that represent the likely range of the parameter values from the average values. The program then carries out a Monte Carlo analysis for a large number of rock fall runs, with a random number generator selecting parameter values for each run from the probability distributions defined by the standard deviations. The result of the Monte Carlo analysis is a plot of all the analyzed rock falls that shows the likely distributions of rock fall behavior that may be expected.

Examples of probabilistic analyses are provided in Section 7.5 for the five case studies described in Chapter 2.

7.3.9 Data sampling points

The usual objective of running rock fall models is to design structures and ditches to protect facilities at the base of the slope. Design information required for these structures are the trajectory height and the impact energy. The modeling programs incorporate sampling points at which information is provided on distributions of analysis data – total, translational and rotational energies, velocity and trajectory height. By moving the sampling point across the slope, it is possible to identify the location with the minimum energy and/or the lowest trajectory.

Examples of data generated at sampling points are provided in the analyses of the case studies in Section 7.5.

7.4 Modeling methods – discrete element model (DEM)

Rock falls models that use a lumped mass in which the mass of the body is defined but the mass is concentrated in a point are described in Section 7.3. Alternatively, discrete element models (DEM) can be used in which the mass, dimensions and shape of the body are defined, and the body can break into smaller fragments as it impacts the slope during the fall (Zhang and Rock, 2012) (Chen et al., 2013).

In DEM analysis, the body is made up of a collection of small spheres, in tight tetrahedral packing, connected with appropriate constitutive models to describe rigidity, heterogeneity and fracture of the model. This model can accurately replicate trajectories, rolling, sliding, launching behavior of the body, and crack propagation within the body. With respect to impact of the body with the slope, the parameters related to impact that are required for DEM modeling are damping, stiffness and friction coefficients.

As of 2013, commercial modeling programs in which the mass, shape and size of the body are defined are not widely available.

7.5 Modeling results of case studies

For each of the five documented rock fall sites described in Chapter 2, a computer simulation has been run using the program *Rocfall 4.0* (RocScience, 2012). These analyses demonstrate the operation and results of the program, and determine the site parameters that are required to produce calculated rock fall paths that closely follows the actual paths.

In defining the modeling parameters required to duplicate the actual field results, it was found that very fine adjustments were necessary in the average values of parameters. That is, analyses of active rock fall sites using apparently appropriate input parameters may show that falls stop part way down the slope, or that unrealistically high trajectories are generated.

7.5.1 Rock fall model of Mt. Stephen events

Section 2.1.1 in Chapter 2 describes the rock fall conditions at Mt. Stephen in the Rocky Mountains near Field, British Columbia in Canada. Figures 2.1 and 2.2 show respectively photographs of a portion of the site, and a typical section of the lower part of the slope. This is a highly active rock fall site, due to the topography, geology and weather. That is, the mountain is about 2000 m (6550 ft) high at an overall face angle of about 50 degrees so that rock falls can fall from great heights and attain high velocities, with most falls reaching the base of the slope.

The geology comprises horizontally bedded limestone and shale where the limestone is much stronger than the shale and occurs in thicker beds; the limestone contains sets of vertical joints. The relatively rapid weathering of the shale compared to the limestone results in the formation of unstable overhangs and columns in the limestone that are the sources of the rock falls. The other factor causing the high rock fall frequency is the weather – very cold winters forming ice on the slope, and rainfall during the spring and fall. Figure 7.4 shows the lower 120 m (400 ft) portion of the slope.

The protection provided for these severe rock fall and snow avalanche conditions comprises a 6.6 m (21.5 ft) high MSE (mechanically stabilized earth) wall, with a 5 m (16.5 ft) high steel wire fence along the top (Figure 7.1). This barrier has been very successful in protecting the railway from both types of hazard.

The actual rock falls at Mt. Stephen have been modeled using the program *RocFall 4.0*. Figure 7.4 shows the calculated trajectories for three falls, and Figures 7.5 and 7.6 show graphs of the distributions of impact location, velocity and energy at the barrier location

The material types used in the analysis was rock for the entire slope, with soil in the ditch behind the barrier. For this case study, all the rock falls were contained by the barrier so it was not possible to use the back analysis feature in *RocFall 4.0*. The parameters for the slope, including the standard deviations (SD) quantifying the range of the values, required to simulate the rock falls are shown in Figure 7.4. It is assumed that all rock falls originated higher on the slope than elevation 118 m (390 ft.) so the x and z seeder velocities have values that generate trajectories that are consistent with observed field conditions.

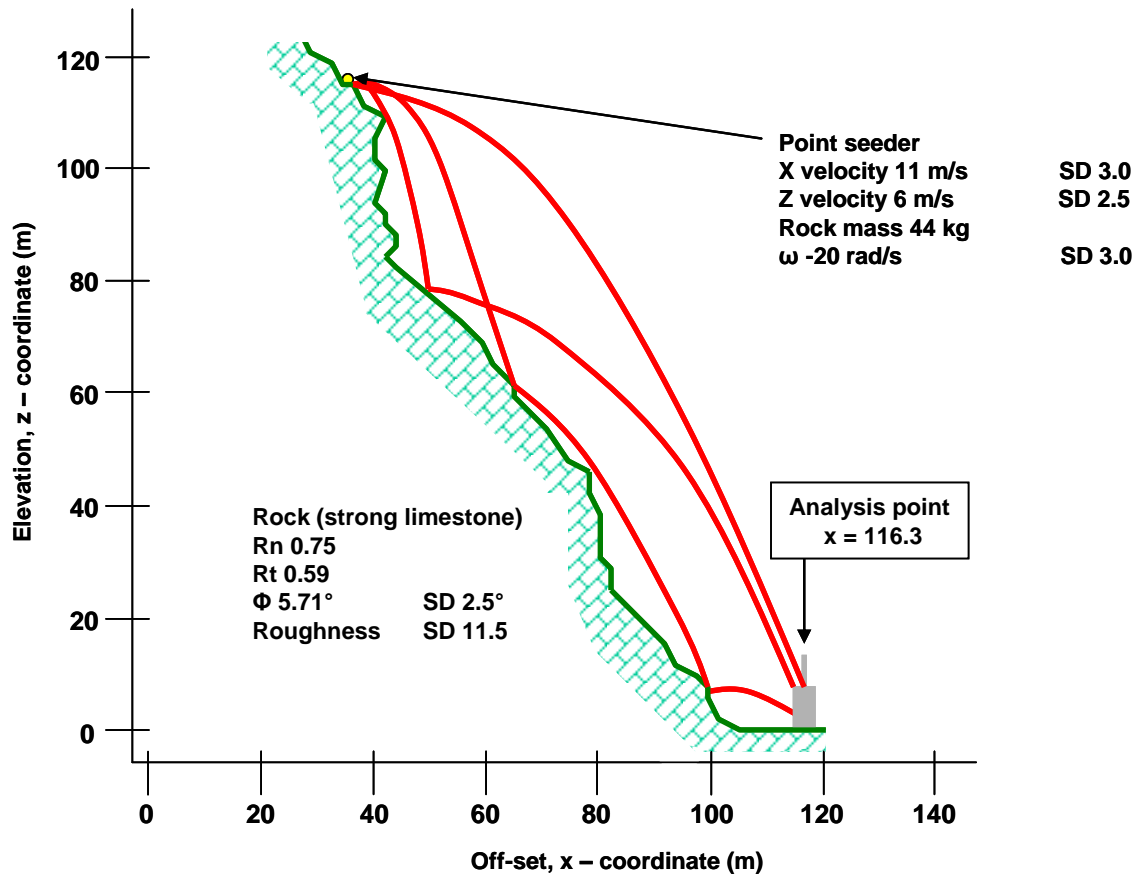


Figure 7.4: Simulation of rock falls at Mt. Stephen for three calculated rock trajectories

Observations of rock fall impacts on the MSE barrier and the fence provided reliable information on the impact locations. In total, it was possible to identify 466 impact points as either chips on the concrete blocks forming the face of the MSE wall, or as deformations of the steel wires in the fence. Analysis of the impact locations showed their vertical distribution, with impacts over the full 11.6 m (38 ft) height of the structure with the maximum impacts at the base and the number of impacts decreasing with height. The horizontal distribution of impacts showed that most occurred where the slope geometry included the lower face sloping at about 45 degrees on which many blocks impacted and then generated a trajectory that impacted the barrier (Figure 7.4). Figure 7.5 shows the calculated vertical distribution of the impacts on the barrier, which closely match the actual impact locations.

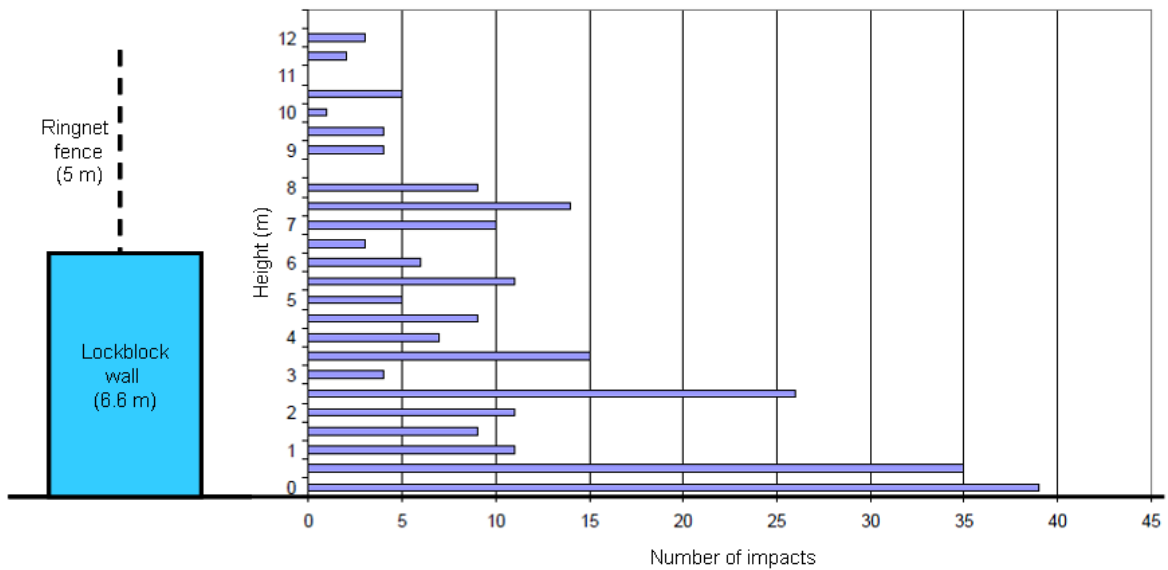
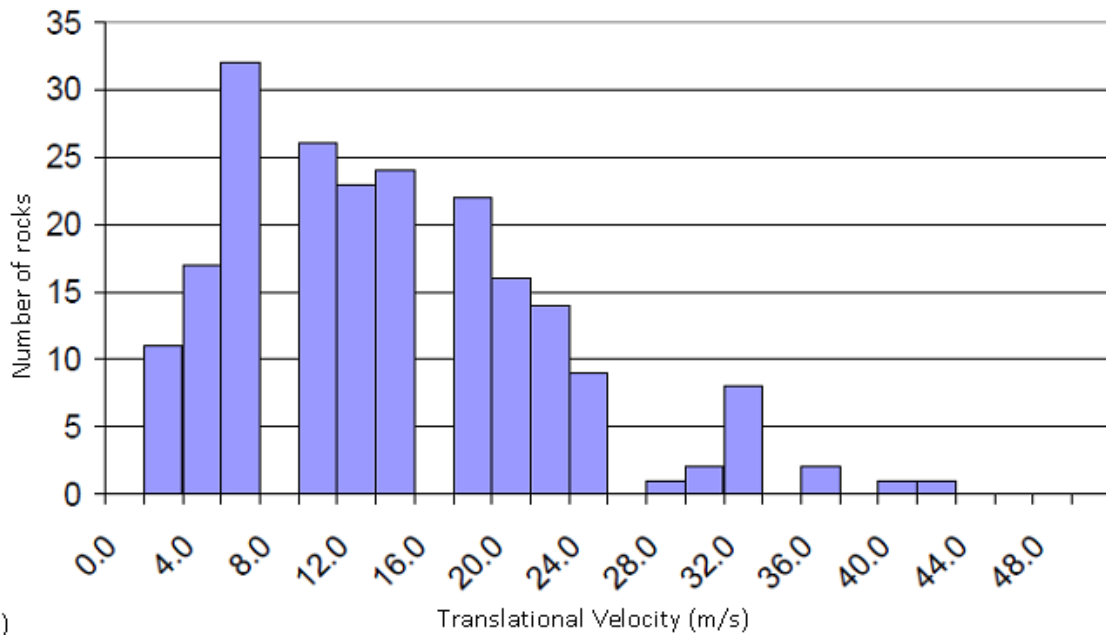


Figure 7.5: Calculated vertical distribution of impact points on barrier at Mt. Stephen

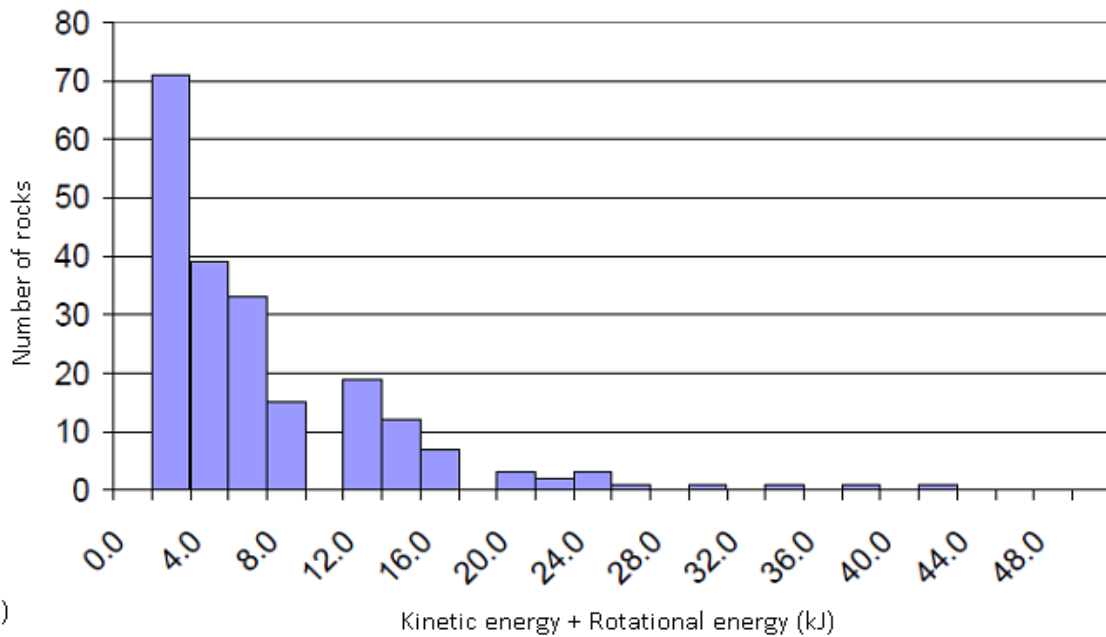
It was also possible to measure the dimensions of blocks that had impacted the fence and were then lying on top of the wall. As would be expected for this condition where rocks had fallen from a considerable height and impacted the slope several times, the maximum block size was only 300 to 500 mm (12 to 20 in) approximately. Figure 7.1b) shows the dimensions of the typical blocks accumulated on the top of the wall.

For the typical trajectories shown on Figure 7.4, the calculated velocities of falls that impacted the barrier were up to $44 \text{ m} \cdot \text{s}^{-1}$ ($145 \text{ ft} \cdot \text{s}^{-1}$). For a block with a mass of 50 kg (110 lb) (ellipsoid with major axis: $2a = 2b = 0.4 \text{ m}$, $2c = 0.2 \text{ m}$, volume = 0.02 cu. m (0.03 cu. yd)) the impact energy would be about 60 kJ (22 ft tonf).

7 Rock fall modeling



a)



b)

Figure 7.6: Analysis using *RocFall 4.0* of rock falls at Mt. Stephen at barrier, analysis point x = 116.3 m a) translational velocity distribution; b) total energy (KE + RE) distribution

The calculated velocities and energies plotted in Figure 7.6 appear to be less than the actual values where falls originate on the steep slope from heights of hundreds of meters above the barrier and attain high velocities.

7.5.2 Rock fall model of Kreuger Quarry, Oregon tests

The purpose of the rock fall tests carried out in the Kreuger Quarry in Oregon was to determine the required dimensions and configurations of catchment areas to contain rock falls on

highways (Pierson et al., 2001). The tests involved dropping rocks down an excavated rock face in to a catchment area at the base of the cut, and measuring both the first impact point and the furthest distance that the block rolled past the base of the cut (see Section 2.1.2). The cut heights ranged from 8 to 24 m (25 to 80 ft) and the face angles from vertical to 45 degrees, with the slopes of the catchment area being horizontal, and sloped at 4H:1V and 6H:1V towards the cut face. The catchment areas were all uniform surfaces with no barriers or depressions since this is the configuration required for catchment areas (“recovery zones”) on highways in the United States. In total, 11,250 separate rock fall tests were conducted.

Although no specific information on rock fall trajectories is available from high speed camera images, for example, it is possible to determine likely trajectories that are mathematically feasible, from the slope and catchment geometry, and the records of the first impact points. Figure 7.7 shows an assumed trajectory for a fall on a 15 m (50 ft) high cut with a face angle of 76 degrees (1/4H:1V) where the first impact point at $x = 11.8$ m (40 ft) is the 95 percentile for this slope configuration. That is, 95 percent of all rock falls first impacted the ditch closer to the slope than the trajectory shown. Figure 7.7 also shows the input parameters for *RocFall 4.0* that are applicable to slope configuration. The point seeder in this case has low values for the x and z velocities because the rocks were pushed off the crest of the cut.

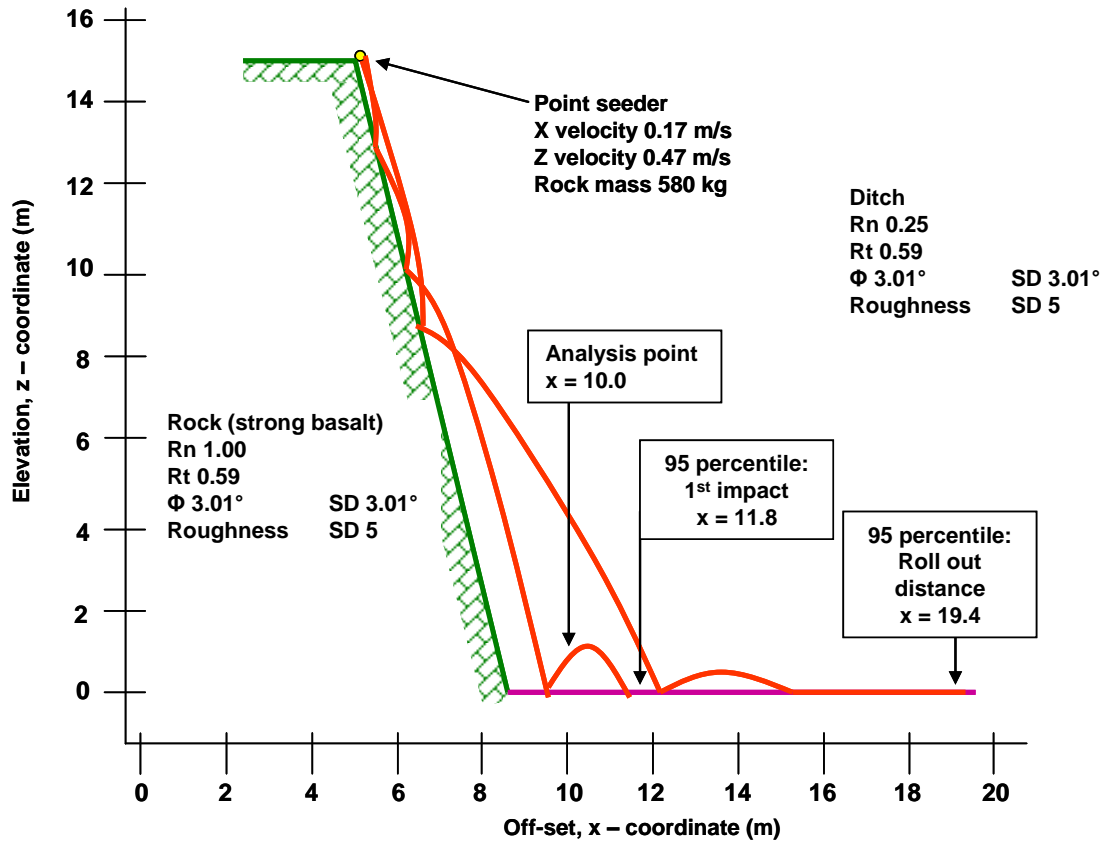


Figure 7.7: Calculated trajectories for two 580 kg (1,280 lb) rocks at Krueger Quarry rock fall tests on 15 m (50 ft) high cut at a face angle of 76 degrees; refer to Fig 10.3 for first impact and roll out distances

Figure 7.7 also shows an analysis point located at x = 10 m (33 ft), or about 1.4 m (5 ft) from the base of the cut; this location represents the 70th percentile of the first impact points. The calculated distributions of translational velocities and energies at x = 10 m (33 ft) are shown on Figure 7.8.

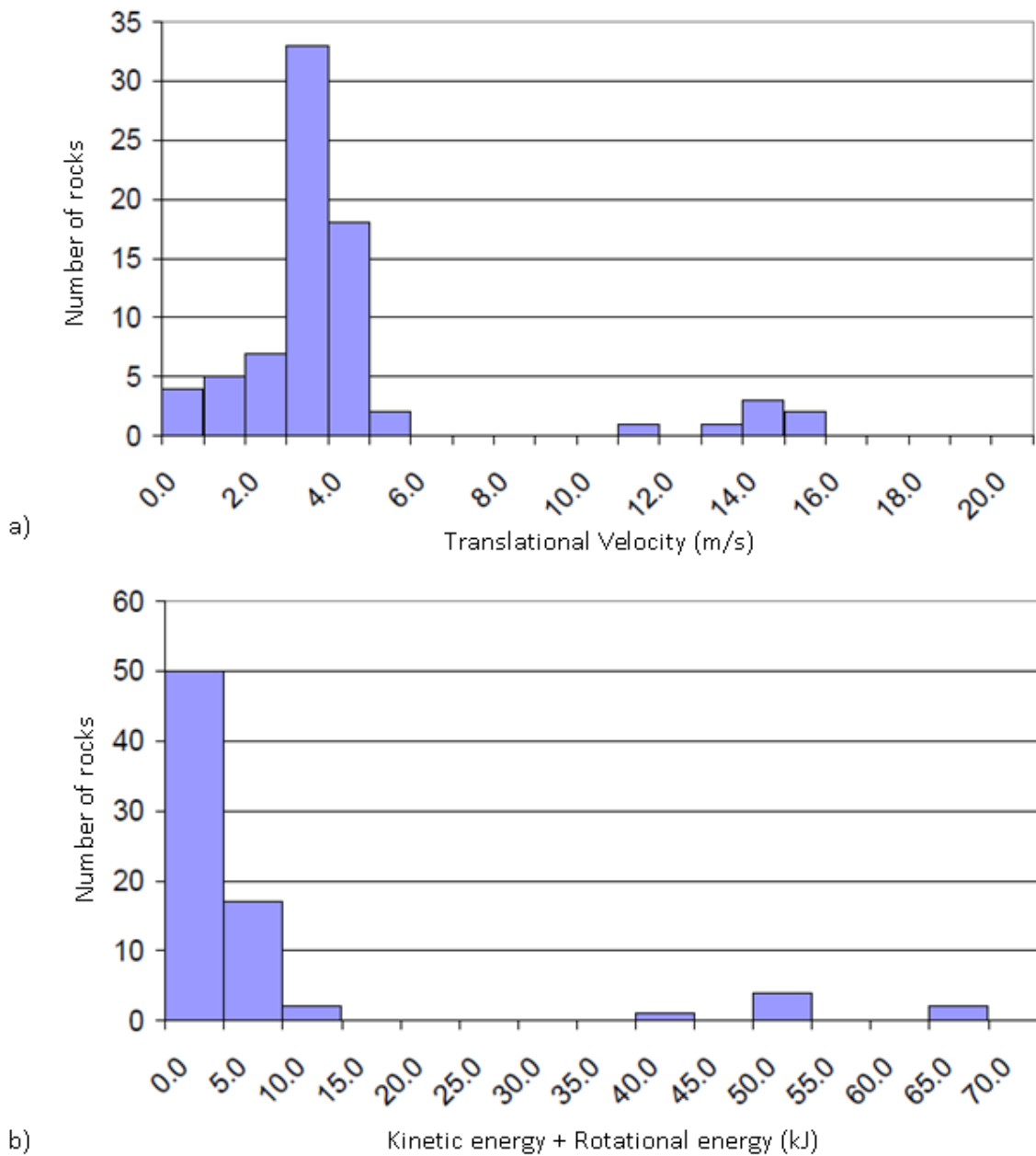


Figure 7.8: Analysis using RocFall 4.0 of rock falls at Krueger Quarry for 15 m (50 ft) high cut at a face angle of 76 degrees, analysis point x = 10 m (33 ft) a) translational velocity distribution; b) total energy (KE + RE) distribution

7.5.3 Rock fall model of Ehime, Japan test site

In 2003 a series of rock fall tests was carried out at a test site in Ehime Prefecture on Shikoku Island in Japan, as part of an extensive testing program that started in about 1961, located at least 16 other sites around Japan (see Sections 2.1.3 and 2.2.1). The Ehime tests were comprehensive in terms of the number of block shapes tested and the range of site conditions, and were documented in detail using 14 high speed cameras on the slope, and accelerometers

sampling at 2 kHz embedded in concrete blocks. The data collected allowed the precise positions of impact points and trajectory paths to be determined throughout each fall, as well as the translational and rotational velocities.

The test slope was a 42 m (140 ft) high natural slope, comprising a 26 m (85 ft) high rock face at an angle of 44 degrees in horizontally bedded sandstone and shale, with a 16 m (50 ft) high talus slope forming the lower part of the slope. The talus cone was sparsely vegetated with pine and oak trees with trunk diameters of 100 to 200 mm (4 to 8 in).

The test conditions were as follows. The test bodies comprised concrete cubes – side length 0.6 m (2 ft) and weight of 520 kg (1,150 lb), concrete spheres – diameter 0.54 m (1.8 ft) and weight of 200 kg (440 lb), and blocks of rock with masses ranging from 120 kg to 2060 kg (260 to 4550 lb). The tests involved rolling ten cubes, ten spheres and 20 blocks of rock, with half the tests being run on the natural treed slope, and the second half after the trees had been removed.

The collected data was used to determine the fall paths and trajectory heights, as well as the translational and rotational velocities. A photograph of the slope is shown in Figure 2.5, and details of the interpreted data are presented in Figure 3.5 – trajectory heights normal to the slope; Figure 3.6 – translational velocities; Figure 3.9 distribution of restitution angles; and Figure 3.10 – angular velocities.

Figure 7.9 shows a simulation, using *RocFall 4.0*, of the actual fall path of a concrete cube as shown on Figure 2.6. The input parameters for the rock and talus material properties and the seeder values are also shown on Figure 7.9.

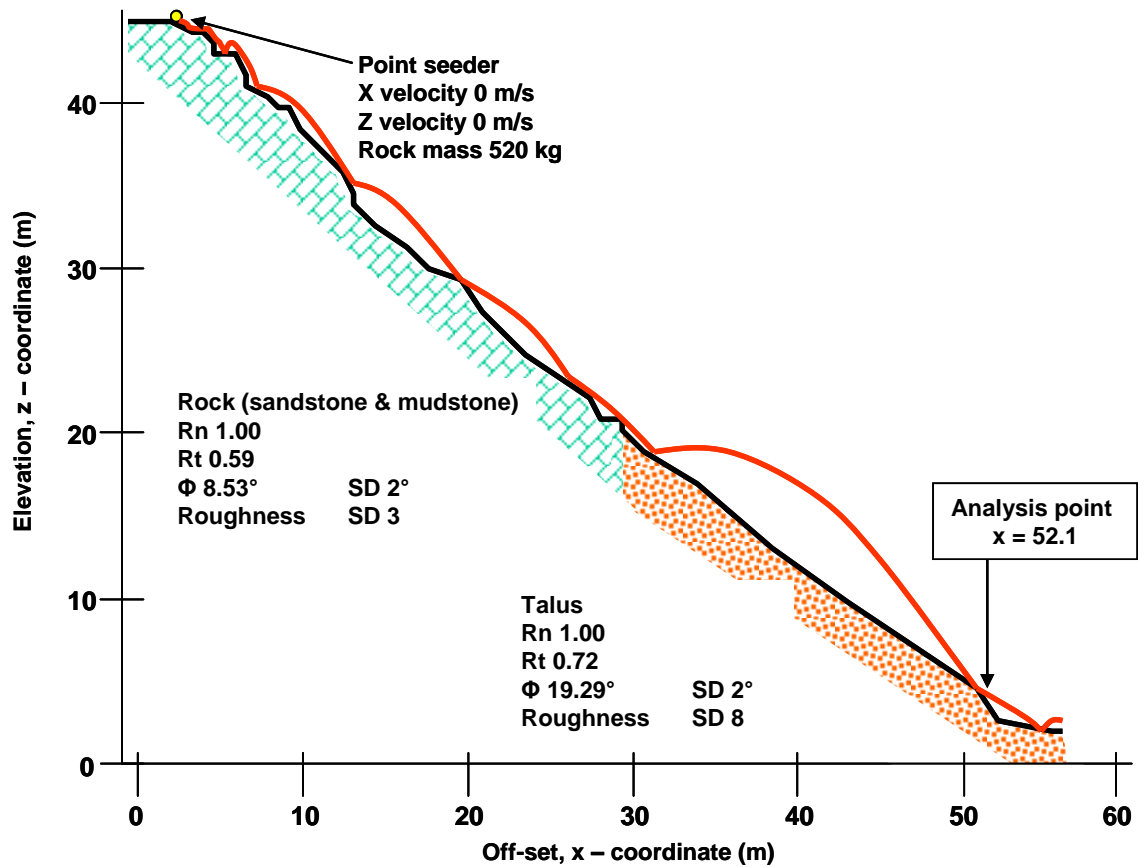


Figure 7.9: Calculated trajectory using *RocFall 4.0* for a 520 kg (1150 lb) concrete cube at the test site in Ehime Prefecture in Japan

Figure 7.10 shows a comparison between the actual and calculated trajectory heights for a test with a concrete cube. The two sets of data are reasonably consistent except for the talus impact at $x = 34$ m where the calculated trajectory is 50 per cent greater than the actual trajectory. Figure 3.5 shows the measured trajectory heights for all the tests, where 99 per cent of the trajectory heights were less than 2 m (7 ft), and 95 per cent were less than 1.5 m (5 ft).

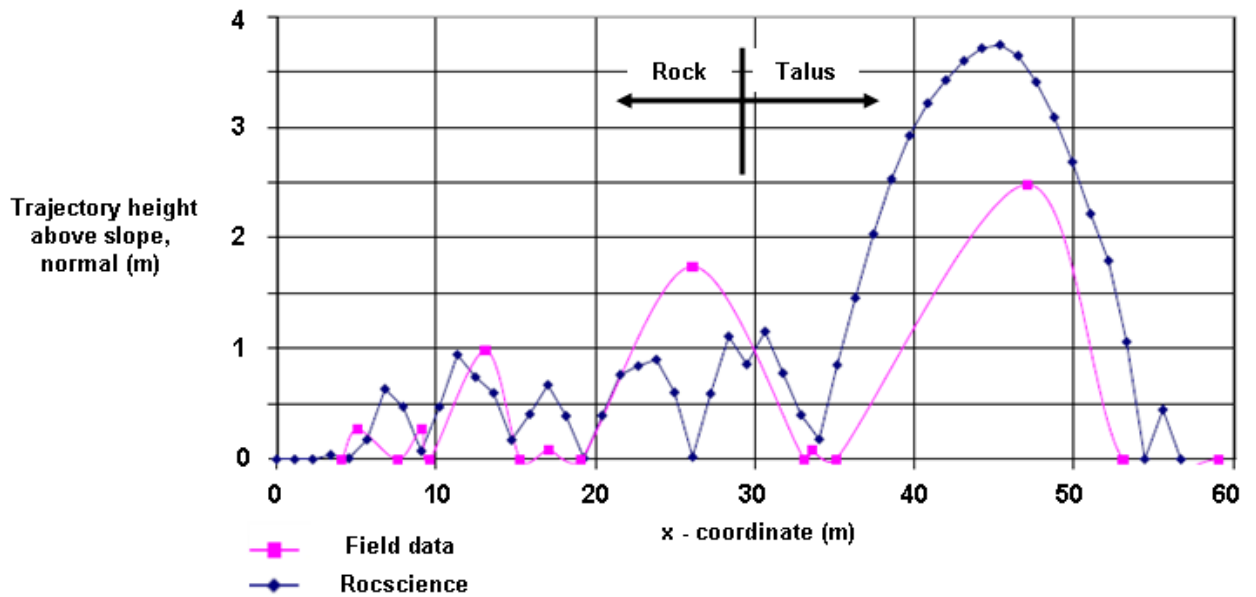


Figure 7.10: Trajectory height envelope comparison between field results and *RocFall 4.0* simulated results for concrete cube at test site in Ehime Prefecture in Japan

Figure 7.11 shows the distributions of the velocity and total energy of 24 tests of concrete cubes. The analysis point ($x = 52.1$ m) is located at the base of the talus slope where a rock fall protection structure may be located. The calculated velocities at the analysis point can be compared with the actual velocities at this location shown on Figure 3.6. Where $H = 41$ m in Figure 2.6, equivalent to $x = 52.1$ m in Figure 7.9, the actual range of velocities is 5 to 15 $\text{m}\cdot\text{s}^{-1}$.

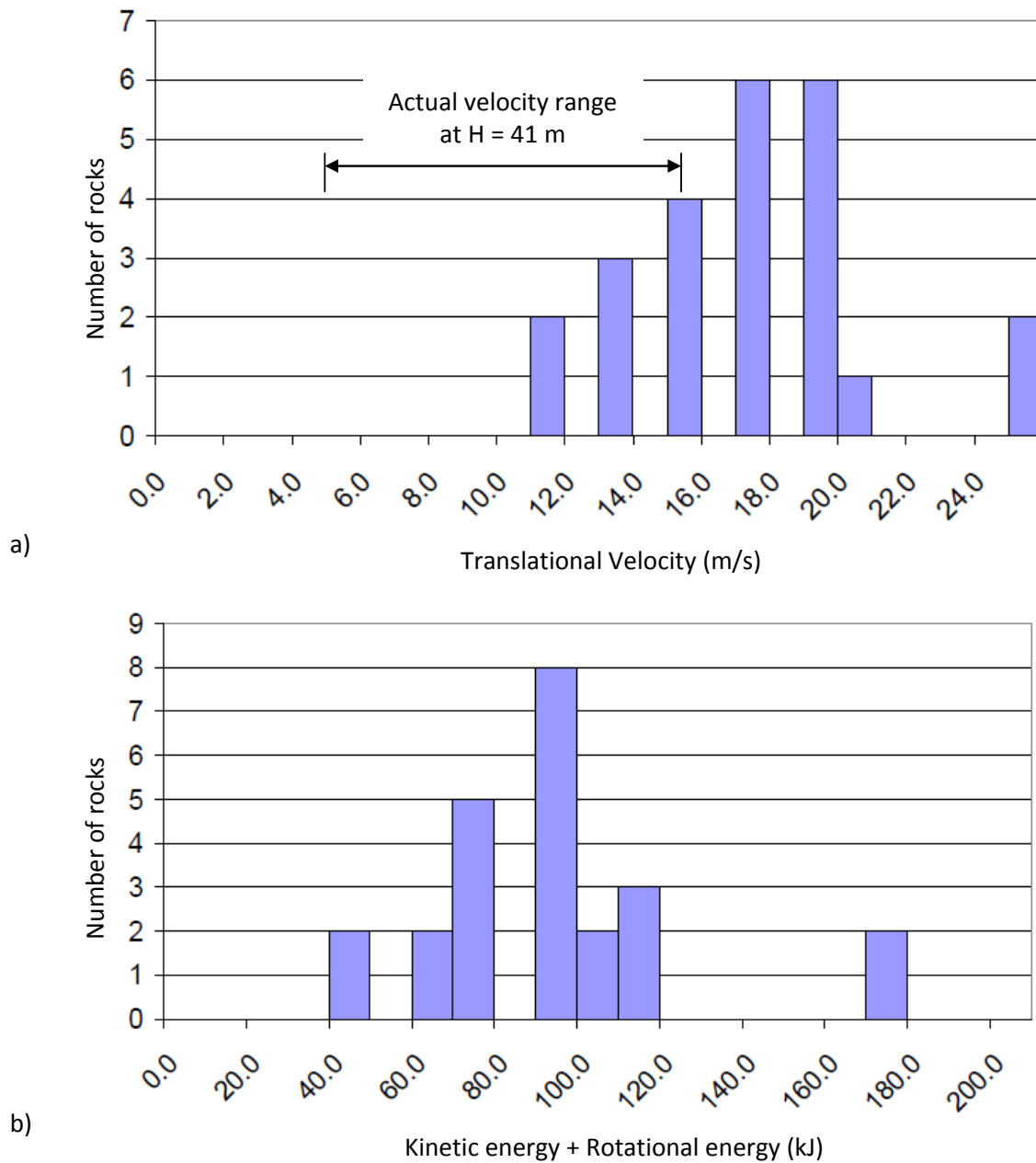


Figure 7.11: Analysis using RocFall 4.0 of rock falls at Ehime test side for 42 m (140 ft) high natural slope comprising bedrock (26 m) (85 ft) and talus (16 m) (50 ft) at analysis point x = 52.1 m a) translational velocity distribution; b) total energy (KE + RE) distribution

7.5.4 Rock fall model of Tornado Mountain events

Tornado Mountain is located in south east British Columbia near the town of Fernie (Section 2.2.2). The site of the rock falls comprises a 50 m (165 ft) high, near vertical rock face in very strong, blocky limestone above a talus/colluvium slope – the talus in the upper part of the slope is at an angle of about 35 degrees, while the colluvium forming most of the slope is at an angle of about 22 degrees (see Figure 7.12, and Figures 2.8 and 2.9). The colluvium forming the lower

slope is a mixture of gravel and soil forming a uniform slope with no significant irregularities; the slope is sparsely vegetated with trees having diameters ranging from about 300 to 500 mm (12 to 20 in).

In 2004, two separate rock falls, with masses of A = 3750 kg (8,300 lb) and B = 5600 kg (12,400 lb), occurred from a source area on the limestone cliff. The rocks travelled total distances of 740 m (2450 ft) down the slope before impacting a horizontal bench where most of the kinetic energy was absorbed and the rocks stopped within 30 m (100 ft). Because the two rocks followed slightly different paths and no previous falls had occurred in this area, it was possible to identify and map most of the impact points in the slope, including 21 trees that were sheared off by the falls. This information on the impact locations allowed velocities and trajectories to be calculated as discussed in Section 2.2.2.

Figure 7.12 shows the results of the *RocFall 4.0* simulation of Tornado Mountain fall A, with the input parameters required to produce trajectories that reasonably closely match the field measurements. Figure 7.13 compares the calculated trajectory heights with the average height measured in the field of 1.5 m (5 ft) and shows that most of the calculated trajectories are significantly higher than actual heights. This discrepancy between calculated and actual heights can lead to the construction of protection structures that are higher than required. It is the author's experience that calculated trajectories are often higher than actual trajectories.

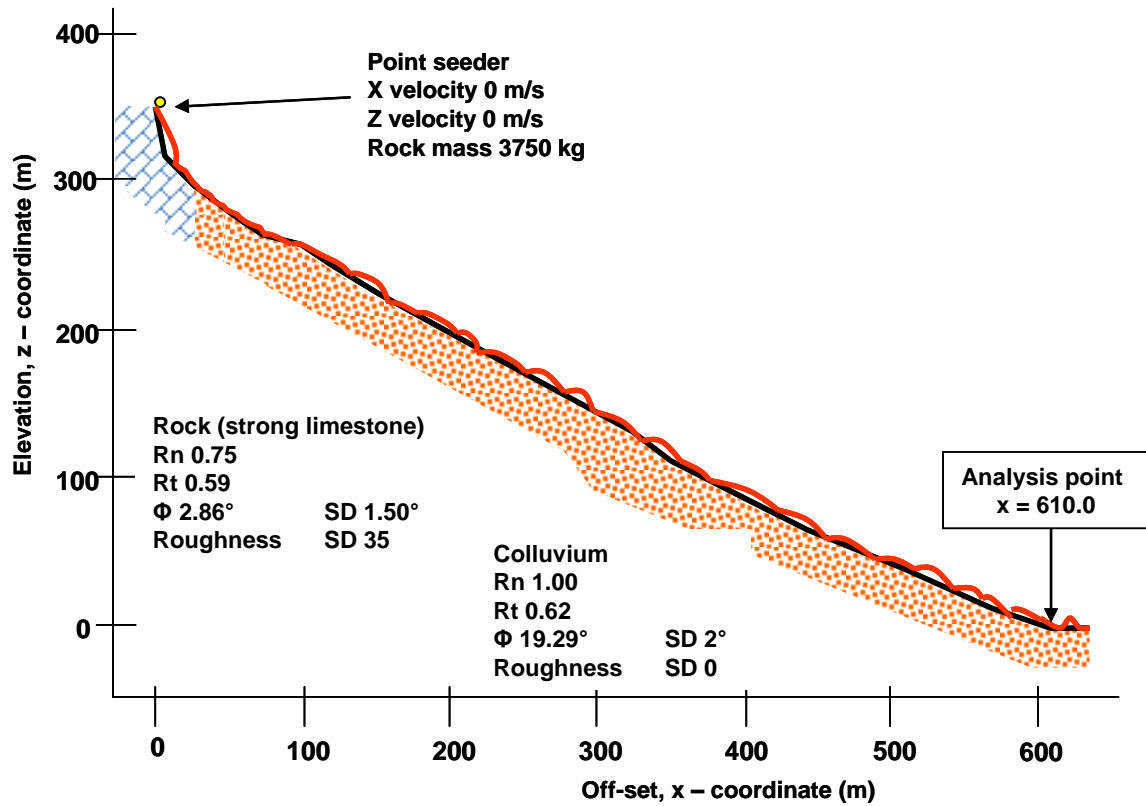


Figure 7.12: Calculated trajectories using *RocFall 4.0* for fall A, a 3750 kg (8300 lb) limestone block at Tornado Mountain

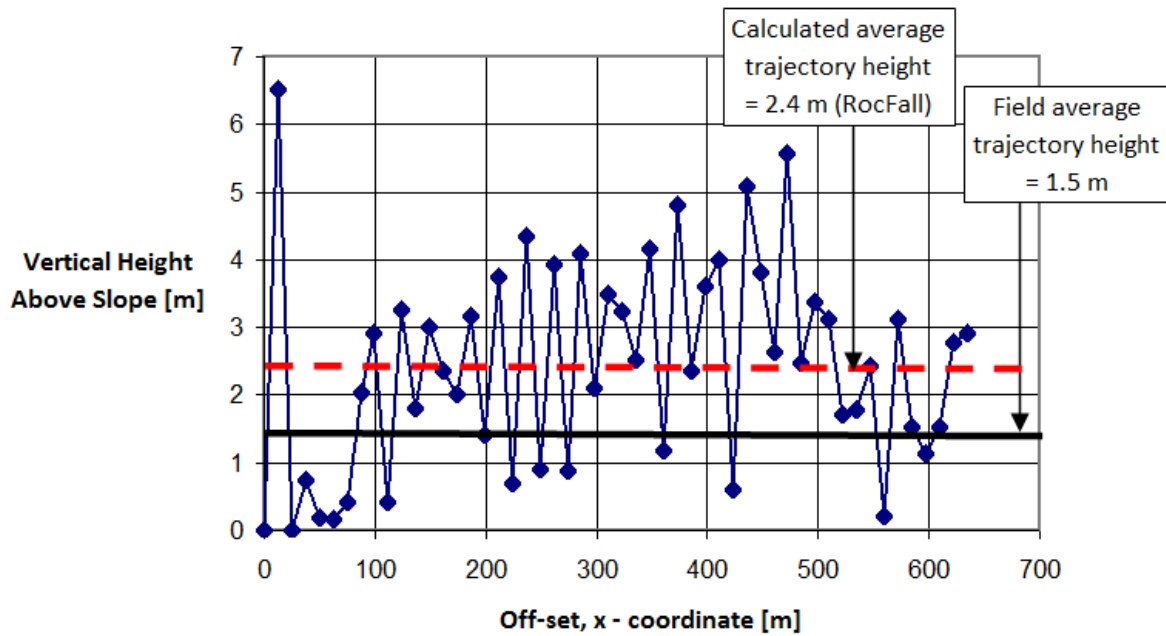


Figure 7.13: Trajectory height envelope from *RocFall 4.0* simulated results for a 3750 kg (8300 lb) limestone block at Tornado Mountain

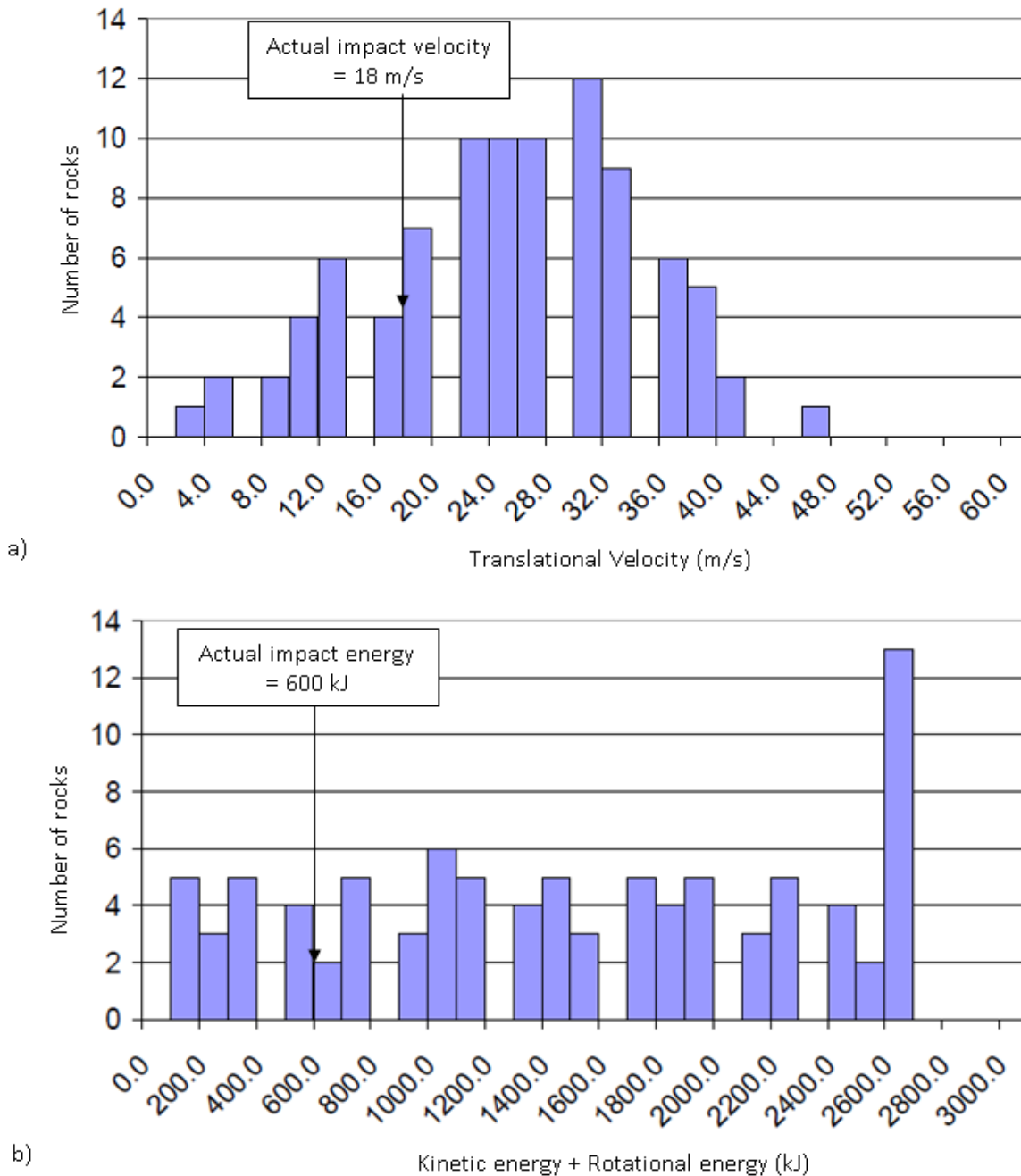


Figure 7.14: Analysis using RocFall 4.0 of rock falls at Tornado Mountain, block A at analysis point $x = 610$ m a) translational velocity distribution; b) total energy (KE + RE) distribution

Figure 7.14 shows the calculated distributions for the velocity and energy at an analysis point located just above the bench on which the railway is sited, and where a fence or barrier would likely be constructed. The actual impact properties of fall A at this location were a velocity of $18 \text{ m} \cdot \text{s}^{-1}$ ($60 \text{ ft} \cdot \text{s}^{-1}$) and a kinetic energy of 600 kJ (220 ft tons). If the block has a moment of inertia of $800 \text{ kg} \cdot \text{m}^2$ and is rotating at $15 \text{ rad} \cdot \text{s}^{-1}$, then the rotational energy, $RE = (\frac{1}{2} I \cdot \omega^2) = 90$

kJ, and the total energy is 690 kJ (255 ft tonf). These actual impact velocity and energy values are plotted on Figure 7.14, showing that they are at the low end of the calculated distributions.

The comparatively high calculated velocities may account for the calculated trajectories being higher than the actual trajectories.

7.5.5 Rock fall model of asphalt impact event

A single rock fall occurred from the crest of a natural 138 m (450 ft) high slope made up of a 56 m (180 ft) high rock slope at an angle of 60 degrees, a 70 m (230 ft) high colluvium slope at an angle of 42 degrees, and a 10 m (33 ft) high rock cut above a highway (see Section 2.3). Figure 7.15 shows two calculated trajectories for the full fall height, together with the *RocFall 4.0* parameters required to generate this simulation.

Figure 7.16 shows the calculated distributions of impact velocity and energy just before the impact with the asphalt at the analysis point $x = 140$ m. These calculated values can be compared with the precise trajectory of the fall from the crest of the rock cut to just before and after impact with the asphalt as shown in Figure 2.10 and discussed in Section 2.3. For a block with a mass of 500 kg (1100 lb), a moment of inertia, $I = (m \cdot k^2) = (500 \cdot 0.295^2) = 43.5 \text{ kg} \cdot \text{m}^2$, an impact velocity of $21.5 \text{ m} \cdot \text{s}^{-1}$ ($70 \text{ ft} \cdot \text{s}^{-1}$), and a rotational velocity of $15 \text{ rad} \cdot \text{s}^{-1}$, the impact kinetic and rotational energies are 115 kJ (42.5 ft tonf) and 4.8 kJ (1.8 ft tonf) respectively. These actual velocity and energy values are plotted on the calculated distributions.

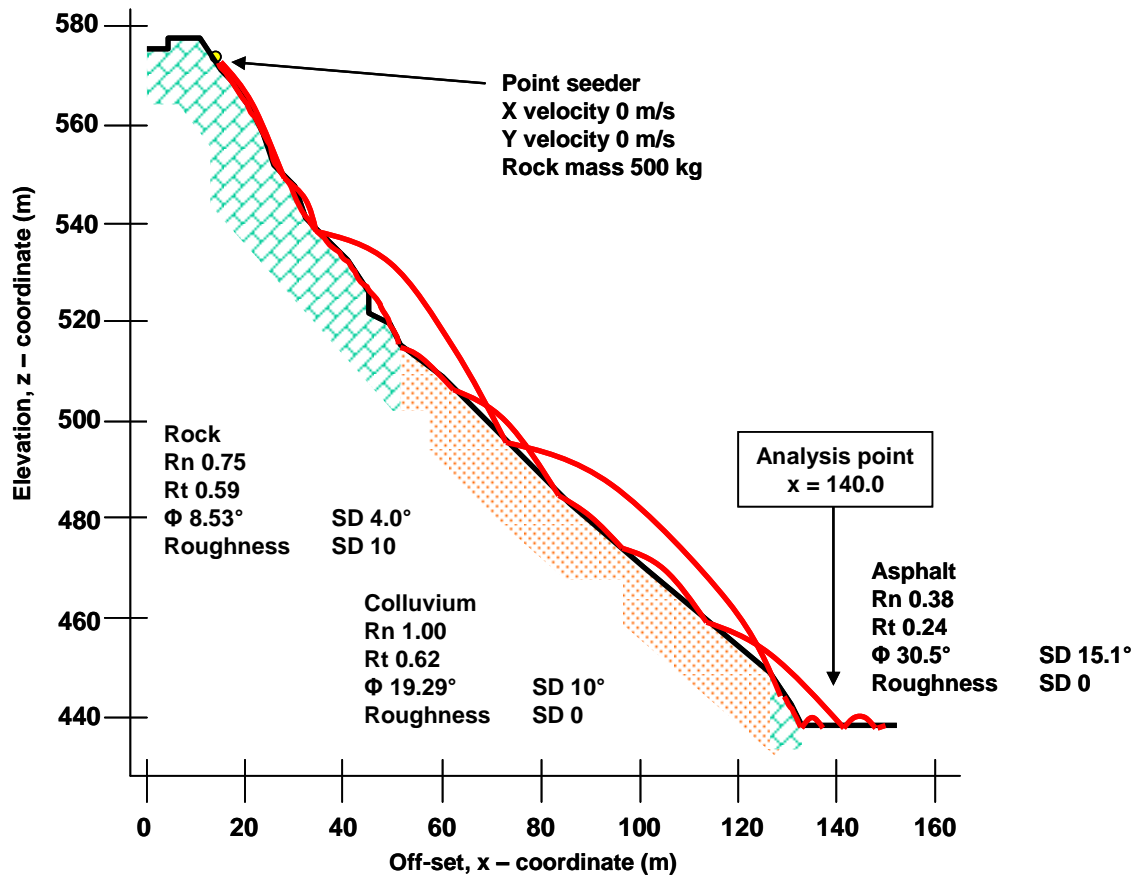


Figure 7.15: Calculated trajectories using *RocFall 4.0* of a single 500 kg (1,100 lb) rock fall from the crest of the slope and impacting the asphalt road; refer to Figure 2.10 for impact details on asphalt

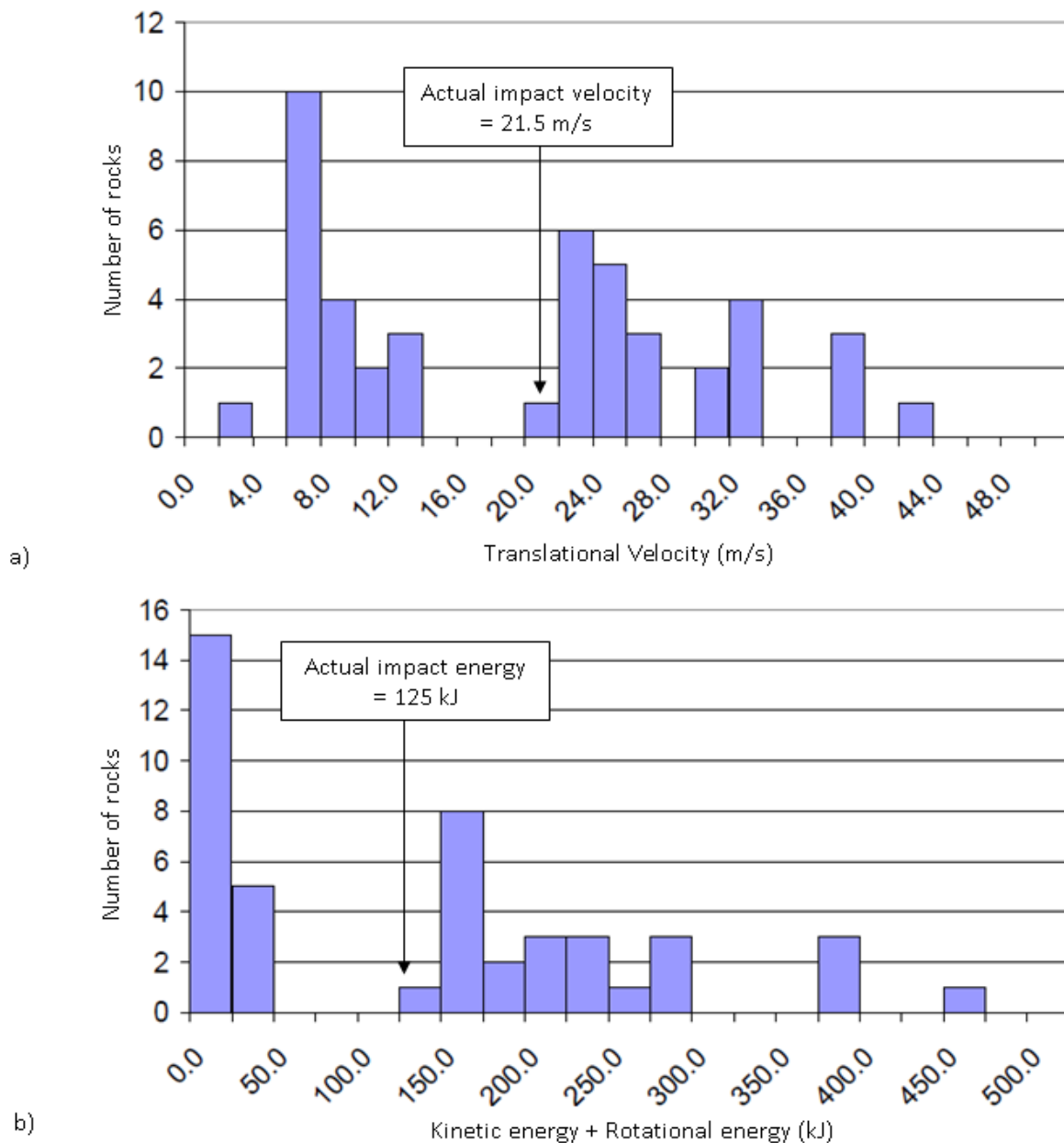


Figure 7.16: Analysis using RocFall 4.0 of rock fall impacting asphalt at analysis point x = 140 m a) translational velocity distribution; b) total energy (KE + RE) distribution

7.6 Summary of rock fall simulation results

Section 7.5 describes the results of rock fall simulations for the five case studies described in Chapter 2. The simulations show the calculated trajectory heights and the velocity and energy distributions at selected analysis points that correspond to locations where reliable field data is available. It was found that it is possible to simulate actual field conditions, although calculated trajectory heights and velocities tend to be higher than actual heights and velocities.

Furthermore, it was found that the calculated results are very sensitive to the input parameters. Table 7-1 lists the input parameters that were used in the simulations, *RocFall 4.0*.

As a general comment on the simulation of rock falls, it is difficult to obtain calculated results that are close to actual conditions without first knowing the actual field conditions in order to calibrate the calculations. That is, small changes in the input parameters can produce large changes in the calculated results that may appear to be reasonable, but are in fact incorrect. It is hoped that the simulation results presented in this chapter will be of assistance in producing reliable simulations.

Table 7-1: Summary of input parameters used in *RocFall 4.0* to stimulate case study rock falls

Site no.	Rock fall site	Slope material	Normal coefficient of restitution, e_N mean*	Tangential coefficient of restitution, e_T mean*	Friction Angle (deg) mean / SD	Slope Roughness (deg) SD
1	Mt. Stephen, Canada	rock	0.75	0.59	5.71 / 2.50	11.50
2	Oregon ditch study (rock face impact)	rock	1.00	0.59	3.01 / 3.01	5.00
2	Oregon ditch study (ditch impact)	rock	0.25	0.59	3.01 / 3.01	5.00
3	Ehime, Japan (rock slope)	rock	1.00	0.59	8.53 / 2.00	3.00
3	Ehime, Japan (talus slope)	talus	1.00	0.72	19.29 / 2.00	8.00
4	Tornado Mountain, Canada	rock	0.75	0.59	2.86 / 1.50	35.00
4	Tornado Mountain, Canada	colluvium	1.00	0.62	19.29 / 2.00	0.00
5	Highway	asphalt	0.38	0.24	30.5 / 15.10	0.00
5	Highway	rock	0.75	0.59	8.53 / 4.00	10.00
5	Highway	colluvium	1.00	0.62	19.29 / 10.00	0.00

*In RocScience 4.0, default SD for e_N and e_T = 0.04

8 Design principles of rock fall protection structures

The design of rock fall protection structures such as wire rope fences is based on the efficient absorption of impact energy. This requires that the structure be both flexible and stiff. That is, the structure must be flexible to deflect during impact, and also stiff so that energy is absorbed during deflection. The most effective protection structures are those in which energy is absorbed uniformly throughout the impact period. This chapter discusses the design principles for protection structures that absorb energy efficiently.

8.1 Structure location with respect to impact points

One of the factors in the location of protection structures is to find a position where the rock fall energy is relatively low. That is, in order to limit the impact energy on the structure, it should be located just after an impact point to benefit from the loss of energy due to plastic deformation that occurs during the time that the rock is in contact with the ground.

Energy loss during impact can be demonstrated for rock falls at the Ehime test site in Japan. For one of the tests, Figure 2.6 shows the impact and restitution velocities at each impact and the energy partition plot in Figure 6.5 shows the corresponding kinetic and rotational energies over the full extent of the rock fall path. The energy partition plot shows how the kinetic energy increases due to gravitational acceleration during the trajectories and is lost during the impacts, while the rotational energy changes (either increases or decreases) during the impacts, but remains constant during the trajectories. For impact #5 at a fall height of 15.5 m (50 ft), the impact kinetic energy is 53.4 kJ (20 ft tonf) while the restitution kinetic energy is 24.5 kJ (9 ft tonf), a loss of 28.9 kJ (11 ft tonf) or 54 per cent during impact.

While this energy loss demonstrates the value in locating the structure immediately after impact points, the generally uniform slope topography at the Ehime test site means that impacts will not occur at well-defined locations on the slope. Therefore, no optimum location for a barrier on the slope can be found.

A common topographic feature that defines an impact point along a rock fall path is a break in slope forming a relatively shallow angle bench on which rock falls will tend to accumulate. If such a feature does not occur naturally, it may be worthwhile to excavate a bench on which to

locate the barrier since it could be designed for a lower impact energy than one located on the uniform slope.

For the rock fall site at Tornado Mountain discussed in Section 2.2.2 and shown in Figure 2.8, an 8 m (25 ft) wide bench was excavated in the slope on which the railway was constructed; Figure 8.1 shows a detail of the bench. Both the documented rock falls at the site impacted this bench and stopped within 30 m (100 ft) of the railway after falling over a slope distance of about 700 m (2,300 ft) down the uniform slope above the railway.

Trajectory calculations for Boulder A show that for rock falls impacting the horizontal bench (impact #A43), the impact velocity was $17.9 \text{ m} \cdot \text{s}^{-1}$ ($60 \text{ ft} \cdot \text{s}^{-1}$) and the restitution velocity was $9.8 \text{ m} \cdot \text{s}^{-1}$ ($30 \text{ ft} \cdot \text{s}^{-1}$), representing a loss of kinetic energy of 422 kN (50 tonf) for the 3750 kg (8270 lb) block (i.e., $KE_{A43i} = 0.5 \cdot 3750 \cdot 17.92^2 = 602 \text{ kJ}$ and $KE_{A43f} = 0.5 \cdot 3750 \cdot 9.8^2 = 180 \text{ kJ}$). That is, 70 per cent of the impact energy was lost during impact #A43, whereas for impacts on the more uniform slope higher on the mountain, the typical energy loss was about 20 per cent. This demonstrates the effectiveness of a horizontal bench on mitigating rock fall hazards - for a fence or barrier located along the outer edge of such a bench, the design energy can be 50 per cent of the energy required on the uniform slope.

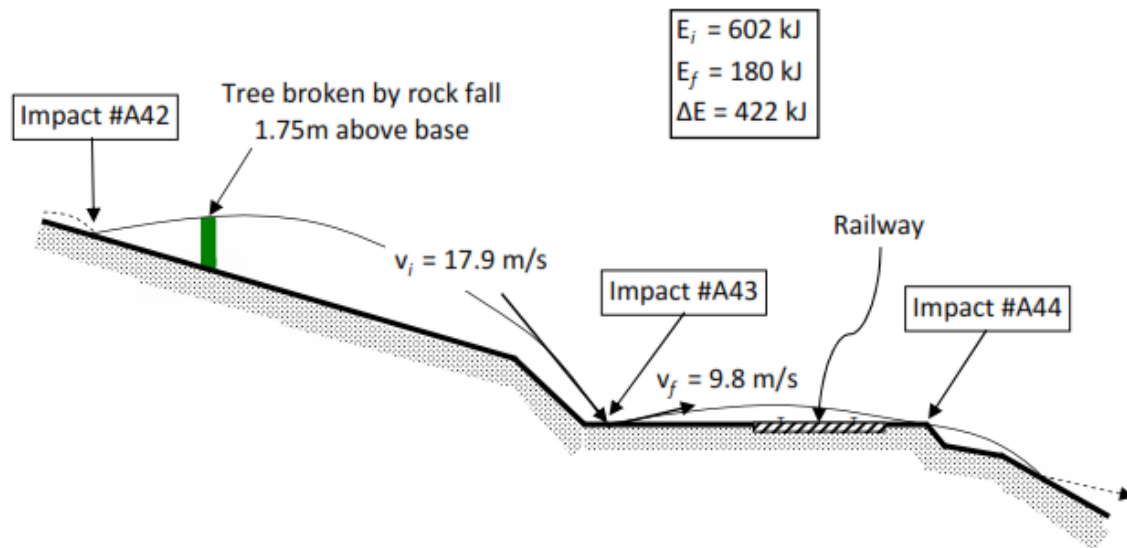


Figure 8.1: Tornado Mountain rock fall site – for impact #A43 on 8 m (25 ft) wide bench excavated for the railway, 70 per cent of the impact energy is lost during impact

8.2 Attenuation of rock fall energy in protection structures

Figure 8.2 illustrates two examples of rock fall barriers - a flexible wire rope fence that has been effective in stopping and containing rock falls, and a rigid concrete wall that has been shattered

by a rock fall. This section demonstrates how protection structures can be designed to attenuate and dissipate a portion of the impact energy rather absorb the entire energy, and how impact mechanics can be used to develop these designs.

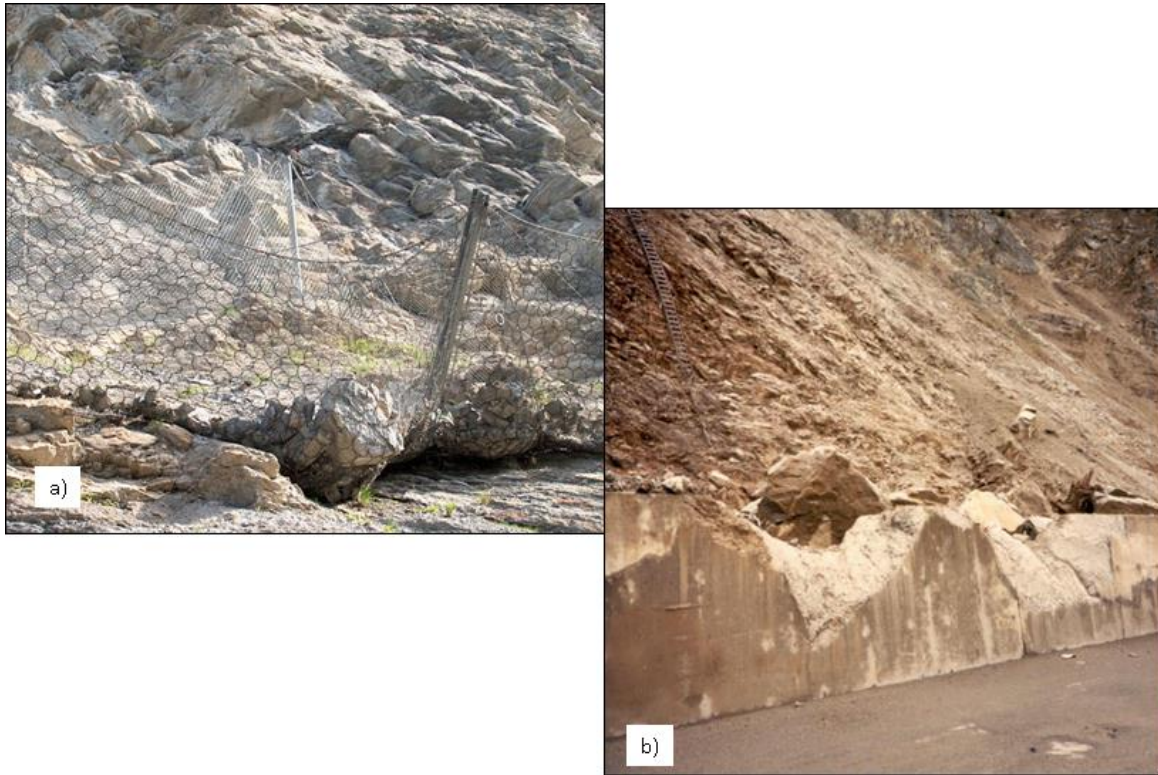


Figure 8.2: Behavior of flexible and rigid structures. a) Flexible steel cable net that stops rock falls by deflection with no plastic deformation of the steel; b) rigid concrete wall shattered by rock fall impact

8.2.1 Velocity changes during impact with a fence

If a rock fall is stopped by a protection structure, then all the impact energy is absorbed in the structure because the impact translational and rotational velocities are reduced to zero. However, if the rock is redirected by the structure, then the restitution velocities have finite values and the difference between the impact and restitution velocities represents the portion of the impact energy absorbed in the structure (Figure 8.3).

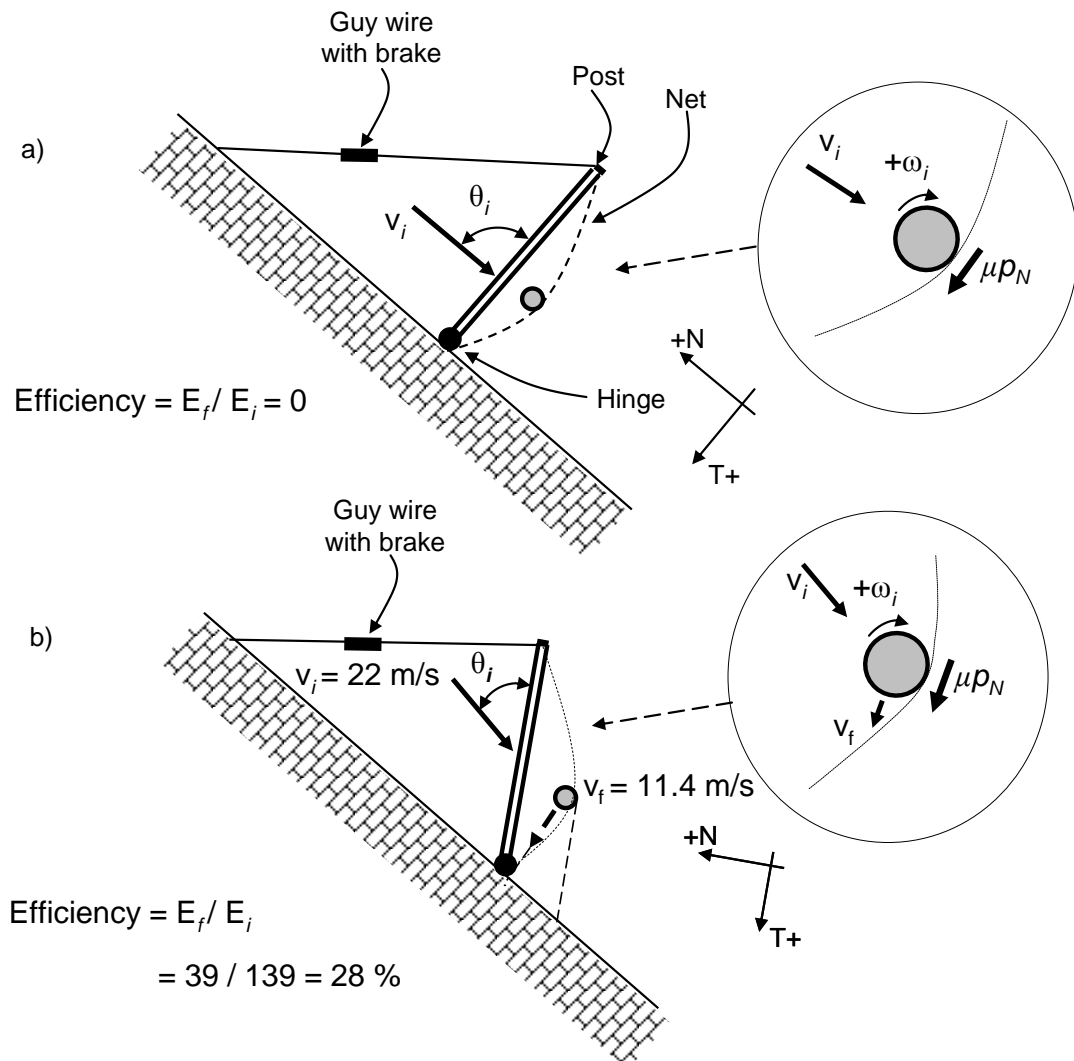


Figure 8.3: Effect of impact angle with fence on energy absorption. a) Normal impact results in the fence absorbing all impact energy; b) oblique impact results in rock being redirected off the net with partial absorption of impact energy

Figure 8.3 shows a rock fall fence on a slope at two orientations – normal to the slope (Figure 8.3a), and inclined up-slope (Figure 8.3b). The fence is impacted by a rock fall with initial translational velocity v_i and rotational velocity ω_i , at an impact angle of the rock with the net of θ_i .

For the fence oriented normal to the slope, the rock impacts the net approximately at right angles ($\theta_i = 90$ degrees). Under these conditions, the rock deflects the net and its velocity progressively diminishes until it is reduced to zero at the point of maximum deflection before it rebounds off the net. At the time of zero velocity, all the impact energy has been absorbed by the net.

In contrast to the normal impact shown in Figure 8.3a), Figure 8.3b) shows the fence oriented up-slope so that the rock fall impacts the net at an oblique angle ($\theta_i < 90$ degrees). For this impact angle, the rock is redirected by the net and the velocity decreases to v_f when it loses contact with the net; at no time during the impact does the velocity become zero. For these conditions, only a portion of the impact energy is absorbed by the fence.

The behavior of a rotating body impacting a net at either a normal or oblique angle as shown in Figure 8.3 can be modeled approximately using the principles of impact mechanics discussed in Chapter 4. That is, equations (4.20) to (4.24) can be used to calculate the influence of the fence configuration on changes in the translational and angular velocities and angles during impact.

For impact of a rotating body with a stationary net, the parameters governing the impact behavior are the normal coefficient of restitution e_N , the radius of the body r , and its radius of gyration, k . In addition, the calculations require that normal and tangential axes be set up, with the positive directions of each defined, as well as the impact and restitution angles of the velocity vectors relative to the fence. Figure 8.3 shows these axes relative to the fence, with the positive normal axis (+N) in the opposite direction to the impact direction, and the positive tangential axis (+T) in the downward direction. This means that the normal component of the impact velocity, which is towards the net, is negative ($-v_i$). The orientations of the impact (i) and restitution (f) velocity vectors – θ_i and θ_f – are defined relative to the fence inclination.

The insets on Figure 8.3 show the usual direction of rotation (clockwise) for rock falls due to the frictional forces acting at the contact point with the slope (see Section 4.5). Since the direction of rotation at the contact point is in the direction of the positive tangential axis, the clockwise rotation is defined as a positive rotational velocity. The combined effect of the rotation and normal impulse p_N is to generate a frictional force ($\mu \cdot p_N$) at the contact point that modifies the shear component of the velocity and the restitution angle as discussed in Section 4.5.

Worked example 8A below shows the method of calculating the restitution velocities of a rock fall impacting a fence at an oblique angle using equations (4.20) to (4.24) that apply impact mechanics to model velocity changes during impact.

Worked example 8A – velocity changes during oblique impact: for oblique impact of a body with a fence at the orientation shown in Figure 8.3b). The values for the impact parameters are:

$$v_i = 22 \text{ m} \cdot \text{s}^{-1}; \quad \omega_i = 18 \text{ rad} \cdot \text{s}^{-1}; \quad \theta_i = 50 \text{ degrees}$$

The body is assumed to be a cube with side length of 0.6 m (see Section 2.1 on Ehime test site, Japan), the properties of which are:

mass, $m = 520$ kg; radius (diagonal) = 0.43 m; radius of gyration, $k = 0.35$ m

For this impact geometry, the impact normal (N) and tangential (T) velocity components are as follows:

$$v_{iT} = v_i \cos \theta_i = 22 \cos 50 = 14.1 \text{ m} \cdot \text{s}^{-1}$$

and

$$v_{iN} = -v_i \sin \theta_i = -22 \sin 50 = -16.9 \text{ m} \cdot \text{s}^{-1}$$

The final tangential velocity component is calculated using equation (4.20):

$$v_{fT} = v_{iT} - \frac{(v_{iT} + r \cdot \omega_i)}{\left(1 + \frac{r^2}{k^2}\right)} \quad (4.20)$$

$$= 9.9 \text{ m} \cdot \text{s}^{-1}$$

The final normal velocity is calculated using the normal coefficient of restitution, e_N .

$$v_{fN} = -v_{iN} \cdot e_N = -(-16.9 \cdot 0.35) = 5.9 \text{ m} \cdot \text{s}^{-1} \quad (4.21)$$

where e_N is defined by the impact angle θ_i as demonstrated in Section 5.2.2 and Figure 5.7. Equation (5.4); approximately relates e_N and θ_i as follows:

$$e_N = 19.5 \cdot \theta_i^{-1.03} \quad (5.4)$$

Therefore, for an impact angle of 50 degrees, the approximate normal coefficient of restitution is 0.35.

The final rotational velocity is given by equation (4.22):

$$\omega_f = \omega_i - \frac{r (v_{iT} + r \cdot \omega_i)}{k^2 \left(1 + \frac{r^2}{k^2}\right)} \quad (4.22)$$

$$= -11.6 \text{ rad} \cdot \text{s}^{-1}$$

The final restitution velocity v_f and angle θ_f can be calculated from the final tangential and normal velocities components as follows:

$$v_f = \sqrt{v_{fT}^2 + v_{fN}^2} = 11.5 \text{ m s}^{-1} \quad (4.23)$$

and

$$\theta_f = \text{atan}\left(\frac{v_{fN}}{v_{fT}}\right) \quad (4.24)$$

$$= 31 \text{ degrees}$$

On Figure 8.3b), the velocity vectors are drawn to scale to show the results of the impact calculations. These calculations show that the redirection of the body by the net results in the velocity being reduced by 48 per cent, from $v_i = 22 \text{ m} \cdot \text{s}^{-1}$ to $v_f = 11.5 \text{ m} \cdot \text{s}^{-1}$. The velocity will decrease up to the point of maximum deflection and will not be zero at any time.

The change in the rotational velocity from $\omega_i = +18 \text{ rad} \cdot \text{s}^{-1}$ to $\omega_f = -11.6 \text{ rad} \cdot \text{s}^{-1}$ indicates that the direction of rotation reverses during impact. Model tests of bodies impacting the net at an oblique angle indicate the reversal of the rotation direction.

8.2.2 Energy changes during impact with a fence

The velocity changes during impact with the fence discussed in Section 8.2.1 above and shown in Figure 8.3 can also be used to calculate the energy changes during impact and determine how much of the energy is absorbed by the net.

For the fence configuration shown in Figure 8.3a) where the impact is normal to the net, the velocity of the rock is reduced from the initial velocity v_i at the moment of impact to zero at the time of maximum deflection. Therefore, the total impact energy of the rock fall is absorbed by the net, i.e. ($E = \frac{1}{2} m \cdot v_i^2$). This type of impact is also illustrated in Figure 8.2a) where the rocks that have been stopped by the net accumulate in the base of the fence.

For the fence configurations shown in Figures 8.3b) and 8.4 where the impact is oblique to the net, the velocity decreases during impact but the rock is not stopped. Therefore, only a portion of the impact energy is absorbed by the fence, with the remainder of the energy being retained by the moving rock.

Worked example 8B below illustrates the calculation method for an oblique impact with a fence.

Worked example 8B – energy changes during oblique impact: calculations of the velocity changes that occur during an oblique impact are described in Worked example 8A. The corresponding energy changes during impact are calculated as follows.

For an oblique impact of 50 degrees with the net, the velocity decreases from $22 \text{ m} \cdot \text{s}^{-1}$ to $11.5 \text{ m} \cdot \text{s}^{-1}$, and the rotational velocity changes during impact from $18 \text{ rad} \cdot \text{s}^{-1}$ to $-11.6 \text{ rad} \cdot \text{s}^{-1}$.

The moment of inertia of the body, $I = m \cdot k^2 = 520 \cdot 0.35^2 = 63.7 \text{ kg} \cdot \text{m}^2$

Assuming that the mass of the rock remains constant during impact, the initial and final energies are as follows:

$$\text{Initial energy: } KE_i = \frac{1}{2} m \cdot V_i^2 = \frac{1}{2} 520 \cdot 22^2 = 125.8 \text{ kJ}; \quad RE_i = \frac{1}{2} I \cdot \omega_i^2 = \frac{1}{2} 63.7 \cdot 18^2 = 10.3 \text{ kJ}$$

$$\text{Total impact energy, } E_i = (125.8 + 10.3) = 136.1 \text{ kJ}$$

$$\text{Final energy: } KE_f = \frac{1}{2} m \cdot V_f^2 = \frac{1}{2} 520 \cdot 11.5^2 = 34.4 \text{ kJ}; \quad RE_f = \frac{1}{2} I \cdot \omega_f^2 = \frac{1}{2} 63.7 \cdot (-11.6)^2 = 4.3 \text{ kJ}$$

$$\text{Total final energy, } E_f = (34.4 + 4.3) = 38.7 \text{ kJ}$$

These calculations show that, for an oblique impact, the impact energy that is absorbed by the net is 97.4 kJ ($136.1 - 38.7$), which is only 72 per cent of the impact energy compared to 100 per cent of the impact energy for a normal impact.

8.2.3 Energy efficiency of fences

The discussion on the velocity and energy changes related to the impact configuration in Sections 8.2.1 and 8.2.2 above can be used to quantify the relationship between energy absorption by the fence and the impact configuration.

For a normal impact where the rock fall is stopped by the net, all the impact energy is absorbed by the structure, which has to be designed to withstand the full impact energy. In contrast, for an oblique impact only a portion of the impact energy is absorbed by the structure. The portion of the impact energy that is deflected by the net can be expressed in terms of the efficiency of the structure as follows:

$$\text{Efficiency, } E_e = \frac{\text{Restitution energy, } E_f}{\text{Impact energy, } E_i} \cdot 100\% \quad (8.1)$$

For the two fence configurations shown in Figures 8.3a) and b), the efficiencies are respectively 0 per cent for the normal impact and $E_e = 39.2/138.8 = 28$ per cent for the oblique impact where the rock fall is redirected by the net.

The benefit of a high efficiency fence is that, for the same impact energy, it can be constructed from lighter weight materials than a zero efficiency fence. Conversely, design impact loads will be greater with increasing energy efficiency of the fence. The influence of fence configuration on energy efficiency is discussed further in Section 8.3 and 8.4 of this chapter.

8.2.4 Configuration of redirection structures

Figure 8.3 shows how an oblique impact on a net can be achieved by inclining the fence up-slope. The same impact configuration occurs for the hanging net shown in Figure 8.4 where a vertical hanging net, that is unconstrained along its lower edge, is suspended from a series of posts attached to the rock face. When rock falls impact the net, their velocity is reduced and they are redirected into a catchment area at the base of the net; the rock falls that accumulate in the catchment area can be readily removed by maintenance equipment. In comparison, for the net shown Figure 8.2a) removal of accumulated rock falls requires access of the slope to detach the lower edge of the net from the support cables.

The hanging net configuration shown in Figure 8.4 is applicable at locations where the rock face is near vertical and the ditch width is limited so that it is not possible to construct the type of fence shown in Figure 8.2a).

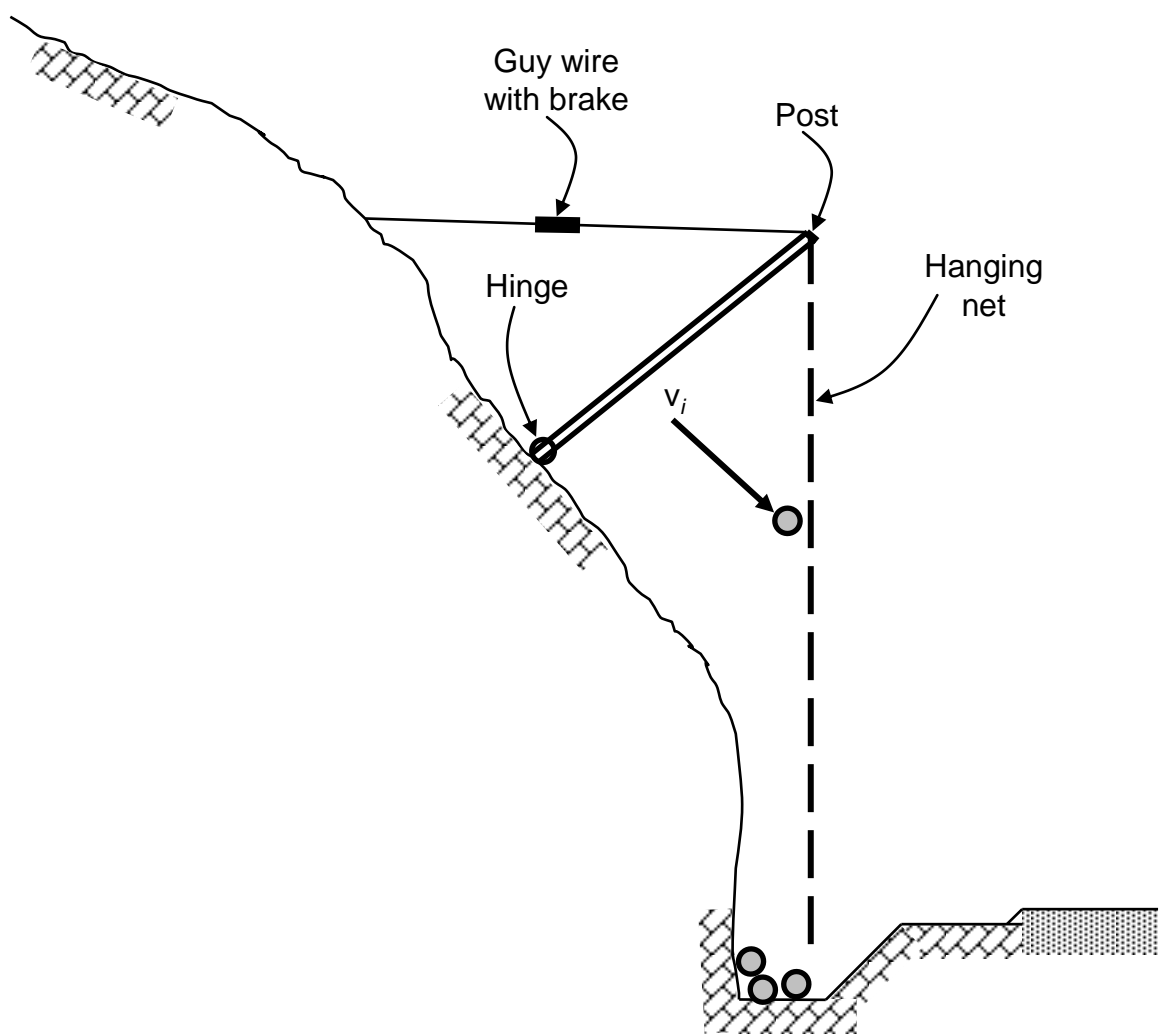


Figure 8.4: Hanging net installed on steep rock face that redirects rock falls into containment area at base of slope, where cleanout of accumulated rock falls is readily achieved

8.2.5 Hinges and guy wires

Both the fence configurations shown in Figures 8.3b) and 8.4 incorporate hinges at the base of the posts, and guy wires, equipped with brakes, to hold the posts in place. These two components of the fences are energy absorbing features that, together with the net itself, ensure that the entire structure is flexible. Ideally, all components of the fence are equally flexible because forces tend to concentrate in the stiffest part of the structure. The absorption of impact energy with time in rock fall containment structures is discussed in Section 8.3, with the design objective being to absorb energy uniformly during impact in order to minimize the forces induced in the structure.

Commercially available braking elements in the guy wires, comprising a variety of loops, coils or sliding connections, that absorb energy by plastic deformation and need to be replaced when

the impact energy exceeds the service limit state. Nets are generally designed for easy replacement of brakes.

Many commercial rock fall fences also incorporate hinges at the base of posts, the primary function of which is to allow the post to deflect in the event of an impact energy that exceeds the Service limit states energy. When this occurs, the post will deflect without damaging the foundation so that repairs to the fence are limited to re-standing the posts and replacing any damaged net and brake components; this is less costly than rebuilding the foundations. Figure 8.5 shows a post for a hanging net that was impacted by a snow avalanche, with an energy that exceeded the Service limit state but was less than the Ultimate limit state. For this impact, the net and posts were deflected by several meters and the brakes on the guy wires were activated and needed to be replaced, but no damage occurred to any net component.



Figure 8.5: Low friction hinge at base of post allowed the post to deflect, with no damage to the foundation, during an impact that exceeded the service limit states energy (above Shuswap Lake, British Columbia, Canada)

In contrast to the energy absorbing features of brakes, most hinges are low friction units that do not absorb energy when the post deflects. It is believed that inclusion of frictional elements into hinges will allow the hinges to both deflect in order to prevent damage to the foundation, and to absorb energy. The combined activation of the guy wire brakes and the post frictional hinges will produce a reasonably uniform absorption of energy during the time of impact. As discussed in Section 8.3 below, uniform energy absorption with time minimizes the forces that are induced in the fence by the impact.

8.3 Minimizing forces in rock fall protection fences

A fundamental design feature of effective rock fall fences and barriers is the flexibility of the structure so that energy is absorbed in the structure during impact. An example of a flexible structure is a net fabricated with woven steel wires that is supported on posts with flexible hinges and deformable guy wires; most components of the net will deform and absorb energy with impact (Figure 8.2a)). This energy absorption will not, up to the design (service) energy, cause any damage to the structure. In contrast, rigid structures such as mass concrete walls have essentially no capacity to absorb energy except by fracturing, resulting in permanent damage (Figure 8.2b)).

8.3.1 Time – force behavior of rigid, flexible and stiff structures

The capacity of a structure to absorb energy can be quantified by examining the force generated in the structure during the time of impact. This behavior is illustrated in Figure 8.6 by [time – force] plots for three different types of structure. These plots do not show the behavior of actual structures, but demonstrate the difference between the rigid, flexible and stiff structures, the characteristics of which are discussed below.

The objective of studying [time – force] behavior is to design structures in which the force induced by the impact in the structure is minimized. That is, it is preferable that structures have high energy efficiency as defined in Section 8.2.3 above. By minimizing the induced force it is possible to construct fences that use lighter weight materials, and are less costly, than if the full impact energy has to be absorbed by the fence.

Figure 8.6 shows typical [time – force] relationships for rigid, flexible and stiff fences, and the equations that define these relationships. The physical characteristics of these three types of structures are discussed below.

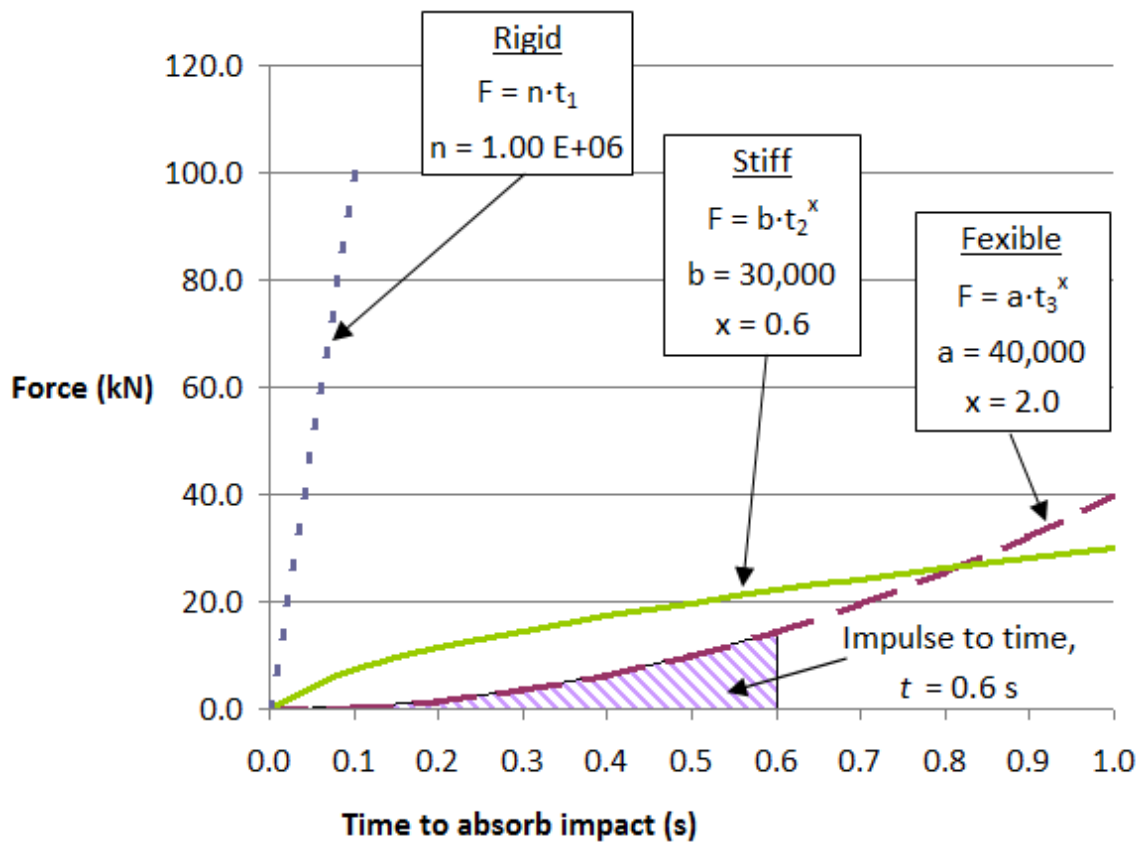


Figure 8.6: Relationship between time of impact and force generated in rigid, flexible and stiff fences

- a) **Rigid structures** – for a rigid structure such as a mass concrete wall, the primary means of energy dissipation is shattering of the brittle concrete and permanent damage to the structure (Figure 8.2b)). This behavior is illustrated in Figure 8.6 as a straight line with a steep gradient representing the very short time of impact before fracturing occurs at a force equal to the strength of the concrete. This behavior shows that concrete walls are not effective rock fall barriers.
- b) **Flexible structures** – a variety of rock fall fences are available in which all the components are flexible, and energy is absorbed by deformation of these components without damage (Figure 8.2a)). For these structures in which the components are highly flexible, a significant amount of deformation has to occur before energy starts to be absorbed. Furthermore, if the bases of the support posts incorporate low friction hinges, no energy is absorbed as the posts rotate on the hinges. This behavior is illustrated in Figure 8.6 by a curve that shows little force generated in the fence during the early time of impact, after which the force increases with increasing deformation of the net and supports. Flexible structures are

effective in containing rock falls, but must be strong enough to absorb the full impact energy since the rock falls are stopped by the net.

c) **Stiff structures** – stiff structures are modified flexible fences that are designed to start absorbing energy from the moment of impact. The behavior is illustrated in Figure 8.6 as a curve with an approximately constant gradient throughout the time of impact, after the initial contact. This [time – force] behavior is achieved by the following characteristics of fence design:

- Attenuation and redirection – Section 8.2.1 above and Figure 8.3 demonstrate the difference between normal and oblique impact of a rock fall with a fence, and how the energy efficiency can be improved by the rock being redirected rather than stopped by the structure.
- Flexible nets – a variety of nets are available in which the steel wire or cable components deform during impact. Nets that are slightly stretched between the support cables will be somewhat stiffer than nets that are very loosely attached to the cables.
- Frictional hinges – posts supporting rock fall nets are usually anchored to the ground with rock or soil anchors, or attached to concrete blocks buried in the ground. The connection between the posts and the foundation can be rigid or hinged, with the advantage of hinged connections being that the post can deflect without damage to the foundation, resulting in reduced maintenance costs. However, if the hinge is very flexible, then no energy is absorbed during deflection. In a stiff structure, hinges are frictional so that the posts can deflect without damaging the foundations, but energy will be absorbed during deflection.
- Energy absorbing guy wires – it is common that the guy wires supporting fence posts incorporate brakes that deform plastically and absorb energy where the impact energy exceeds a design threshold.

If these four features have the same [time – force] and stiffness characteristics then they will absorb energy simultaneously, starting at the time of first contact. These features and the performance of stiff fences are discussed in more detail in Section 8.5, Model testing.

8.3.2 Energy absorption by rigid, flexible and stiff structures

The [time (t) – force (F)] plots in Figure 8.6 are modeled as a straight line for the rigid concrete wall, and as power curves for the flexible and stiff fences according to the following relationships:

- **Rigid structure** – $F = n \cdot t_1$ (8.2)

where n is the gradient of the line analogous to the stiffness of the structure, and t_1 is the duration of contact. For a mass concrete, unreinforced wall an assumed value for the gradient is 1E6 units [MLT⁻³], consistent with the short duration of contact and the large force generated in the structure in this time.

- **Flexible structure** – $F = a \cdot t_2^x$ (8.3)

where a is a constant, t_2 is the duration of contact and x is an exponent that has a value greater than 1; an exponent greater than 1 generates a curve for which the force is negligible during the initial contact and then increases rapidly with time. For this illustration of the behavior of a flexible structure, the value of a is 40,000 and the exponent x is 2.0.

- **Stiff structure** – $F = b \cdot t_3^x$ (8.4)

where b is a constant, t_3 is the duration of contact and x is an exponent that has a value less than 1; an exponent less than 1 generates a curve for which the force increases steadily throughout the contact time. For this illustration of the behavior of a stiff structure, the value of b is 30,000 and the exponent x is 0.6.

For [time – force] plots illustrated in Figure 8.6, the area under the curve equals the impulse of a rock fall absorbed by the structure over any specified time interval (see Section 4.2 and equation (4.1)). The impulse (or momentum) of the rock fall at the time of contact with the structure is equal to $(m \cdot v_i)$, where m is the mass of the rock fall and v_i is the impact velocity. The duration of the contact time must be sufficient for the impact impulse to be absorbed, and this contact duration will differ with the stiffness of the structure. That is, for a rigid structure, the contact duration, t_1 will be short because of the rapid increase in the force, while for flexible and stiff structures the contact duration t_2 and t_3 will be longer than t_1 as the force increases slowly

during contact. The objective of this design approach is to minimize the force in the structure, and this is achieved with a relatively long duration contact time.

The impulse absorbed by the structure can be obtained by integration of the [time – force] plots to find the areas under the curves over the duration of contact, as follows:

- **Rigid structure** – from equation (8.2), impulse absorbed by the structure over contact time t_1 is:

$$p = \int_0^{t_1} F dt = n \int_0^{t_1} t dt = \frac{1}{2} n \cdot t_1^2 \quad (8.5)$$

- **Flexible structure** – from equation (8.3), impulse absorbed by the structure over contact time t_2 , for $x > 1$ is:

$$p = \int_0^{t_2} F dt = a \int_0^{t_2} t^x dt = \frac{a}{(x+1)} t_2^{(x+1)} \quad (8.6)$$

- **Stiff structure** – from equation (8.4), impulse absorbed by the structure over contact time t_3 , for $x < 1$ is:

$$p = \int_0^{t_3} F dt = b \int_0^{t_3} t^x dt = \frac{b}{(x+1)} t_3^{(x+1)} \quad (8.7)$$

In Figure 8.7, these integrated equations are plotted to show the relationship between the time of contact and the impulse absorbed by the fence.

If the impulse of the rock fall is defined by the mass and velocity at the time of contact, then equations (8.5), (8.6) and (8.7) can be solved to find the duration of contact for each type of structure. Referring to the Worked Example 9A above, for a rock fall mass, m of 520 kg (1150 lb) and impact velocity, v_i of 22 m · s⁻¹ (70 ft · s⁻¹), the impulse is 11,440 kg · m · s⁻¹. For this impulse, the corresponding contact durations are:

- **Rigid structure:** for $n = 1E6$, $t_1 = 0.15$ seconds.
- **Flexible structure:** for $a = 4E4$ and $x = 2.0$, $t_2 = 0.95$ seconds.
- **Stiff structure:** for $b = 3E4$ and $x = 0.6$, $t_3 = 0.73$ seconds.

These contact duration can be substituted in equations (8.2), (8.3) and (8.4) to find the maximum forces generated in the structures during contact as follows:

- **Rigid structure:** for $t_1 = 0.15$ seconds, $F = 151$ kN.
- **Flexible structure:** for $t_2 = 0.95$ seconds, $F = 36.1$ kN.
- **Stiff structure:** for $t_3 = 0.73$ seconds, $F = 22.0$ kN.

Figure 8.7 shows the [time – impulse] plots for the three types of structure that are given by equations (8.5), (8.6) and (8.7) and represent the areas under the [time – force] plots given in Figure 8.6. Figure 8.8 shows the force generated in the structure due to the absorption of the applied impulse. The plots in Figures 8.7 and 8.8 and the values of the maximum forces show that stiff structures absorb impact energy more efficiently than both rigid and highly flexible structures. For the example presented in this section, the maximum force generated in a stiff structure is only 15 per cent ($22.0/151 = 0.15$) of that for a rigid structure, and 61 per cent ($22.0/36.1 = 0.61$) of that for a flexible structure.

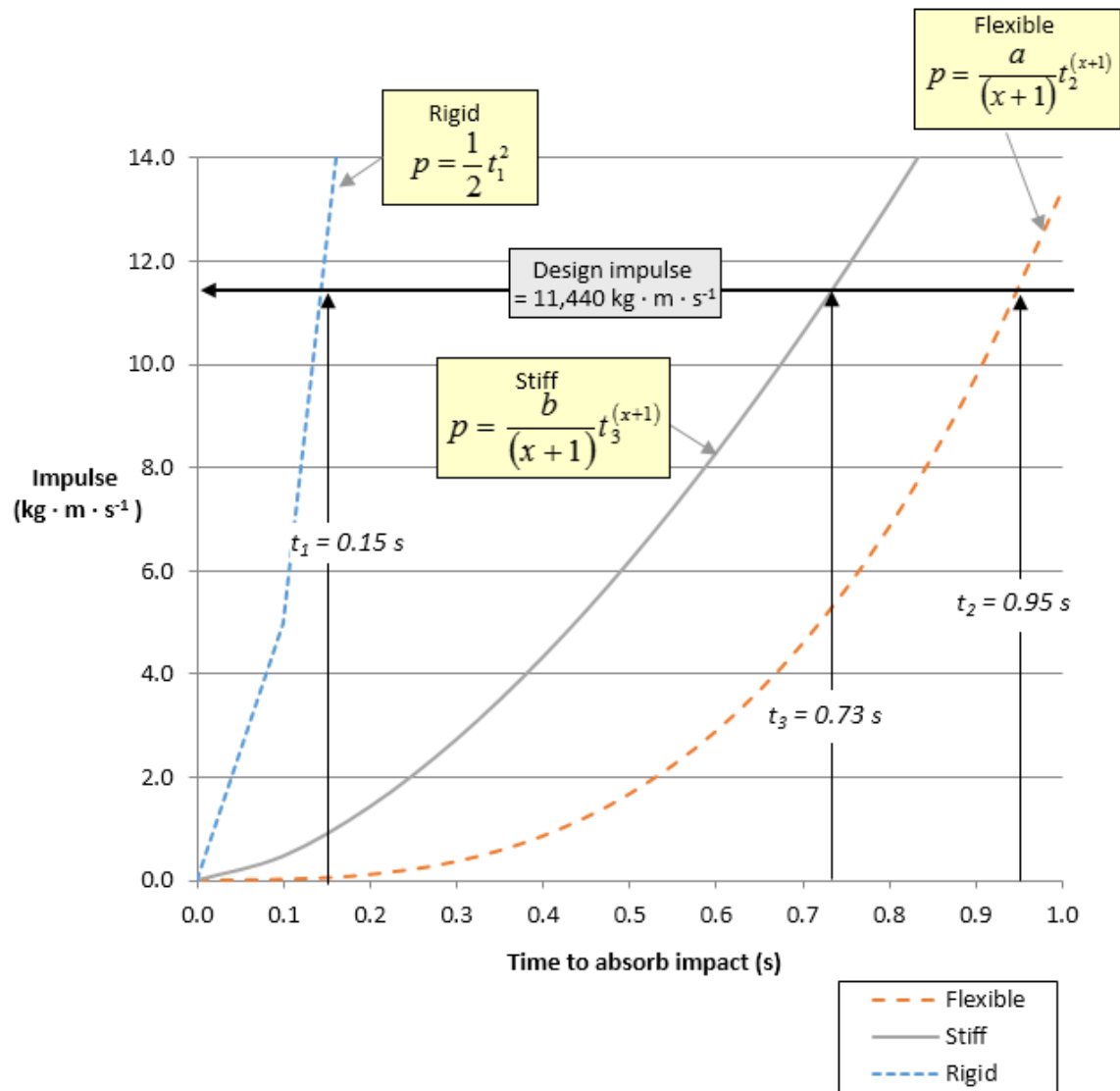


Figure 8.7: Plot of duration of impact against rock fall impulse absorbed by fence; curves are developed by integrating [time-force] equations shown in Figure 8.6 to give the area under [time – force] curves

The calculated forces in the three structures can be illustrated graphically on the [time – force] plot in Figure 8.8.

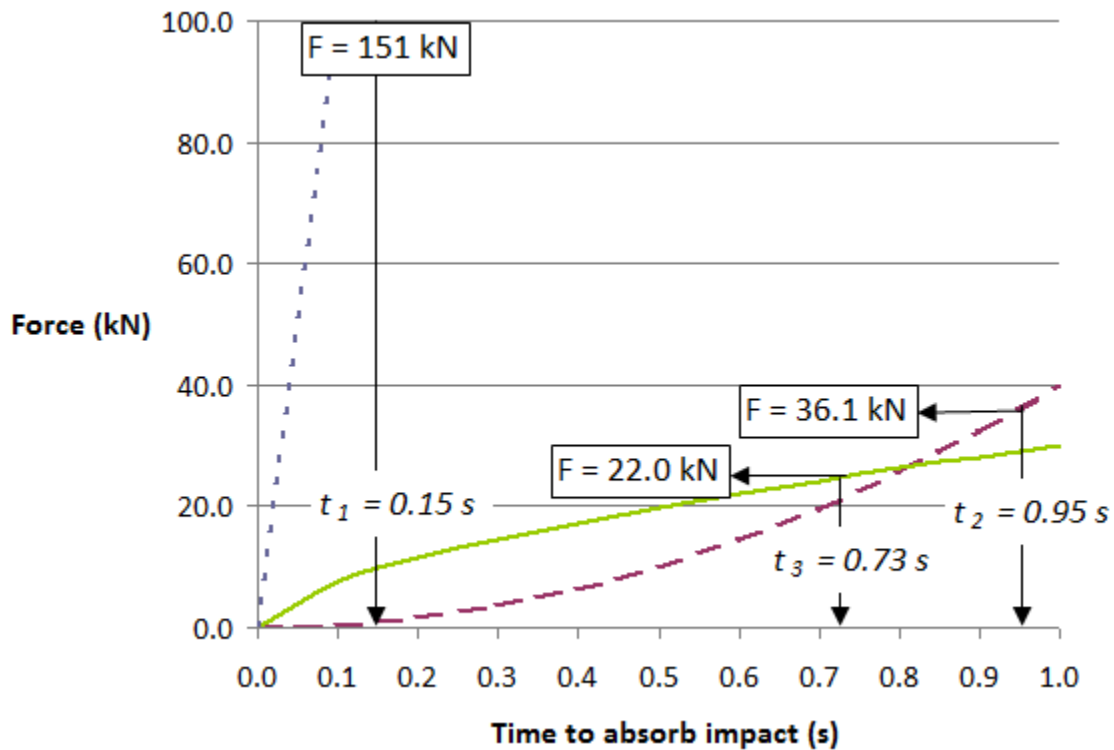


Figure 8.8: [Time – force] plot for rigid, flexible and stiff structures showing force generated in structure at time taken to absorb impact impulse

8.4 Design of stiff, attenuator fences

This chapter has discussed two concepts related to the energy absorption efficiency of rock fall fences – attenuation and uniform energy absorption. First, an oblique impact in which the rock is redirected by the net results in only a portion of the impact energy being absorbed by the fence, with the remainder of the energy being retained in the moving rock. This is in contrast to normal impact between the net and a rock fall where all the energy is absorbed as the rock is brought to rest by the fence. Fences that deflect rock falls may be termed “attenuator” structures.

Second, for a fence designed so that the energy is absorbed uniformly with time, the forces generated in the fence by the impact will be less than that for both rigid and highly flexible structures. Fences with uniform energy absorption with time may be termed “stiff” structures.

Figure 8.3b) shows a fence that is inclined up-slope, while Figure 8.9 shows an alternative configuration in which the posts supporting the net are made of two segments; in both cases, a hinge is located at the connection between the base of the post and the foundation. The function of the up-slope segment of the net is to create impacts at an oblique angle so that the

net acts as an attenuator, with the rock falls being redirected so only a portion of the impact energy is absorbed by the fence. Also, if the net is slightly tensioned between the support posts, and the hinge has frictional resistance to movement, energy is absorbed approximately uniformly during impact. For the fence configuration shown in Figure 8.9, rock falls impacting the lower (down-sloping) segment of the net will deform the net and then impact the slope, with the ground taking out the remaining energy.

The functions of the two net segments are related to the trajectories of rock falls and their related energies (Figure 8.9). Rock fall energies are lowest immediately after impact with the ground where much of the energy is lost in plastic deformation, and highest at the end of the trajectory when the fall has been subject to gravity acceleration. The energy changes during impact and trajectory phases of rock falls are illustrated graphically on energy partition diagrams (Figures 6.5 and 6.7), on which the low energy portions of the fall after each impact can be clearly identified. Based on the principles shown in the energy partition diagrams, fences should be designed to withstand the high energy portion of falls, i. e., at the end of trajectories, if it is not possible to locate the fence on the outside of a bench where rock falls will impact as shown in Figure 8.1.

Figure 8.9 shows three trajectories: trajectory A is a low energy impact occurring soon after impact, while trajectories B and C are higher energy impacts occurring a longer time after impact. In Figure 8.9, trajectory B impacts the upper portion of the fence at an oblique angle and is redirected toward the ground by the net so the energy is attenuated. Trajectory C impacts the lower part of the fence such that the net is deflected and impacts the ground where the impact energy is absorbed.

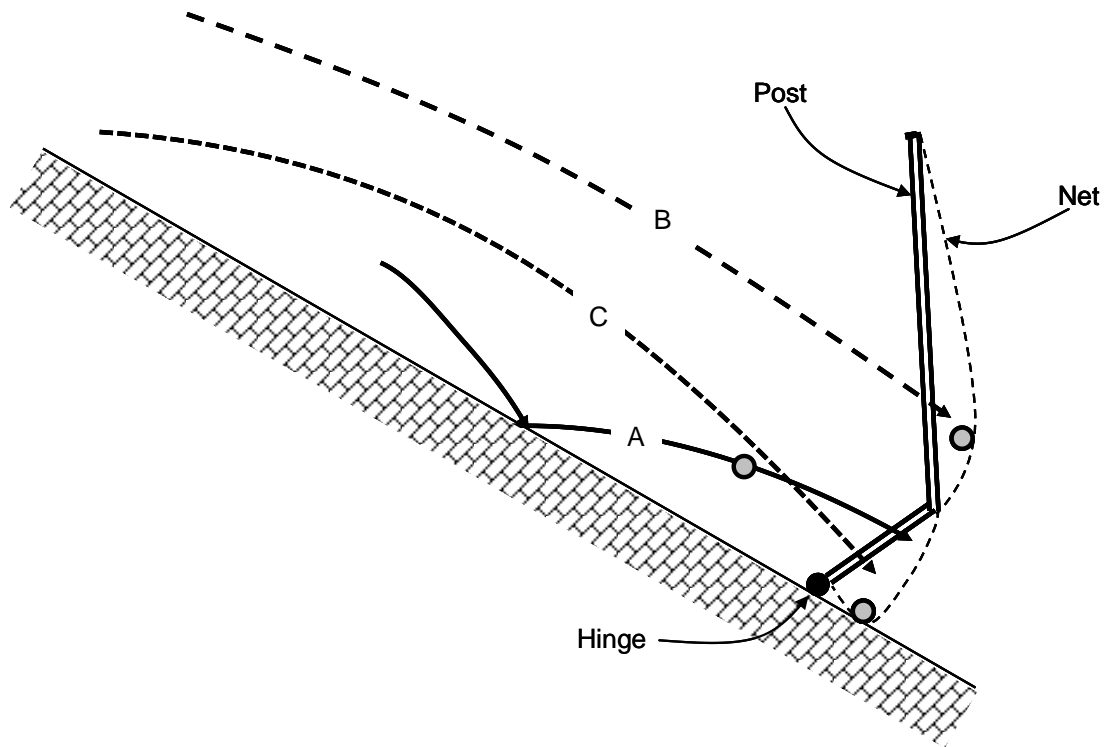


Figure 8.9: Rock fall trajectories impacting attenuator type fence. Trajectory A – low energy impact close to slope impact point; trajectories B and C – high energy impacts distant from prior impact point

The fence configuration shown in Figure 8.9 is a concept that illustrates the principles of efficient fence design that may have application in commercial products⁴.

8.5 Model testing of protection structures

This chapter discusses both attenuation of rock falls by rock fall fences, and the performance of stiff structures in terms of impact mechanics. In order to validate these concepts and calculations, model tests of an attenuator fence were carried out as described below.

8.5.1 Model testing procedure

The model testing procedure involved using a baseball pitching machine to propel baseball-size projectiles at a 1/20 scale model of a rock fall fence. It was possible to closely control the velocity of the projectiles, and to have both rotating and non-rotating impact. Rotation of the projectile was achieved by having the projectile impact the slope just above fence so that the direction of rotation was counter-clockwise, which is the same direction as usually occurs in

⁴ United States patent pending, Energy Absorbing Barrier; European patent pending.

actual rock falls. Impact of non-spinning particles was achieved by having the projectiles impact the net without first impacting the slope. Translational and rotational velocities were recorded using a high speed camera running at 1205 frames per second.

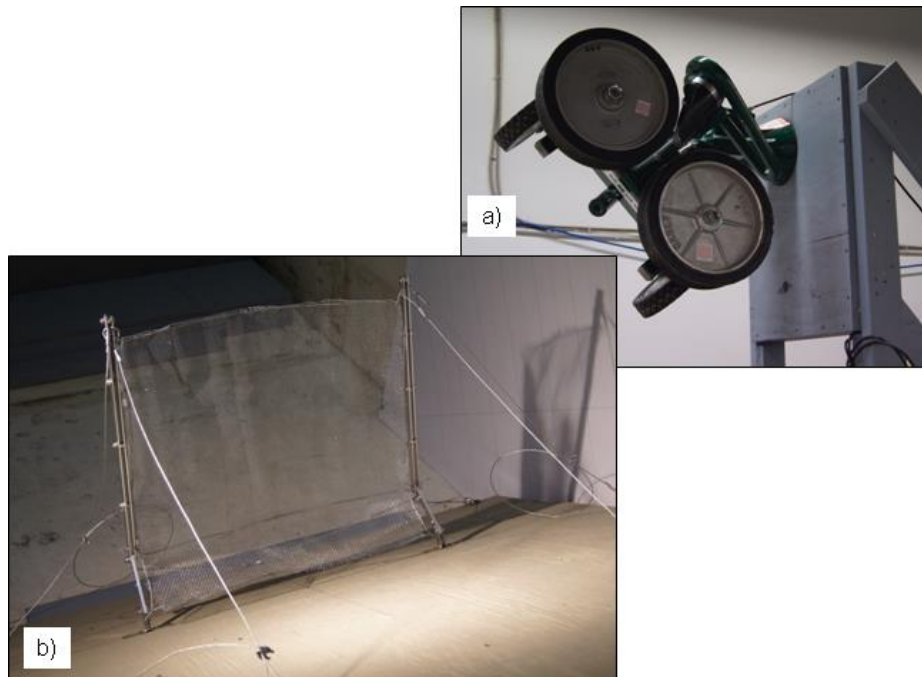


Figure 8.10: a) Baseball pitching machine and b) wave net.

The model tests were carried out on the fence with the configuration shown in Figure 8.11 that is designed to have both “attenuation” and “stiff” force-deformation characteristics as discussed in this chapter.

The orientations of the two post segments are defined by the angles α and β are measured relative to the normal to the slope, with up-slope angle being positive. For the tests, the lower post was fixed at an orientation of $\alpha = -25$ degrees, and the orientation of the upper post was varied between $\beta = -25$ degrees for normal impacts, and $\beta = +60$ degrees for oblique impacts. For each orientation, rotating and non-rotating impacts were tested. The objective of the tests was to find a relationship between the orientation of the upper net and the energy absorption efficiency – see equation (8.1).

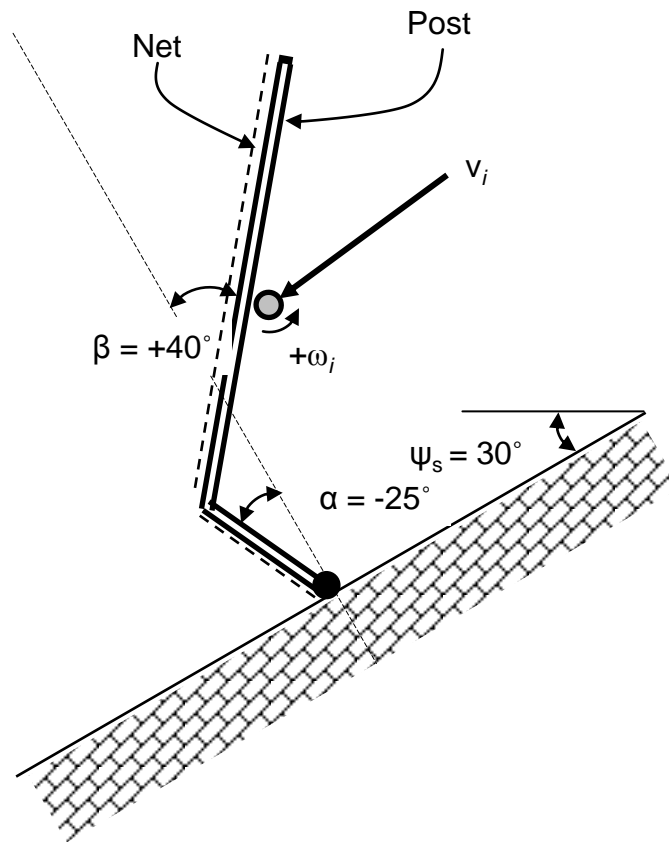


Figure 8.11: Configuration of rock fall fence used in model tests. Orientations of hinged posts are defined by angles α and β , measured relative to the normal to the slope

8.5.2 Model test parameters

The baseball pitching machine allowed the translational velocity of the projectile, as well as its rotational velocity to be controlled, with values selected to achieve impacts with high enough energy to significantly deflect the net. The translational velocities varied between 7 and $27 \text{ m} \cdot \text{s}^{-1}$ (25 to $90 \text{ ft} \cdot \text{s}^{-1}$), and the rotation was counter-clockwise for the model shown in Figure 8.12.

The projectile was a dense rubber ball with a dimpled surface, a diameter of 75 mm (3 in) and a mass of 140 gram (0.3 lb). For a sphere, the rotation parameters are: radius of gyration, $k = (2/5)^{0.5} \cdot r = 0.024 \text{ m}$ and moment of inertia, $I = m \cdot k^2 = 7.9\text{E-}5 \text{ kg} \cdot \text{m}^2$.

8.5.3 Results of model tests

For the model tests, the image analysis software, ProAnalyst© (Xcitex, 2008), was used to find the impact (initial) velocities, V_i , ω_i and final (restitution) velocities, V_f , ω_f from which the initial and final total energies could be calculated. Figure 8.12 shows a typical result of an oblique angle impact between the projectile and the fence inclined up-slope, and the reduction in velocity that occurs during impact. The image shows the redirection by the net of the body,

which “rolls” down the net during impact; contact duration is 0.0506 seconds (61 frames). During this contact duration the velocity decreases from $V_i = 14.6 \text{ m} \cdot \text{s}^{-1}$ (48 ft \cdot s $^{-1}$) at the point of impact to a minimum velocity of $8.3 \text{ m} \cdot \text{s}^{-1}$ (27 ft \cdot s $^{-1}$) between frames #90 to #99, approximately 0.03 seconds after impact. After this time, the velocity increases slightly to $V_f = 9.41 \text{ m} \cdot \text{s}^{-1}$ (31 ft \cdot s $^{-1}$) as projectile starts to rebound off the net. These velocity changes illustrate “attenuation” type behavior of the fence.

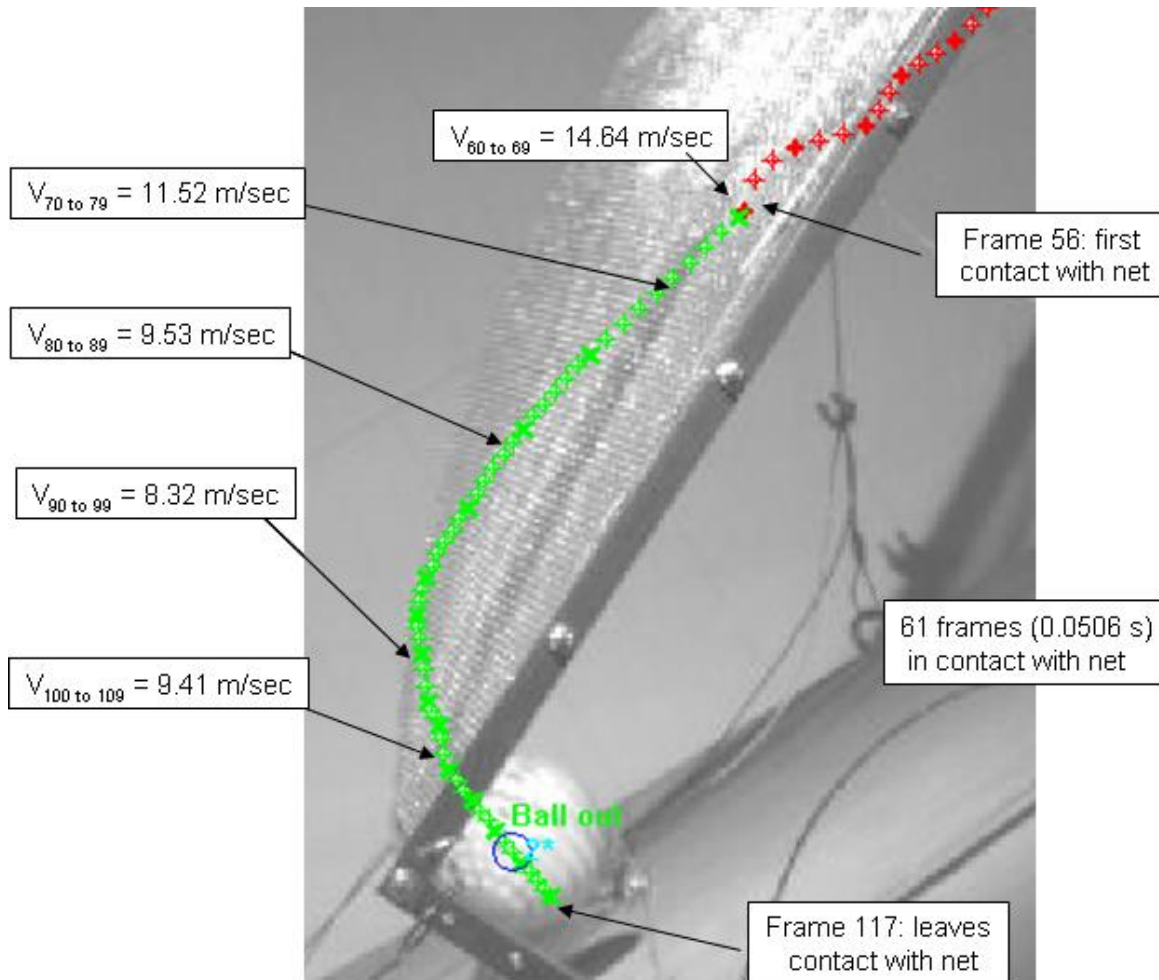


Figure 8.12: Path of deflected projectile after impact with net oriented up-slope ($\beta = +60$ degrees). Approximate velocities at ten frame intervals (0.0083 s) during impact shown

The changes in velocity were then used to find a relationship between the fence orientation defined by the angle β and the energy efficiency E_e (see equation (8.1)), where the energy efficiency increases when more of the impact energy retained by the moving projectile and less is absorbed by the net. For a projectile that is stopped by the net and all the impact energy is absorbed, the energy efficiency is zero.

Figure 8.13 shows the relationship between the angle β and the energy efficiency. That is, when normal impact occurs ($\beta = 0$), all the energy is absorbed and $E_e = 0$. For a non-rotating body, the energy efficiency increases as the upper net is inclined further up-slope (angle β increases) showing the effect of the body being re-directed due to the oblique impact angle. When $\beta = 60$ degrees, only about 50 per cent of the impact energy is absorbed.

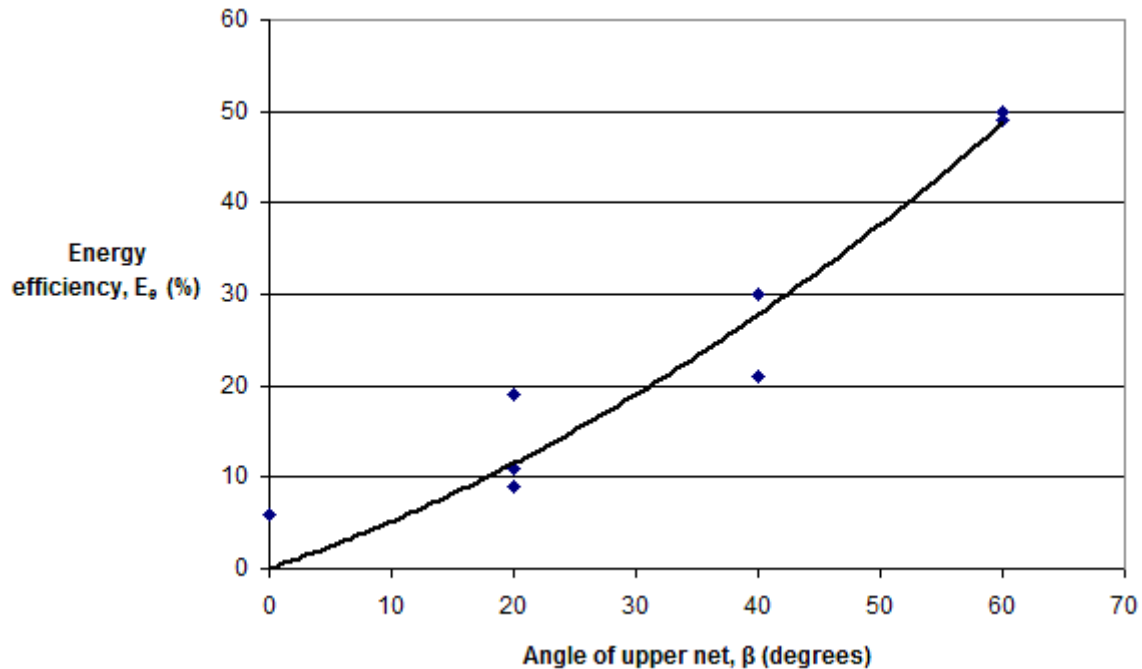


Figure 8.13: Relationship between energy efficiency and angle β of upper net, for a non-rotating body

The test results also provided information on the changes in velocity and impulse over the duration of the impact. For example, the relationship between the velocity and duration that the body is in contact with the net is shown in Figure 8.14 for a variety of tests in which the β angle varied from 0 to 60 degrees. The velocity decreases during contact from an initial value of about $15 \text{ m}\cdot\text{s}^{-1}$ to a minimum value of about $7 \text{ m}\cdot\text{s}^{-1}$ before increasing slightly as the body starts to rebound off the net. At no time does the velocity approach zero indicating that only a portion of the impact energy is absorbed by the net.

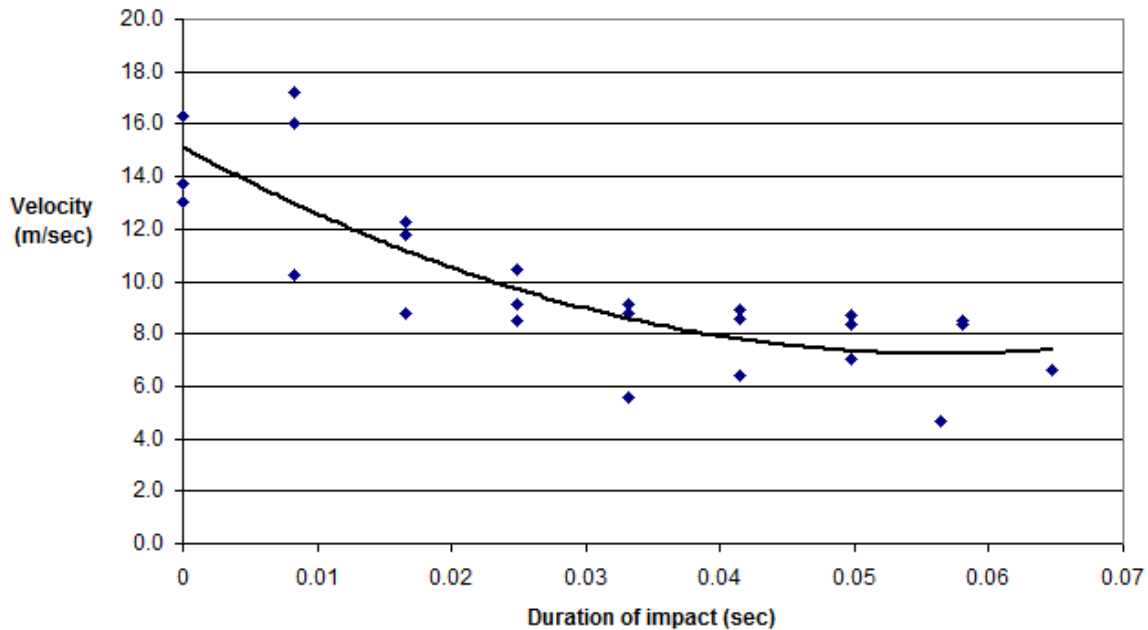


Figure 8.14: Relationship between the duration of impact and change in velocity during impact

The velocity, V data shown in Figure 8.15 can be expressed as an impulse, ($p = m \cdot V$) where m is the mass of the body. For the baseball-size body used in the tests with a mass of 0.14 kg (0.3 lb), impulse values were calculated for the corresponding velocities measured during the impact. Figure 8.15 shows the relationship between the duration of the impact and the percentage of the impact impulse that is absorbed by the fence during impact. That is, the impulse begins to be absorbed very soon after impact, and increases steadily during the impact.

The form of the actual [time – impulse] relationship shown in Figure 8.15 can be compared with the theoretical relationship between [time – force] shown in Figure 8.6 where the behavior of rigid, flexible and stiff structures are compared. It is apparent that the fence configuration used for the model tests has produced a stiff structure that absorbs energy throughout the impact, thus minimizing the induced force.

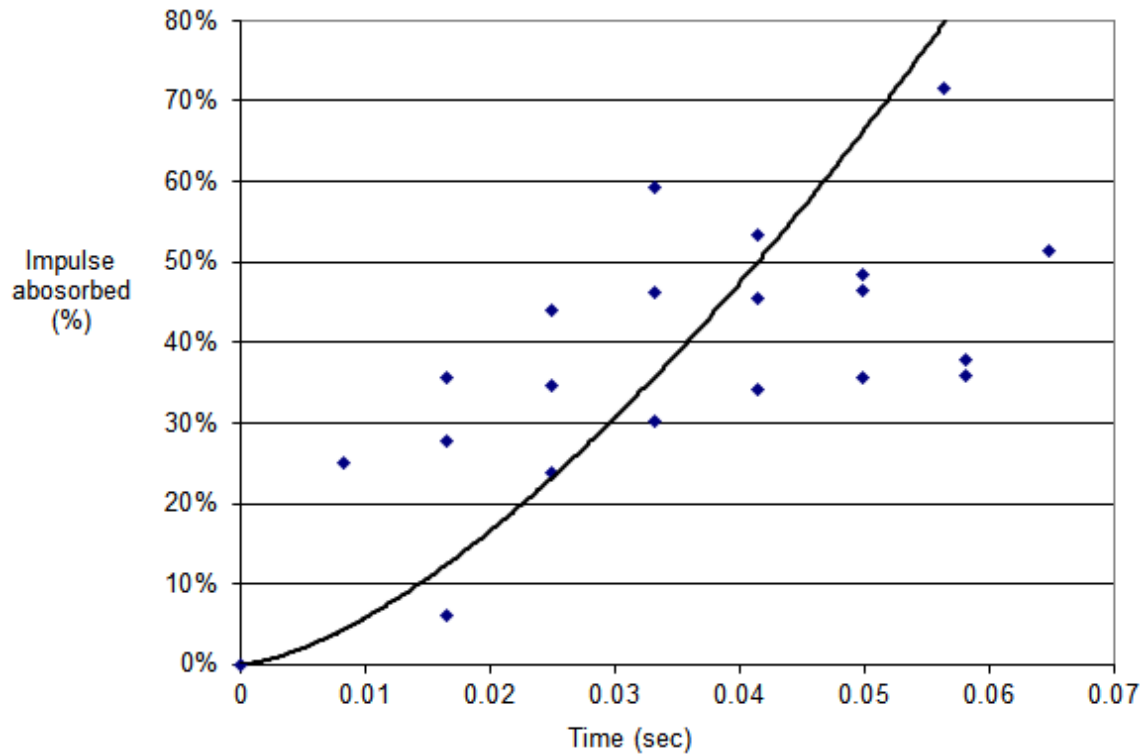


Figure 8.15: Relationship between duration of impact and the amount of impulse that is absorbed by the fence; compare with Figure 8.7 for stiff structures

This chapter has examined the theory of designing efficient protection structures that redirect (attenuate) rather than stop rock falls. This concept has been used in the construction of hanging net-type fences as shown in Figure 8.4. The author has been involved with the design and construction of about 25 hanging nets that have been impacted by many hundreds of rock falls, almost all of which have caused no significant damage to the fence. This performance, together with theory and model tests, would indicate that attenuator-type structures are effective in containing rock falls.

9 Conclusions and On-going Research

The research that I have conducted between 2009 and 2013 has been a very rewarding experience in terms of the intellectual challenge of applying impact mechanics theory to rock falls, and developing equations defining velocity and energy changes during rock fall impacts. I started this research with wide experience of rock fall events, and practical knowledge of the design, construction and performance of protection structures, but little knowledge of the theoretical aspects of impact behavior and how protection structures function in absorbing impact energy. My research has provided me with this valuable theoretical knowledge.

I consider that my research over the last five years is a phase in my on-going work to improve the design and function of rock fall protection structures, and provide better safety for the public from these hazards.

This chapter summarizes the conclusions that I have developed on rock fall behavior, and the work that I plan to carry out in the future.

9.1 Conclusions

The three main conclusions that I have drawn from my research are discussed below.

9.1.1 Case studies of rock fall events and testing sites

Because it is difficult to accurately simulate rock falls using mathematical models, it is important to have documented case studies that can be used to calibrate simulation programs. The five case studies provide reliable data on rock falls for a wide range of topographic and geologic conditions that I believe will be good calibration tools. In fact, as of November 2013, the data are being used to calibrate a modeling program that is under development.

I have a number of other case studies in my files that I hope will be useful to interested researchers, in addition to those described in this thesis.

One of the interesting findings from examining the case studies was that the normal coefficient of restitution, e_N can be greater than 1 for shallow impact angles, θ_i ($\theta_i < \sim 20$ degrees) and that a power curve defines the relationship between e_N and θ_i . Furthermore, the normal coefficient of restitution is not a function of the slope material on which the rock falls impact. That is, it was found that one of the lowest values for e_N (0.18) was for a rock dropped on to a horizontal concrete surface, while e_N values greater than 1 occurred for shallow impacts ($\theta_i \approx 20$ degrees)

on the relatively soft soil/gravel colluvium at Tornado Mountain. This apparent paradox can be explained by impact mechanics theory for impact of rotating, non-spherical bodies (see Section 9.1.2 below).

Also, it is important to note that $e_N > 1$ does not mean that energy is being created during impact. Impact mechanics analysis separates the normal velocities and energy changes due to inelastic compression and hysteresis of the slope materials, from the tangential velocity and energy changes due to friction at the contact surface. Therefore, while energy may be gained in the normal direction, energy will always be lost in the tangential direction, and a net energy loss will occur for the impact.

The implication of this research finding is as follows. The existing rock fall modelling programs relate e_N and e_T values to the slope material and assume that these are material properties. However, the research shows that it would be more appropriate to use a specific e_N value for each impact related to the impact angle θ_i , with the value of θ_i determined from the geometrics of the impact.

Values of e_T to use in rock fall modelling are always less than 1 due to friction acting on the contact surface, and may be related to the roughness of the surface. The field data shows that e_T values lie between about 0.3 and 0.9, and that e_T is independent of the slope material and the body shape. The lowest value for e_T was 0.24 for the relatively smooth asphalt surface.

9.1.2 Impact mechanics theory

I found that my application of Dr. Stronge's impact mechanics to rock falls has been most useful in developing a detailed understanding of the impact behavior; I believe that this is the first application of Dr. Stronge's methods to rock falls. That is, the use of the normal impulse, p_N as an independent variable that is tracked during impact, shows that a linear relationship exists between the normal impulse and the relative velocity, v . This linear relationship between p_N and v can be plotted on a $[p_N - v]$ diagram that shows the normal, tangential and rotational velocity components at any stage of the impact. Equations for velocity and angle changes during impact were developed for collinear impact of a rough, rotating sphere.

A further function of $[p_N - v]$ diagrams is that inelastic compression and rebound phases of impact are separated so that the corresponding energy changes can be calculated, in both the normal and tangential directions.

The finding that the normal coefficient of restitution is related to the impact angle, and can be greater than 1, only occurs for eccentric impact where a non-spherical, rough rotating body impacts the slope at a shallow angle ($\theta_i < \sim 20$ degrees) . These impact conditions can be examined using $[p_N - v]$ diagrams where the changes in the normal and shear components of velocity during impact are represented as straight lines. The slope of the line depends on the mass and shape of the impacting body and its rotational velocity, while the intercept of the line depends on the normal component of impact velocity. Typical $[p_N - v]$ plots show that values of e_N increase as the impact angle θ_i decreases, i.e., becomes flatter, and that e_N can have values greater than 1.

This theoretical relationship between e_N and θ_i with e_N being greater than 1 for shallow impacts, supports the findings of the field studies.

9.1.3 Performance of rock fall protection structures

Rock fall fences and nets can provide protection against rock falls by either stopping or redirecting rock falls. If a rock fall is stopped by the net, then all the impact energy is absorbed by the net. However, if the rock is redirected by the net so that its velocity is only reduced, then a portion of the impact energy is absorbed with the remainder of the energy being retained in the moving rock. The lower velocity falls can then be contained in a less expensive containment structures such as a ditch or low energy capacity barrier.

Furthermore, if a “stiff” structure is used in which the impact energy is absorbed uniformly during impact, compared to highly “flexible” nets that only absorb energy at large deflections, then impact forces induced in the net are minimized. This behavior of stiff nets and fences that redirect rock falls is demonstrated both from the theory of impact mechanics and scale model tests. The tests involved using a baseball pitching machine to project baseballs at the net and a high speed camera to record the changes in translational and rotational velocities during impact. The impact calculations and model test results provide consistent results.

Structures that redirect and reduce the velocity of falls, rather than stop falls, are termed “attenuators”. Various net configurations that achieve this function are hanging nets, fences that are inclined up-slope (“Wave nets”) and canopies.

The implication of this performance of stiff, attenuator protection structures is that it should be possible to use lighter, smaller structures to contain rock falls. That is, these structures will be

less expensive than structures currently used so that more nets can be installed to provide greater protection for the public in rock fall hazard environments.

9.2 Future research work

As stated above, my research over the past five years is part of my on-going study of rock fall behavior. It is my intention to continue with this work in the future that I plan will involve the following activities.

9.2.1 Additional case studies

Over the course of my engineering work I expect that I will study other rock fall events and that these will be added to my compendium of case studies. If this work provides useful results, I would make them available to others working in this field.

It will be most valuable to collect additional field data on the relationship between the normal coefficient of restitution and the impact angle. These data will help to refine the relationship between these two parameters, and may show how that other characteristics of rock fall impacts influence e_N , in addition to the impact angle.

9.2.2 Impact mechanics

The impact model described in this thesis applies to bodies of any shape defined by their radius, r and radius of gyration, k . However, the equations developed in this thesis for changes in velocity and energy during impact apply to only collinear impact for translating and rotating, rough spheres. It is my intention to develop equations for velocity and energy changes that apply to eccentric impact for any body shape. These equations will then be used to compare theoretical behavior with the case study results where eccentric impacts of non-spherical bodies occur.

Another valuable investigation would be to analyze high speed photography of actual rock fall impacts to measure changes in relative velocity and normal impulse during impact. These results could then be plotted on $[p_N - v]$ diagrams to see how closely actual impact behavior matches impact mechanics theory. This information would be used to make appropriate modifications to the theoretical equations in order to develop equations that would reliably map actual velocity and energy changes during impact.

It is noted in this thesis that the actual velocity and energy changes during impact are greater than those calculated using theoretical impact mechanics, probably because the theory does not fully account for the plastic conditions that occur in actual impacts.

9.2.3 Protection structures

The model tests of rock fall fences carried out with the baseball pitching machine showed that stiff structures that redirect falls are effective in efficiently containing rock falls. It is now planned to carry out full scale testing in a local quarry. The tests will involve various configurations of both wave nets and hanging nets, with concrete blocks of various sizes used as the projectile; the velocity and impact energy will be controlled by varying the fall height. Data will be collected using a three-dimensional accelerometer in the concrete block, load cells in the guy cables and a high speed camera. The information will be recorded in a data acquisition system operating at 2 kHz.

It is intended that the field tests, together with theoretical studies of impact mechanics, will be used to develop improved rock fall protection nets and fences. Specifically, the tests will investigate the relationships between changes in velocity and energy during impact, and the configuration of the net, such as the incidence angle and the stiffness of the net. One of the potential benefits of stiff nets compared to the present highly flexible nets will be that less deformation will occur with a stiff net. This will allow nets to be located closer to the structure being protected which will reduce installation and maintenance costs.

References

- Ashayer, P. (2007). *Application of rigid body impact mechanics and discrete element modeling to rockfall simulation*. Ph.D. thesis, University of Toronto, Grad. Dept. of Civil Engineering.
- Asteriou, H., Saroglou, G. and Tsiambaos, T. (2012). Geotechnical and kinematic parameters affecting the coefficient of restitution for rock fall analysis. *Int. J. Rock Mechanics and Mining Sciences*, **54**, pp 103 – 113, September.
- Beladjine, D., Ammi, M., Oger, L. and Valance, A. (2007). Collision process between an incident bead and a three-dimensional granular packing. *Physical Review E*, **75**: 1-12.
- Benjamin, J. R. and Cornell, A. C. (1979). *Probability, Statistics and Decision for Civil Engineers*. McGraw-Hill, New York.
- Bichler, A. and Stelzer, G. (2012). A fresh approach to the hybrid/ attenuator rockfall fence. Proc. 11th Int. Symp. on Landslides (ISL) and the 2nd North American Symp. on Landslides, June 2-8, Banff, Alberta, Canada.
- Brunet, G. and Giacchetti, G. (2012). Design software for secured drapery. *Proc. 63rd Highway Geology Symp.*, Redding, CA.
- Bugnion, L., Wendeler, C. and Shevlin, T. (2012). Impact pressure measurements in shallow landslides for flexible barrier design. *Proc. of the 11th Int. Symp. on Landslides (ISL) and the 2nd North American Symp. on Landslides*, June 2-8, 2012, Banff, Alberta, Canada
- Bunce, C. M., Cruden, D. M. and Morgenstern, N. R. (1997). Assessment of the hazard from rock fall on a highway. *Canadian Geotech. J.*, Vol. 34, 344-56.
- Buzzi, O., Giacomini, A. and Spadari, M. (2012). Laboratory investigation of high values of restitution coefficients. *J. Rock Mech. Rock Eng.*, **43**: 35-43.
- California Polytechnical State University (1996). *Response of the Geobrugg cable net system to debris flow loading*. Department of Civil and Environmental Engineering, San Luis Obispo, CA, pp 3, 35, 59.
- Canadian Geotechnical Society (2006). *Canadian Foundation Engineering Design Manual*, 4th Edition. BiTech Publishing, Richmond, British Columbia, 488 pages.
- Chau, K. T., Wong, R. H. C., Liu, J. and Lee, C. F. (2003). Rockfall hazard analysis for Hong Kong based on rockfall inventory. *Rock Mech Rock Eng*, **36**(5):383 - 408.
- Chau, K. T., Wong, R. H. C. and Wu, J. J. (2002). Coefficient of restitution and rotational motions of rock fall impacts. *Int. J. Rock Mech. & Mining Sciences*, **39**:69-77.
- Chen, G., Zheng, L., Zhang, Y. and Wu, J. (2013). Numerical Simulation in Rockfall Analysis: A Close Comparison of 2-D and 3-D DDA. *Rock Mechanics and Rock Engineering*, **46**(3), 527-541.
- Dellow, G., Yetton, M., Archibald, G., Barrell, D.J.A., Bell, D., Bruce, Z., Campbell, A., Davies, T., De Pascale, G., Easton, M., Forsyth, P.J., Gibbons, C., Glassey, P., Grant, H., Green, R., Hancox, G., Jongens, R., Kingsbury, P., Kupec, J., MacFarlane, D., McDowell, B., McKelvey, B., McCahon, I., McPherson, I., Molloy, J., Muirson, J., O'Halloran, M., Perrin, N., Price, C., Read, S., Traylen, N., Van Dissen, R., Villeneuve, M. and Walsh, I. (2011) Landslides Caused by the 22 February 2011 Christchurch Earthquake and Management of Landslide Risk in the

Immediate Aftermath. *Bulletin of the New Zealand Society for Earthquake Engineering* 44(4): 227-238.

- Dijkstra, T. A., Chandler, J., Wackrow, R., Meng, X. M., Ma, D. T., Gibson, A., Whitworth, M., Foster, C., Lee, K., Hobbs, P. R. N., Reeves, H. J. and Wasowski, J. (2012). Geomorphic controls and debris flows - the 2010 Zhouqu disaster, China. Proceedings of the 11th International Symposium on Landslides (ISL) and the 2nd North American Symposium on Landslides, June 2-8, 2012, Banff, Alberta, Canada.
- Dorren, L. K. A. and Berger, F. (2012). Integrating forests in the analysis and management of rock fall risks: experience from research and practice in the Alps. *Proc. 11th Int. Conf. and 2nd North American Symp. on Landslides and Engineered Slopes*. Banff, Canada, June 2012, p. 117-127.
- Dorren, L. K. A., Berger, F. and Putters, U. S. (2006). Real size experiments and 3-D simulation of rock fall on forested and non-forested slopes. *Natural Hazards and Earth Science Systems*, **6**: 145-53.
- Dorren, L. K. A., and Berger, F. (2005). Stem breakage of trees and energy dissipation during rock fall events. *Tree Physiology*, **26**:63-71.
- European Organisation for Technical Approvals (February 1, 2008). ETAG 27, Guideline for European Technical Approval of Falling Rock Protection Kits. *EOTA*. Retrieved on May 22, 2013, from <http://www.eota.be/pages/home/>
- Geobrugg (2012). RUVOLUM Online Tool, Version 2012 software. *Geobrugg AG, Switzerland*. Retrieved on May 22, 2013, from <http://applications.geobrugg.com/>
- Geobrugg (2010). *Product literature - TECCO damping modules for rock fall protection galleries*. Romanshorn, Switzerland.
- Giacchetti, G., Grimod, A. and Cheer, D. (2011). Soil nailing with flexible facing: design and experience. *Proc. Second World Landslide Forum*, Rome, October.
- Giacchetti, G. and Zotti, I. M. (2012). Design Approach for Rockfall Barriers. *Geotechnical XI National Congress in Costa Rica* (August 9 and 10). San Jose, Costa Rica, 2012.
- Giacomini, A., Thoeni, K., Lambert, C., Booth, S. and Sloan, S. W. (2012). Experimental study on rockfall drapery systems for open pit highwalls. *Int. J. of Rock Mechanics and Mining Sciences* **56**(0): 171-181.
- Giacomini, A., Spadari, M., Buzzi, O., Fityus, S. G. and Giani, G. P. (2010). Rockfall motion characteristics on natural slopes in eastern Australia. *Eurock 2010*, Lausanne, Switzerland, 15 to 17, June.
- Goldsmith, W. (1960). *Impact – Theory and Physical Behaviour of Colliding Solids* (2001 edition). Dover Publications, New York, 379 pages.
- Grimod, A. and Giacchetti, G. (2011). Protection from high energy impacts using reinforced earth embankments: design and experience. *Proc. 2nd World Landslide Forum*, Rome, October.
- Gutenberg, B. and Richter, C. F. (1954). *Seismicity of the Earth, 2nd*. Ed. Princeton University Press, Princeton, NJ.
- Hambleton, J. P., Buzzi, O., Giacomini, A., Spadari, M. and Sloan, S. W. (2013). Perforation of Flexible Rockfall Barriers by Normal Block Impact. *Rock Mechanics and Rock Engineering* **46**(3): 515-526.

- Harp, E. L., Jibson, R. W., Kayen, R. E., Keefer, D. K., Sherrod, B. L., Carver, G. A., Collins, B. D., Moss, R. E. S. and Sitar, N. (2003). Landslides and liquefaction triggered by the M7.9 Denali Fault earthquake of 3 November, 2002. *GSA Today*, August 2003, 10 pages.
- Harp, E. L. and Jibson, R. W. (1995). Inventory of landslides triggered by the 1994 Northridge, California earthquake. *Dept. of the Interior, USGS*, Open file Report 95-213, 17 pages.
- Harp, E. L. and Wilson, R. C. (1995). Shaking intensity thresholds for rock falls and slides: evidence from 1987 Whittier Narrows and Superstition Hills earthquakes strong motion records. *Bull. Seismological Soc. Am.*, **85**(6), 1739-57.
- Harr, M. E. (1977). *Mechanics of Particulate Matter - a Probabilistic Approach*." McGraw-Hill, New York: 543 pages.
- Hungr, O. and Evans, S. G. (1988). Engineering evaluation of fragmental rock fall hazards. *Proc. 5th Inter. Symp. on Landslides*, Lausanne, Switzerland, July, 685-90.
- Hungr, O., Evans, S. G. and Hazzard, J. (1999). Magnitude and frequency of rock falls and rock slides along the main transportation corridors on southwestern British Columbia. *Can. Geotech. J.*, **36**: 224-238.
- Jacquemoud, J. (1999). Swiss Guideline for the design of rock fall protection galleries: background, safety concept and case histories. *Proc. Joint Japan-Swiss Seminar on Impact Load by RockFalls and Design of Protection Measures*. Kanazawa, Japan, October, 161 pages.
- Japan Road Association (2000). *Rock Fall Control Manual* (in Japanese). 422 pages.
- Jibson, R. W. and Harp, E. L. (1995). Inventory of Landslides Triggered by the 1984 Northridge, California Earthquake. *U. S. Dept. of the Interior, USGS*, Open file 95-213, 17 pp.
- Jones, C. L., Higgins, J. D. and Andrew, R. D. (2000). *Colorado Rockfall Simulation Program, version 4.0 (CRSP)*. CO Dept. of Transportation, Denver, CO, Report no. CDOT-STMB-CGS-99-1, 127 pages.
- Keefer, D. K. (1992). The susceptibility of rock slopes to earthquake-induced failure. *Proc. 35th Annual Meeting of the Assoc. of Eng. Geologists*, (ed. Martin L. Stout), Long Beach, CA, 529-38.
- Kirsten, H. A. D. (1982). Design and construction of the Konwyn's Pass rock fall shelter. *Civ. Engr. S. Afr.*, **24**(9), 477-92.
- Kobayashi, Y., Harp, E. L. and Kagawa, T. (1990). Simulation of rock falls triggered by earthquakes. *J. Rock Mech. Rock Eng.*, **23**(1):1-20.
- Komura, T., Muranishi, T., Nisizawa, K. and Masuya, H. (2001). Study on parameters concerning impact of falling rock on field slopes and rock fall simulation method. *Proc. 4th Asia-Pacific Conf. on Shock and Impact Loads on Structures*, 345-352.
- Labouise, V., Descoeurdes, F. and Montani, S. (1996). Experimental study of rock sheds impacted by rock blocks. *Struct. Eng. Int.*, Vol. 3, 171-6.
- Maccaferri S.p.A. (2012). *Slope mesh design software, BIOS and Mac.Ro1*. Maccaferri S.p.A., Bologna, Italy.
- Maccaferri S.p.A, Bologna, Italy (2012). *Rockfall and Debris Flow Protection Embankments*. Product literature, www.maccaferri.ca.

- Maggs, Micheal (2007, October 8). Bouncing ball strobe edit, in *Wikimedia Commons*. Retrieved May 22, 2013, from https://en.wikipedia.org/wiki/File:Bouncing_ball_strobe_edit.jpg
- Mamaghani, I. H. P, Yoshida, H. and Obata, Y. (1999). Reinforced expanded polystyrene Styrofoam covering rock sheds under impact of falling rocks. *Joint Japan-Swiss scientific seminar on impact loads by rock falls and design of protective structures*, Kanazawa, Japan, Oct., 79-89.
- Masuya, H., Amanuma, K., Nishikawa, Y. and Tsuji, T. (2009). Basic rock fall simulation with consideration of vegetation and application of protection measures. *Nat. Hazards and Earth Systems Sciences*, **9**:1835-43.
- Masuya, H., Ihara, T., Onda, S. and Kamijo, A. (2001). Experimental study on some parameters for simulation of rock fall on slope. *Proc. 4th Asia-Pacific Conf. on Shock and Impact Loads on Structures*, 63-69.
- McCauley, M. L., Works, B. W. and Naramore, S. A. (1985). *Rock fall mitigation*. Report FHWA/CA/TL-85/12. FHWA, U.S. Department of Transportation.
- National Cooperative Highway Research Program (NCHRP) (1999). *Geotechnical related development of load and resistance factor design (LRFD)*. Synthesis of Highway Practice (276), TRB, Washington, D. C., 69 pages.
- Newmark, N. M. (1965). Effects of earthquakes on dams and embankments. *Geotechnique*, **15**(2), 139-160.
- Newton, I. (1687). *Philosophiae Naturalis Principia Mathematica*. Cambridge, U.K.: Cambridge University Press.
- Nocilla, N., Evangelista, A. and di Santolo, A. S. (2009). Fragmentation of rock falls: two Italian case studies of hard and soft rocks. *Rock Mech. Rock Eng.* **42**:815-833.
- Nishikawa, Y., Masuya, H. and Moriguti, Y (2012). Three dimensional simulation of rock fall motion with consideration of roughness of the slope surface. *Trans. Japan Soc. for Computational Engineering and Science*, 2012, 20120003.
- Palisade Corporation (2012). Computer program @RISK, version 5.0. Palisade Corporation, Ithaca, New York, USA. www.palisade.com
- Patton, F. D. (1974). Multiple modes of shear failure in rock. *Proc. 1st. Int. Cong. on Rock Mechanics*, Lisbon, 1, 509-13.
- Peckover, F. L. (1975). Treatment of rock falls on railway lines. *American Railway Engineering Association*, Bulletin 653, Washington, D. C., pp. 471-503.
- Pfeiffer, T. J. and Bowen, T. D. (1989). Computer simulation of rock falls. *Bull. Assoc. Engineering Geologists*, Vol XXXVI, No. 1, 135-46.
- Pfeiffer, T. J., Higgins, J. D.D. J., Andrew, R. D., Schultz, R. J. and Beck, R. B. (1995). *Colorado Rock Fall Simulation Program. Version 3.0, User's Manual*. Colorado Department of Transportation.
- Pfeiffer, T. J. and Higgins, J. D. (1995). Rockfall hazard analysis using the Colorado Rockfall Simulation Program. TRB, Washington, DC, *Transportation Research Record 1288*, 117-26.
- Pierson, L. A., Davis, S. A., and Van Vickie, R. (1990). *The Rock Fall Hazard System, Implementation Manual*. Technical Report, #FHWA-OR-EG-90-01, Washington, D. C.

- Pierson, L. A., Gullixson, C. F. and Chassie, R. G. (2001). *Rockfall Catchment Area Design Guide*. Research Report SPR-3(032): Oregon Department of Transportation-Research Group, Federal Highway Administration.
- Piteau and Associates Ltd. (1980). Slope stability analysis for rockfall problems: the computer rockfall model for simulating rockfall distributions, Part D. *Rock Slope Engineering, reference manual FHWA-TS-79-208*. FHWA, Department of Transportation, Washington D.C., 62-8.
- Poisson, S. D. (1811). *Traité de Méchanique*. Courier, Paris. (English translation by Rev. H. H. Harte, Longman & Co 1817).
- Proteng Engineering, Niigata, Japan (2012). *MSE embankments for rock fall containment*. Technical literature, www.proteng.co.jp.
- Raiffa, H. (1968). *Decision analysis: introductory lectures on choices under uncertainty*. Addison-Wesley, Reading MA, 309 pages.
- Ritchie, A. M. (1963). An evaluation of rock fall and its control. *Highway Research Record 17*, Highway Research Board, NRC, Washington DC, pp. 13-28.
- RGHRG (Railway Ground hazard Research Group), 2012. Annual Meeting, Vancouver, Canada, December.
- Rochet, L. (1987). Application des modeles numeriques de propagation a l'tude des eboulements rocheux. *Bulletin de liaison laboratoires des ponts et chaussees*. **150-1**, Sept.-Oct..
- RocScience (2012). *Computer program RocFall 4.0*. RocScience Inc., Toronto, Canada.
- Schellenberg, K. and Vogel, T. (2009). A dynamic design method for rockfall protection galleries. *J. Int. Assoc. Bridge and Structural Eng.*, SEI Vol. 19(3), 321-6.
- Skermer, N. A. (1984). M Creek debris flow disaster. *Canadian Geotechnical Conference: Canadian Case Histories, Landslides*, Toronto, pp.187-94.
- Spadari, M., Giacomini, A., Buzzi, O., Fityus, S. G. and Giani, G. P. (2012). In situ rock fall testing in New South Wales, Australia. *Int. J. Rock Mechanics and Mining Sciences*, **49**, pp 84 – 93.
- Stevens, W. D. (1998). *RocFall: a tool for probabilistic analysis, design of remedial measures and prediction of rock falls*. Thesis for M. App. Sc. degree, University of Toronto, Dept. of Civil Eng., 28 pages.
- Stock, G. M., Luco, N., Harp, E. L., Collins, B. D., Reichenbach, P., Frankel, K. L., Matasci, B., Carrea, D., Jaboyedoff, M., Oppikofer, T. (2012). Quantitative rock fall hazard and risk assessment in Yosemite Valley, California, USA. *Proc. 11th Int. Conf. and 2nd North American Symp. on Landslides and Engineered Slopes*. Banff, Canada, Vol.2, 1119-1125.
- Stock, G. M., Sitar, N., Borchers, J. W., Harp, E. L., Snyder, J. B., Collins, B.D., Bales, R.C., Wiezorek, G.F. (2012). Evaluation of hypothesized water-system triggers for rock falls from Glacier Point, Yosemite National Park, California, USA. *Proc. 11th Int. Conf. and 2nd North American Symp. on Landslides and Engineered Slopes*. Banff, Canada Vol.2, 1165-1171.
- Stronge, W. J. (2000). *Impact Mechanics*. Cambridge University Press, Cambridge, U. K., 280 pages.
- Transportation Research Board (TRB) (1996). *Landslides, Investigation and Mitigation*. National Research Council, Special Report 247, Washington DC, 673 pages.

- Ushiro, T. and Tsutsui, H. (2001) T. Hideki. Movement of a Rockfall and a Study on Its Prediction. Proceeding of the International Symposium on Geotechnical & Environmental Challenges in Mountainous Terrain. Ehime, Japan, Nov. 2001: 275-285
- Ushiro, T., Kusumoto, M., Shinohara, S. and Kinoshita, K. (2006). An experimental study related to rock fall movement mechanism. *J. Japan Soc. of Civil Engineers*, Series F, 62(2), 377-386 (in *Symp. on Geotechnical and Environmental Challenges in Mountainous Terrain*, Kathmandu, Nepal, 366-375.
- Vogel, T., Labiouse, V. and Masuya, H. (2009). Rockfall protection as an integral task. *Structural Engineering International, SEI* Vol. 19(3), 304-12, IABSE, Zurich, Switzerland, www.iabse.org
- Watts, C.F., Underwood, S.A., Haneberg, W.C., Rogers, J.D. (2012). Fully rationalized equations for incorporating joint water pressure in rock slope stability analyses at Glacier Point in Yosemite National Park, California. *Proc. 11th Int. Conf. and 2nd North American Symp. on Landslides and Engineered Slopes*. Banff, Canada, Vol.2, 1173-1178.
- Wu, Shie-Shin (1985). Rockfall Evaluation by Computer Simulation, Transportation Research Record 1031, 1-5.
- Wyllie, D. C. (1987). Rock slope inventory system. *Proc. Federal Highway Administration Rock Fall Mitigation Seminar*, FHWA, Region 10, Portland, OR.
- Wyllie, D. C. (1999). *Foundations on Rock (second edition)*. E&FN Spon, London, UK, 401 pages.
- Wyllie, D. C. and Mah, C. W. (2002). *Rock Slope Engineering, fourth edition*. Taylor and Francis, London, UK, 422 pages.
- Wyllie, D. C. (2006). Risk management of rock fall hazards. *Proc. 59th Annual Canadian Geotechnical Conference*, Canadian Geotech. Soc., Vancouver, Canada.
- Wyllie, D. C., McCammon, N. R. and Brumund, W. F. (1979). Use of risk analysis in planning slope stabilization programs on transportation routes. Transportation Research Board, Research Record 749, Washington D.C..
- Xcitex (2008). *Proanalyst©, Motion Analysis Software*. Xcitex Inc., Cambridge, MA, USA.
- Yokoyama, K., Ohira, M. and Yoshida, H. (1993). Impulsive properties due to rock fall on a steel rock shed (in Japanese), *J. of Struct. Eng.*, Vol.39A, 1573-1586.
- Yoshida, H., Nomura, T., Wyllie, D. C., & Morris, A. J. (2007). Rock fall sheds - application of Japanese designs in North America. *Proc. 1st. North American Landslide Conference*, Vail, CO., AEG Special Publication No. 22., ed. Turner, A. K., Schuster, R. L., 179-196.
- Zhang, R. and Rock, A. (2012). Rockfall stimulation using a 3-D discrete element model with engineering validation. *Proc. 11th Int. Conf. and 2nd North American Symp. on Landslides and Engineered Slopes*. Banff, Canada, Vol.2, 1153-1164.

Appendix A: Documentation of rock fall impacts at Mount Stephen

One of the rock fall case studies discussed in Chapter 2 is at Mount Stephen near Field in south east British Columbia where a 12.6 m high barrier was constructed to contain frequent rock falls and snow avalanches (Figure A.1). Section 2.1.1 describes the topography and geology of the site and gives typical rock fall trajectories, while Section 7.5.1 presents the simulation of the falls using the analysis software *RocFall 4.0*. The topography of the site was established with an aerial Lidar survey from which x sections were drawn at a spacing of y m of the lower 120 m of the 2000 m high slope.

Part of the information collected at the site was the locations of 466 impact points on the concrete facing blocks, and on the wire rope fence along the top of the barrier. This appendix provides details of these impact points showing both their vertical and horizontal distribution (Figures A.2 to A.4). The profile of the slope varies considerably along the site, and it was decided that three sections – #3, #7 and #12 – would be representative of typical conditions above the barrier. For each of these three slopes, the rock fall impact locations were analyzed as shown on Figures A.2 to A.4. On these three figures, the actual impact points on the fence are shown as red bars. In addition, these points are projected to the vertical plane at the face of the concrete barrier, shown as orange bars, to show the impact locations on a single plane.

The actual impact locations shown on Figures A.2 to A.4 are compared with a typical vertical distribution of impact points calculated using *RocFall 4.0* showing that the actual and simulated results are similar (Figure A.5). It is noted that few impact points were observed on the lower part of the wall because this is often buried in snow. However, observations of a large number of rock falls in the snow indicate that rock falls on lower part of the wall would be common.

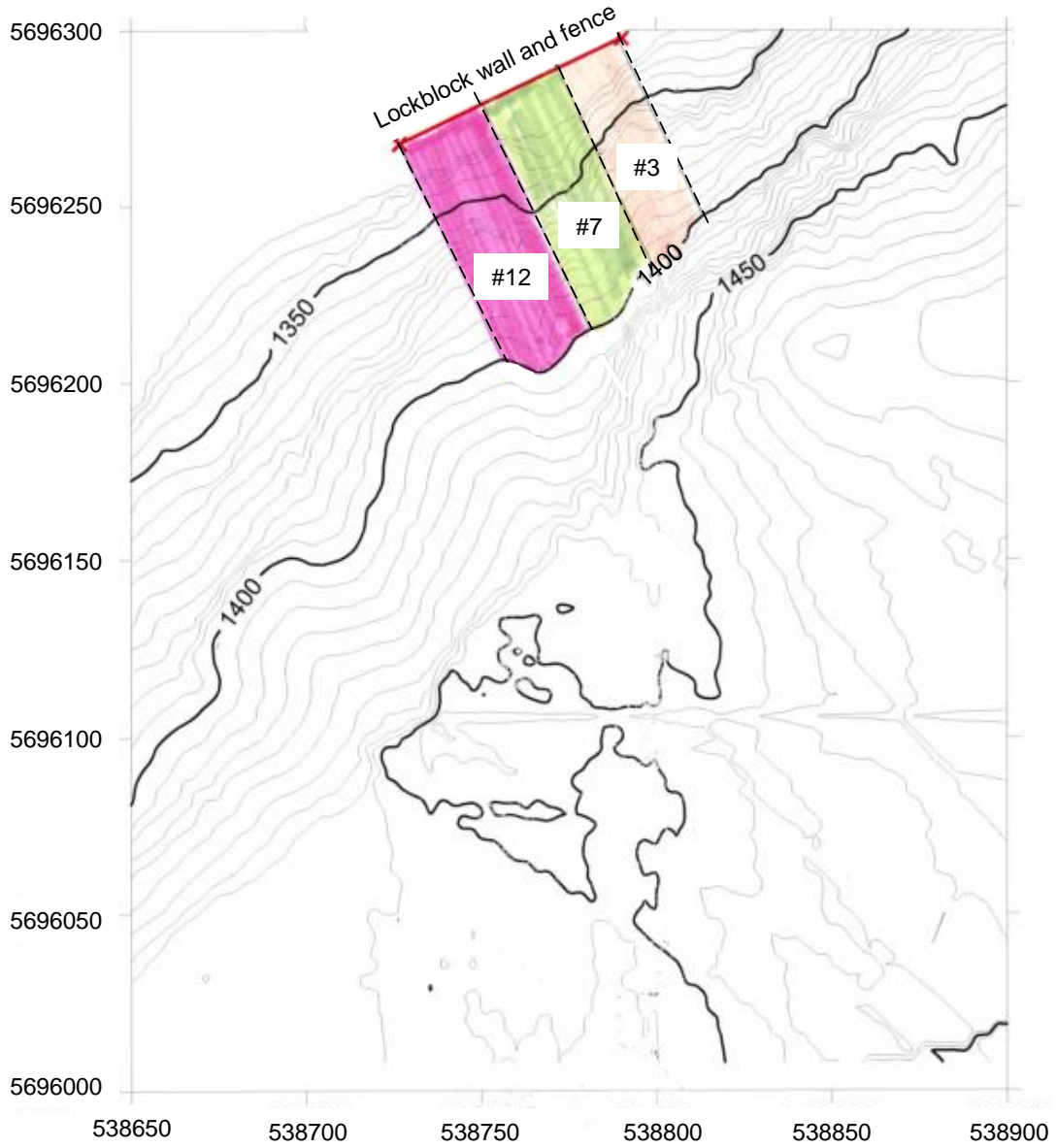


Figure A.1: Plan of Lockblock wall/ fence and slope

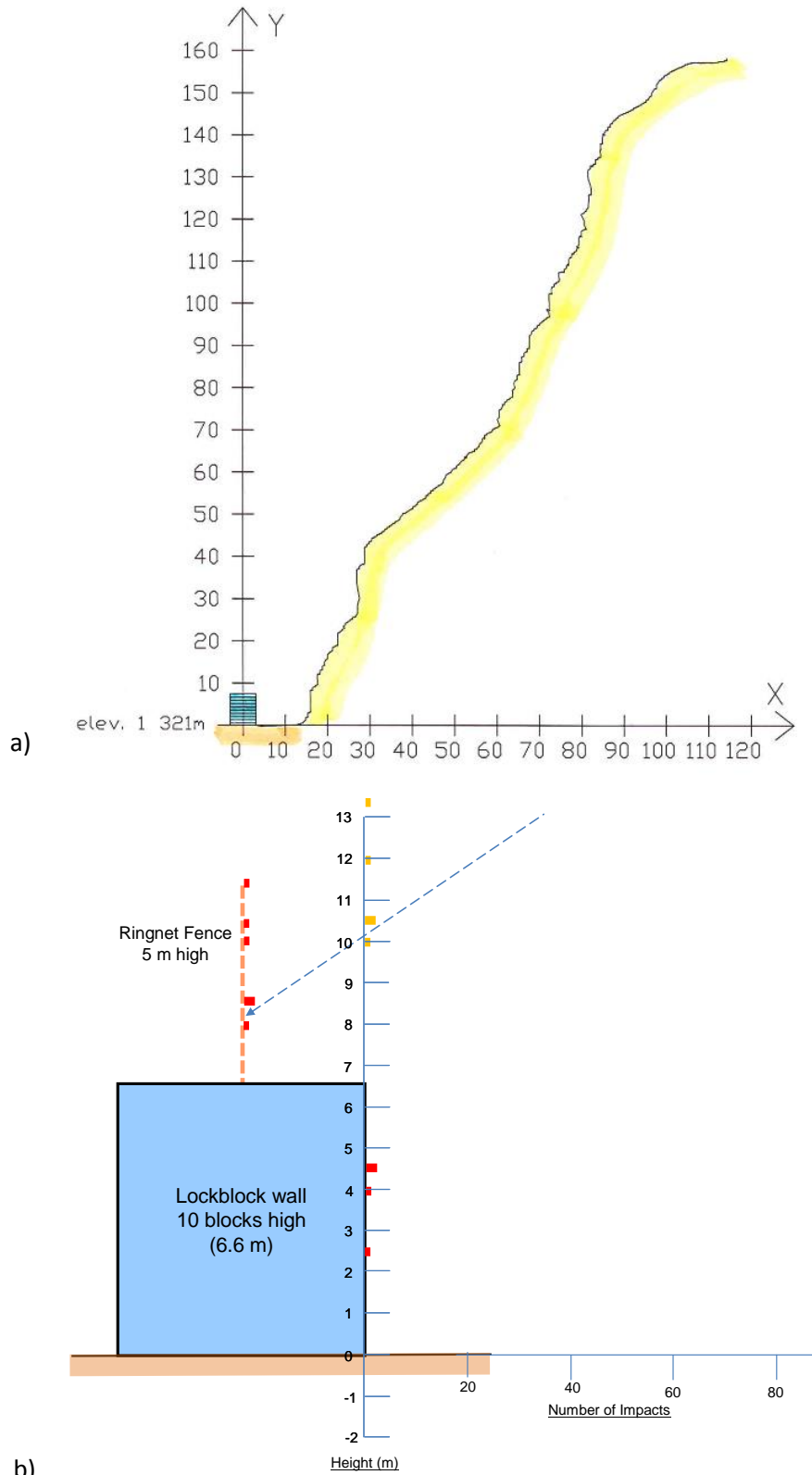


Figure A.2: Section #3. a) Cross section view, b) distribution of impact points

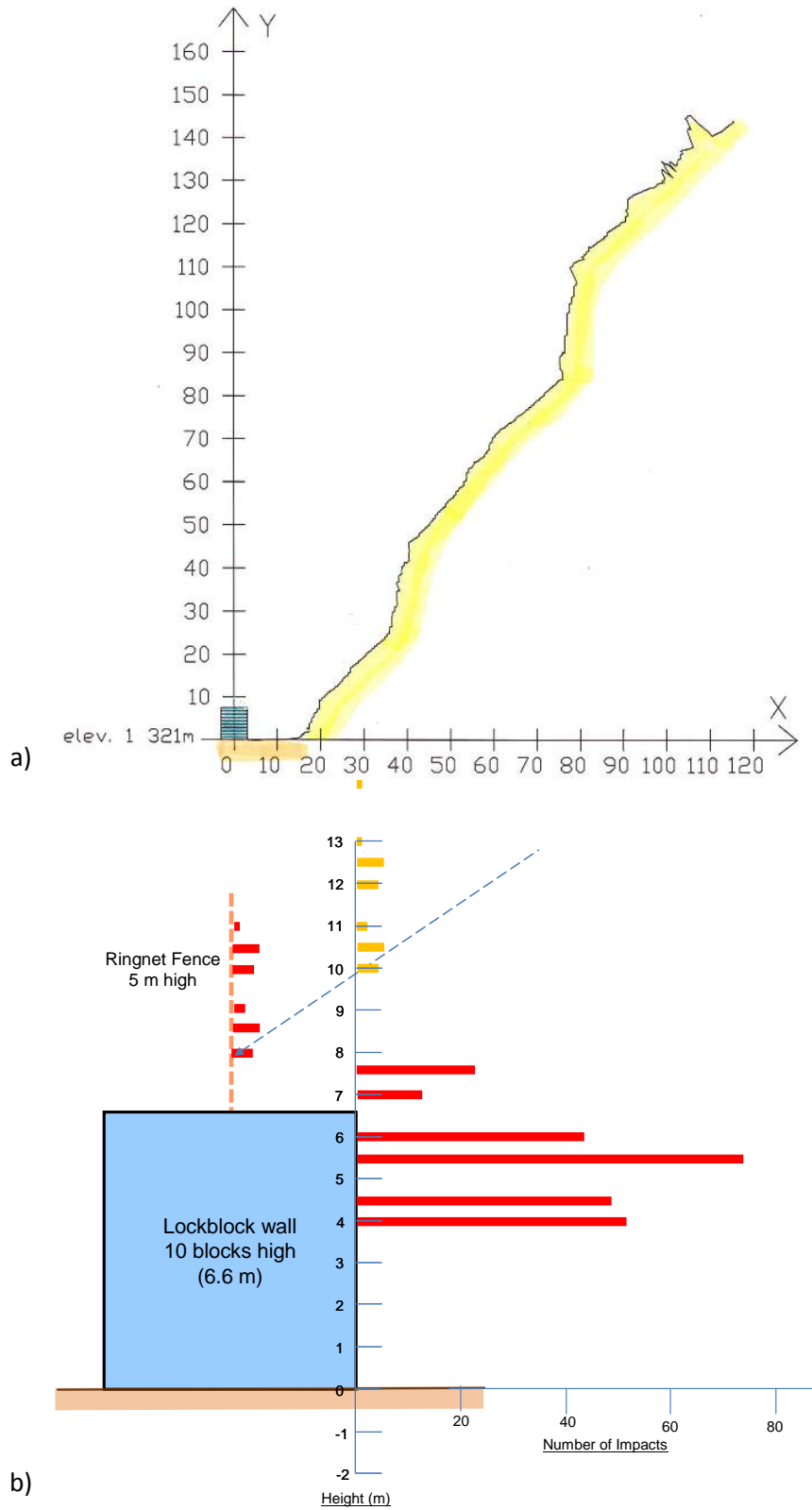


Figure A.3: Section #7. a) Cross section view, b) distribution of impact points

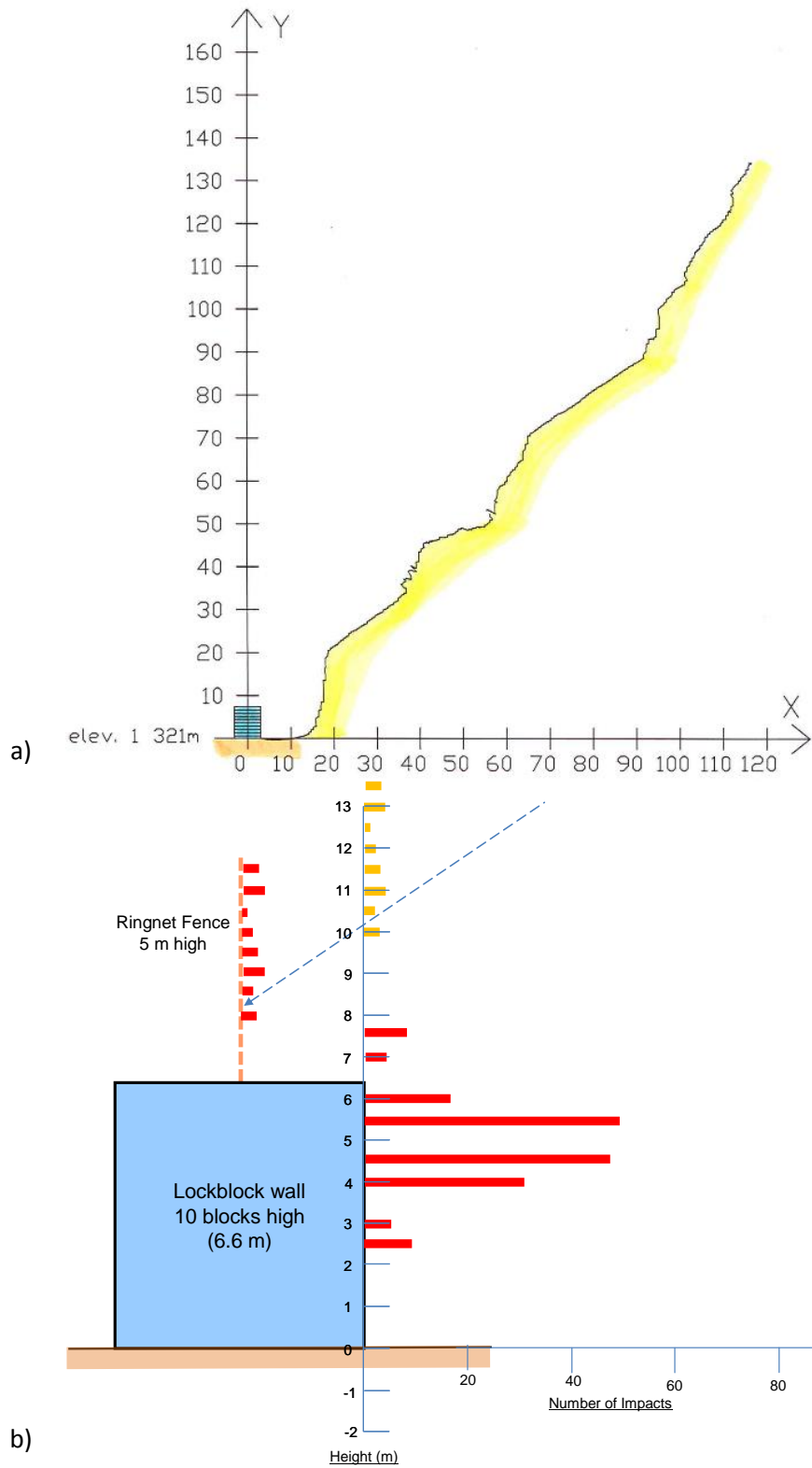


Figure A.4: Section #12. a) Cross section view, b) distribution of impact points

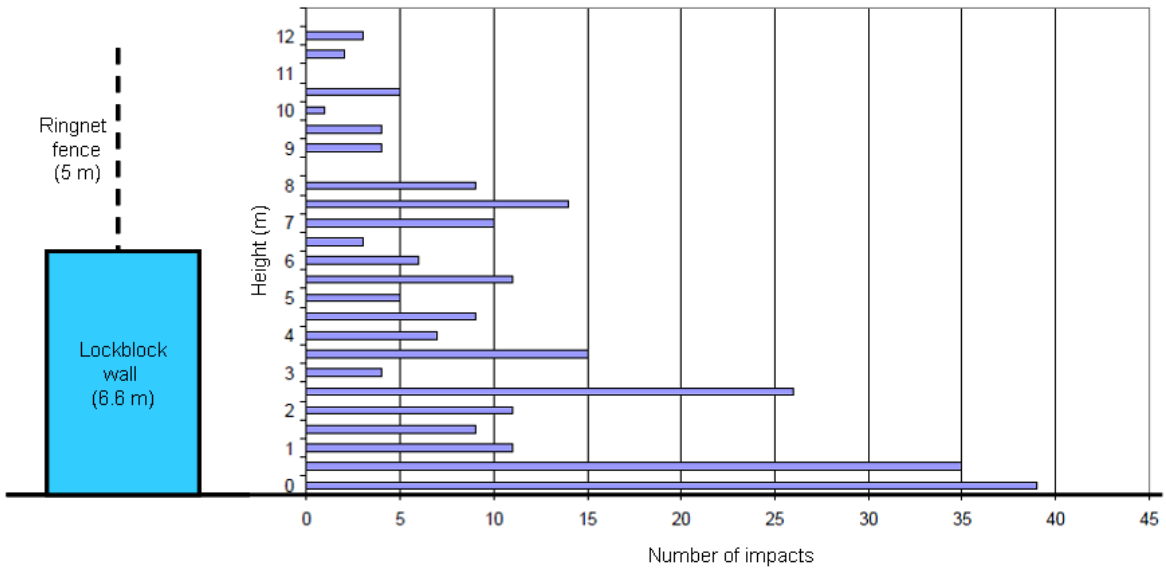


Figure A.5: Calculated vertical distribution impact points on barrier at Mt. Stephen

Appendix B: Impact mechanics – normal coefficient of restitution

This appendix shows the derivation of the equations defining the normal coefficient of restitution in terms of the energy loss during compression and the energy recovery during restitution phases of impact. This is an expansion of the information contained in Section 4.4 of the main text.

The principle of separating the compression and restitution phases of impact can be demonstrated on a normal impulse p_N , relative velocity v [$p_N - v$] plot as shown in Figure B.1; v is the velocity at the center of gravity of the body. On this plot, the normal velocity changes during impact, starting with a negative value ($-v_{iN}$) at the point of impact, increasing to zero at the point of maximum compression p_c , and finally reaching a positive value (v_{fN}) at the point of separation. Also, the tangential velocity v_T decreases continuously during impact from v_{iT} at the point of impact, to v_{fT} at the point of separation. The change in normal velocity is the result of plastic deformation of the body and slope during impact, while the change in tangential velocity is the result of frictional resistance on the contact surface.

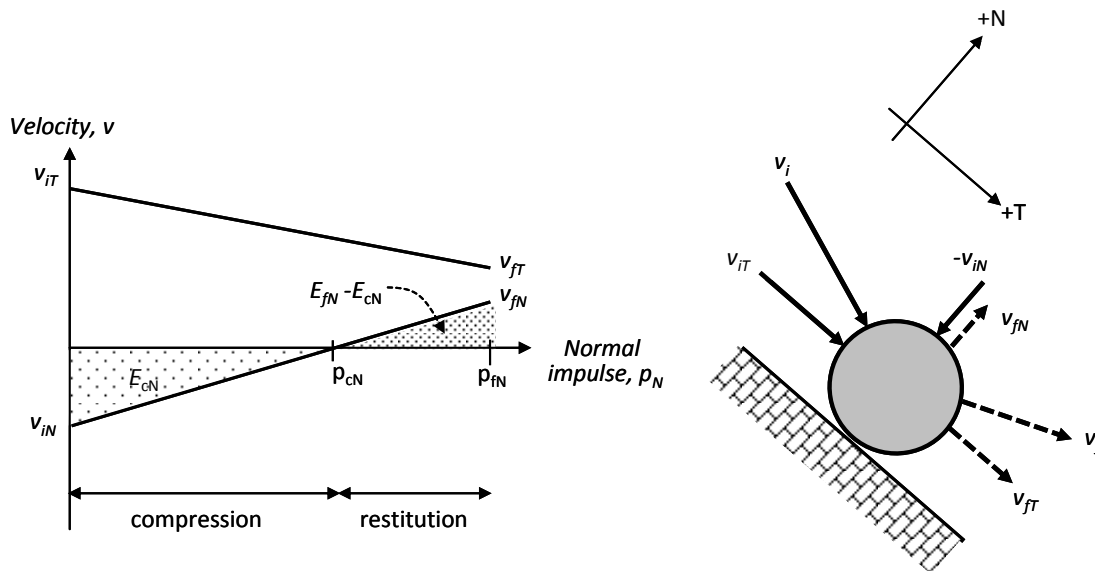


Figure B.1: Relationship between normal impulse p_N and changes in tangential and normal velocities v_T , v_N , and energy during impact

The [$p_N - v$] plot on Figure B.1 shows the changes in both the normal (v_N) and tangential (v_T) velocity components, and the magnitude of the internal energy of deformation generated during impact. These changes in velocity, as well as energy, can be quantified in terms of the coefficient of restitution, e that has normal (N) and tangential (T) components as follows:

$$e_N = -\frac{v_{fN}}{v_{iN}} \quad (\text{B.1})$$

and

$$e_T = \frac{v_{fT}}{v_{iT}} \quad (\text{B.2})$$

where the subscript “*i*” refers to the initial velocity at the moment of impact, and the subscript “*f*” refers to the final velocity at the end of the impact.

The normal impulse, p_N is defined as the application of a force, F over time:

$$dp_N = m(v_N - v_{iN}) = F dt$$

or

$$dv_N = \frac{dp_N}{m} \quad (\text{B.3a})$$

and the normal impulse p_N , between times $t = i$ and $t = t$ is given by:

$$m(v_N - v_{iN}) = \int_i^t F dt = p_N \quad (\text{B.3b})$$

The relative normal velocity v_N at any time t during the impact can be obtained by integration of equation (B.3b), for the initial condition that at the moment of impact $t=i$, the normal velocity is v_{iN} and:

$$v_N = \int_i^t \frac{1}{m} dp_N \quad (\text{B.4})$$

$$= \frac{1}{m}(p_N - p_{iN})$$

$$v_N = v_{iN} + \frac{p_N}{m} \quad (\text{B.5})$$

where $v_{iN} < 0$

The impacting normal velocity is negative because, as shown in Figure B.1, the positive normal axis is in the direction away from the point of impact.

Equation (B.5) shows that the relative velocity is a linear function of the normal impulse, which is expressed as a straight line on Figure B.1.

Equation (B.5) can be used to find the impulse at maximum compression (p_{cN}). At the point of maximum compression ($t = c$), the normal velocity is momentarily equal to zero and the corresponding normal impulse has a value p_{cN} given by equation:

$$0 = v_{iN} + \frac{p_{cN}}{m}$$

and

$$p_{cN} = -m \cdot v_{iN} \quad (\text{B.6})$$

At the end of the impact ($t = f$), the final normal velocity is v_{fN} and the final normal impulse (p_{fN}) can also be found from equation (B.5),

$$p_{fN} = (m \cdot v_f - m \cdot v_i) \quad (\text{B.7})$$

With respect to the energy of deformation, the triangular area E_{cN} on Figure B.1 represents the kinetic energy of normal motion that is absorbed in compressing the deformable region, while triangular area ($E_{fN} - E_{cN}$) represents the elastic strain energy recovered during restitution that drives the body from the slope.

Expressions for these two energy changes are:

Compression:

$$\begin{aligned} E_{cN} &= \int_0^{p_{cN}} v_N dp_N = \int_0^{p_{cN}} \left(v_{iN} + \frac{p_N}{m} \right) dp_N \\ &= \left(v_{iN} \cdot p_{cN} + \frac{p_{cN}^2}{2m} \right) \\ &= -\frac{1}{2} m \cdot v_{iN}^2 \end{aligned} \quad (\text{B.8})$$

Equation (B.8) shows that all the normal impact kinetic energy is absorbed up to the point of maximum compression.

Restitution:

$$\begin{aligned}
 (E_{fN} - E_{cN}) &= \int_{p_{cN}}^{p_{fN}} \left(v_{iN} + \frac{p_N}{m} \right) dp_N = \left[v_{iN} \cdot p_N + \frac{p_N^2}{2 \cdot m} \right]_{p_{cN}}^{p_{fN}} \\
 &= \left[v_{iN} + \frac{p_{fN}^2}{2 \cdot m} - \left(-v_{iN} \cdot p_{cN} + \frac{p_{cN}^2}{2 \cdot m} \right) \right] \\
 &= v_{iN} + \frac{p_{fN}^2}{2 \cdot m} - \left(-m \cdot v_{iN}^2 + \frac{m \cdot v_{iN}^2}{2} \right)
 \end{aligned}$$

where: $p_{cN}^2 = m^2 \cdot v_{iN}^2$

$$(E_{fN} - E_{cN}) = v_{iN} \cdot p_{fN} + \frac{p_{fN}^2}{2 \cdot m} + \frac{m \cdot v_{iN}^2}{2}$$

where: $v_{iN} = \frac{-m \cdot v_{iN}^2}{p_{cN}}$

and $\frac{1}{m} = \frac{m \cdot v_{iN}^2}{p_{cN}^2}$

$$\begin{aligned}
 (E_{fN} - E_{cN}) &= \frac{m \cdot v_{iN}^2}{2} + \left(-\frac{m \cdot v_{iN}^2}{p_{cN}} \right) p_{fN} + \left(\frac{m \cdot v_{iN}^2}{2 \cdot p_{cN}^2} \right) p_{fN}^2 \\
 &= \frac{m \cdot v_{iN}^2}{2} \left(1 - 2 \frac{p_{fN}}{p_{cN}} + \frac{p_{fN}^2}{p_{cN}^2} \right) \\
 &= \frac{1}{2} m \cdot v_{iN}^2 \left(\frac{p_{fN}}{p_{cN}} - 1 \right)^2 \tag{B.9}
 \end{aligned}$$

where $v_{iN} < 0$.

The expressions in equations (B.8) and (B.9) for the partially irreversible changes in kinetic energy of normal motion that occur during impact can be used to define the normal coefficient of restitution, e_N as follows:

$$e_N^2 = -\frac{E_N(p_{fN}) - E_N(p_{cN})}{E_N(p_{cN})} \tag{B.10}$$

This definition of the coefficient of restitution in terms of energy separates the energy loss due to plastic compression and hysteresis of the contact forces from that due to friction and slip between the colliding bodies.

The relationships shown in equations (B.8), (B.9) and (B.10) can be combined, for normal impact, to find the following expression for the normal coefficient of restitution in terms of the normal impulses at maximum compression (p_{cN}) and at the completion of the impact (p_{fN}):

$$e_N^2 = \left(\frac{p_{fN}}{p_{cN}} - 1 \right)^2 \quad (\text{B.11})$$

Substitution of the expressions for p_{cN} and p_{fN} in equations (B.6) and (B.7) into equation (B.11), yields the following expression relating impulse to the coefficient of restitution:

$$p_{fN} = -m \cdot v_{iN}(1 + e_N) = p_{cN}(1 + e_N) \quad (\text{B.12})$$

and for the normal coefficient of restitution,

$$e_N = -\frac{v_{fN}}{v_{iN}} \quad (\text{B.1})$$

$$e_N = \frac{(p_{fN} - p_{cN})}{p_{cN}}$$

As shown in Figure B.1 and expressed in equation (B.1), the normal coefficient of restitution is the ratio of final normal velocity to the impact normal velocity, and is also the square root of the negative ratio of the energy recovered during the restitution phase of the impact to the energy lost during the compression phase (equation (B.10)).

For rough bodies where slip occurs at the contact point, but the direction of slip is constant, the two expressions for the coefficient of restitution in equations (B.1) and (B.13) are equivalent.

Appendix C: Impact mechanics – impact of rough, rotating bodies

This appendix shows the derivation of equations defining the final translational and rotational velocities due to impact of a rough, rotating body. This is an expansion of the information contained in Section 4.6.2.

C.1 Equations of relative motion

For a rotating body impacting a slope at an oblique angle, the body will have both translational v , and angular ω , velocities. The relative velocities at the impact points, expressed as normal and tangential components, are v_N and v_T . (Figure C.1). At the contact point, equal and opposite forces, F , $-F$ are developed that oppose interpenetration of the body into the slope and give differentials of impulse dp over time dt in the normal and tangential directions that are related by:

$$dp = F dt \quad (C.1)$$

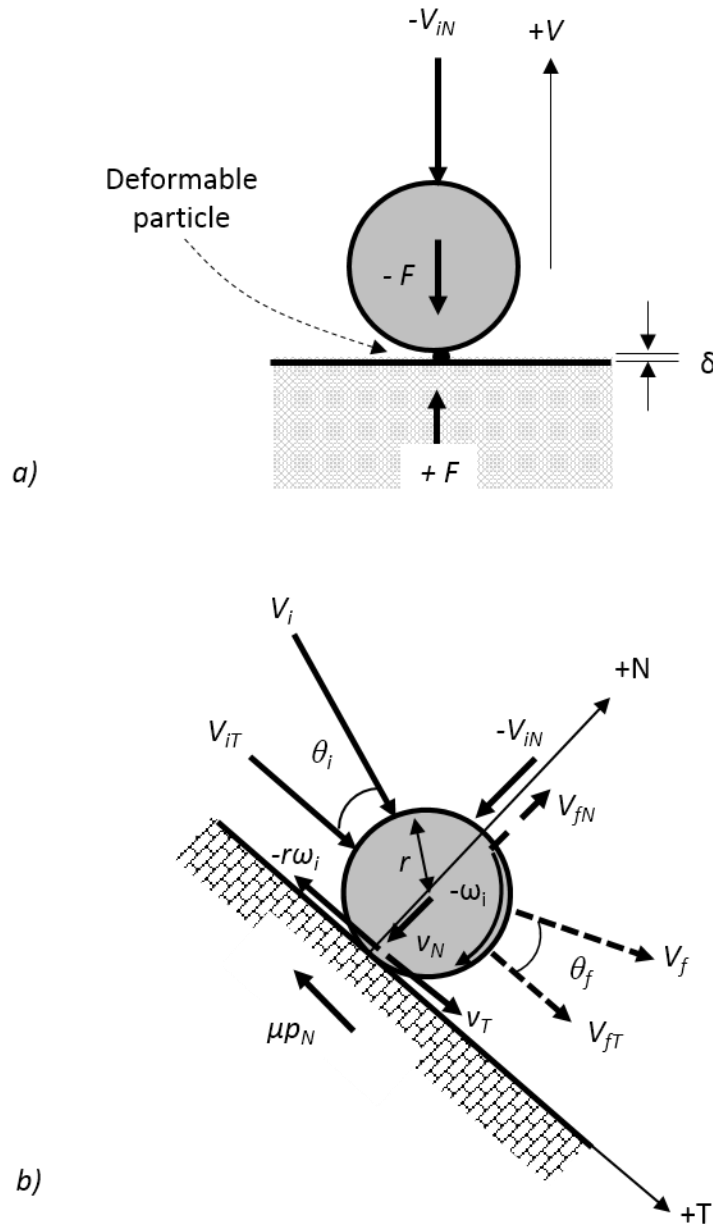


Figure C.1: Impact mechanics principles for two dimensional (planar) motion a) forces generated at contact point during normal impact; b) impact of rough, rotating sphere on a slope, v = velocity at center of mass, V = relative velocity at impact point

From Newton's second law (see Section 4.1.2), equations of motion for translation of the centre of the body with mass m and velocity v , for the normal N and tangential T axes are:

$$dV_N = \frac{dp_N}{m} \tag{C.2}$$

and

$$dV_T = \frac{dp_T}{m} \quad (C.3)$$

and for planar rotation of a body with radius r and radius of gyration k :

$$d\omega = \frac{r}{m \cdot k^2} dp_T \quad (C.4)$$

The relative velocity at the contact point, v , is the difference between the velocity at the center of mass, V , and the peripheral velocity $r \cdot \omega$. The relative velocity has components v_N and v_T in the normal and tangential directions.

Based on these relationships, the planar relative velocity changes are given by:

$$\begin{Bmatrix} dv_T \\ dv_N \end{Bmatrix} = m^{-1} \begin{bmatrix} \beta_1 & -\beta_2 \\ -\beta_2 & \beta_3 \end{bmatrix} \begin{Bmatrix} dp_N \\ dp_T \end{Bmatrix} \quad (C.5)$$

from which the tangential and normal components of the velocity changes are

$$dv_T = \frac{(\beta_1 dp_T - \beta_2 dp_N)}{m} \quad (C.6a)$$

and

$$dv_N = \frac{(-\beta_2 dp_T + \beta_3 dp_N)}{m} \quad (C.6b)$$

where β_1 , β_2 and β_3 are inertial coefficients. The definition of the inertial coefficients is shown in Figure C.2 where a body with mass M impacts the slope with mass M' . A local axis system is set up at the impact point with the tangential (T) axis parallel to the slope, and the normal (N) axis normal to the slope with positive away from the slope. The dimensions of the body relative to its centre of mass and the point of impact are defined by tangential and normal radii, r_T and r_N and the radius of gyration k . If the body is rotating about a fixed z axis, the components of the moments of inertia for plane motion are defined by the tensor, I' :

$$I' = \begin{bmatrix} m(r_N^2 + z^2) & -m \cdot r_T \cdot r_N \\ -m \cdot r_N \cdot r_T & m(z^2 + r_T^2) \end{bmatrix} \quad (C.7)$$

that yields three components of the moment of inertia I :

$$I_{TT} = m(r_N^2 + z^2); \quad I_{TN} = -m \cdot r_T \cdot r_N; \quad I_{Tz} = -m(z^2 + r_T^2) \quad (C.8)$$

Inertial coefficient β_1 is in relation to the term $(r_N^2 + z^2)$ where $z = 1$:

$$\beta_1 = 1 + \frac{m \cdot r_N^2}{M \cdot k_r^2}$$

Inertial coefficient β_2 is in relation to the term $(m \cdot r_T \cdot r_N)$:

$$\beta_2 = \frac{m \cdot r_N \cdot r_T}{M \cdot k_r^2}$$

Inertial coefficient β_3 is in relation to the term $(z^2 + r_T^2)$:

$$\beta_3 = 1 + \frac{m \cdot r_T^2}{M \cdot k_r^2}$$

(C.9)

where m is the effective mass of the two impacting bodies and is defined as

$$m = (M^{-1} + M'^{-1})^{-1} \quad (C.10)$$

Since the mass of the slope M' is very large, $m = M$, the inertial coefficients are reduced to:

$$\beta_1 = 1 + \frac{r_N^2}{k^2}$$

$$\beta_2 = \frac{r_N \cdot r_T}{k^2}$$

$$\beta_3 = 1 + \frac{r_T^2}{k^2}$$

(C.11)

Equations (C.11) for the inertial coefficients can be applied to any body shape with radius r and radius of gyration k .

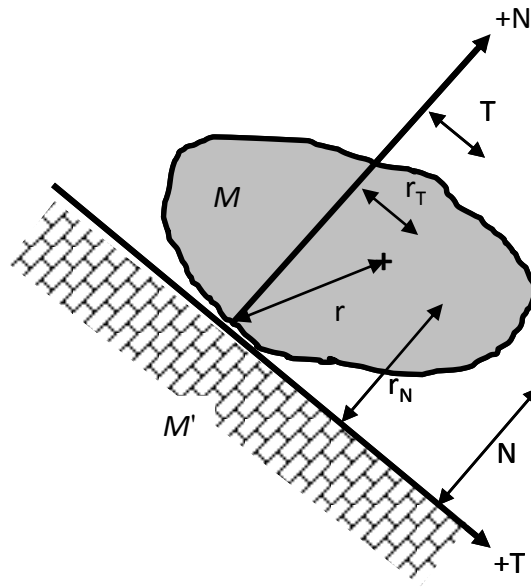


Figure C.2: Dimensions of rotating, impacting body defining inertial coefficients for plane motion, rotating about z axis through centre of gravity (+)

C.2 Equations of planar motion for impact of rough bodies

For usual rock fall conditions where friction is generated at the impact point, the body may initially slip from the point of impact until a normal impulse value p_{sN} , and then roll during which time the relative tangential velocity at the contact point v_T , is zero (Figure C.3). According to Coulomb's law, if the coefficient of friction is μ , then the body will slip at the contact point when the relationship between the tangential and normal impulses is:

$$p_T = -\mu \cdot p_N \tag{C.12}$$

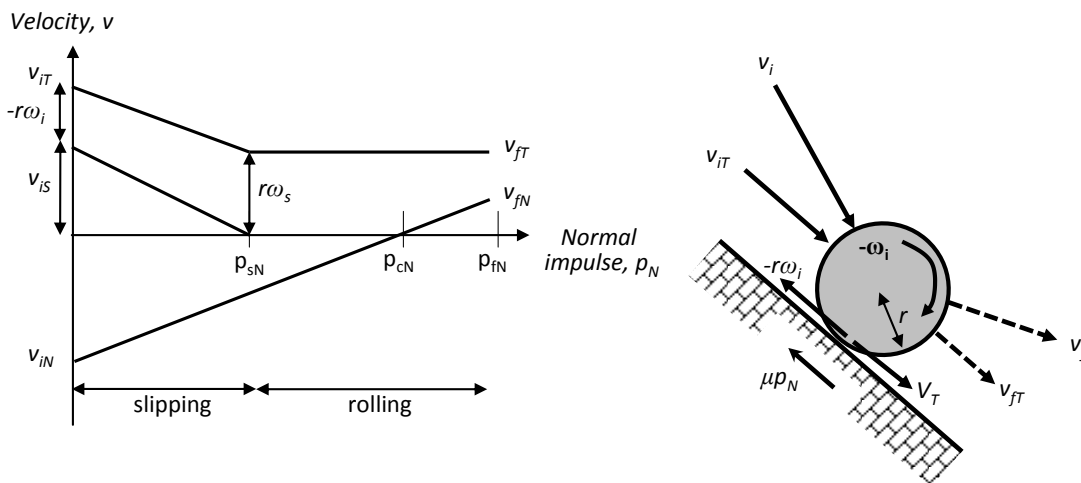


Figure C.3: Changes in rotational (ω) and slip (v_s) velocities during impact, and transition from slip to rolling mode when $v_s = 0$; for negative angular velocity: $v_s = (v_T - r \cdot \omega)$

From equation (C.5), the change in relative velocity components during the period of slip in terms of the normal impulse p_N , are:

$$\begin{Bmatrix} dv_T \\ dv_N \end{Bmatrix} = m^{-1} \begin{bmatrix} \beta_1 & -\beta_2 \\ -\beta_2 & \beta_3 \end{bmatrix} \begin{Bmatrix} -\mu dp_N \\ dp_N \end{Bmatrix} \quad (\text{C.13})$$

and the equations for the change in relative velocity components are given by:

$$dv_T = \frac{(-\mu \cdot \beta_1 - \beta_2) dp_N}{m} \quad (\text{C.14a})$$

and

$$dv_N = \frac{(\mu \cdot \beta_2 + \beta_3) dp_N}{m} \quad (\text{C.14b})$$

Integration of these equations for dv_T and dv_N for the period $t = i$ to $t = v_s$ gives components of velocity for any normal impulse p_N , during the period of slip

$$v_T = v_{iT} - \frac{(\beta_2 + \mu \cdot \beta_1)}{m} p_N \quad (\text{C.15a})$$

and

$$v_N = v_{iN} + \frac{(\beta_3 + \mu \cdot \beta_2)}{m} p_N \quad (\text{C.15b})$$

Equations (C.15a, b) show that the relationship between v and p_N is linear with the gradient being proportional to $(1/m)$. The equations also show that tangential velocity decreases throughout the impact from the impact value v_{iT} , while the normal velocity increases from an initial negative value to a final positive value as it leaves the slope.

At the point of maximum compression during impact, the normal velocity is zero and equation (C.15b) gives the following expression for the normal impulse p_{cN}

$$v_N = 0 = v_{iN} + \frac{(\beta_3 + \mu \cdot \beta_2)}{m} p_{cN}$$

and

$$p_{cN} = \frac{-m \cdot v_{iN}}{(\beta_3 + \mu \cdot \beta_2)} \quad (\text{C.16})$$

From Appendix B, equation (B.12), the relationship between the impulses at maximum compression and the completion of the impact is:

$$p_{fN} = -m \cdot v_{iN}(1 + e_N) = p_{cN}(1 + e_N) \quad (C.17)$$

from which it is possible to develop, for a rough, rotating body, an expression for the impulse at the end of the impact, p_{fN}

$$p_{fN} = \frac{-(1 + e_N)m \cdot v_{iN}}{(\beta_3 + \mu \cdot \beta_2)} \quad (C.18)$$

C.3 Equations of motion for translating and rotating bodies – final velocities

The angular velocity ω can be incorporated into the impact mechanics equations (C.5) to (C.11) as follows.

For a collinear impact of a sphere with radius r , Figure C.3 shows that $r_T = 0$ and $r_N = r$, and equations (C.11) are further reduced to:

$$\beta_1 = 1 + \frac{r_N^2}{k^2}; \quad \beta_2 = 0; \quad \beta_3 = 1$$

and equations (C.15a) and b)) for the tangential and normal velocity components simplify to:

$$v_T = v_{iT} - \frac{(\mu \cdot \beta_1)}{m} p_N \quad (C.19a)$$

$$v_N = v_{iN} + \frac{p_N}{m} \quad (C.19b)$$

For the impacting sphere that is a rigid body, the translational velocity components at the centre of mass are designated by V_T and V_N and the differential equations for the changes in velocity components in terms of the normal impulse are:

$$dV_T = \frac{-\mu}{m} dp_N; \quad dV_N = \frac{dp_N}{m}; \quad d\omega = \frac{-\mu \cdot r}{m \cdot k^2} dp_N \quad (C.20)$$

The components of relative velocity at the contact point for collinear impact are:

$$v_T = V_T + r \cdot \omega; \quad v_N = V_N \quad (C.21)$$

The equations for the relative velocity at the point of impact in terms of the normal impulse are obtained by integration, for the initial conditions ($v_{iT} = V_{iT} + r \cdot \omega_i$) and ($v_{iN} = V_{iN}$) as follows:

Tangential velocity:

$$v_T = v_{iT} + \int dv_T + r \int d\omega$$

$$v_T = v_{iT} + \int \frac{-\mu}{m} dp_N + r \int \frac{-\mu \cdot r}{m \cdot k^2} dp_N$$

$$v_T = v_{iT} - \frac{\mu}{m} \left(1 + \frac{r^2}{k^2} \right) p_N \quad (C.22)$$

Normal velocity:

$$v_N = v_{iN} + \frac{1}{m} \int dp_N$$

$$v_N = v_{iN} + \frac{p_N}{m} \quad (C.23)$$

The transition from compression to restitution occurs at the point of maximum compression when ($v_{cN} = 0$) and ($p_{cN} = -m \cdot v_{iN}$). Using these relationships, the equations for the tangential and normal relative velocities can be expressed as dimensionless ratios as follows:

$$\frac{v_T}{v_{iN}} = \frac{v_{iT}}{v_{iN}} + \mu \left(1 + \frac{r^2}{k^2} \right) \frac{p_N}{p_{cN}} \quad (C.24)$$

and

$$\frac{v_N}{v_{iN}} = 1 - \frac{p_N}{p_{cN}} \quad (C.25)$$

When slip stops prior to separation ($p_s < p_f$), the relative tangential velocity $v_{sT} = 0$, and equation (C.24) can be solved to determine an expression for the impulse ratio at time $t = s$:

$$\frac{p_{sN}}{p_{cN}} = - \frac{\frac{v_{iT}}{v_{iN}}}{\mu \left(1 + \frac{r^2}{k^2} \right)} = - \frac{(V_{iT} + r \cdot \omega)}{V_{iN} \cdot \mu \cdot \left(1 + \frac{r^2}{k^2} \right)} \quad (C.26)$$

Furthermore, when sliding halts prior to separation, no changes occur to either the tangential velocity or the angular velocity from this point until the point of separation, i.e., ($v_{fT} = v_{sT}$) and ($\omega_f = \omega_s$).

Expressions for the final tangential and normal velocity components at the centre of mass are:

$$\begin{aligned} V_{fT} &= V_{iT} + \mu \frac{P_{sN}}{P_{cN}} V_{iN} \\ &= V_{iT} - \frac{(V_{iT} + r \cdot \omega_i)}{\left(1 + r^2/k^2\right)} \end{aligned} \quad (C.27)$$

$$V_{fN} = -V_{iN} \cdot e_N \quad (C.28)$$

and the final rotational velocity is:

$$\begin{aligned} r \cdot \omega_f &= r \cdot \omega_i + \mu \frac{r^2}{k^2} \frac{P_{sN}}{P_{cN}} V_{iN} \\ \omega_f &= \omega_i - \frac{r}{k^2} \frac{(V_{iT} + r \cdot \omega_i)}{\left(1 + r^2/k^2\right)} \end{aligned} \quad (C.29)$$

Equations (C.27) and (C.28) for the final tangential and normal velocity components respectively can then be solved to find the final restitution velocity V_f and angle θ_f as follows:

$$V_f = \sqrt{V_{fT}^2 + V_{fN}^2} \quad (C.30)$$

$$\theta_f = \text{atan}\left(\frac{V_{fN}}{V_{fT}}\right) \quad (C.31)$$

Figure C.4 shows these equations for the final velocities and angles diagrammatically, in terms of the three impact parameters: V_i , θ_i and ω_i .

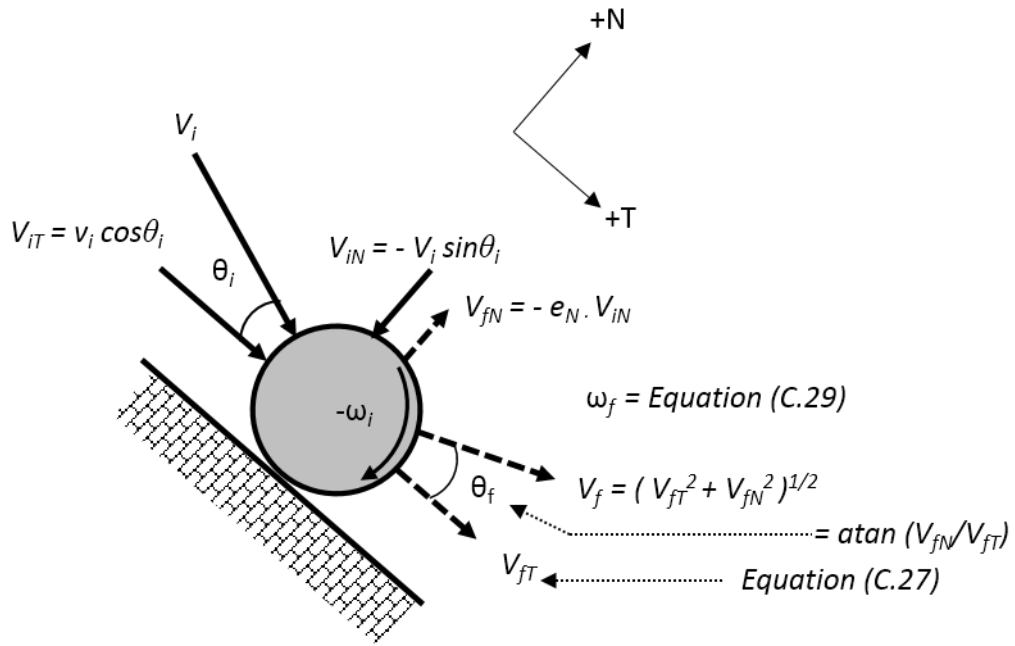


Figure C.4: Diagram of impact showing impact and restitution velocity vectors and equations for calculating final velocities

Appendix D: Energy loss equations

This appendix shows the derivation of equations defining the energy changes that occur during normal impact of a non-rotating body, and is an expansion of the equations described in Section 6.1 in the main text.

Equations for the energy changes during impact can be developed from the $[p_N - v]$ plot illustrated in Figure D.1 where the impact process is divided into compression and restitution phases. The energy change during each phase is represented by the areas on the $[\delta - F]$ plot or the $[p_N - v]$ plot. The appendix derives the energy changes in terms of the normal impulse p_N and relative velocity v using the linear relationship between these two parameters established in Appendix B, equation (B.5).

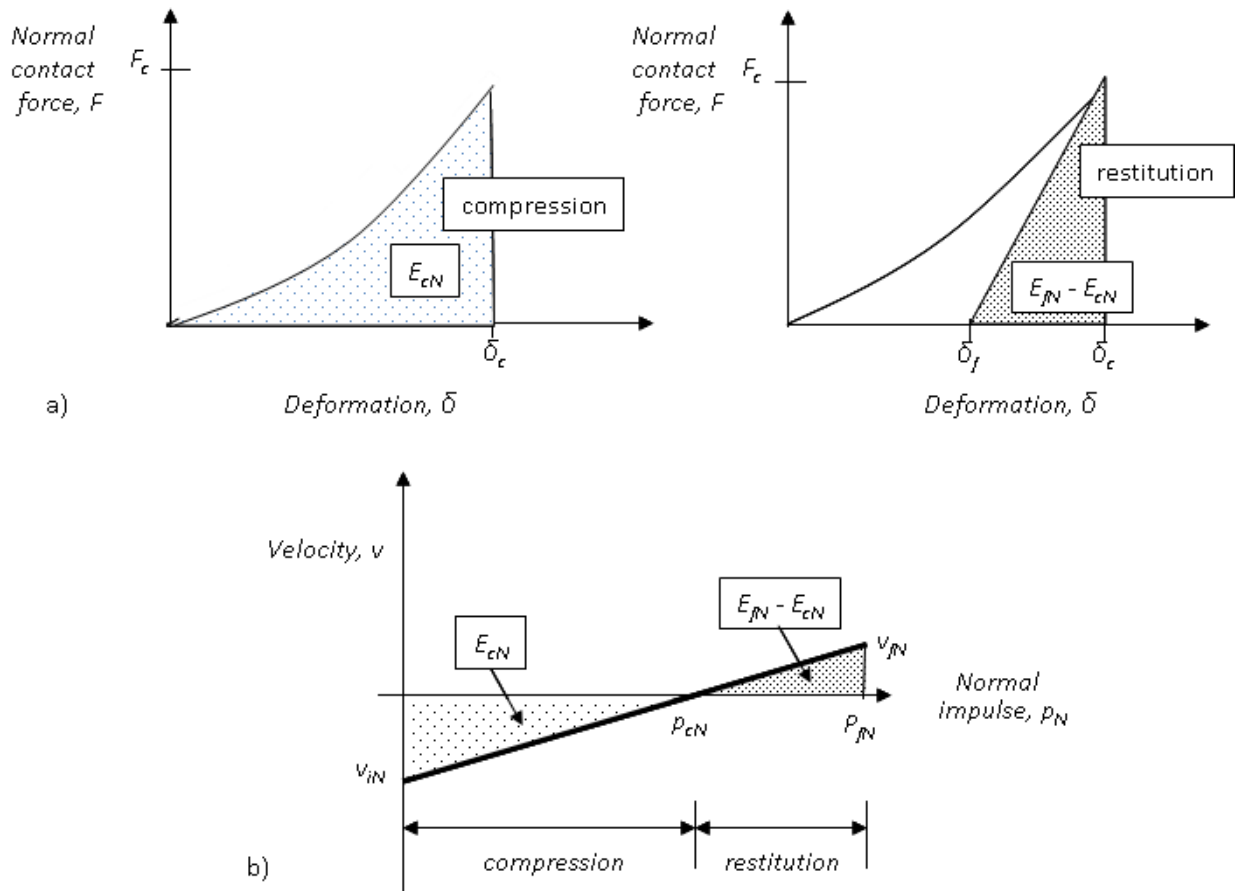


Figure D.1: Energy changes (normal) during compression and restitution phases of impact. a) Forces generated at contact point during normal impact, with energy changes plotted on [force, F – deformation, δ] graph; b) energy changes plotted on [normal impulse, p_N – velocity, v] graph

The impact process can be simulated by an infinitesimal deformable particle at the impact point.

During impact, the energy E_N generated in the particle by the normal component of the force F_N

can be calculated from the relationship between the force and the differential normal impulse: $dp_N = F_N dt = m dv$, so that the energy generated from the moment of impact ($t = i$) up to time t is:

$$E_N = \int_i^t F_N \cdot v_N dt = \int_i^{p_N} v_N dp_N \quad (D.1)$$

For the compression phase of the impact up to the impulse p_{cN} , the relationships between impulse and velocity are as follows:

$$p_{cN} = -m \cdot v_{iN} \quad (\text{see equation (B.6)})$$

where v_{iN} is negative because it acts towards the slope in the direction of the $(-N)$ axis (see Figure C.1a).

$$\text{and } v_N = \left(v_{iN} + \frac{p_N}{m} \right) \quad (\text{see equation (B.5)})$$

Therefore, the energy lost during the compression phase of the impact is given by:

$$\begin{aligned} E_N(p_{cN}) &= \int_i^{p_{cN}} v_N dp_N \\ &= \int_0^{p_{cN}} \left(v_{iN} + \frac{p_N}{m} \right) dp_N \\ &= v_{iN} \cdot p_{cN} + \frac{p_{cN}^2}{2 \cdot m} \\ &= -\frac{1}{2} m \cdot v_{iN}^2 \end{aligned} \quad (D.2)$$

where v_{iN} is the normal impact velocity and m is the mass of the body.

Equation (D.2) shows that all the normal impact kinetic energy is lost ($E_N(p_{cN})$ is negative) up to the point of maximum compression, δ_c when the normal velocity is reduced to zero ($v_N = 0$).

A similar approach can be used to find the energy recovered during the restitution phase of the impact, ($E_N(p_f) - E_N(p_c)$) between maximum compression (p_{cN}) and the end of the impact (p_{fN}):

$$E_N(p_{fN}) - E_N(p_{cN}) = \int_{p_{cN}}^{p_{fN}} \left(v_{iN} + \frac{p_N}{m} \right) dp_N$$

$$\begin{aligned}
 &= \left[v_{iN} \cdot p_{fN} + \frac{p_{fN}^2}{2 \cdot m} \right] - \left[v_{iN} \cdot p_{cN} + \frac{p_{cN}^2}{2 \cdot m} \right] \\
 &= \frac{m \cdot v_{iN}^2}{2} \left(1 - \frac{p_{fN}}{p_{cN}} \right)^2
 \end{aligned}$$

The energy recovered during restitution is termed the elastic strain energy. A complete derivation of equation (D.3) is given in Appendix B, equation (B.9).

Alternatively, the elastic strain energy can be calculated from the area of the restitution triangle between impulse values p_{cN} and p_{fN} on Figure C.1b as follows:

$$\begin{aligned}
 E_N(p_{fN}) - E_N(p_{cN}) &= \frac{1}{2} (p_{fN} - p_{cN}) v_{fN} \\
 &= \frac{1}{2} p_{cN} \left(\frac{p_{fN}}{p_{cN}} - 1 \right) \left(v_{iN} + \frac{p_{fN}}{m} \right) \\
 &= \frac{m \cdot v_{iN}}{2} \left(\frac{p_{fN}}{p_{cN}} - 1 \right) \left(v_{iN} + \frac{p_{fN} \cdot v_{iN}}{p_{cN}} \right) \\
 &= \frac{m \cdot v_{iN}^2}{2} \left(1 - \frac{p_{fN}}{p_{cN}} \right) \left(1 - \frac{p_{fN}}{p_{cN}} \right) \\
 &= \frac{m \cdot v_{iN}^2}{2} \left(1 - \frac{p_{fN}}{p_{cN}} \right)^2
 \end{aligned} \tag{D.3}$$

Equations (D.2) and (D.3) together define the net energy loss during normal impacts as;

$$\begin{aligned}
 E_N(\text{net}) &= [\text{energy lost in compression}] + [\text{energy gained in restitution}] \\
 &= [E_N(p_{fN})] + [E_N(p_{fN}) - E_N(p_{cN})] \\
 &= -\frac{m \cdot v_{iN}^2}{2} + \frac{m \cdot v_{iN}^2}{2} \left(1 - \frac{p_{fN}}{p_{cN}} \right)^2 \\
 &= -\frac{m \cdot v_{iN}^2}{2} \left[1 - \left(1 - \frac{p_{fN}}{p_{cN}} \right)^2 \right]
 \end{aligned} \tag{D.4}$$

Equation (B.12) defines the relationship between normal impulses p_{fN} , p_{cN} and the normal coefficient of restitution e_N as:

$$p_{fN} = -m \cdot v_{iN} (1 + e_N) = p_{cN} (1 + e_N) \quad (D.5)$$

and

$$\frac{P_{fN}}{P_{cN}} = (1 + e_N)$$

and

$$e_N^2 = \left(1 - \frac{P_{fN}}{P_{cN}} \right)^2$$

Substitution of equation of (D.5) into equation (D.4) gives the following expression for the net energy loss during normal impact:

$$E_N(\text{net}) = -\frac{1}{2} m \cdot v_{iN}^2 (1 - e_N^2) \quad (D.6)$$

In the development of equation (D.6) for normal impact, the value of e_N is always less than 1 because it is defined by the energy losses for a spherical body.

Appendix E: Conversion factors

Imperial Unit	SI Unit	SI Unit Symbol	Conversion Factor (Imperial to SI)	Conversion Factor (SI to Imperial)
Length				
Mile	kilometer	km	1 mile = 1.609 km	1 km = 0.6214 mile
Foot	Meter	m	1 ft = 0.3048 m	1 m = 3.2808 ft
	millimeter	mm	1 ft = 304.80 mm	1 mm = 0.003 281 ft
Inch	millimeter	mm	1 in = 25.40 mm	1 mm = 0.039 37 in
Area				
Square mile	square kilometer	km ²	1 mile ² = 2.590 km ²	1 km ² = 0.3861 mile ²
	hectare	ha	1 mile ² = 259.0 ha	1 ha = 0.003 861 mile ²
Acre	hectare	ha	1 acre = 0.4047 ha	1 ha = 2.4710 acre
	square meter	m ²	1 acre = 4047 m ²	1 m ² = 0.000 247 1 acre
Square foot	square meter	m ²	1 ft ² = 0.092 90 m ²	1 m ² = 10.7639 ft ²
Square inch	square millimeter	mm ²	1 in ² = 645.2 mm ²	1 mm ² = 0.001 550 in ²
Volume				
Cubic yard	cubic meter	m ³	1 yd ³ = 0.7646 m ³	1 m ³ = 1.3080 yd ³
Cubic foot	cubic meter	m ³	1 ft ³ = 0.028 32 m ³	1 m ³ = 35.3147 ft ³
	liter	/	1 ft ³ = 28.32 /	1 liter = 0.035 31 ft ³
Cubic inch	cubic millimeter	mm ³	1 in ³ = 16 387 mm ³	1 mm ³ = 61.024 x 10 ⁻⁶ in ³
	cubic centimeter	cm ³	1 in ³ = 16.387 cm ³	1 cm ³ = 0.061 02 in ³
	liter		1 in ³ = 0.016 39 /	1 liter = 61.02 in ³
Imperial gallon	cubic meter	m ³	1 gal = 0.004 55 m ³	1 m ³ = 220.0 gal
	liter	/	1 gal = 4.546 /	1 liter = 0.220 gal
Pint	liter	/	1 pt = 0.568 /	1 liter = 1.7598 pt
US gallon	cubic meter	m ³	1 US gal = 0.0038 m ³	1 m ³ = 264.2 US gal
	liter	/	1 US gal = 3.8 /	1 liter = 0.264 US gal
Mass				
Ton	tonne	t	1 ton = 0.9072 tonne	1 tonne = 1.1023 ton
ton (2000 lb) (US)	kilogram	kg	1 ton = 907.19 kg	1 kg = 0.001 102 ton
ton (2240 lb) (UK)	kilogram	kg	1 ton = 1016.0 kg	1 kg = 0.000 984 ton
Kip	kilogram	kg	1 kip = 453.59 kg	1 kg = 0.002 204 6 kip
Pound	kilogram	kg	1 lb = 0.4536 kg	1 kg = 2.204 6 lb

Appendix E

Imperial Unit	SI Unit	SI Unit Symbol	Conversion Factor (Imperial to SI)	Conversion Factor (SI to Imperial)
Mass Density				
ton per cubic yard (2000 lb) (US)	kilogram per cubic meter	kg/m ³	1 ton/yd ³ = 1186.55 kg/m ³	1 kg/m ³ = 0.000 842 8 ton/yd ³
	tonne per cubic meter	t/m ³	1 ton/yd ³ = 1.1866 t/m ³	1 t/m ³ = 0.8428 ton/yd ³
ton per cubic yard (2240 lb) (UK)	kilogram per cubic meter	kg/cm ³	1 ton/yd ³ = 1328.9 kg/m ³	1 kg/m ³ = 0.000 75 ton/yd ³
	pound per cubic foot	kilogram per cubic meter	1 lb/ft ³ = 16.02 kg/m ³	1 kg/cm ³ = 0.062 42 lb/ft ³
Pound per cubic inch	tonne per cubic meter	t/m ³	1 lb/ft ³ = 0.01602 t/m ³	1 t/m ³ = 62.42 lb/ft ³
	gram per cubic centimeter	g/cm ³	1 lb/in ³ = 27.68 g/cm ³	1 g/cm ³ = 0.036 13 lb/in ³
	tonne per cubic meter	t/m ³	1 lb/in ³ = 27.68 t/m ³	1 t/m ³ = 0.036 13 lb/in ³
Force				
ton force (2000 lb) (US)	kilonewton	kN	1 tonf = 8.896 kN	1 kN = 0.1124 tonf (US)
ton force (2240 lb) (UK)	kilonewton	kN	1 tonf = 9.964 KN	1 kN = 0.1004 tonf (UK)
kip force	kilonewton	kN	1 kipf = 4.448 kN	1 kN = 0.2248 kipf
pound force	newton	N	1 lbf = 4.448 N	1 N = 0.2248 lbf
tonf/ft (2000 lb) (US)	kilonewton per meter	kN/m	1 tonf/ft = 29.189 kN/m	1 kN/m=0.034 26 tonf/ft (US)
tonf/ft (2240 lb) (UK)	kilonewton per meter		1 tonf/ft = 32.68 kN/m	1 kN/m = 0.0306 tonf/ft (UK)
pound force per foot	newton per meter	N/m	1 lbf/ft = 14.59 N/m	1 N/m = 0.068 52 lbf/ft

Appendix E

Imperial Unit	SI Unit	SI Unit Symbol	Conversion Factor (Imperial to SI)	Conversion Factor (SI to Imperial)
Flow Rate				
cubic foot per minute	cubic meter per second	m ³ /s	1 ft ³ /min = 0.000 471 9 m ³ /s	1 m ³ /s = 2118.880 ft ³ /min
	liter per second	l/s	1 ft ³ /min = 0.4719 l/s	1 l/s = 2.1189 ft ³ /min
cubic foot per second	cubic meter per second	m ³ /s	1 ft ³ /s = 0.028 32 m ³ /s	1 m ³ /s = 35.315 ft ³ /s
	liter per second	l/s	1 ft ³ /s = 28.32 l/s	1 l/s = 0.035 31 ft ³ /s
gallon per minute	liter per second	l/s	1 gal/min = 0.075 77 l/s	1 l/s = 13.2 gal/min
Pressure, Stress				
ton force per square foot (2000 lb) (US)	kilopascal	kPa	1 tonf/ft ² = 95.76 kPa	1 kPa = 0.01044 ton f/ft ²
ton force per square foot (2240 lb) (UK)	kilopascal	kPa	1 tonf/ft ² = 107.3 kPa	1 kPa = 0.00932 ton/ft ²
pound force per square foot	pascal	Pa	1 lbf/ft ² = 47.88 Pa	1 Pa = 0.020 89 lbf/ft ²
	kilopascal	kPa	1 lbf/ft ² = 0.047 88 kPa	1 kPa = 20.89 lbf/ft ²
pound force per square inch	pascal	Pa	1 lbf/in ² = 6895 Pa	1 Pa = 0.000 1450 lbf/in ²
	kilopascal	kPa	1 lbf/in ² = 6.895 kPa	1 kPa = 0.1450 lbf/in ²
Weight Density*				
pound force per cubic foot	kilonewton per cubic meter	kN/m ³	1 lbf/ft ³ = 0.157 kN/m ³	1 kN/m ³ = 6.37 lbf/ft ³
Energy				
Foot lbf	joules	J	1 ft lbf = 1.356 J	1 J = 0.7376 ft lbf

* Assuming a gravitational acceleration of 9.807 m/s².

Index

A

Accelerometer	
Japan test site	22
Air friction	88
Angular velocity	
block radius	56, 85
block shape (sphere, cube, boulder)	56
clockwise/counter clockwise	84
effect on trajectory	59, 83
energy change	116
final value equation	80, 217
friction effects	73
impact with fence	164
impulse relationship	78
Japan test site	56
rock fall modeling	140
rotation during trajectory	75
Asperity	101
Asphalt	
impact energy (calculated)	156
normal coefficient of restitution/impact angle relationship	96
rock fall modeling	156
test site	30
trajectories (calculated)	156
Attenuation	
high speed camera image	183
impact energy	173
impact with fence	179
model testing	180
oblique impact with fence	178
rock fall energy	161
stiff protection structures	181

B

Back analysis	
rock fall modeling	131
Basalt	
Oregon	18
Baseball pitching machine	182
Bench	
rock fall containment	160
Best fit curve	
normal coefficient of restitution/impact angle relationship	97
Block shape	

angular velocity	56
restitution angle	53
Brake	
guy wire	169

C

Canada	
Mt. Stephen	13, 141
Shuswap Lake	170
Tornado Mountain	24
Vancouver Island	129
Case study.....	11
asphalt	31
Japan, Ehime.....	20
Mt. Stephen.....	13
Oregon test site	18
restitution velocity	85
summary of results.....	33
Tornado Mountain	24
Christchurch, New Zealand	
impact points.....	35
Coefficient of restitution	
case studies	12, 33
tree impacts.....	127
velocity changes	70
Coefficient of restitution, normal	
concrete.....	95
definition	89
energy changes.....	72
energy definition	207
final velocity	81
greater than 1.....	91
impact angle relationship.....	90, 137
impact mechanics.....	204
material property	88
plot, normal value/impact angle	95
rock fall modeling	98, 136
Coefficient of restitution, tangential	
case study values	33, 100
rock fall modeling	138
Collinear impact.....	93, 188, 215
Colluvium	
asphalt test site	30
coefficient of restitution, normal	97
Tornado Mountain	24
<u>Colorado Rockfall Simulation Program.....</u>	131
Compression	
energy loss equations.....	219

Concrete	
coefficient of restitution	95
drop test	32, 97
friction coefficient test	102
Concrete block	
Japan test site	22
Mt. Stephen	15
Concrete wall	
rigidity	161
shattered by rock fall	162
Contact duration (model tests)	183
Conversion factors	223
Correlation coefficient	
normal coefficient of restitution/impact angle relationship	97
Coulomb's law of friction	73, 113, 213
Cross-section down gully	60
Cube	
angular velocity	See Angular velocity
concrete	150
Japan test site	22
volume, radius of gyration	79
Cuboid	
asphalt test site	32
Oregon case study	20
Cylinder	
rock fall modeling	135
volume, radius of gyration	79

D

Decision analysis	
protection options	62
Deformable particle	64, 108, 209, 219
Deformation/velocity plot	
energy change	106
Design principles	
rock fall protection	160
Digital terrain model (DTM)	134
Discoid	
rock fall modeling	135
Discrete element model (DEM)	141
Dispersion of rock falls	
angle	62
effect of trees	127
Ditch	
hanging net	168
Oregon case study	18
Drop test	
concrete	95

Duration	
contact time with structure.....	174
impact in model testing.....	185

E

Eccentric impact	94, 189
Effective friction coefficient	50
Elastic impact.....	67
$e_N = 1$	72
Elastic strain energy	
conversion to kinetic energy	105
derivation of equation.....	221
recovery during restitution	71, 109
velocity of body after impact	206
Ellipsoid	
Mt. Stephen.....	18
Tornado Mountain	28
volume, radius of gyration	79
Energy	
[Force - time] curve	67
Energy absorption	
rigid, flexible, stiff structures.....	171, 174
Energy change	
derivation of equations	219
during impact	67
energy partition diagram.....	120
impact and trajectory.....	104
inclined impact/rotating body.....	110
mitigation structure design	160
normal impact/non-rotating body	105
normal impact/rotating body.....	111
normal, recovery/restitution.....	112
relationship to impact angle.....	91
rotational energy	116
tangential/rotating body	113
total change during impact	117
Energy efficiency	
impact with fence.....	167
rock fall fence	183
Energy head.....	121
Energy loss	
compression phase.....	71, 108
loss and recovery.....	106
Energy partition diagram	
mass constant.....	119
mass loss.....	126
Energy recovery	
restitution.....	109

Europe	
tree impacts.....	128
Exclusion zone	61

F

Fence	
energy changes during impact	166
energy efficiency	167
flexibility	161
hinge, guy wire, brake	169
impact energy absorption	162
inclined up-slope	164
Mt. Stephen.....	15
normal to slope	163
partial energy absorption.....	164
Final velocities	
translational, rotational equations.....	80, 217
Flexible protection structure	172
Force	
minimized impact force.....	171
Foundation	
hinged post.....	170
Fragmentation on impact.....	124
Friction	
fence hinges, brakes.....	171
hinge.....	173
tangential velocity	69
Friction coefficient	
angular velocity	73
effect on velocity	48
effective friction values	50
laboratory tests – soil, gravel, concrete	102
list of slope materials	50
rock fall modeling	138
tree	138

G

Gabion	
plastic impact.....	68
Geogrid	
Mt. Stephen.....	15
Golf course	62
GPS.....	27
graphical solution	
impulse calculations	94
Gravel	
friction coefficient	102
Gravity	

trajectory equation.....	36
Gully	
concentration of rock falls.....	60
rock fall modeling.....	134
Guy wire	
rock fall fence.....	169

H

Hanging net	
redirection of rock falls.....	168
Height	
trajectory, normal.....	45
trajectory, vertical.....	42
Hertz.....	63
High speed camera.....	89
Japan test site.....	22
model tests.....	181
Highway	
asphalt case study.....	30
ditch design tests.....	18
rock fall modeling.....	156
Hinge	
friction.....	173
rock fall fence.....	169

I

Impact	
compression phase.....	64
duration.....	64
energy changes.....	67
restitution phase.....	64
rough rotating body.....	76
stress induced.....	63
Impact angle	
normal coefficient of restitution relationship.....	90
Impact energy	
Mt. Stephen.....	17
Impact mechanics.....	11, 63
coefficient of restitution, normal.....	93
coefficient of restitution, normal.....	204
rough, rotating body.....	209
Impact points	
Japan test site.....	22
Mt. Stephen.....	17
Oregon case study.....	19
Tornado Mountain.....	27
Impulse	
[time – force] plot.....	174

absorption by fence.....	185
change in momentum	65
end of impact (final value).....	67
fence design.....	175
function of time.....	64
linear function of velocity.....	66
mass/velocity equation	77
maximum compression	66, 206
Newton second law	209
normal component.....	66
normal, maximum compression.....	91
relationship to impact angle.....	90
Inertial coefficient	111, 211
Integration	
[time – force] plot.....	175
final velocity calculations	216
impulse calculation.....	205
slip calculations	214
trajectory calculation.....	36
Italy	
Naples.....	122
Palermo	123

J

Japan	
Ehime test site	20
tree impacts.....	127
Japan test site	
energy loss at impact.....	160
energy partition diagram.....	119
impact energies (calculated)	151
normal coefficient of restitution/impact angle relationship.....	96
rock fall modeling	148
trajectory (calculated)	150
trajectory calculations	133
trajectory heights (calculated)	150
velocities (calculated).....	151

K

Kinetic energy	
energy partition diagram.....	119

L

Lidar	15
Limestone	
loss of mass, Italy.....	123
Mt. Stephen case study	13

Tornado Mountain case study.....	24
Limit equilibrium analysis.....	48
Linear relationship, impulse-velocity	214
Location	
protection structure	160
Loss of mass	
energy changes.....	122
rock fall modeling.....	141
Low compliance impact.....	63
Lumped mass	
rock fall modeling.....	134

M

Mass	
constant, rock fall modeling.....	135
effective, of two bodies.....	212
loss of.....	See Loss of mass
Maximum compression (impact).....	66, 204
Model testing	
angular velocity	181
baseball.....	180
duration of impact.....	185
energy absorption	181
rock fall fence	180
stiff structure.....	185
Moment of inertia	
body shapes.....	78
energy change	116
impact of rough, rotating bodies.....	211
Monte Carlo analysis	
rock fall modeling.....	140
MSE barrier	
Mt. Stephen.....	15, 143
Mt. Stephen	
case study	13
impact energies (calculated)	145
impact points (calculated).....	144
MSE barrier.....	15
normal coefficient of restitution/impact angle relationship.....	96
rock fall modeling	141
rock fall simulation	131
trajectories (calculated).....	143
velocities (calculated).....	145

N

New Zealand.....	35
Newton.....	63
coefficient of restitution.....	88

second law	65, 79, 210
third law.....	65, 88
Newtonian mechanics	11, 40, 134
Normal impulse/velocity plot	
energy change	106
Normal velocity	
changes during impact	69
final value equation.....	80, 217
negative value	69

O

Oblique impact	
partial energy absorption.....	166
Oregon test site	
case study	18
impact energies (calculated)	147
normal coefficient of restitution/impact angle relationship.....	96
rock fall modeling	145
trajectories (calculated).....	146
velocities (calculated).....	147

P

Parabola.....	11
Partial energy absorption	
fence inclined upslope.....	164
Pendulum (Newton)	88
Planar motion equations, rough bodies	213
Plastic impact	
$e_N = 0$	72
gabion	68
Poisson.....	63
Potential energy	
energy partition diagram.....	119
ProAnalyst software	182
Probabilistic analysis	
design of protection structures	90
rock fall modeling	140

R

Radius of gyration.....	211
body shapes.....	79
Railway	161
Mt. Stephen.....	13
Tornado Mountain	27
Recovery of kinetic energy	67
Redirection	
impact with fence (image).....	182

oblique impact with fence	164
rock fall fence	173
Reduction coefficient	
loss of mass	124
Relative motion equations	209
Restitution	
energy equations	219
Restitution angle	
block shape	55
effect on trajectory	51
Japan test site	52
Tornado Mountain	53
Restitution velocity	
calculated vs. case study values	85
Rigid body impact	63
Rigid body kinetics	65
Rigid protection structure	172
<i>RocFall 4.0</i>	131
Rock fall modeling	
angular velocity	135, 139
case studies	141
coefficient of restitution, normal	136
coefficients of restitution (summary)	158
CRSP coefficient of restitution, normal	136
discrete element model (DEM)	141
friction coefficients (summary)	159
Japan test site	149
mass	134
Mt. Stephen	141
Oregon test site	146
probabilistic analysis	140
sampling point	140
seeder	135
shape	134
slope parameters	135
slope roughness	134, 138, 159
tangential coefficient of restitution	138
Tornado Mountain	152
Rocky Mountains	13
Rolling contact	74
Rotational energy	
energy partition diagram	118
Rough, rotating body	
impact mechanics	209
Roughness	
coefficient of restitution, tangential	101
rock fall modeling	135
Rubber ball	

model testing of fence.....	182
trajectory image	87
Run-out distance	
protection of facilities	61

S

Sampling point	
rock fall modeling	140
Sandstone/mudstone	
Japan test site.....	20
Scaling factor	
rock fall modeling	136
Seeder	
rock fall modeling	135
Service limit state	
hanging net.....	170
Shale	13
Simulation	
rock fall programs.....	131
Sliding	
rock fall modeling	138
Slip velocity.....	73, 213
Slope angle	
trajectory calculations	39
Slope material	
normal coefficient of restitution/impact angle relationship.....	98
Snow avalanche.....	170
Soil	
friction coefficient	102
Sphere	
angular velocity	56
CRSP analysis	135
impact equations.....	215
impact mechanics.....	93
Japan test site.....	22
rock fall modeling	138
volume, radius of gyration	79
Spline function (rock fall modeling)	135
Spreadsheet	
trajectory calculations	132
Standard deviation	
rock fall modeling	139
Stiff protection structure	
fence	173
Surface roughness	
rock fall modeling	138

T

Tabular	
rock fall modeling	138
Talus	
cone	62
Japan test site	23
treed slope.....	128
Tangential velocity	
changes during impact	69
final value equation.....	80, 217
Terminal velocity	47
Tetrahedral packing (DEM analysis)	141
Three dimensional modeling.....	134
Time – force plot	
fence design.....	171
protection structure	174
Tornado Mountain	
case study	24
energy loss.....	104
energy loss on bench.....	161
impact energy (calculated)	156
loss of mass	123
normal coefficient of restitution/impact angle relationship.....	96
restitution angles.....	53
rock fall modeling	152
trajectories (calculated).....	153
trajectory heights (calculated)	156
tree impact	127, 129
velocities (calculated).....	156
Trajectory	
asphalt test site	31
effect of angular velocity.....	59
effect of restitution angle.....	51
end points.....	11
equation	36
height.....	41
height equation	52
height, block shape.....	45
Japan test site	22, 44
length.....	41
Mt. Stephen	17
Oregon case study	19
spreadsheet calculations	133
Tornado Mountain	28, 46
Translational kinetic energy	
energy loss diagram.....	118
Tree	
friction coefficient	138

impact.....	24, 53, 133
impact energy.....	129
impact mark.....	35
impact, velocity reduction.....	128
stopping rock fall.....	127
whipping action.....	129
Tuff	
loss of mass.....	122
Two dimensional modeling.....	133
U	
Uniform energy absorption	
protection structures.....	169
V	
Velocity	
friction effect.....	48
Japan test site.....	47
rock fall.....	47
rock slope.....	47
slope angle effect.....	48
slope height effect.....	48
talus slope.....	47
trajectory calculations.....	38
Volume	
body shapes.....	78
W	
Windshield (damage).....	1
Worked example	
3A - trajectory co-ordinates.....	38
3B - trajectory calculations.....	43
3C - fall velocity.....	50
4A - impact final velocity.....	82
6A - energy loss normal impact.....	110
6B - energy loss oblique impact.....	114
6C - change in rotational energy.....	116
8A - velocity changes during oblique impact.....	164
8B - energy changes during oblique impact.....	167